FUEL PROCESSING SIMULATION TOOL FOR LIQUID-FUELED NUCLEAR REACTORS

BY

ANDREI RYKHLEVSKII

DISSERTATION

Submitted in partial fulfillment of the requirements
for the degree of Doctor of Philosophy in Nuclear, Plasma, and Radiological Engineering
in the Graduate College of the
University of Illinois at Urbana-Champaign, 2020

Urbana, Illinois

Doctoral Committee:

Assistant Professor Kathryn D. Huff, Chair
Associate Professor Tomasz Kozlowski
Professor James F. Stubbins
Professor Luke N. Olson

Abstract

Nuclear reactors with liquid fuel offer multiple advantages over their solid-fueled siblings: improved inherent safety, fuel utilization, thermal efficiency, online reprocessing, and potential for nuclear fuel cycle closure. To advance this promising reactor design, researchers need a simulation tool for fuel depletion calculations while taking into account online reprocessing and refueling.

This work presents a flexible, open-source tool, SaltProc, for simulating the fuel depletion in a generic nuclear reactor with liquid, circulating fuel. SaltProc allows the user to define realistically constrained extraction efficiency of fission products based on physical models of fuel processing components appearing in various Molten Salt Reactor (MSR) systems. Developed using a Python Object-Oriented Programming paradigm, SaltProc can model a complex, multi-zone, multi-fluid MSR operation and is sufficiently general to represent myriad reactor systems. Moreover, SaltProc can maintain reactor criticality by adjusting the geometry of the core. Finally, the tool can analyze power variations in the context of depletion.

This thesis also demonstrates and validates SaltProc for two prospective reactor designs: the Molten Salt Breeder Reactor (MSBR) and the Transatomic Power (TAP) MSR. A 60-year full-power MSBR depletion calculation with ideal fission product extraction (e.g., 100% of target poison removed) has been validated against Betzler *et al.* simulation results obtained with ChemTRITON at ORNL. The average ^{232}Th feed rate obtained is the current work is 2.40 kg/d, which is consistent with ORNL results (2.45 kg/d). This simulation showed that the online fission product extraction and online refueling with ^{232}Th allowed the MSBR to

operate at full power for 60 years due to exceptionally low parasitic neutron absorption.

This work shows fuel depletion simulations with SaltProc for the TAP MSR to demonstrate the tool capability to model liquid-fueled reactors with movable/adjustable moderator. This dissertation also validated depletion calculations for a realistic multi-component model of the fuel salt reprocessing system with assumed ideal extraction efficiency against full-core TAP depletion analysis by Betzler *et al.* from ORNL. The average SaltProc-calculated 5%-enriched uranium feed rate is 460.8 kg/y, which agrees well with the reference (480 kg/y).

This dissertation illuminated the impact of xenon extraction efficiency on the long-term fuel cycle performance for the realistic reprocessing system model of the TAP concept with non-ideal removal efficiency. For limited gas removal efficiency, the fuel salt composition is strongly influenced by the neutron spectrum hardening due to the presence of neutron poisons (^{135}Xe) in the core. Thus, more effective noble gas extraction significantly reduced neutron loss due to parasitic absorption, which led to better fuel utilization and extended core lifetime.

Additionally, this work investigated MSR load-following capability through short-term depletion analysis with the power level variation $P \in [0, 100\%]$. Online gas removal significantly improved the load-following capability of the MSBR by reducing xenon poisoning from -1457 *pcm* to -189 *pcm*. The TAP MSR demonstrated a negligible xenon poisoning effect even without online gas removal because its neutron energy spectrum is relatively fast throughout its lifetime.

This work also analyzed safety parameter (temperature and void coefficient of reactivity, total control rod worth, kinetic parameters) variation during operation using fuel composition evolution obtained with SaltProc. On a lifetime-long timescale, the safety parameters worsened during operation for both considered MSRs due to a significant spectral shift. On a short-term timescale, the safety parameters during MSBR load-following slightly worsened right after power drop because ^{135}Xe concentration peak caused substantial neutron spectrum hardening. However, during the next few hours, the gas removal system removed almost all ^{135}Xe from the fuel, which led to significant improvement in all safety parameters. Overall, a reduced amount of neutron poisons (e.g., ^{135}Xe) due to online gas extraction improved the safety case for both MSR designs.

Finally, a simple uncertainty propagation via Monte Carlo depletion calculations in this work showed that the nuclear-data-related error (0.5-8% depending on the nuclide) is two orders of magnitude greater than the stochastic error ($< 0.07\%$).

To my parents and my wife for their unconditional love and support.

To my daughters, Sofiya and Zoe, for being an inspiration.

Acknowledgments

I am grateful to many outstanding professors and colleagues at the University of Illinois at Urbana-Champaign, as well as the national laboratories, who have supported and encouraged me. I want to express my sincere gratitude towards my advisor, Professor Kathryn Huff, for her valuable support throughout this project. She offered perpetual encouragement, patience, and guidance without which I would not have been able to complete this thesis.

I would also like to thank the professors who served in my committee: Tomasz Kozlowski, James Stubbins, and Luke Olson, not only for reviewing and assessing this work but also for the knowledge and guidance they offered. I am similarly grateful to my internship advisor, Dr. Benjamin Betzler from ORNL, for his technical and practical guidance. Finally, I would like to thank Professor Rizwan Uddin for his expert assessment of this work.

Special thanks to the NPRE faculty and staff, who have continuously aided and guided me since my very first day on campus. I would like to thank Becky Meline for her help in planning and managing my graduate study process. At the risk of neglecting someone, I thank Barbara, Hannah, Margaret, Grace, and Kristie for their help in processing my paperwork, arranging examinations, and this thesis format check.

I would also like to thank my colleagues Jin Whan Bae, Alex Lindsay, Gavin Ridley, Gyu Tae Park, Greg Westphal, Sun Myung Park, Anshuman Chaube, Gwendolyn Chee, Roberto Fairhurst Agosta, Zoe Richer, Sam Dotson, and Mehmet Turkmen for their thoughts, valuable discussion, and help during my doctoral research and writing. I would like to recognize Matt Kozak for constructive criticism of the manuscript.

This work would not be accomplished without limitless love and support of my wife, Nelli, and my daughters, Sofiya and Zoe. Their support in my dark days and patience in listening to my complaints are priceless. I have wholehearted thankfulness for my mother and my sisters, who have always encouraged me in all my beginnings and without whom this work would not have been possible. Above all, I am particularly indebted to my father, Igor Rykhlevskii. He passed away shortly after my doctoral studies began but was and always will be in my heart, inspiring me in all my endeavors.

This work was carried out in the Advanced Reactors and Fuel Cycles Group (ARFC) of the University of Illinois at Urbana-Champaign. This work was supported by the U.S. Department of Energy ARPA-E MEITNER Program (award DE-AR0000983). This research is part of the Blue Waters sustained-petascale computing project, which is supported by the National Science Foundation (awards OCI-0725070 and ACI-1238993) and the state of Illinois. Blue Waters is a joint effort of the University of Illinois at Urbana-Champaign and its National Center for Supercomputing Applications.

Table of Contents

Chapter 1

Introduction

1.1 Motivation

Humankind has only a few ways to generate reliable, non-intermittent baseload power: fossil fuels, hydropower, geothermal power, and nuclear energy. Because of increasing global climate change concerns, sources with negligible CO_2 footprints are crucial measures for global temperature control. Thus, from an environmental viewpoint, hydro and nuclear power are preferable ways to generate reliable power. However, local geographical conditions limit the potential for hydropower; hence, the only option left is nuclear power. Nuclear power plants provided 10% of the global electricity supply in 2018 [51]. Moreover, nuclear share in energy generation is projected to stay constant through 2040, while electricity demand will increase by 30% [1]. This work pushes simulation tools with the potential to advance this vital option.

The Generation IV International Forum (GIF) chose MSRs among the six advanced reactor concepts for further research and development. MSRs offer significant improvements "in the four broad areas of sustainability, economics, safety and reliability, and proliferation resistance and physical protection" [34]. To achieve the goals formulated by the GIF, MSRs simplify the reactor core and improve inherent safety by using liquid coolant, which is also a fuel[1]. In a thermal spectrum MSR, liquid fuel consists of carrier salt (i.e., LiF, LiF-BeF_2, or LiF-NaF-KF) and fluorides of fissile and/or fertile materials (i.e., UF_4, PuF_3 and/or ThF_4). The fuel salt circulates in a loop-type primary circuit [47]. This innovation

---

[1] Herein MSRs are assumed to be reactors with liquid fuel, which simultaneously serves as a coolant.

leads to immediate advantages over traditional, solid-fueled reactors. These include near-atmospheric pressure in the primary loop, relatively high coolant temperature, outstanding neutron economy, a high level of inherent safety, reduced fuel preprocessing, and the ability to continuously remove fission products and add fissile and/or fertile elements without shutdown [59]. The possibility of continuously removing neutron poisons increases the potential fuel burnup and thus improves the resource utilization of MSRs. Finally, MSRs also could be employed for the transmutation of spent fuel from current Light Water Reactors (LWRs) [41].

Recently, interest in MSRs has resurged, with multiple new companies pursuing commercialization of MSR designs both domestically and internationally[2]. China's MSR program was initiated in 2011 and promises to start up a 2MW$_{th}$ liquid-fueled test MSR in 2020, a 10MW$_{th}$ demonstration reactor in 2025, and a gigawatt-level commercial reactor in 2050 [116]. The European Union funds the Safety Assessment of the Molten Salt Fast Reactor (SAMOFAR) project, in which several European research institutes and universities are developing various molten salt reactor prototypes such as the Molten Salt Fast Reactor (MSFR) [38] and the Molten Salt Actinide Recycler and Transmuter (MOSART) [52]. To advance these MSR concepts, particularly concerning their strategies for online reprocessing and refueling, we need computational analysis methods capturing their unique reactor physics, fuel reprocessing mechanics, and chemistry.

The context of this Ph.D. dissertation is the development and assessment of an advanced neutronics tool for fuel depletion calculations in circulating-fuel nuclear reactors. The present work introduces the open-source reprocessing simulation package, SaltProc [87], which couples with the continuous-energy Monte Carlo depletion calculation code, Serpent 2 [63], for fuel composition dynamics analysis in various MSRs taking into account a realistic, physics-driven model of an online fuel reprocessing system.

---

[2] Examples include liquid-fueled MSR designs from Terrapower, Terrestrial, ThorCon, Flibe, Copenhagen Atomics, Elysium, etc.

1.2 Fuel burnup and online reprocessing

All liquid-fueled MSR designs involve various levels of online fuel processing. Minimally, noble gaseous fission products (e.g., Kr, Xe) escape from the fuel salt during routine reactor operation and must be captured. Other systems might be used to enhance the removal of those elements. Most designs also call for the removal of rare earth metals from the core since these metals act as neutron poisons. Some designs suggest a more elaborate list of elements to process (Figure 1.1), including the temporary removal of protactinium from the salt or other regulation of the actinide inventory in the fuel salt [2]. Fresh fuel salt with dissolved fissile and/or fertile material (e.g., ^{233}U, ^{232}Th, low-enriched uranium (LEU), a transuranic vector from LWR spent nuclear fuel (SNF)) make up the salt mass loss caused by poison removal and conserves the total mass in the primary loop.

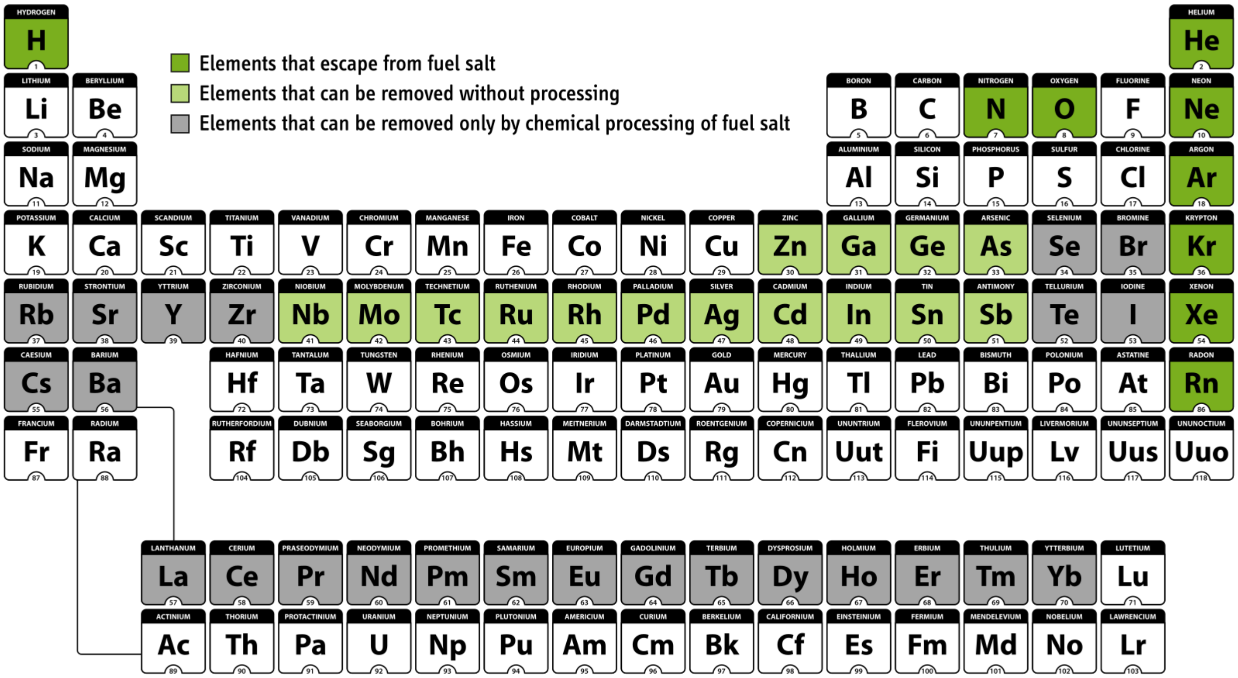

Figure 1.1: Processing options for MSR fuels (reproduced from Ahmed *et al.* [2]).

Most liquid-fueled nuclear reactor concepts adopt continuous separations and feeds: the core material is circulated to or from the core at all times (continuously) or specific intervals (batch-wise). In contrast, in a solid-fueled reactor, fission products and actinides remain within the initial fuel material throughout its time in the core.

The ability to perform online fuel salt reprocessing improves the potential neutronics performance of liquid-fueled reactors. First, liquid-fueled reactors can operate with relatively low excess reactivity because fissile material can be continuously added to the core. Second, continuously removing fission products, including strong absorbers (poisons), can significantly improve fuel utilization and decrease parasitic neutron absorption. Third, online reprocessing decreases the amount of decay heat, dissipating after shutdown. Finally, for a breeder[3] excess of fissile material might be continuously extracted from the core and used to startup new reactors. Nevertheless, the removal of each element from the liquid fuel salt presents a unique challenge in terms of chemical separation, storage, and disposal of the separated materials.

Contemporary nuclear fuel depletion software lacks continuous fuel salt reprocessing modeling. To handle material flows in potential online removal and feed of liquid-fueled systems, early MSR simulation methods at Oak Ridge National Laboratory (ORNL) integrated neutronics and fuel cycle codes (i.e., Reactor Optimum Design (ROD) [8]) into operational plant tools (i.e., Multiregion Processing Plant (MRPP) [55]) for MSR fuel reprocessing system design. Extensive research in fast and thermal MSR analysis has yielded specialized tools for burnup calculations in liquid-fueled nuclear systems [39, 97, 6, 48, 73, 15, 13]. Table 1.1 presents a list of recent efforts, along with the main features of the employed methods and software.

Two main online reprocessing simulation approaches have been demonstrated in the literature: batch-wise and continuous. In the batch-wise approach, the burnup simulation stops at a given time and restarts with a new liquid fuel composition (after removal of discarded materials and addition of fissile/fertile materials).

ORNL researchers have developed ChemTriton, a Python script for SCALE/TRITON,

---

[3] conversion ratio (CR) ≡ fissile generated/fissile consumed: if CR < 1, the reactor is a “converter”; CR $\equiv 1$, an “isobreeder”; CR > 1, a “breeder.”

Table 1.1: Tools and methods for liquid-fueled MSR fuel salt depletion analysis.

	Nuttin *et al.*, 2005 [71]	Aufiero *et al.*, 2013 [6]	Betzler *et al.*, 2018 [18]	Present work
Neutronics software	MCNP REM stochastic	Serpent 2 stochastic	SCALE6.2 ORIGEN-S deterministic	Serpent 2 stochastic
Geometry	unit cell	full-core 3D	unit cell	full-core 3D
Removal/feed	continuous	continuous	batch-wise	batch-wise
Separation efficiency	fixed, must be defined by user before simulation			function of many parameters
Fuel reprocessing plant	single component, "black" box model			realistic multi-component model
Reactivity control	continuous adjustment of fissile material injection		batch injection of fissile material	periodical adjustment of geometry and fissile material injection
Safety parameters evolution	thermal feedback	not considered	thermal feedback	thermal feedback, void reactivity coefficient, control rod worth

which employs the batch-wise approach to simulate a continuous reprocessing and refill for either single or multiple fluid designs. ChemTriton models salt treatment, separations, discharge, and refill using SCALE/TRITON depletion simulation over small time steps to simulate continuous reprocessing and deplete the fuel salt [18, 77].

In the continuous approach, accounting for removal or addition of material presents a greater challenge since it requires adding a term to the Bateman equations. Both ORIGEN [45] and the Serpent burnup routine [64] solves a set of the Bateman equations using one-group averaged flux and transmutation cross sections obtained from a transport calculation. The Bateman equations describe the rate of change of each isotope, i, due to neutron induced reactions and decay processes [109]:

$$\frac{dN_i}{dt} = \underset{(1)}{\sum_{m=1}^{M} l_{im}\lambda_m N_m} + \underset{(2)}{\phi\sum_{m=1}^{M} f_{im}\sigma_m N_m} - (\underset{(3)}{\lambda_i} + \underset{(4)}{\phi\sigma_i} + \underset{(5)}{r_i} - \underset{(6)}{f_i})N_i + F_i \Big| i \in [1, M] \tag{1.1}$$

where

N_i = number density of nuclide i $[cm^{-3}]$

M = number of nuclides $[-]$

l_{im} = fraction of decays of nuclide m that result in formation of nuclide i $[-]$

λ_i = radioactive decay constant of nuclide i $[s^{-1}]$

ϕ = neutron flux, averaged over position and energy $[cm^{-2}s^{-1}]$

f_{im} = fraction of neutron absorption by nuclide m leading to the formation of nuclide i $[-]$

σ_m = average neutron absorption cross section of nuclide m $[cm^2]$

r_i = continuous removal rate of nuclide i from the system $[s^{-1}]$

f_i = continuous feed rate of nuclide i $[s^{-1}]$

F_i = production rate of nuclide i directly from fission $[cm^{-3} \cdot s^{-1}]$.

The terms on the right-hand side of the equation represent:

(1) production of species i as a result of the decay of all the nuclides present;

(2) production of species i as a result of neutron capture by all nuclides present;

(3) loss of nuclide i through its own decay;

(4) loss of nuclide i as a result of neutron capture;

(5) loss of nuclide i through continuous removal from the system;

(6) gain of nuclide i as a result of continuous feed to the system.

Nuttin *et al.* developed an in-house depletion code called Rules for Evolution calculations with MCNP (REM), which directly couples with MCNP [111] to simulate fuel salt material evolution in a simplified MSBR-like liquid-fueled system. That work directly integrated the

Bateman differential equations using neutron flux from MCNP, tracking all the isotopes available in the data library, and controlling reactivity to maintain reactor criticality [71].

In a similar vein, Aufiero *et al.* extended Serpent 2 for continuous reprocessing simulations by adding an explicit pseudo-decay term representing fission product removal ($-N_i r_i$ term in Equation 1.1) for each target poisonous nuclide [6]. The developed extension directly accounts for the effects of online fuel reprocessing on depletion calculations and features a reactivity control algorithm. The extended version of Serpent 2 was assessed against a dedicated version of the deterministic ERANOS-based EQL3D procedure in [39] and applied to analyze the MSFR fuel salt isotopic evolution.

More recently, Betzler *et al.* added to SCALE/TRITON continuous removals capability for depletion simulation [13]. Similar to Aufiero *et al.* this extended SCALE/TRITON directly adds feed and removal terms in the burnup matrix and solves it using existing ORIGEN capabilities. TRITON's continuous reprocessing capability was validated against the batch-wise script ChemTriton for single-channel Molten Salt Reactor Experiment (MSRE)-like model. Unlike ChemTriton, this new capability will be available for all SCALE users in the 6.3 release. However, at the moment, it is undergoing extensive testing and validation procedures and unavailable for external users.

Some of the tools listed in Table 1.1 used significant approximations that may lead to inaccurate fuel evolution predictions and others unavailable for external users. This work introduces an open-source simulation package, SaltProc, which expands the capability of the continuous-energy Monte Carlo Burnup calculation code, Serpent 2, for depletion calculations of liquid-fueled MSRs.

Most of the existing tools in the literature represented the fuel salt reprocessing plant as an invariable "black box" model, which removes target elements all at once with a fixed efficiency, determined by the user before starting the depletion simulation. Typically, such a "black box" model is characterized by a vector of removing elements and their extraction efficiencies:

$$\begin{bmatrix} N_0^b \\ \vdots \\ N_e^b \\ \vdots \\ N_E^b \end{bmatrix} \times \begin{bmatrix} \epsilon_0 \\ \vdots \\ \epsilon_e \\ \vdots \\ \epsilon_E \end{bmatrix} = \begin{bmatrix} N_0^a \\ \vdots \\ N_e^a \\ \vdots \\ N_E^a \end{bmatrix} \tag{1.2}$$

where

N^b = number density vector before reprocessing $[cm^{-3}]$

N^a = number density vector after reprocessing $[cm^{-3}]$

ϵ = extraction efficiency $[-]$ vector for all elements e in $(0, E)$.

The main issues related to static "black box" model assumptions in the literature neglect:

Time varying extraction. Realistically, long-term reactor operation will require a time-dependent extraction efficiency vector. The current tools treat separation efficiency as constant.

The impact of operational parameters on separation efficiency. In reality, the extraction efficiency depends on temperature, power level, current fuel salt isotopic composition, and material mass flow rate. Gas solubility in the salt is inversely proportional to the salt temperature; hence, the extraction efficiency expected to be lower for the higher temperature of the salt.

Discrete component performance and dynamics in the multi-component system. All reprocessing plant components are treated as a single "black box" component in existing simulation tools. However, the fuel salt in a reprocessing plant undergoes many separate components (e.g., helium bubbling, nickel mesh filter, etc.) that target specific elements. Some of these components can be connected in series, parallel, or series-parallel. The "black box" model (only single process) requires extensive pre-simulation analytic work from the user to calculate the lumped separation efficiency vector before a simulation is run and cannot be adjusted during the simulation. Additionally, treating the processing system as a single "black box" neglects dynamics related to relative component flow rates. Finally, the discrete waste streams from each component are not tracked separately in "black box" tools. However, this information is necessary for fuel reprocessing system optimization.

In contrast with tools listed in Table 1.1, SaltProc, does not make these approximations. SaltProc allows the user define the separation efficiency as a function of time or operational parameters, and is able to simulate multi-component fuel reprocessing system instead of "black box".

1.3 Operational and safety parameter evolution

In contrast with conventional solid-fueled reactors with in-core fuel residence averaging 4-5 years[4], an initial MSR fuel salt batch stays in the MSR primary loop throughout the reactor lifetime. Therefore, the fuel salt accumulates Fission Products (FPs) not captured by the fuel reprocessing system as well as transuranic elements[5]. Continuous fuel salt composition evolution has a significant influence on the neutron energy spectrum and, consequently, affects the reactor behavior, necessitating additional safety analysis.

Nuttin *et al.* studied the evolution of a key safety parameter, the temperature reactivity feedback coefficient, estimating it for the MSBR at startup and equilibrium. The temperature coefficient of reactivity quantified reactivity changes due to temperature increase in the

---

[4] For the typical 18-month cycle, during refueling personnel removing 1/3 of the fuel assemblies, re-arranging other assemblies, and loading fresh fuel into the core. Thus, each fuel assembly is kept in the core at most $3 \times 18 = 54$ months.

[5] The chemical elements with atomic numbers greater than uranium (92).

core and was calculated in that work as:

$$\alpha = \frac{k_{1200} - k_{900}}{\delta T} \tag{1.3}$$

where

$$k_{900}, k_{1200} = \text{multiplication factor at 900K and 1200K } [-]$$
$$\delta T = 300 \; [K].$$

That work showed that the fuel temperature coefficient (FTC) at startup and equilibrium is -1.5 and -1.0 pcm/K, respectively[6]. Nuttin *et al.* also reported a positive and time-invariant total temperature coefficient (+0.8 pcm/K) [71]. Recently, Park and colleagues expanded that approach to a full-core high-fidelity MSBR model and estimated safety parameters evolution over 20 years of operation [73]. These calculations showed a relatively large negative total temperature coefficient during the 20-year reactor operation. During that time, the coefficient magnitude weakens from -3.21 to -1.41 pcm/K from startup to equilibrium, respectively. Additionally, that work reported a control rod worth deterioration from 2099 to 1970 pcm due to neutron spectrum hardening during reactor operation.

More recently, Betzler *et al.* [17] reported safety parameter evolution for the TAP MSR: the fuel reactivity coefficient at Beginning of Life (BOL) and 15 years from BOL was negative and decreasing slowly over the reactor lifetime (from -4.0 to -4.1 pcm/K when temperature was perturbed from 900K to 1200K); the moderator reactivity coefficient was +0.43 pcm/K at BOL and -2.7 pcm/K after 15 years of operation. Overall, thermal feedback seems to be stronger in the TAP reactor and deteriorates insignificantly during the reactor operation. Notably, the authors ignored material density change with temperature to simplify temperature coefficient calculation; thus, only Doppler broadening was taken into account. The

---

[6] 1 pcm = $10^{-5}\Delta k_{eff}/k_{eff}$

researchers reported the total worth of all control rods in the TAP core only for the startup fuel composition.

The evolution of control rod worth in the TAP has not been reported in the literature before. Section 4.4 of this dissertation illuminated the evolution of essential safety parameters (fuel, moderator, total temperature coefficient, control rod worth) for the TAP MSR at various moments during the reactor operation. Additionally, I investigated the impact of neutron poison accumulation (e.g., ^{135}Xe) in the fuel salt during short-term transients (i.e., load following) on major safety characteristics [94].

1.4 Background Summary

State-of-the-Art software packages for depletion analysis and evolution of safety parameters in the liquid-fueled MSR are reviewed in Section 1.2. Based on this summary, I have identified a few possible directions for the improvement of MSR tools:

Reproducibility/availability. Serpent is the only contemporary nuclear reactor physics software that can perform depletion calculations that can take into account online fuel salt reprocessing regimes. However, this built-in online reprocessing routine is undocumented: the discussion forum for Serpent users is the only useful source of information at the moment. Other mentioned tools are available for internal users only. These issues can be a barrier to reuse research software and to reproduce scientific results. Thus, a new, open-source, reproducible tool for fuel processing simulation would assist in the production of reproducible research in the area of liquid-fueled reactor modeling.

Realistic fuel reprocessing system model. Significant approximations in fuel reprocessing parameters deteriorate fuel salt composition predictions since the evolution of safety parameter accuracy is strongly dependent on fuel salt composition. A realistic fuel reprocessing system model will allow reprocessing component parameter optimization, increase the fidelity of fuel and waste stream composition calculations, and advance reprocessing system design.

Variable extraction efficiency. Most research efforts in the literature (except Nuttin *et al.*[7]) assume ideal 100% extraction efficiency of all removed elements, which stayed constant during the whole reactor lifetime. Realistically the efficiency is time-dependent and changes with respect to operational parameters: temperature, power level, salt composition, etc. Thus, the ability to set up dynamic separation efficiency must be added in MSR simulation tools to advance depletion calculations.

Reactivity control. Reconfigurable moderator configuration in the TAP core presents a challenge because of the core geometry changes with time. The reactivity control module, which adjusts the core geometry to maintain criticality, is an exceptional capability for simulating new, more advanced MSR concepts and short-term transients.

Safety characteristics evolution during reactor operation. The MSR fuel salt accumulates FPs and transuranic elements, which significantly shift the neutron energy spectrum. This spectrum shift might worsen the core safety during operation. The impact of the fuel salt evolution on the MSR safety parameters must be carefully investigated and reported.

This work aims to overcome these issues and demonstrate the tool capabilities for a two promising MSR concepts.

1.5 Objectives and outline of the work

Most of the existing MSR depletion simulators usually assume ideal efficiency (100% of the target nuclide is being removed) of the neutron poison removal process (see Section 1.2). The

---

[7] Nuttin *et al.* assumed 100% extraction efficiency for noble gases (Xe, Kr) and protactinium, 20% for rare earths, 5% for semi-noble metals, and 1% for alkaline elements [71].

main goal of this dissertation is to develop a generic, open-source tool, SaltProc, capable of simulating a wide range of liquid-fueled systems — including multi-fluid and multi-region designs — and validate it against existing modeling efforts. Additionally, SaltProc enables poison extraction simulation based on a realistic physics-based fuel processing model.

The structure of the thesis is as follows. Chapter 1 serves as a literature review, providing background on fuel burnup, online fuel reprocessing approaches, safety parameter evolution during reactor operation, and how these concepts have been applied to a wide range of MSRs in the literature. Chapter 2 details online reprocessing modeling and the proposed computation tool architecture. In an attempt to avoid the pitfalls of a "black box" understanding and to identify method limitations at an early stage, governing equations and working principles are stated and discussed. Chapter 3 presents equilibrium-seeking results for the MSBR as well as essential operational and safety parameters for both the initial and equilibrium states.

Additionally, the benefits of continuous fission product removal for a thermal MSR are evaluated at the end of chapter 3. Chapter 4 covers SaltProc demonstration and validation efforts with a focus on the TAP MSR, taking into account adjustable moderator configuration. In addition, Chapter 4 gives the safety parameter overview and its evolution during the TAP lifetime-long reactor operation. SaltProc demonstration for short-term depletion calculations and evaluation of load-following potential of the TAP MSR and the MSBR are presented in Chapters 5 and 6. Moreover, the safety parameters dynamics during short-term transients have been evaluated at the end of Chapter 5 and 6. Chapter 7 presents a simple uncertainty propagation via depletion calculation for the TAP concept. The final chapter summarizes this work's contribution to the nuclear community, and a conclusion is offered together with an outlook for future work on the topic.

Chapter 2

Online reprocessing modeling approach

2.1 Fuel salt reprocessing overview

Removing specific chemical elements from a molten salt is a complicated task that requires intentional design (e.g., chemical separations equipment design, fuel salt flows to equipment). This section contains a brief overview of a generic MSR fuel salt reprocessing system; modeling such systems is the focus of the current dissertation.

2.1.1 Gas separation system

Gaseous fission products (e.g., Xe) must be removed from the fuel salt to avoid reactor poisoning, especially during startup and power maneuvering. This is particularly true for ^{135}Xe, with its strong neutron capture cross section ($\approx 10^6 \ldots 10^7$ b in a thermal energy range). ^{135}Xe is produced directly from fission in about 0.2% of ^{235}U fissions ($\gamma_{^{135}Xe}$), but an even larger fraction of ^{135}Xe is produced by the decay of ^{135}I and ^{135}Te (Table 2.1). ^{135}I and ^{135}Te yields from fission are $\gamma_{^{135}I} = 3.1\%$ and $\gamma_{^{135}Te} = 3.3\%$, respectively. Thus, the total ^{135}Xe production from fission is about 6.6% of fissions (of ^{235}U), most of this is from ^{135}I and ^{135}Te decay. Noble gases (e.g., tritium, xenon, and krypton) can be removed from the fuel salt as follows:

(a) a bubble generator injects helium bubbles in the salt stream;

(b) noble gases migrate to the helium bubbles due to their insolubility in the salt [83];

(c) and a gas separator discharges the fission-product-rich bubbles from the salt to the off-gas system.

Table 2.1: ^{135}Xe production sources and principal rate constants involved (reproduced from Kedl *et al.* [54]).

^{135}**Xe gain mechanism**	**Principal rate parameters involved**
Direct from fission yield $\gamma_{^{135}Xe}$= 0.0022	$\Sigma_f \gamma_{^{135}Xe} \phi$ (for ^{235}U fission)
^{135}I decay yield $\gamma_{^{135}Xe}$= 0.031, it decays to ^{135}Xe with $\tau_{1/2}$ = 6.68 h	$\Sigma_f \gamma_{^{135}I} \phi$ (for ^{235}U fission)
^{135}Te decay yield $\gamma_{^{135}Xe}$= 0.033, it decays to ^{135}I with $\tau_{1/2}$ = 19 s	$\Sigma_f \gamma_{^{135}Te} \phi$ (for ^{235}U fission)

Figure 2.1 shows the key pathways for xenon production, accumulation, and removal in a typical MSR. Figure 2.2 shows the conceptual design of the MSBR gas separation system. In that system, helium bubbles of a specific size are introduced in a salt stream via the primary pump bowl. These bubbles absorb noble gases before being separated from the salt by a gas separator. ORNL suggested that the MSBR off-gas system would inject $d = 0.508mm$ helium bubbles in the pump bowl, redirect 10% of the fuel salt flow through a bubble separator to remove the bubbles, and then return the flow into the pump suction. Robertson *et al.* reported that the helium bubble size was approximately 25% of the throat width (blue circle on Figure 2.3) and was independent of the gas flow rate [83]. Consequently, it is possible to regulate the helium bubble size by changing the throat width in the bubble generator.

To realistically model the gas separation system, we need a mathematical model that describes noble gas extraction efficiency during reactor operation. Particularly, a model of xenon extraction efficiency as a function of sparger design parameters is needed to accurately model the ^{135}Xe removal in a fuel salt depletion simulation. The gain and loss terms for ^{135}Xe dissolved in the fuel salt are listed in Tables 2.1 and 2.2. The removal efficiency for the xenon in the pump bowl was measured during Molten Salt Reactor Experiment (MSRE) operation.

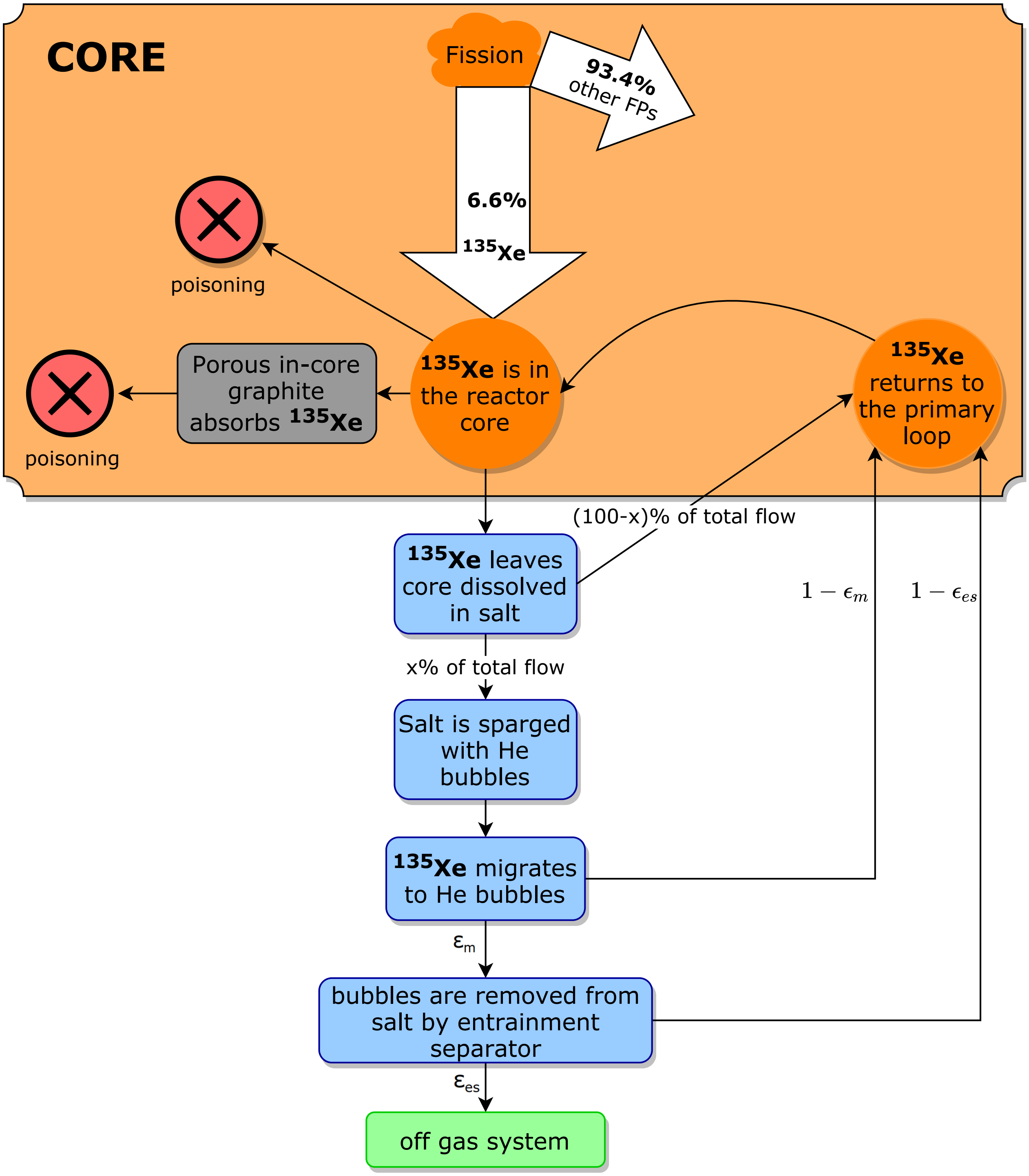

Figure 2.1: Schematic of ^{135}Xe circulation in a generic MSR. x is the fraction of fuel salt flow from the pump discharge redirected to the gas separation system, while ϵ_m and ϵ_{es} are the efficiencies of migration (of ^{135}Xe to the helium bubbles in the sparger) and separation (of gas in the entrainment separator), respectively. The orange color represents the fuel salt in the primary loop, the blue color represents the gas separation system, and the gray color is the moderator in the core. Fission yields assume ^{235}U fission only.

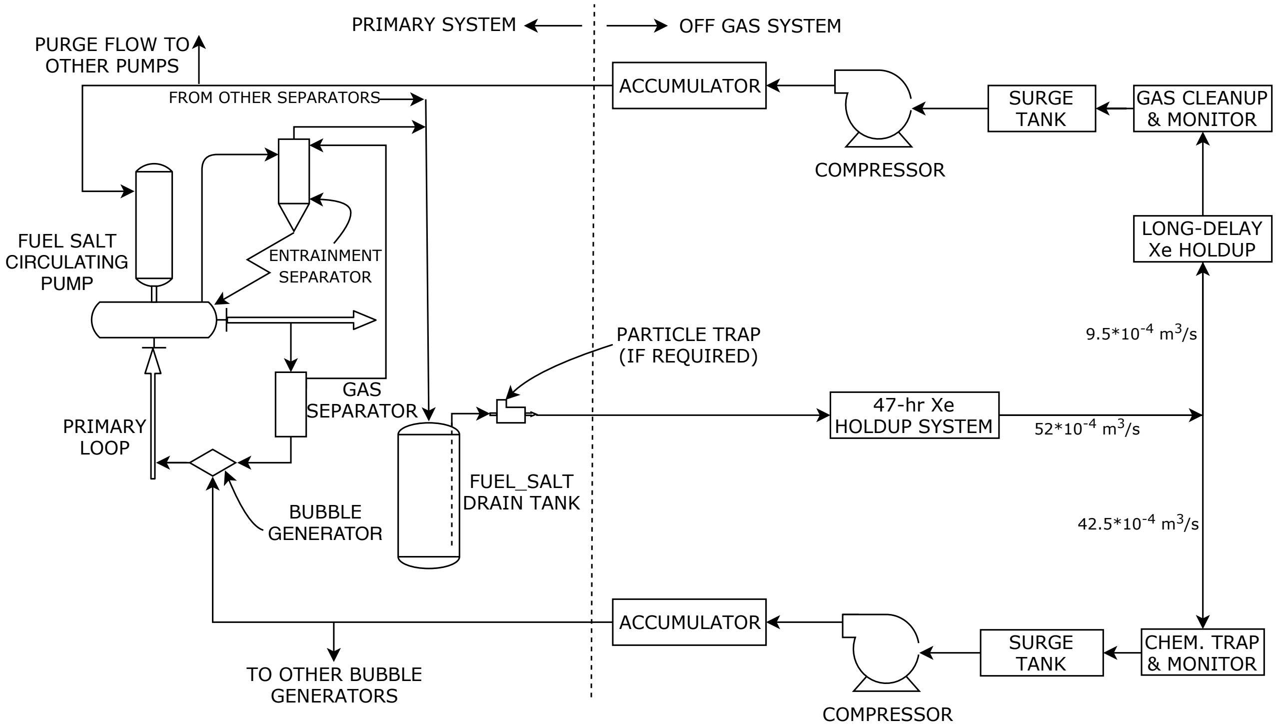

Figure 2.2: Schematic flow diagram of the MSBR gas separation system (reproduced from Robertson *et al.* [83]).

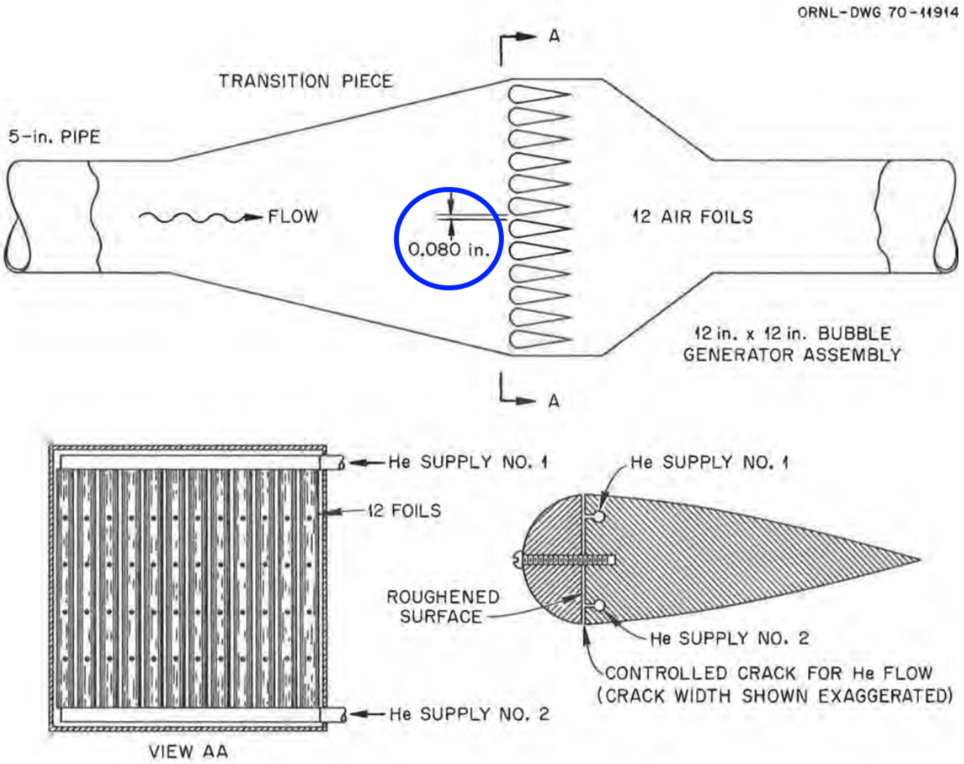

Figure 2.3: Preliminary concept of an MSBR bubble generator (reproduced from Robertson *et al.* [83]). The blue circle shows throat width, which determines bubble size.

Table 2.2: ^{135}Xe loss terms and principal rate constants involved (reproduced from Kedl *et al.* [54]).

^{135}Xe loss mechanism	**Principal rate parameters involved**
Decay of dissolved ^{135}Xe ($\tau_{1/2}$ = 9.1 h)	Decay constant (λ)
^{135}Xe burnup dissolved ^{135}Xe burnup as it passes through the core	Neutron flux (ϕ)
^{135}Xe migrated to helium bubbles	Removal efficiency (ϵ_m)
^{135}Xe transferred into circulating He bubbles; this xenon will eventually be burnup, decay, or stripped via bubble separator	Mass transfer coefficient (h), decay constant (λ), neutron flux (ϕ), bubble removal efficiency (ϵ_{es})

However, the technical report ORNL-4069 by Kedl-Houtzeel only stated its range (from 50 to 100%) and concluded, "It is probably a complex parameter like the circulating-void fraction and depends on many reactor operational variables" [54].

Peebles *et al.* in ORNL-TM-2245 has reported xenon removal efficiency (ϵ_{Xe}) in a gas separation system as a function of many parameters [74]:

$$\epsilon_m = \frac{1 - e^{-\beta}}{1 + \alpha} \tag{2.1}$$

where

$$\alpha = \frac{RT}{H} \cdot \frac{Q_{salt}}{Q_{He}} \tag{2.2}$$

$$\beta = \frac{K_L a A_C L(1 + \alpha)}{Q_{salt}} \tag{2.3}$$

R = universal gas constant $[L \cdot Pa \cdot mol^{-1} \cdot K^{-1}]$

T = salt temperature $[K]$

H = Henry's law constant for solute gas $[Pa \cdot mol^{-1} \cdot L]$

Q_{salt} = volumetric salt flow rate $[m^3/s]$

Q_{He} = volumetric helium flow rate $[m^3/s]$

K_L = liquid phase mass transfer coefficient $[m/s]$

a = gas-liquid interfacial area per unit volume $[m^{-1}]$

A_C = contactor cross section $[m^2]$

L = contactor length $[m]$.

Most of the input parameters for that correlation are obvious and easy to obtain from the system component design. The mass transfer coefficient for transferring xenon into helium bubbles (K_L) can be estimated experimentally, but published information is currently insufficient to inform an accurate mathematical model appropriate for Computational Fluid Dynamics (CFD). Thus, Peebles *et al.* reported the mass transfer coefficient correlation for the MSBR salt (LiF-BeF$_2$-ThF$_4$-UF$_4$) but for a limited case. While it is out of the scope of this work to accurately estimate mass transfer coefficient, this work seeks to provide a tool which would allow the user to specify any mathematical model for a separation efficiency. Provided a mass transfer coefficient, the user can incorporate it into the model.

Equation 2.1 would apply to other noble gases (e.g., Kr), but Henry's law constant (H) varies by element. Current effort at the University of Illinois at Urbana-Champaign, namely "Enabling Load Following Capability in the Transatomic Power MSR," [50] has a goal to determine mass transfer coefficients for various gaseous fission products (Ar, Kr, Xe) using experiments, enabling CFD and multi-physics simulations of such reactors. As a result, the obtained mathematical model for gas removal efficiency might be employed to inform a realistic physics-based fuel reprocessing model in SaltProc.

2.1.2 Insoluble fission product filtering

Approximately 40% of FPs have gaseous elements in their decay chains. Some of the non-gaseous FPs produced in the MSR core (e.g., noble and semi-noble metals) have negligible solubility in the molten salt. Some fraction of noble and semi-noble solid FPs plate out onto the internal surfaces of the primary loop equipment, complicating their removal [22]. The remaining noble and semi-noble metals can be removed along with corrosion products using a mechanical filtration system, which "consists largely of a high surface area mechanical filter, likely a nickel mesh, to promote deposition of suspended, undissolved fission and corrosion products," according to Holcomb *et al.* [49]. The filter is manufactured from porous metal, has limited capacity, and needs periodic replacement. The filter replacement must be done using remote-controlled equipment due to high radiotoxicity of undissolved FPs and residual fuel salt remaining on the filter [69].

The historic MSRE program provided basic information design and performance of the large mechanical filter. Figure 2.4 shows the piping layout of the filter, storage, and processing tanks. The filter pressure vessel is made of high-nickel alloy (Inconel) and accommodates 40-μm pore size sintered Inconel fibers. This large molten salt filter had a total filtering area of $0.8m^2$ and was designed to filter approximately 1 kg of the molten salt per minute, but the removal efficiency has never been reported. Also, the design of the filter, the filter holder, and the remotely operated equipment for the filter replacement for commercial-scale MSR designs presents a significant engineering challenge [69].

In this work, we assumed ideal, constant separation efficiency in the filtering system. However, in the future, a physics-driven mathematical formula can be used when the experimental data or analytical model will be available.

2.1.3 Fuel chemical processing facility

In addition to noble gases, noble metals, and semi-noble metals, the fuel salt reprocessing system must extract other FPs such as the lanthanides. These absorb fewer neutrons than ^{135}Xe, but their removal is crucial to guarantee normal operation. Unfortunately, lanthanides have relatively high solubility in the carrier salt and must be removed by chemical extraction.

In thorium-fueled MSR designs, ^{232}Th in the fuel salt absorbs thermal neutrons and produces ^{233}Pa, which then decays into the fissile ^{233}U (Figure 2.5). Protactinium presents a

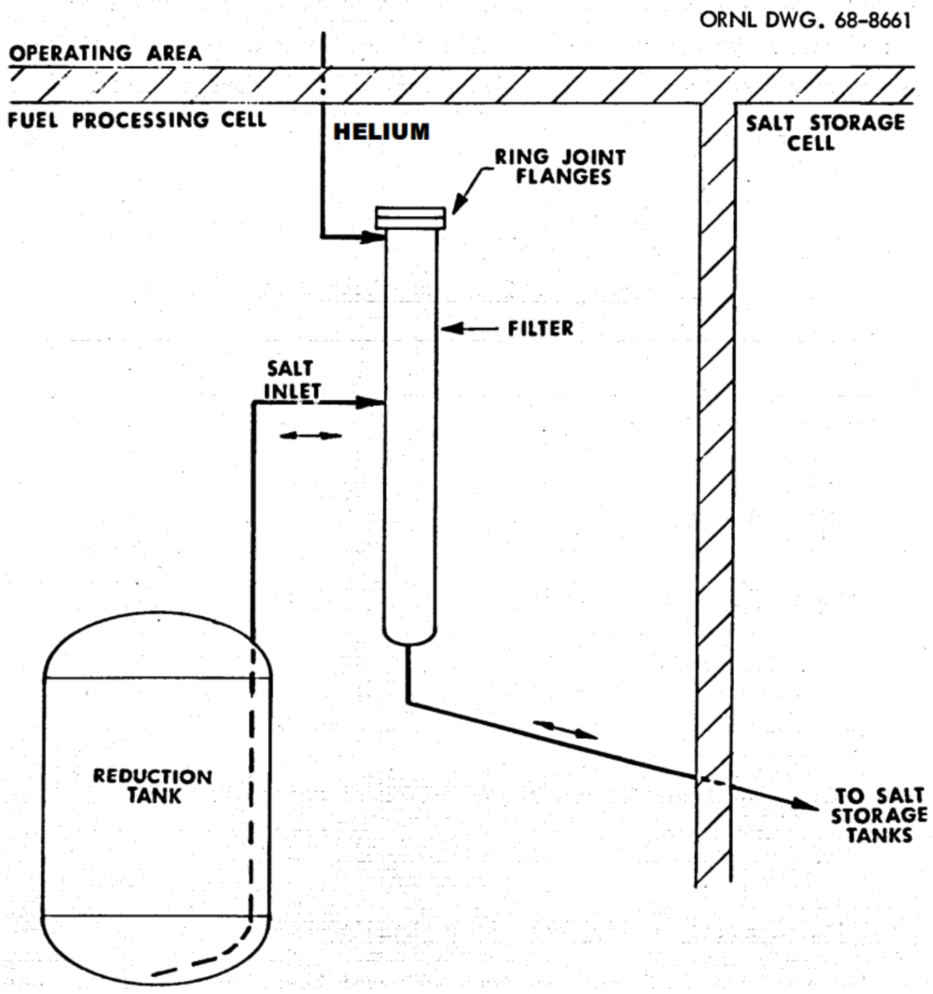

Figure 2.4: Schematic flow diagram of the large molten salt mechanical filter designed and operated during the MSRE (reproduced from Lindauer *et al.* [65]).

challenge since it has a large absorption cross section in the thermal energy spectrum. Accordingly, ^{233}Pa is continuously removed from the fuel salt into a tank in which ^{233}Pa decays to ^{233}U without poisoning the reactor. This feature allows the thorium-fueled MSR to avoid neutron losses to protactinium, keeps FPs on a trace level, and increases the efficiency of ^{233}U breeding.

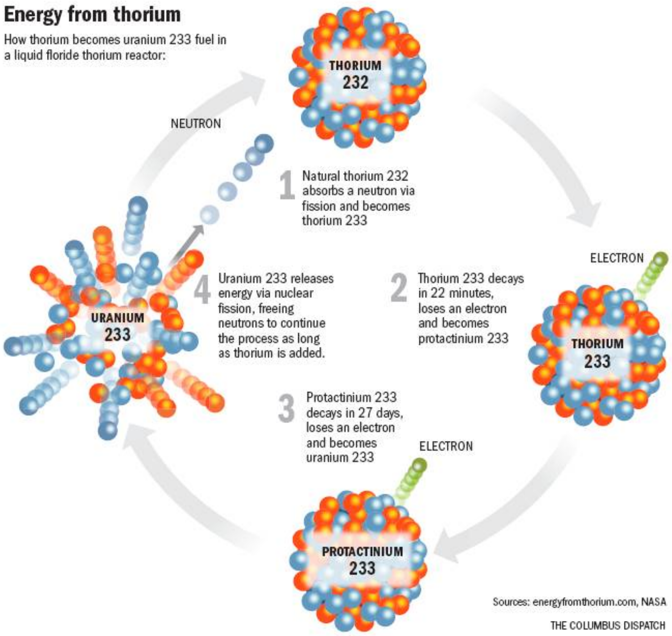

Figure 2.5: Production of ^{233}U from ^{232}Th (reproduced from Sorensen [98]).

Many authors report that a liquid-liquid reductive extraction process is the best option for removing protactinium and soluble FPs from molten fluoride salts [23, 33, 35]. In that process, the protactinium or lanthanides can be selectively stripped from the salt into liquid bismuth due to different chemical potentials. Moreover, the MSRE experience indicated that the extraction could be carried out rapidly and continuously [112].

The principal scheme of the MSBR reprocessing facility concept is shown in Figure 2.6. The fuel salt is first temporarily stored for cooling and decay of the shortest-lived fission products, then it is directed to the primary fluorinator. There, most of the uranium is removed by fluorination to UF_6. After that, the salt is routed to an extraction column where it is combined with a mixture containing metallic bismuth, lithium, and thorium reductants.

The remaining uranium and protactinium are reductively extracted to a bismuth solution, leaving a salt that only contains fission products dissolved in carrier salt (base composition LiF-BeF_2-ThF_4). The salt then goes through a reduction column where UF_6 is reduced to UF_4, preparing it for return to the reactor. BeF_2 and ThF_4 are also added and all residual bismuth is removed from the salt. After a final cleanup step and valence adjustment, the purified salt returns to the reactor [26, 98].

The bismuth, accommodating some uranium and protactinium, is routed to a hydrofluorination column where metallic solutes in the bismuth are oxidized into their fluoride forms in the presence of a decay salt[1]. The decay salt, containing UF_4, PaF_4, and ThF_4, passes into a decay tank where ^{233}Pa decays to ^{233}U. The uranium generated by protactinium decay is removed through fluorination to UF_6 and directed to the reduction column to refuel the purified fuel salt. A hydrofluorinator and a fluorinator can remove approximately 95% of the uranium from the stream [83].

To maintain or adjust the fissile material concentration in the reactor (and, consequently, control the reactivity), ^{233}U is added from the protactinium decay tank to fully processed salt on its way back to the reactor. Adding fissile material is performed by sparging the salt with UF_6 and hydrogen to produce UF_4 in the salt and HF gas [83].

After these separation steps, the fuel salt stream from the protactinium isolation system contains only traces of protactinium and uranium but contains practically all of the rare earths. A fraction of this salt stream is redirected to a reductive extraction process for removing rare earths. The principal scheme of a rare earth removal system is shown in Figure 2.7. A molten salt flow that contains rare earth fluorides is fed to the center of an extraction column. The salt flows countercurrent to a liquid bismuth stream, which contains thorium and lithium. In the upper part of the column, the rare earths are reduced and transferred to the downflowing liquid metal stream. Below the feed point, the rare earth

---

[1] The decay salt contains UF_4, PaF_4, ThF_4 and FPs. Uranium produced after ^{233}Pa decay is extracted and directed back into the reactor. Decay salt is the precursor for the waste salt as it was periodically discarded every 220 days [83].

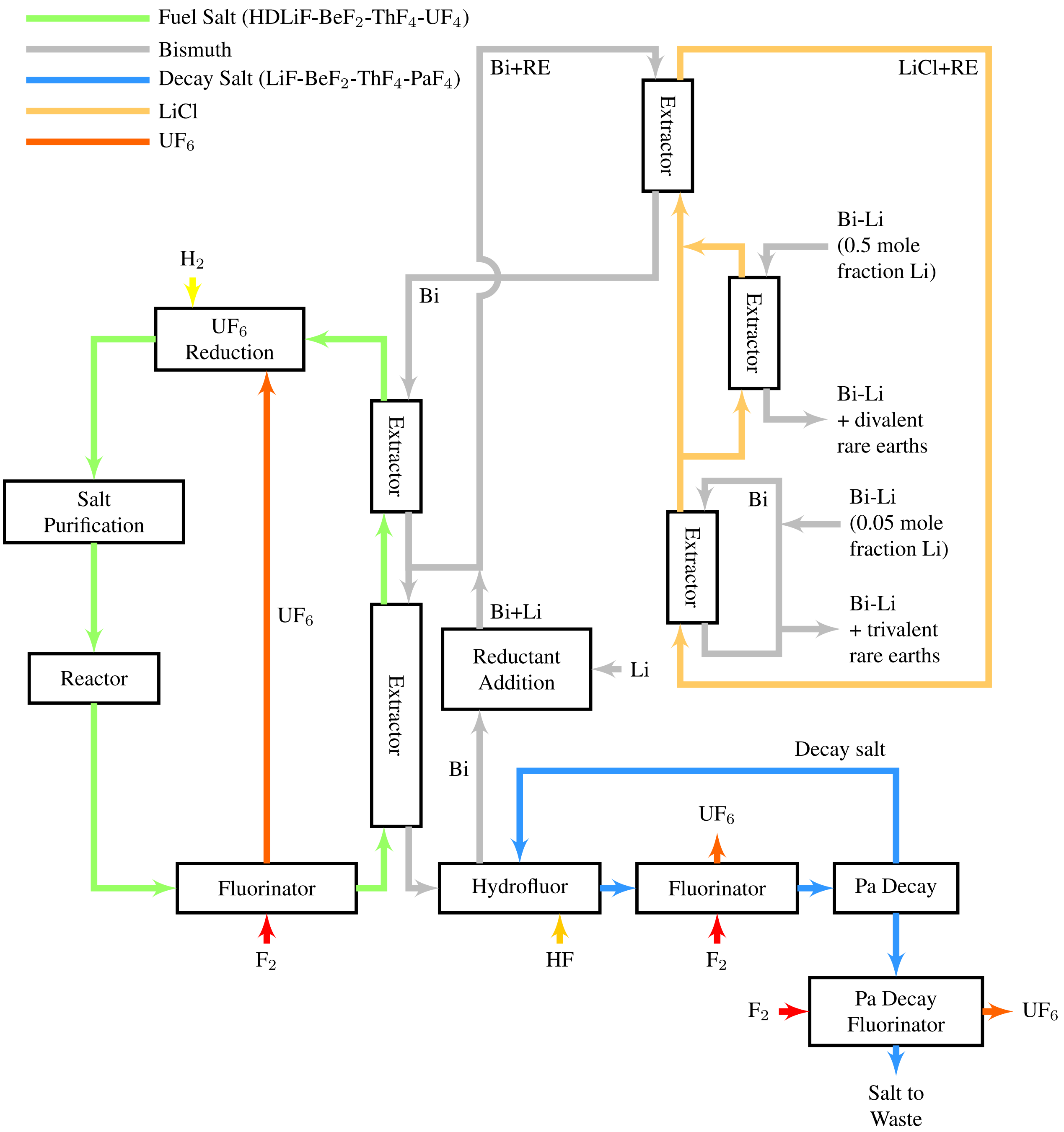

Figure 2.6: Simplified block diagram of chemical processing scheme for a single-fluid MSBR (reproduced from Sorensen [98]). *RE* represents the rare earth elements extracted from the salt.

concentration is increased in the salt and metal streams in order to produce a concentration high enough for disposal [23].

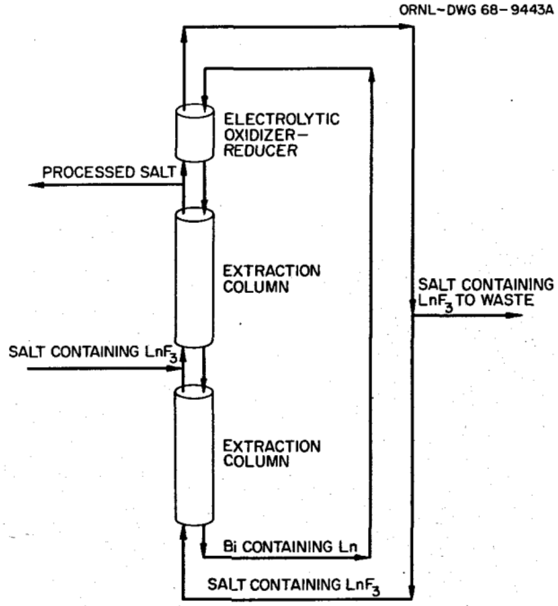

Figure 2.7: Rare earth removal from a fuel salt by reductive extraction (reproduced from Briggs *et al.* [23]).

While it is out of the scope of this work to derive the accurate chemistry-based mathematical formula for rare earths and protactinium separation efficiency, this work seeks to provide a flexible tool that is able to simulate chemical processes in significant detail concerning vital system design parameters.

2.2 Serpent overview

Serpent is a continuous-energy Monte Carlo neutronics software capable of solving the neutron transport problem by tracking individual neutrons within the problem geometry and using the stochastic method to determine the chain of events for each neutron [63]. Serpent is under active development at the VTT Technical Research Centre of Finland since 2004, where it was initially conceived as a tool to simplify group constant generation in a high-fidelity Monte Carlo environment. Serpent is now widely used by more than 500 registered individuals in 155 organizations located in 37 countries around the world. The burnup calculation capability in Serpent is based on built-in calculation routines without using any external solvers. A restart feature enables fuel shuffling simulation or applying any modifications to the input by dividing the calculation into several parts, which is crucial for online reprocessing simulations.

The latest version, Serpent 2, supports advanced geometries and universe transformation that are necessary for neutronics modeling of advanced nuclear reactors. Additionally, multiphysics simulations using Serpent 2 have been demonstrated, including calculations with thermal-hydraulics, CFD, and fuel performance codes [62].

Serpent 2 can be effectively run in parallel on computer clusters and multi-core workstations. Parallelization is handled by thread-based OpenMP, which enables all processors to use shared memory space. Calculations can be divided into several nodes by distributed-memory Message Passing Interface (MPI) parallelization. Serpent 2 is an improvement upon Serpent 1 and contains a complete redesign of memory management using hybrid OpenMP [32] + MPI parallelization. This hybrid parallelization is substantial for depletion calculations using computer clusters with multiple nodes and allows us to achieve significant speed-up in depletion calculations on computer clusters with more than 4,000 cores [63].

Simulations herein were performed using Serpent 2 version 2.1.31 on both the National Center for Supercomputing Applications' Blue Waters and Idaho National Laboratory's Falcon supercomputers. The JEFF-3.1.2 [72] and ENDF/B-VII.1 [27] libraries provided nuclear data for all calculations in this dissertation.

2.3 Simulation tool design and capabilities

The first version of the SaltProc tool for calculating MSR fuel composition evolution, taking into account an online reprocessing system, was developed in 2018 as a part of my M.S. thesis [87, 85]. The tool was designed to expand Serpent 2 depletion capabilities for modeling liquid-fueled MSRs with online fuel reprocessing systems. SaltProc v0.1 uses HDF5 [46] to store data and the PyNE Nuclear Engineering Toolkit [96] for Serpent 2 output file parsing and nuclide naming. SaltProc v0.1 is an open-source Python package that uses a batch-wise approach to simulate continuous feeds and removals in MSRs.

SaltProc v0.1 only allows 100% separation efficiency for either specific elements or groups of elements at the end of the specific "cycle time"[2]. Capabilities of the developed tool, working with the Monte Carlo software Serpent 2, were demonstrated using the full-core MSBR design for a simplified case with ideal removal efficiency (100% of mass for target elements removed) [88]. Chapter 3 covers the summary of this effort. The SaltProc v0.1 architecture and the principal structure were not designed for flexible implementation of sophisticated online reprocessing systems, including realistic variable extraction efficiencies.

In the current work, SaltProc v0.1 was completely refactored using Object-Oriented Programming (OOP) to create a comprehensive generic tool to realistically model complex MSR fuel reprocessing systems while taking into account variable extraction efficiencies, time-dependent core geometry, and the mass balance between the core and the reprocessing plant.

2.3.1 Software architecture

The SaltProc v1.0 Python toolkit couples directly with Serpent 2 input and output files, to couple the reprocessing system to depletion calculation. Python 3 OOP standard features are used to create a flexible, user-friendly tool with great potential for further improvement and collaboration. Figure 2.8 shows the SaltProc v1.0 class structure which includes 4 main classes:

Depcode. *Depcode* class contains attributes and methods for reading the user's input file for the depletion software, initial material (e.g., fuel and/or fertile salt) composition,

---

[2] The MSBR program defined "cycle time" as the time required to remove 100% of a target nuclide from a fuel salt [83].

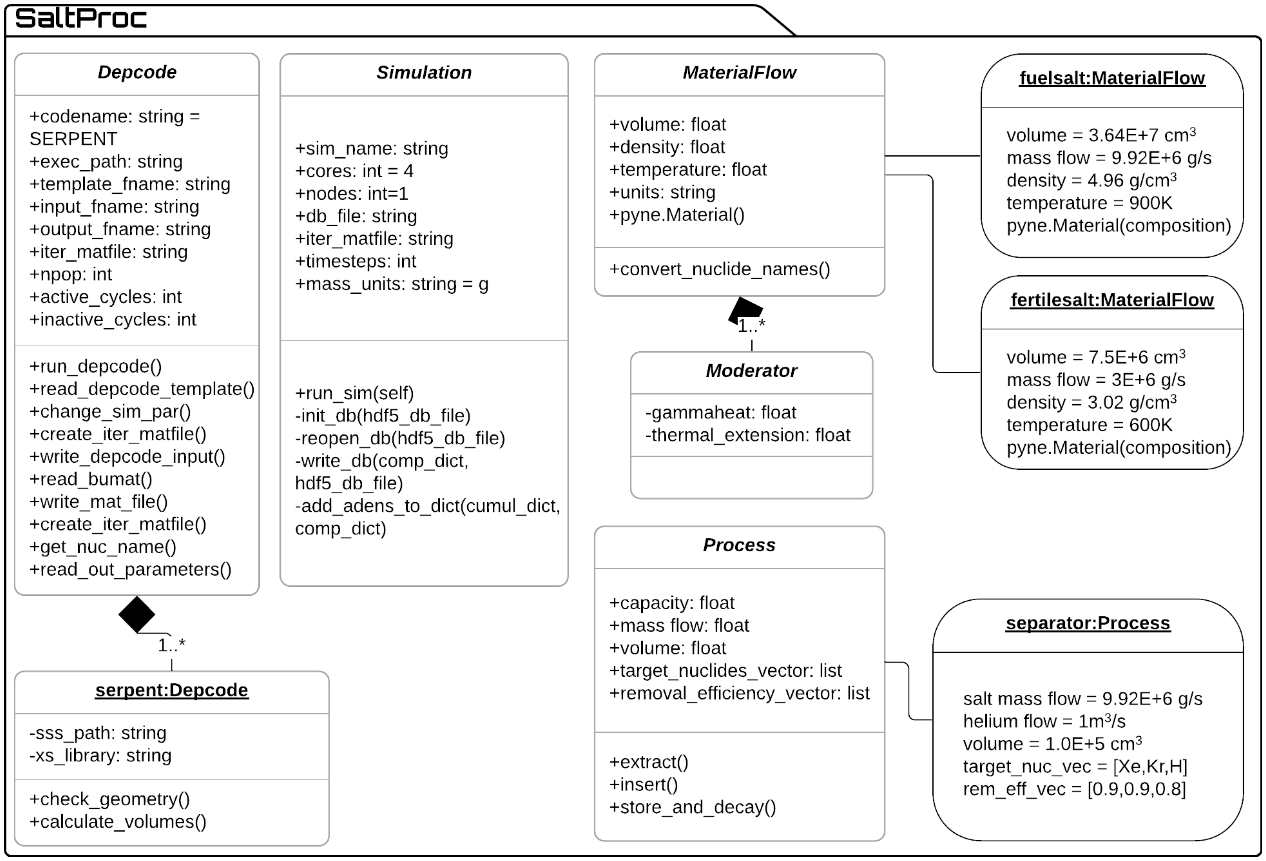

Figure 2.8: SaltProc v1.0 Python package class diagram in UML notation with examples of object instances.

principal parameters for burnup simulation (e.g., neutron population and number of cycles for Monte Carlo neutron transport), and running the depletion code.

Simulation. *Simulation* class runs a depletion step, creates and writes an HDF5 database, tracks time, and converts isotopic composition vector nuclide names from a depletion code format to human-readable format.

MaterialFlow. Each *MaterialFlow* object represents the material flowing between *Process* objects (Figures 2.9 and 2.10). All instances of this class contain an isotopic composition vector stored in PyNE Material object [96], mass flow rate, temperature, density, volume, and void fraction. Existing PyNE Material capabilities convert the units of the isotopic composition vector (e.g., from the atomic density provided by Serpent to a mass fraction or absolute mass in desired units) and decay the material (i.e., model the MSBR protactinium decay tank). The main idea of the *MaterialFlow* object is to pass detailed information about the salt starting at the MSR vessel outlet throughout reprocessing components (*Processes*), which modify the *MaterialFlow* object before depleting the material in the next depletion step.

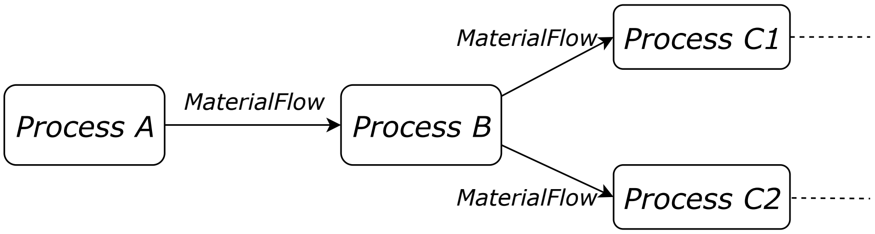

Figure 2.9: Schematic for passing material data between fuel processing system components shown for a general case.

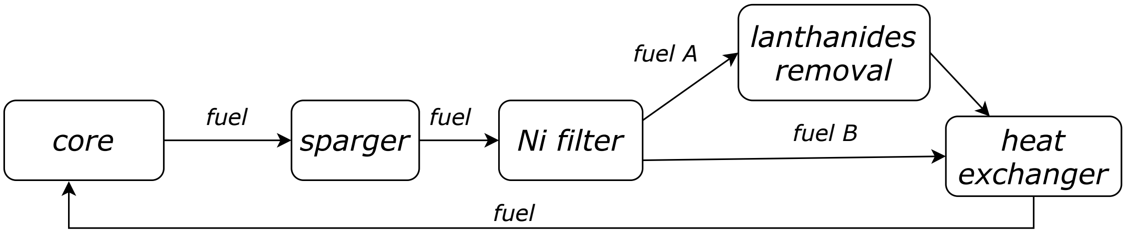

Figure 2.10: Schematic for passing material data between fuel processing system components shown for the TAP concept.

Process. Each *Process* object represents a realistic fuel processing step characterized by its throughput rate, volumetric capacity, extraction efficiency for each target element (can be a function of many parameters), waste streams, and other process-specific parameters. The feed *Process* injects fresh fuel salt *MaterialFlow* directly into the reactor core (e.g., adding fissile material with a specific mass flow rate to *MaterialFlow* after performing all removals).

Such a class structure provides outstanding flexibility in simulating various MSR fuel processing system designs. I created a library of various *MaterialFlow* (e.g., fuel salt flow, fertile salt flow, refueling salt flow) and *Process* (e.g., helium sparging facility, gas separator, nickel filter) object examples to help a user to create a model of a desired reprocessing scheme quickly. At runtime, the user should connect *Process* objects in series, parallel, or both with *MaterialFlow* objects to form a comprehensive reprocessing system. To make the reprocessing system definition self-explanatory and straightforward, I employed a standardized graph description language, *dot*, which is widely used in computer science for describing undirected and directed graphs [43]. A directed graph is a set of objects (vertices) connected by edges, where the edges have a direction associated with them. In the context of this work, a vertex is *Process* object (a component of the fuel processing systems), and a directed graph edge is *MaterialFlow* object (salt flow).

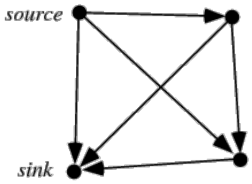

Figure 2.11: General example of directed graph with a source (e.g., a reactor outlet) and sink (e.g., a reactor inlet).

The reprocessing plant structure described with *dot* can be simply plotted using Graphviz [36] and those plots can be used for analysis, optimization, and publication purposes. The user also has the flexibility to create custom objects with desired attributes and methods and contribute back to the code package using GitHub (`https://github.com/arfc/saltproc`).

2.3.2 Tool flowchart

Figure 2.12 illustrates the online reprocessing simulation algorithm coupling SaltProc v1.0 and Serpent. A *json*-compatible user input file for SaltProc contains depletion software parameters such as paths to the depletion software executable, neutron population and number of criticality cycles, and total heating power. Additionally, the input file contains reprocessing system parameters such as structure of reprocessing system, capacity and efficiency of the system components, and molten salts thermophysical properties. To perform a depletion step, SaltProc v1.0 reads a user-defined Serpent template file. This file contains input parameters such as the path to a nuclear data library, material isotopic composition at startup, burnup calculation parameters, and boundary conditions. SaltProc v1.0 fills in the template file and runs Serpent single-step depletion.

After the depletion calculation, SaltProc v1.0 reads the depleted fuel composition file into the *MaterialFlow* object (*core_outlet* in Figure 2.12). This object contains an isotopic composition vector, total volume of material, total mass, mass flow rate, density, temperature, void fraction, etc. For the simplest reprocessing case, if all fuel processing components are connected in series (100% of total material flow goes through a chain of separation components), the *core_outlet* object flows sequentially between *Processes*, and each *Process* removes a mass fraction of target elements with specified extraction efficiency. After that the removed material mass is compensated by fresh fuel salt to maintain the salt inventory in a primary loop. Finally, the resulting isotopic composition after reprocessing is stored in the HDF5 database and dumped in a new composition file for the next Serpent depletion run. SaltProc v1.0 also stores the isotopic composition before reprocessing and waste stream from each fuel processing component in the HDF5 database.

For a more general case with multiple concurrent extraction processes, separate *MaterialFlow* objects are created for each branch with a user-defined mass flow branching percentage (e.g., 90% of total mass flow rate flows via left branch and 10% throughout a right branch). The total mass and isotopic composition vector for each *MaterialFlow* object are calculated as a fraction of incoming *core_outlet* flow. Then each *MaterialFlow* object is passed via a cascade of *Processes* to separate selected chemical elements with specific efficiency. Finally, the left-hand-side *MaterialFlow* object is merged with the right-hand-side, and similarly to the previous case, fresh fuel salt feed compensates for mass losses in the *Processes* and keeps the fuel salt mass in the primary loop constant.

The UML diagram (Figure 2.8) allows the user to model a complex, multi-zone, multi-fluid MSR operation and is sufficiently general to represent myriad reactor systems. SaltProc v1.0

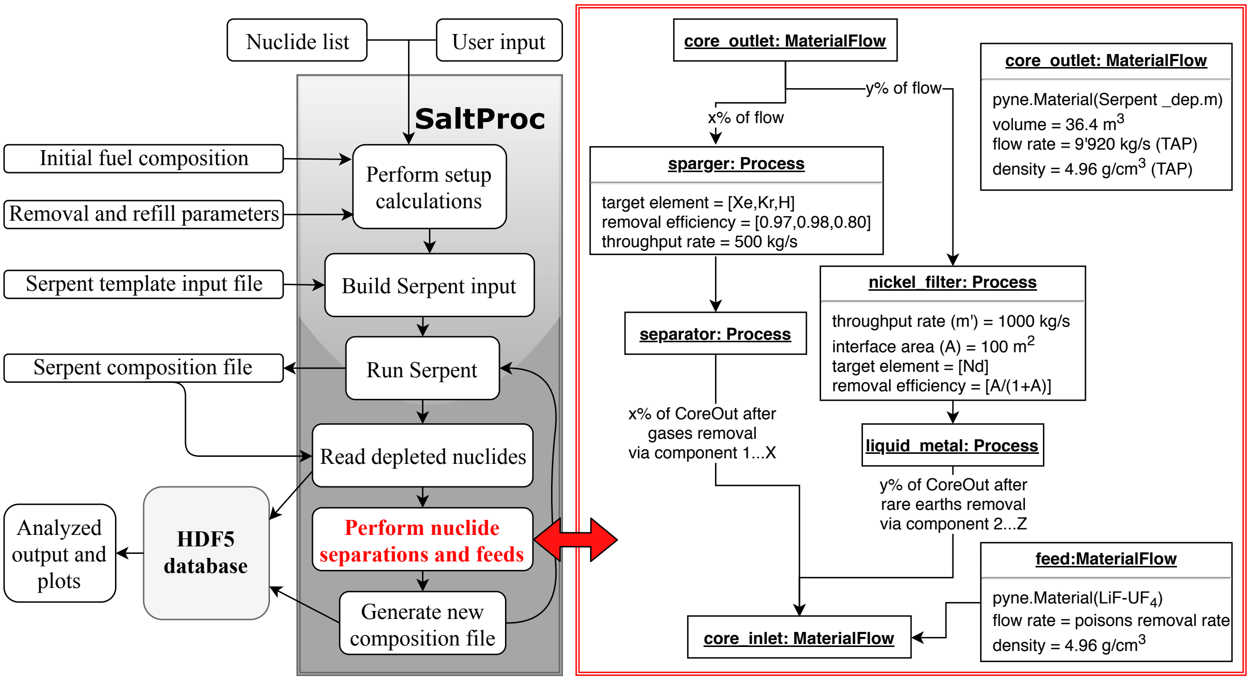

Figure 2.12: Flow chart for the SaltProc v1.0 Python package.

only stores and changes the isotopic composition of the fuel stream, which makes it a flexible tool to model any geometry: an infinite medium, a unit cell, a multi-zone simplified assembly, or a full-core. This flexibility allows the user to perform simulations of varying fidelity and computational intensity. SaltProc v1.0 is an open-source tool available on GitHub. Although the user needs Serpent ≥2.1.31 installed on his computer to use SaltProc. The tool leverages unit tests and continuous integration crucial for software sustainability [57, 108]. The documentation automatically generated using Sphinx [21] is available here: `https://arfc.github.io/saltproc/`. In summary, the development approach of SaltProc v1.0 is focused on producing a generic, flexible and expandable tool that extends Serpent 2 Monte Carlo code for advanced in-reactor fuel cycle analysis as well as simulate many online refueling and fuel reprocessing systems.

2.3.3 Reactivity control module

Simulation of specific MSR concepts requires changing the reactor core geometry during lifetime-long operation modeling. For instance, the TAP concept aims to increase the core lifetime by using continuous fresh fuel feeds, removing FPs, and reconfiguring moderator rod assemblies to compensate for negative reactivity insertion due to fissile material burnup. The concept proposes maintaining reactivity in the long term by replacing stationary moderator assemblies with denser lattices to increase the moderator-to-fuel ratio [17]. SaltProc v1.0 can switch from one core geometry to another core geometry (e.g., with larger moderator-to-fuel ratio) to mimic moderator or absorber movement if the effective multiplication factor, k_{eff}, falls below 1. This unique capability allows SaltProc v1.0 to analyze the fuel cycle performance of any liquid-fueled MSR system, including advanced designs with a moving moderator (e.g., TAP MSR).

2.4 Concluding remarks

This chapter presented an overview of an fuel salt reprocessing in MSRs. It described various components of the plant and the physical or chemical mechanism responsible for neutron poison extraction from the salt. General core physics aspects and Serpent 2 depletion software capabilities have then been discussed. It also introduced SaltProc, a Python package developed and used to simulate continuous feeds and removals in various MSR designs.

In the following chapters, SaltProc v1.0 will be demonstrated and validated for two liquid-fueled MSR designs: the MSBR and the TAP MSR.

Chapter 3

Tool demonstration for lifetime-long depletion: Molten Salt Breeder Reactor

This chapter describes the fuel cycle analysis of the MSBR obtained using the open-source Python package, SaltProc. The development was initially started as a part of my master thesis [85] in 2017. This effort, for verification purposes, assumed ideal extraction efficiency (e.g., 100% of the target isotope mass extracted) because all results available in the literature also rely on this assumption.

The main results presented in this chapter have been published in: A. Rykhlevskii, J.W. Bae, and K. D. Huff, "Modeling and simulation of online reprocessing in the thorium-fueled molten salt breeder reactor," *Annals of Nuclear Energy*, 128 (2019): 366–379. The high-fidelity, full-core MSBR model has been presented at the 2017 American Nuclear Society (ANS) Winter Meeting in Washington, D.C. The fuel salt composition evolution has been presented at the 2018 Blue Waters Symposium in Sunriver, OR [86]. The obtained results relevant to MSBR analysis have been compared against those obtained by Benjamin R. Betzler and colleagues for a simplified unit cell model, adopting the in-house code ChemTriton [15].

3.1 Introduction

The thorium-fueled MSBR was developed in the early 1970s by ORNL, specifically to explore the promise of the thorium fuel cycle, which uses natural fertile thorium feed material instead of enriched uranium fissile fuel. With continuous fuel reprocessing, the MSBR realizes the advantages of the thorium fuel cycle because the ^{233}U bred from ^{232}Th is almost instantly[1] recycled back into the core [14]. The chosen fuel salt, LiF-BeF$_2$-ThF$_4$-UF$_4$, has a melting point of 499°C, low vapor pressure at operating temperatures, and beneficial flow and heat transfer properties [83].

In this work, we analyzed the MSBR neutronics and fuel cycle to establish its equilibrium core composition. Additionally, we compared predicted operational and safety parameters of the MSBR at both the initial and equilibrium states to characterize the evolution of its safety case over time. Moreover, these depletion simulations determined the appropriate ^{232}Th feed rate for maintaining criticality and enabled analysis of the overall MSBR fuel cycle performance. Finally, the benefits of online fission product removal in the thermal spectrum MSBR were identified.

3.2 Molten Salt Breeder Reactor design and model description

Figure 3.1 shows the MSBR vessel which has a diameter of 680 cm and a height of 610 cm. It contains a molten fluoride fuel-salt mixture that generates heat in the active core region and transports that heat to the primary heat exchanger by way of the primary salt pump. In the active core region, the fuel salt flows through channels in moderating and reflecting graphite blocks. Fuel salt at 565°C enters the central manifold at the bottom via four 40.64-cm-diameter nozzles and flows upward through channels in the lower plenum graphite. The fuel salt exits at the top at about 704°C through four equally spaced nozzles, which connect to the salt-suction pipes leading to primary circulation pumps. The fuel salt drain lines connect to the bottom of the reactor vessel inlet manifold.

Figure 3.2 shows the configuration of the MSBR vessel, including the "fission" (zone I)

---

[1] The fertile ^{232}Th is transmuted into the ^{233}Th after capturing a neutron. Next, this isotope decays to the ^{233}Pa ($\tau_{1/2}$=21.83m), which finally decays to the ^{233}U ($\tau_{1/2}$=26.967d).

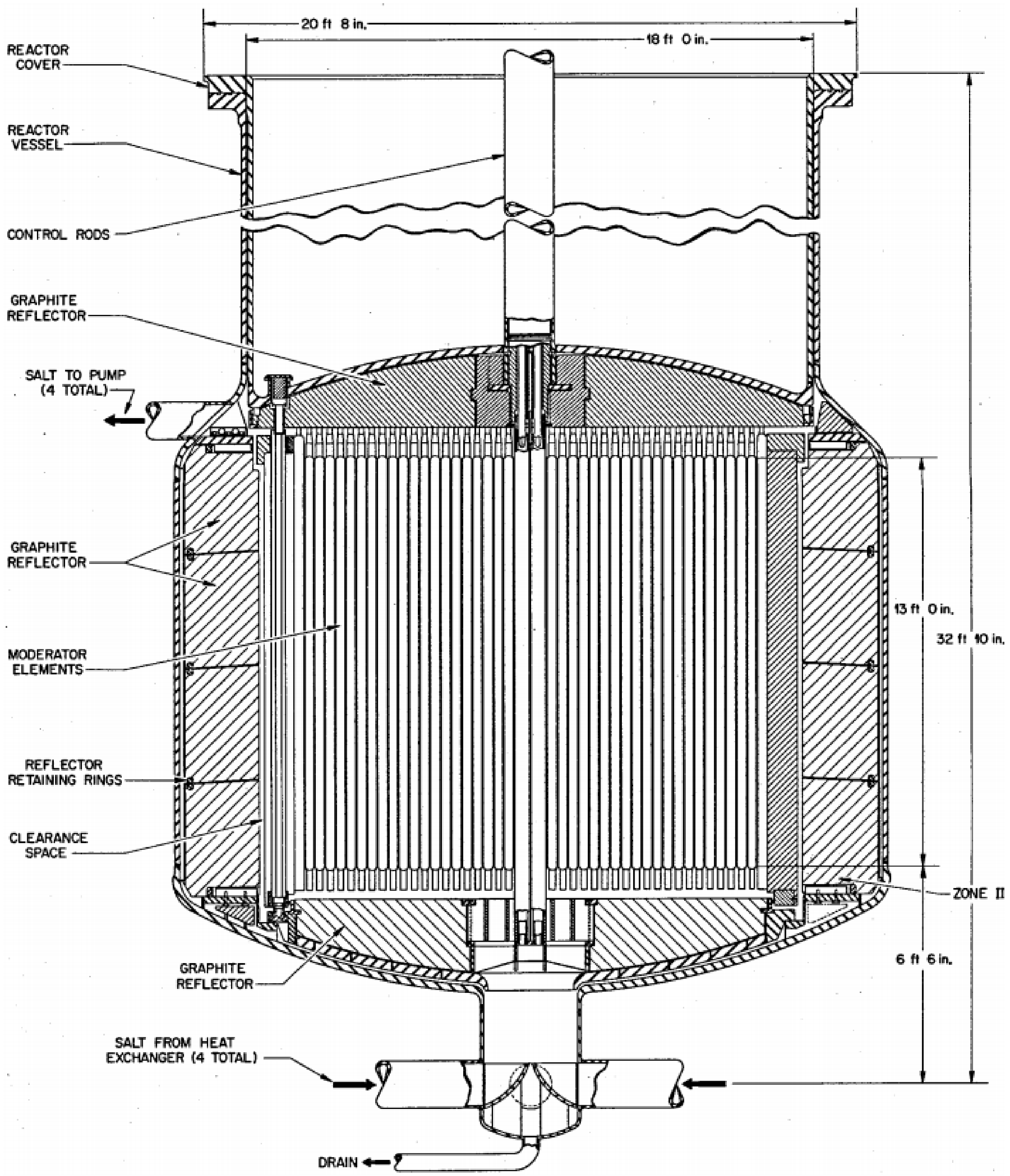

Figure 3.1: XZ view of the MSBR (reproduced from Robertson *et al.* [83]).

and "breeding" (zone II) regions inside the vessel. The core has two radial zones bounded by a solid cylindrical graphite reflector and the vessel wall. The central zone, zone I, in which

13% of the volume is fuel salt and 87% is graphite, is composed of 1,320 graphite cells, 2 graphite control rods, and 2 emergency shutdown rods. The under-moderated zone, zone II, in which 37% of the volume is fuel salt and 63% is graphite, and radial reflector, surrounds the zone I core region and serves to diminish neutron leakage. Zones I and II are surrounded radially and axially by fuel salt (Figure 3.3); this space for fuel is necessary for the injection and flow of molten salt.

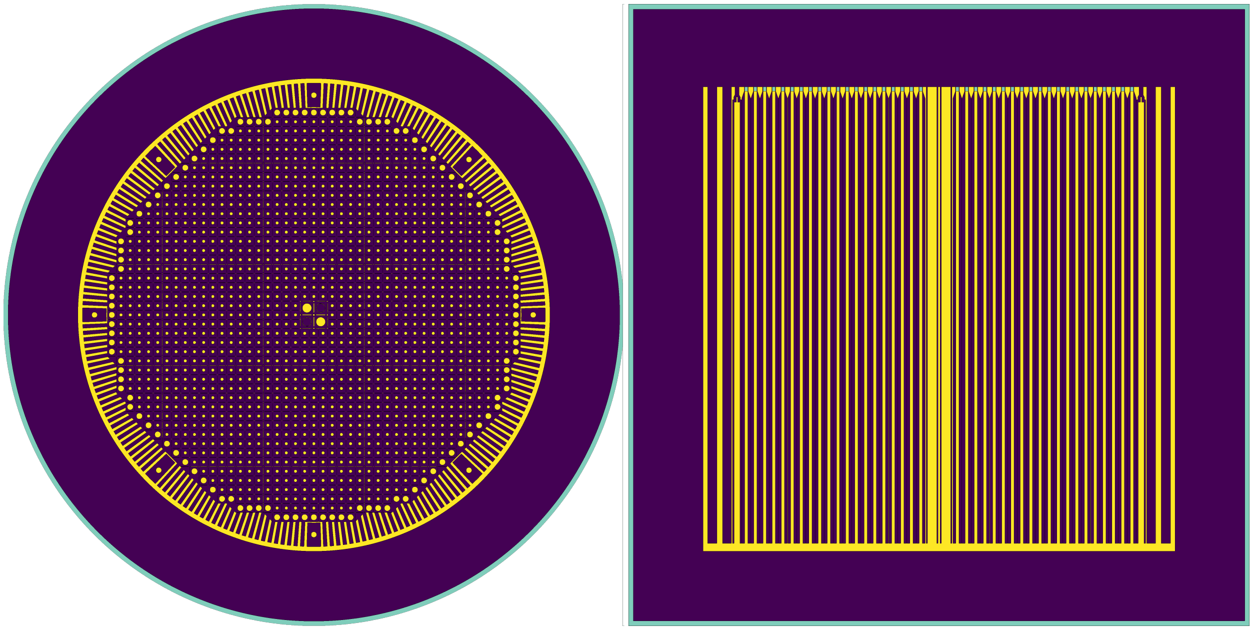

Figure 3.2: XY (left) and XZ (right) views of a Serpent MSBR model (reproduced from Rykhlevskii *et al.* [88]).

Since reactor graphite experiences significant dimensional changes due to neutron irradiation, the reactor core was designed for periodic replacement. Based on the experimental irradiation data from the MSRE, the core graphite lifetime is about 4 years, and the reflector graphite lifetime is 30 years [83].

The core design also has eight symmetric graphite slabs with a width of 15.24 cm in zone II, one of which is illustrated in Figure 3.3. The holes in the centers are for the core lifting rods used during the core replacement operations. These holes also allow a portion of the fuel salt to flow to the top of the vessel for cooling the top head and axial reflector. Figure 3.3 also shows the 5.08-cm-wide annular space between the removable core graphite in zone II-B

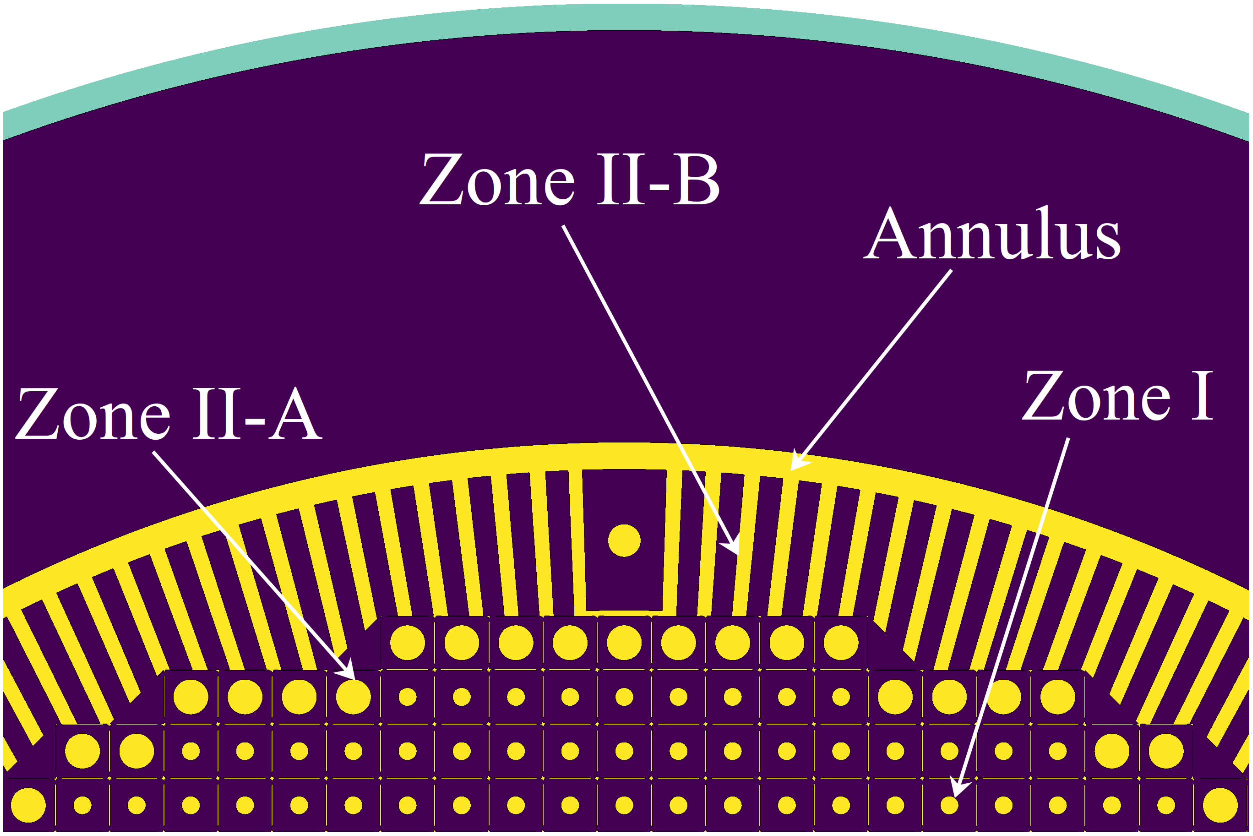

Figure 3.3: Detailed view of the MSBR two-zone model. Yellow represents fuel salt, purple represents graphite, and aqua represents the reactor vessel (reproduced from Rykhlevskii *et al.* [88]).

and the permanently mounted reflector graphite. This annulus consists entirely of fuel salt, provides space for moving the core assembly, helps compensate for the elliptical dimensions of the reactor vessel, and serves to reduce the damaging flux at the surface of the graphite reflector blocks.

^{135}Xe is a strong neutron poison, and some fraction of this gas is absorbed by graphite during MSBR operation. ORNL calculations showed that for unsealed commercial graphite with a helium permeability of 10^{-5} cm^2/s, the calculated ^{135}Xe poison fraction[2] is less than 2% [83]. This parameter can be improved by using experimental graphite types or by applying sealing technology. The effect of the gradual poisoning of the core graphite with xenon is

---

[2] The original ORNL report by Robertson *et al.* defined ^{135}Xe poison fraction as the number of neutrons absorbed by ^{135}Xe compared with the total number of neutrons (both fast and thermal) absorbed by ^{233}U.

outside of the scope of this work.

3.2.1 Core zone I

The central region of the core, called zone I, is made up of graphite elements, each 10.16cm× 10.16cm×396.24cm and has 13% fuel salt by volume. Zone I has 4 channels for control rods: two for graphite rods, which both regulate and shim during normal operation, and two for backup safety rods consisting of boron carbide clad to assure sufficient negative reactivity for accidents.

Zone I graphite elements have a mostly rectangular shape with lengthwise ridges at each corner that leave space for salt flow around the elements. Figure 3.4 shows the elevation and plan views of graphite elements of zone I [83] and their Serpent model [92].

3.2.2 Core zone II

Zone II, which is undermoderated, surrounds zone I. Combined with the bounding radial reflector, zone II serves to diminish neutron leakage. Two kinds of elements form this zone: large-diameter fuel channels (zone II-A) and radial graphite slats (zone II-B).

Zone II has 37% fuel salt by volume, and each element has a fuel channel diameter of 6.604cm. The graphite elements for zone II-A are prismatic, with elliptical dowels running axially between the prisms. These dowels isolate the fuel salt flow in zone I from that in zone II. Figure 3.5 shows the shapes and dimensions of these graphite elements and their Serpent model. Zone II-B elements are rectangular slats spaced far enough apart to provide the 0.37 fuel salt volume fraction. The reactor zone II-B graphite 5.08cm-thick slats vary in the radial dimension (average width is 26.67cm) as shown in Figure 3.3. Zone II serves as a blanket to achieve the best performance: a high breeding ratio and a low fissile inventory. The harder neutron energy spectrum in zone II enhances the rate of thorium resonance capture relative to the fission rate, thus limiting the neutron flux in the outer core zone and reducing the

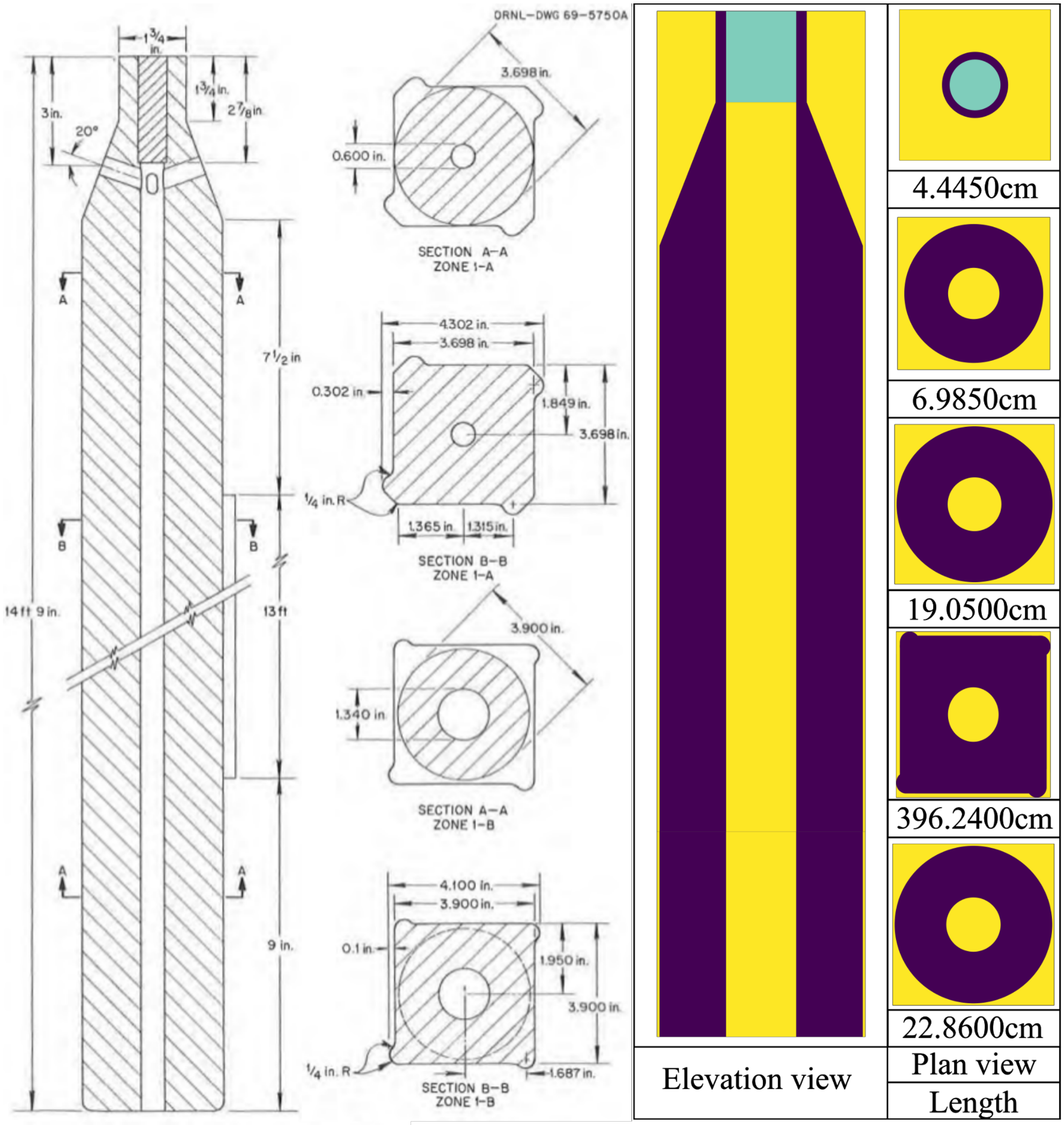

Figure 3.4: Graphite moderator elements for zone I: reference design (left) [83] and Serpent model (right) [92]. Yellow represents fuel salt, purple represents graphite, and aqua represents the reactor vessel (reproduced from Rykhlevskii *et al.* [88]).

neutron leakage [83].

The sophisticated, irregular shapes of the fuel elements challenge an accurate representation of zone II-B. The suggested design [83] of zone II-B has eight irregularly-shaped graphite elements as well as dozens of salt channels. These graphite elements were simplified into right-circular cylindrical shapes with central channels. Figure 3.3 illustrates this core region in the Serpent model. The volume of fuel salt in zone II was kept exactly at 37% so this simplification did not impact the core neutronics. Simplifying the eight edge channels was the only simplification made to the MSBR geometry in this work.

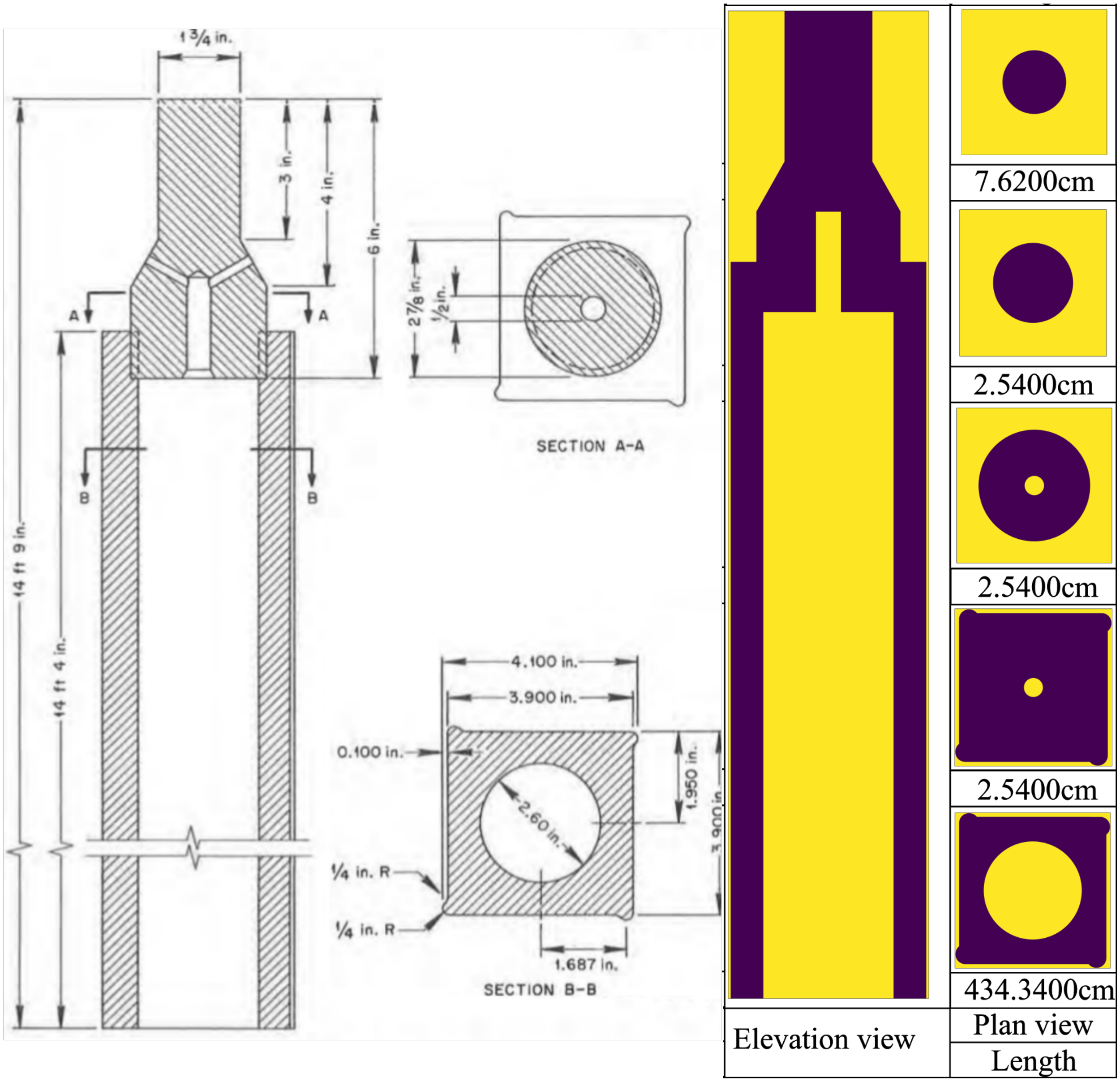

Figure 3.5: Graphite moderator elements for zone II-A: reference design (left) [83] and Serpent model (right) [92]. Yellow represents fuel salt, purple represents graphite, and aqua represents the reactor vessel (reproduced from Rykhlevskii *et al.* [88]).

3.2.3 Material composition and normalization parameters

The fuel salt, reactor graphite, and modified Hastelloy-N are all materials invented at ORNL specifically for the MSBR. The fuel salt selected for use in the MSBR is LiF-BeF_2-ThF_4-$^{233}UF_4$ (71.75-16-12-0.25 mole % which has density of 3.35 g/cm^3 [83]. The lithium in the molten salt fuel is fully enriched to 99.995% ^{7}Li because ^{6}Li is an extremely strong neutron poison and becomes tritium upon neutron capture.

The specific temperature was fixed for each material and stays constant during reactor operation. The isotopic composition of each material at the initial state was described in detail in the MSBR conceptual design study [83] and has been applied to the Serpent model without any modification. Table 3.1 is a summary of the major MSBR parameters used to inform the Serpent model [83].

Table 3.1: Summary of principal data for the MSBR (reproduced from Robertson *et al.* [83]).

Thermal power	2250 MW_{th}
Electric power	1000 MW_e
Gross thermal efficiency	44.4%
Salt volume fraction (Zone I)	0.13
Salt volume fraction (Zone II)	0.37
Fuel salt inventory (Zone I)	8.2 m^3
Fuel salt inventory (Zone II)	10.8 m^3
Fuel salt inventory (annulus)	3.8 m^3
Total fuel salt inventory	48.7 m^3
Fissile mass in fuel salt	1303.7 kg
Fuel salt components	LiF-BeF_2-ThF_4-$^{233}UF_4$
Fuel salt composition	71.75-16-12-0.25 mole%
Fuel salt density	3.35 g/cm^3

As mentioned in section 2.1, the MSBR design requires online reprocessing to completely remove neutron gaseous FPs (Xe, Kr) and noble metals (e.g., Se, Nb, and Mo) every 20 seconds. The ^{232}Th in the fuel absorbs thermal neutrons and produces ^{233}Pa, which then decays into the fissile ^{233}U. Protactinium presents a challenge since it has a large absorption cross section in the thermal energy spectrum. Moreover, ^{233}Pa left in the core produces ^{234}Pa and ^{234}U, neither of which are useful as fuel. Accordingly, ^{233}Pa is continuously removed from the fuel salt into a temporary storage tank to allow ^{233}Pa to decay to ^{233}U without the corresponding negative neutronic impact. The reactor chemical processing system must separate ^{233}Pa from the molten salt fuel over 3 days, hold it while ^{233}Pa decays into ^{233}U, and return it to the primary loop. This feature allows the reactor to avoid neutron losses to protactinium, lowers in-core fission product inventory, and increases the efficiency of ^{233}U breeding.

Table 3.2 summarizes a full list of nuclides and their cycle time used for modeling salt treatment and separations [83]. The removal rates vary among chemical elements in this reactor concept and dictate the necessary resolution of depletion calculations. If the depletion time intervals are short, an enormous number of depletion steps are required to obtain the equilibrium composition. On the other hand, if the depletion calculation time interval is too long, effective multiplication factor k_{eff} would be lower than expected in reality due to higher equilibrium concentration of strong poisons (e.g., ^{135}Xe) in fuel salt. To compromise, a 3-day time interval was selected for depletion calculations to correlate with the removal interval of ^{233}Pa as suggested by Powers *et al.* [77]. Finally, ^{232}Th was continuously added every 3 days to maintain the initial mass fraction of ^{232}Th in the fuel salt.

Table 3.2: The cycle times for protactinium and fission product removal from the MSBR (reproduced from Robertson *et al.* [83]).

Processing group	**Nuclides**	**Cycle time (at full power)**
Rare earths	Y, La, Ce, Pr, Nd, Pm, Sm, Gd	50 days
	Eu	500 days
Noble metals	Se, Nb, Mo, Tc, Ru, Rh, Pd, Ag, Sb, Te	20 sec
Semi-noble metals	Zr, Cd, In, Sn	200 days
Gases	Kr, Xe	20 sec
Volatile fluorides	Br, I	60 days
Discard	Rb, Sr, Cs, Ba	3435 days
Protactinium	^{233}Pa	3 days
Higher nuclides	^{237}Np, ^{242}Pu	16 years

3.3 Fuel salt isotopic composition dynamics and equilibrium search

The SaltProc online reprocessing simulation package is demonstrated in four applications: (1) analyzing the MSBR neutronics and fuel cycle to find the equilibrium core composition and fuel salt depletion, (2) demonstrating that in a single-fluid two-region MSBR conceptual design the undermoderated outer core zone II works as a virtual "blanket", reduces neutron leakage, and improves breeding ratio due to neutron energy spectral shift, (3) studying operational and safety parameters evolution during MSBR operation, and (4) determining the effect of fission product removal on the core neutronics. This section discusses the first two applications.

Input parameters for Serpent Monte Carlo code (neutron population, active/inactive cycles) were chosen to compromise between reasonable uncertainty for a transport problem (≤ 15 *pcm* for the effective multiplication factor) and computational time. The MSBR depletion and safety parameter computations were performed on 64 Blue Waters XK7 nodes (two AMD 6276 Interlagos CPU per node, 16 floating-point Bulldozer core units per node or 32 "integer" cores per node, nominal clock speed is 2.45 GHz). The total computational time for calculating fuel salt depletion during 60 years of operation was approximately 9,900 node-hours (18 core-years.)

3.3.1 Effective multiplication factor dynamics

Figures 3.6 and 3.7 show the effective multiplication factors obtained using SaltProc v0.1 and Serpent. The effective multiplication factors were calculated after removing fission products listed in Table 3.2 and adding the fertile material at the end of each depletion step (3 days). The effective multiplication factor fluctuates significantly as a result of the batch-wise nature of this online reprocessing strategy.

First, Serpent calculates the effective multiplication factor for the beginning of the cycle.

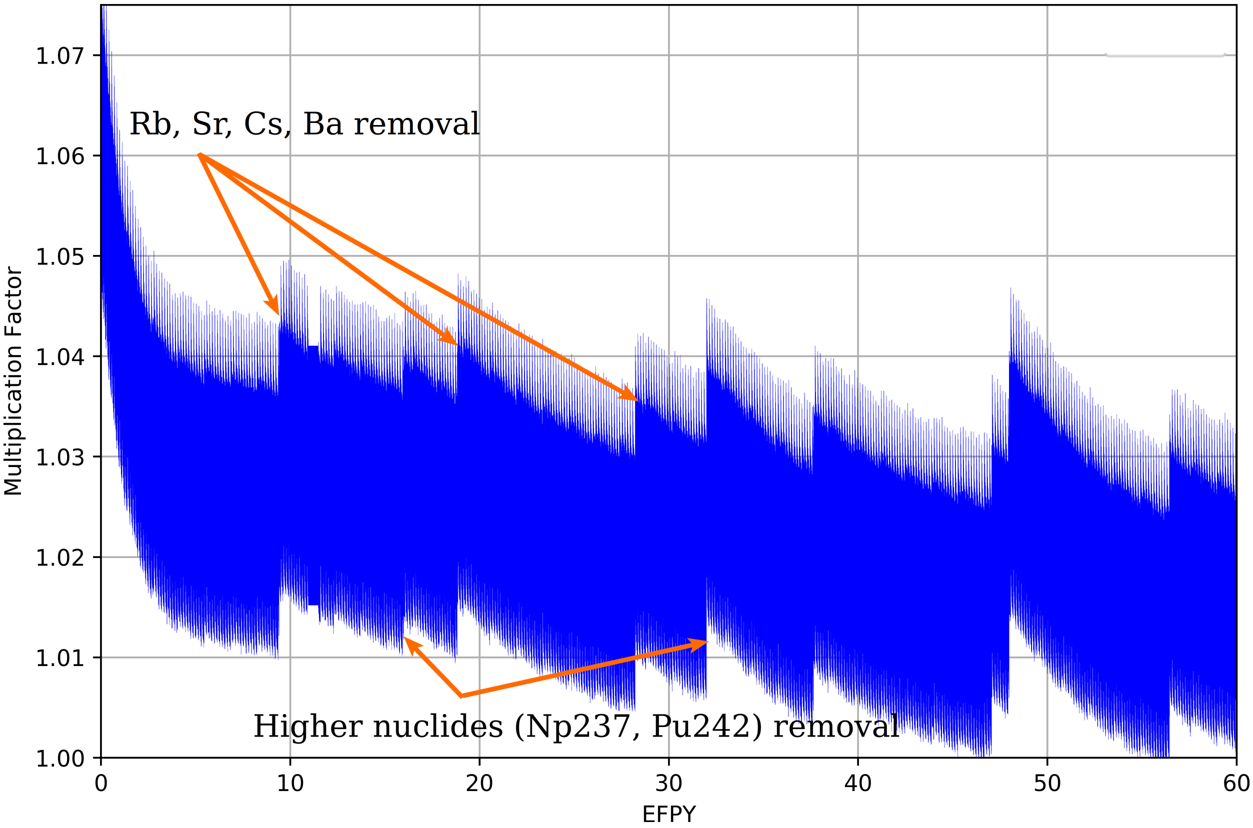

Figure 3.6: Effective multiplication factor dynamics for full-core MSBR model over a 60-year reactor operation lifetime (reproduced from Rykhlevskii *et al.* [88]).

Next, it computes the new fuel salt composition at the end of a 3-day depletion. The corresponding effective multiplication factor is much smaller than the previous one. Finally, Serpent calculates k_{eff} for the depleted composition after applying feeds and removals. The k_{eff} increases accordingly since major reactor poisons (e.g., Xe, Kr) are removed, while fresh fissile material (^{233}U) from the protactinium decay tank is added.

Additionally, the presence of rubidium, strontium, cesium, and barium in the core are disadvantageous to reactor physics. Overall, the effective multiplication factor gradually decreases from 1.075 to ≈1.02 at equilibrium after approximately 6 years of irradiation.

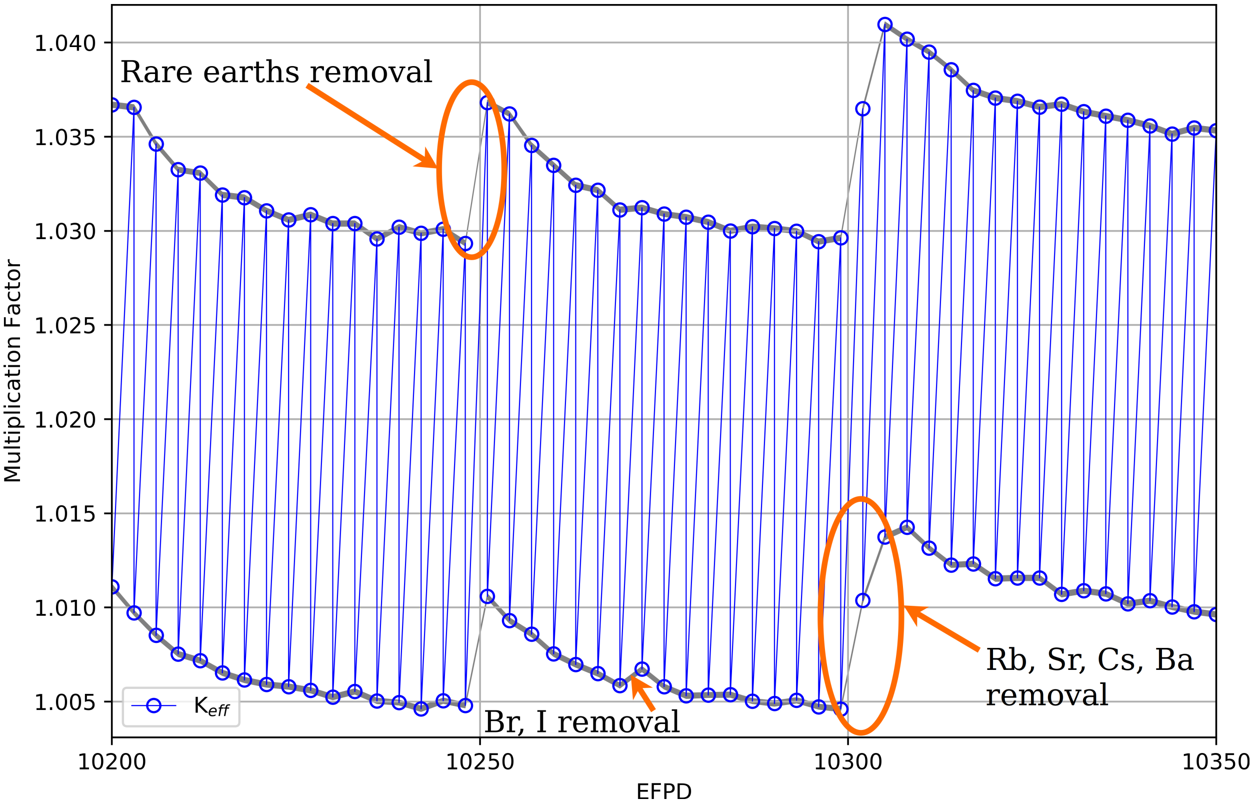

Figure 3.7: Zoomed effective multiplication factor for a 150-EFPD time interval (reproduced from Rykhlevskii *et al.* [88]).

3.3.2 Fuel salt composition dynamics

The analysis of the fuel salt composition evolution provides more comprehensive information about the equilibrium state. Figure 3.8 shows the number densities of major nuclides, which have a strong influence on the reactor core physics. The concentration of ^{233}U, ^{232}Th, ^{233}Pa, and ^{232}Pa in the fuel salt change insignificantly after approximately 2500 days of operation. In particular, the ^{233}U number density fluctuates by less than 0.8% between 16 and 20 years of operation. Hence, a quasi-equilibrium state was achieved after 16 years of reactor operation.

In contrast, a wide variety of nuclides, including fissile isotopes (e.g., ^{235}U) and non-fissile strong absorbers (e.g., ^{234}U), kept accumulating in the core. Figure 3.9 demonstrates the production of fissile isotopes in the core. At the end of the considered operational time, the core contained significant ^{235}U ($\approx 10^{-5}$ atoms/b-cm), ^{239}Pu ($\approx 5 \times 10^{-7}$ atoms/b-cm), and

^{241}Pu ($\approx 5 \times 10^{-7}$ atoms/b-cm). Meanwhile, the equilibrium number density of the target fissile isotope ^{233}U was approximately $7.97{\times}10^{-5}$ atoms/b-cm. Small dips in neptunium and plutonium number density every 16 years are caused by removing ^{237}Np and ^{242}Pu (included in Processing group "Higher nuclides", see Table 3.2) which decay into ^{235}Np and ^{239}Pu, respectively. Thus, the production of new fissile materials in the core, as well as ^{233}U breeding, made it possible to compensate for the negative effects of strong absorber accumulation (^{234}U) and keep the reactor critical.

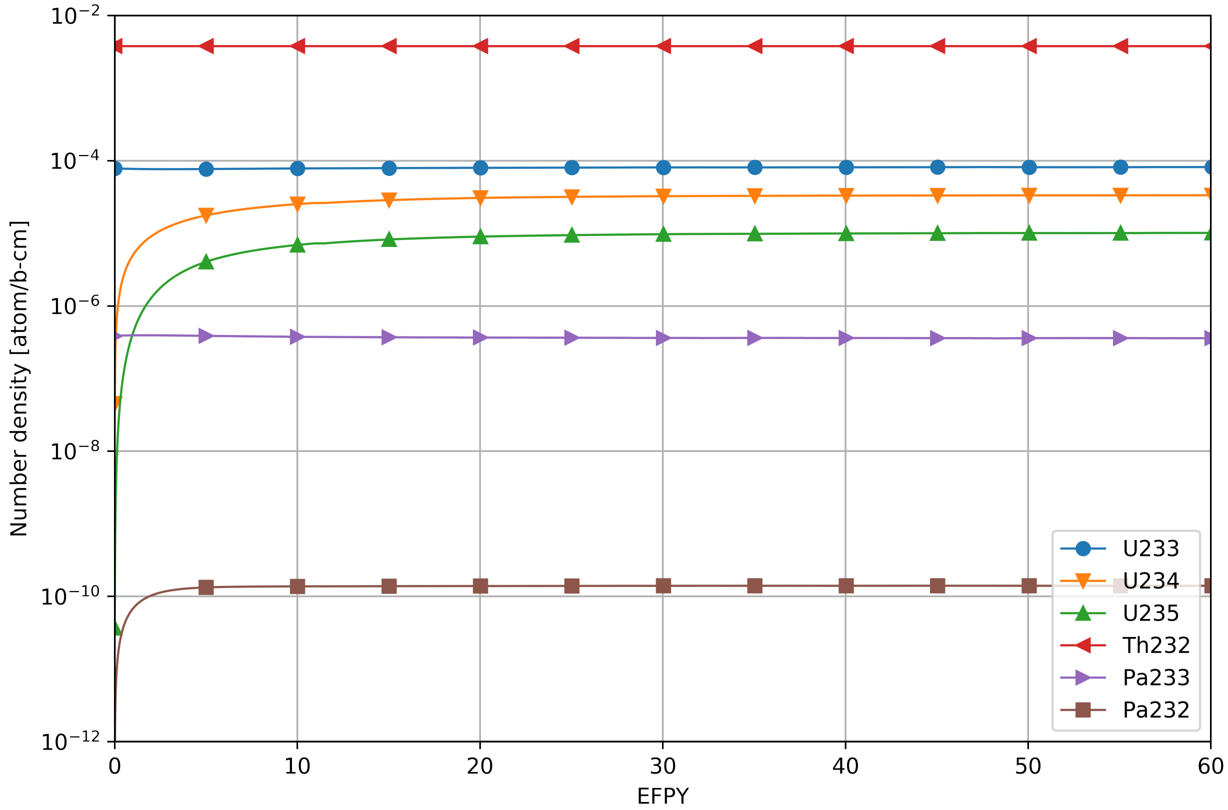

Figure 3.8: The number density of major nuclides during 60 years of reactor operation (reproduced from Rykhlevskii *et al.* [88]).

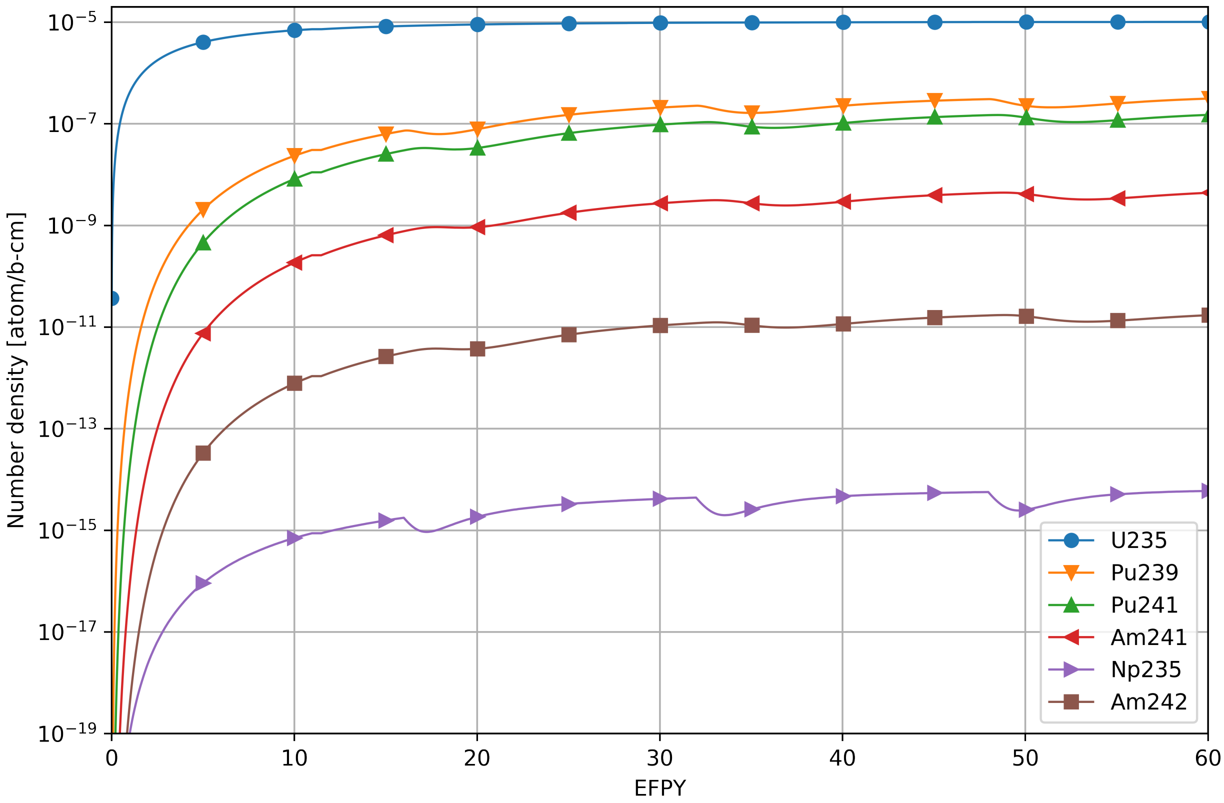

Figure 3.9: The number density of *fissile in epithermal spectrum* nuclides during 60 years of the reactor operation (reproduced from Rykhlevskii *et al.* [88]).

3.3.3 Neutron spectrum

Figure 3.10 shows the normalized neutron flux spectrum for the full-core MSBR model in the energy range from 10^{-8} to 10 MeV. The neutron energy spectrum at equilibrium is harder than at startup due to plutonium and other strong absorbers accumulating in the core during reactor operation.

Figure 3.11 shows that zone I produced more thermal neutrons than zone II, corresponding to a majority of fissions occurring in the central part of the core. In the undermoderated zone II, the neutron energy spectrum is harder, which leads to more intensive neutron capture by ^{232}Th and helps achieve a relatively high breeding ratio. Moreover, the (n,γ) resonance energy range in ^{232}Th is from 10^{-4} to 10^{-2} MeV. Thus, the moderator-to-fuel ratio for zone II was chosen to shift the neutron energy spectrum in this range. Furthermore, in the central core region (zone I), the neutron energy spectrum shifts to a harder spectrum over 20 years of reactor operation; meanwhile, in the outer core region (zone II), a similar spectral shift takes place at a reduced scale. These results are in good agreement with the original ORNL report [83] and the most recent whole-core steady-state study [73].

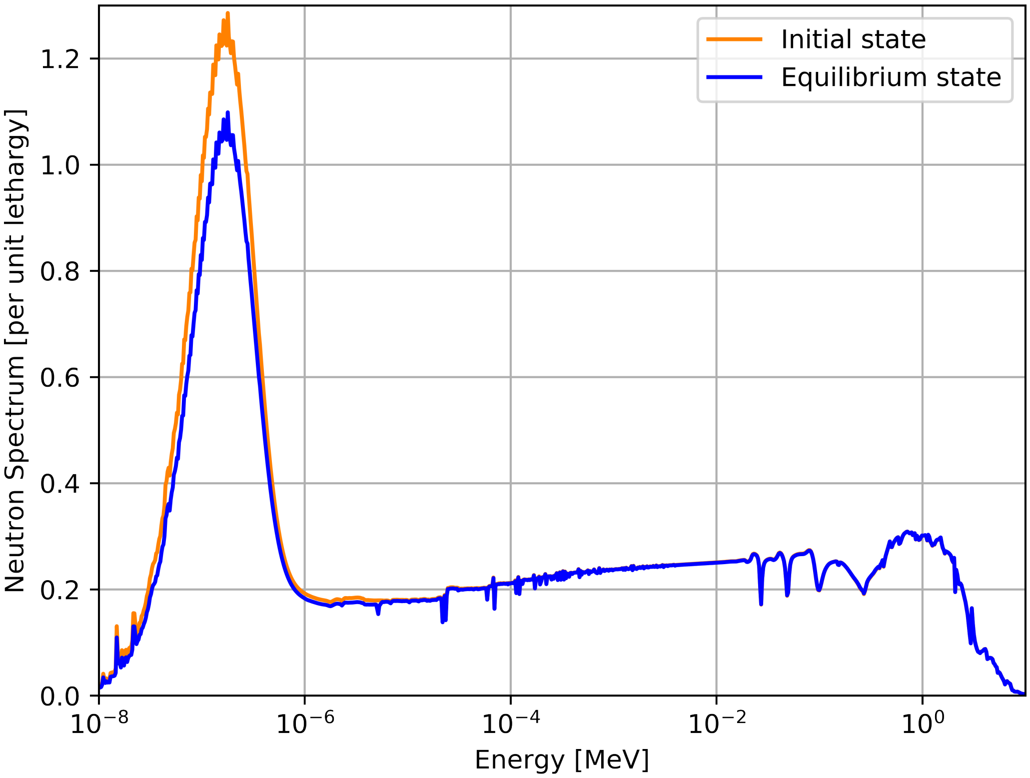

Figure 3.10: The neutron flux energy spectrum for initial and equilibrium state normalized by unit lethargy (reproduced from Rykhlevskii *et al.* [88]).

It is important to obtain the epithermal and thermal spectra to produce ^{233}U from ^{232}Th because the radiative capture cross section of thorium decreases monotonically from 10^{-10} MeV to 10^{-5} MeV. Hardening the spectrum tends to significantly increase resonance absorption in thorium and decrease absorptions in fissile and construction materials.

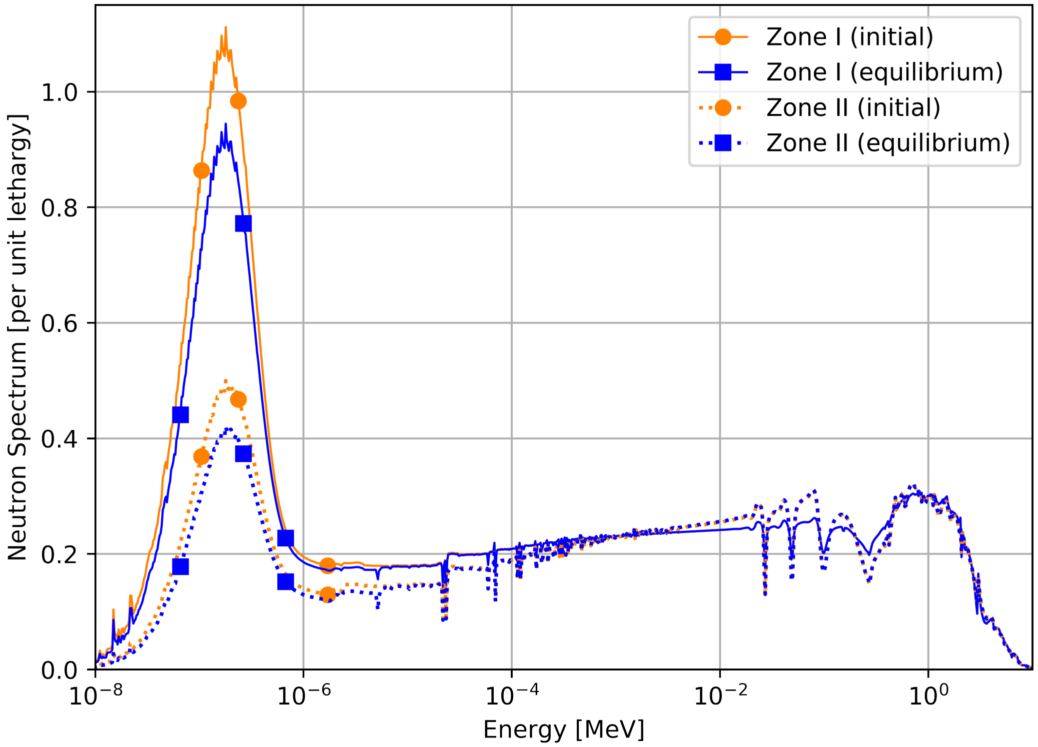

Figure 3.11: The neutron flux energy spectrum for initial and equilibrium state normalized by unit lethargy (reproduced from Rykhlevskii *et al.* [88]).

3.3.4 Neutron flux

Figure 3.12 shows the radial distribution of fast and thermal neutron flux for initial and equilibrium compositions. The neutron fluxes have similar shapes for both compositions, but the equilibrium case has a harder spectrum. A significant spectral shift was observed in the central region of the core (zone I). In the outer region (zone II), annulus and graphite reflector, spectral shift is negligible. These neutron flux radial distributions agree with the fluxes in the original ORNL report [83]. Overall, spectrum hardening during MSBR operation should be carefully studied when designing the reactivity control system.

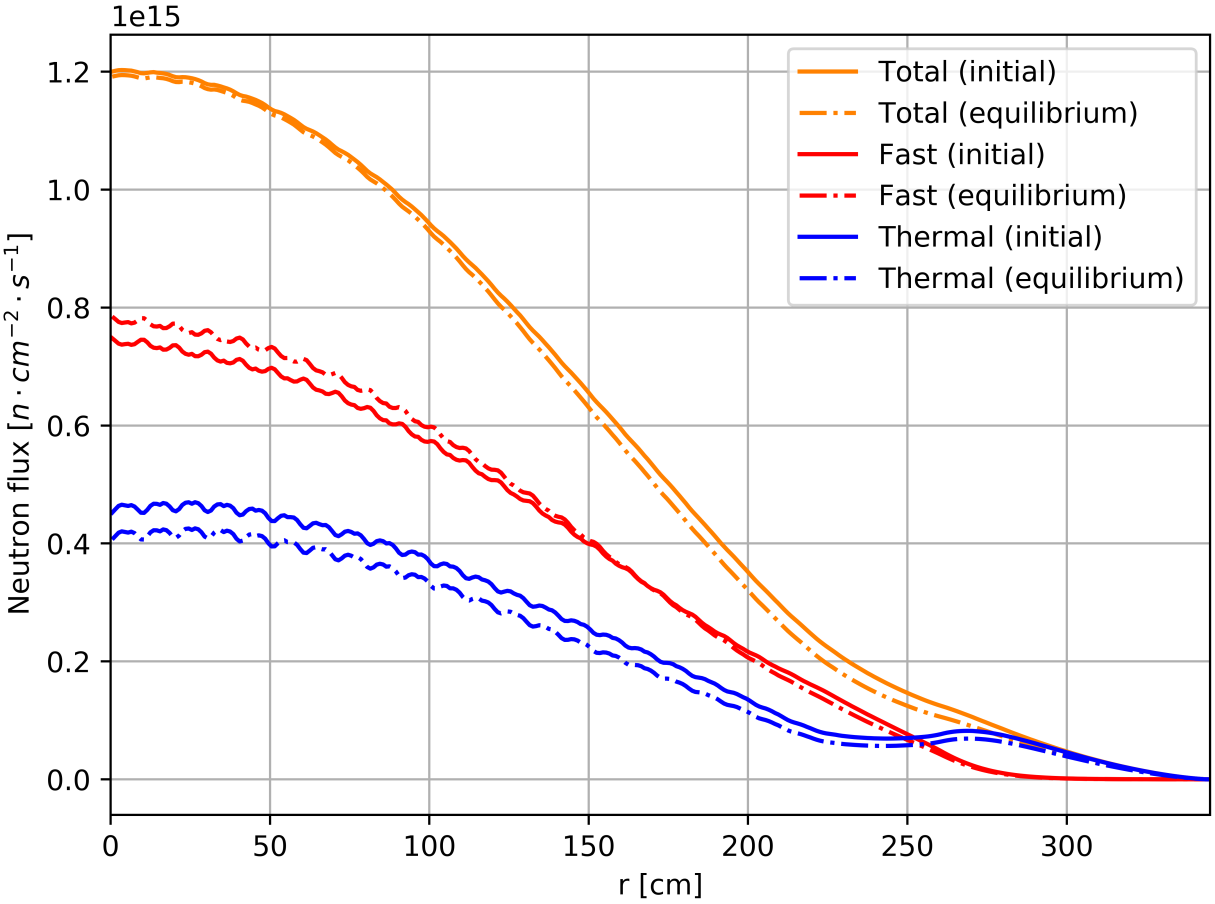

Figure 3.12: Radial neutron flux distribution for initial and equilibrium fuel salt compositions (reproduced from Rykhlevskii *et al.* [88]).

3.3.5 Power and breeding distribution

Table 3.3 shows the power fraction in each zone for initial and equilibrium fuel compositions. Figure 3.13 reflects the normalized power distribution of the MSBR quarter core for equilibrium fuel salt composition. For both the initial and equilibrium compositions, fission primarily occurs in the center of the core, namely zone I. The spectral shift during reactor operation results in slightly different power fractions at startup and equilibrium, but most of the power is still generated in zone I at equilibrium (Table 3.3).

Table 3.3: Power generation fraction in each zone for initial and equilibrium state (reproduced from Rykhlevskii *et al.* [88]).

Core region	Initial	Equilibrium
Zone I	97.91%	98.12%
Zone II	2.09%	1.88%

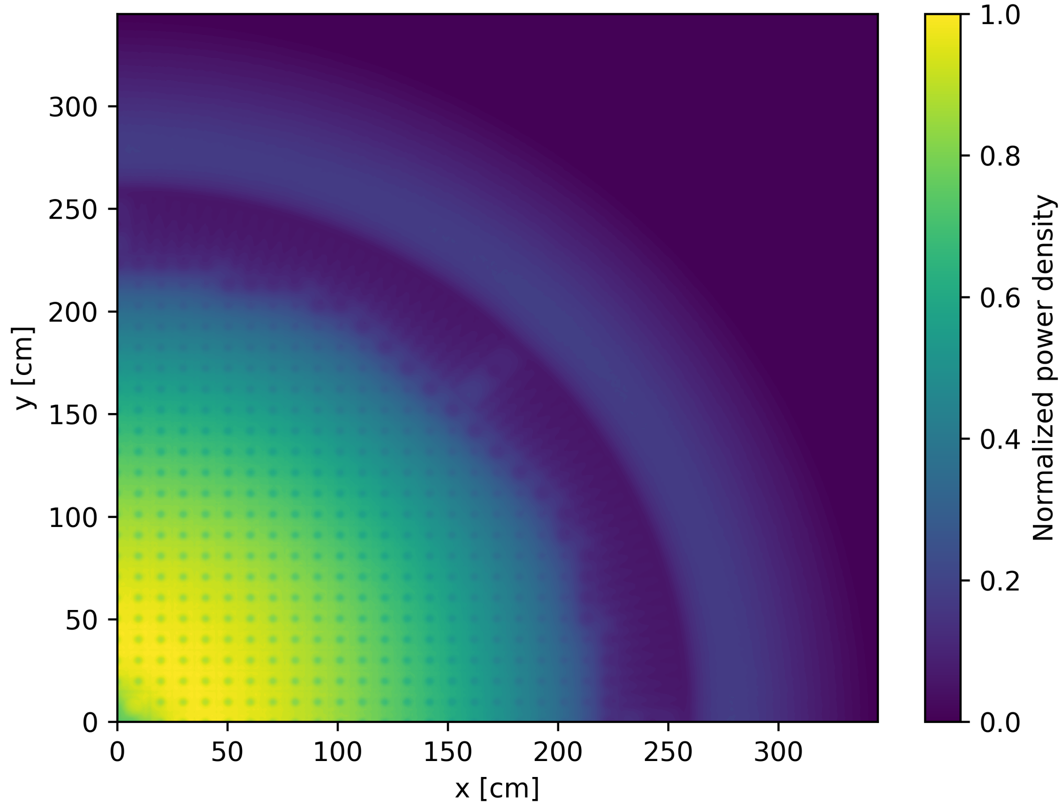

Figure 3.13: Normalized power density for equilibrium fuel salt composition (reproduced from Rykhlevskii *et al.* [88]).

Figure 3.14 shows the distribution of the neutron capture reaction rate for ^{232}Th normalized by the total neutron flux for the initial and equilibrium states. The distribution reflects the spatial distribution of ^{233}U production in the core. ^{232}Th neutron capture produces ^{233}Th, which then β-decays to ^{233}Pa, the precursor for ^{233}U production. Accordingly, this characteristic represents the breeding distribution in the MSBR core. The power and breeding distribution remained almost constant during the reactor operation. Even after 20 years of operation, most of the power is still generated in zone I.

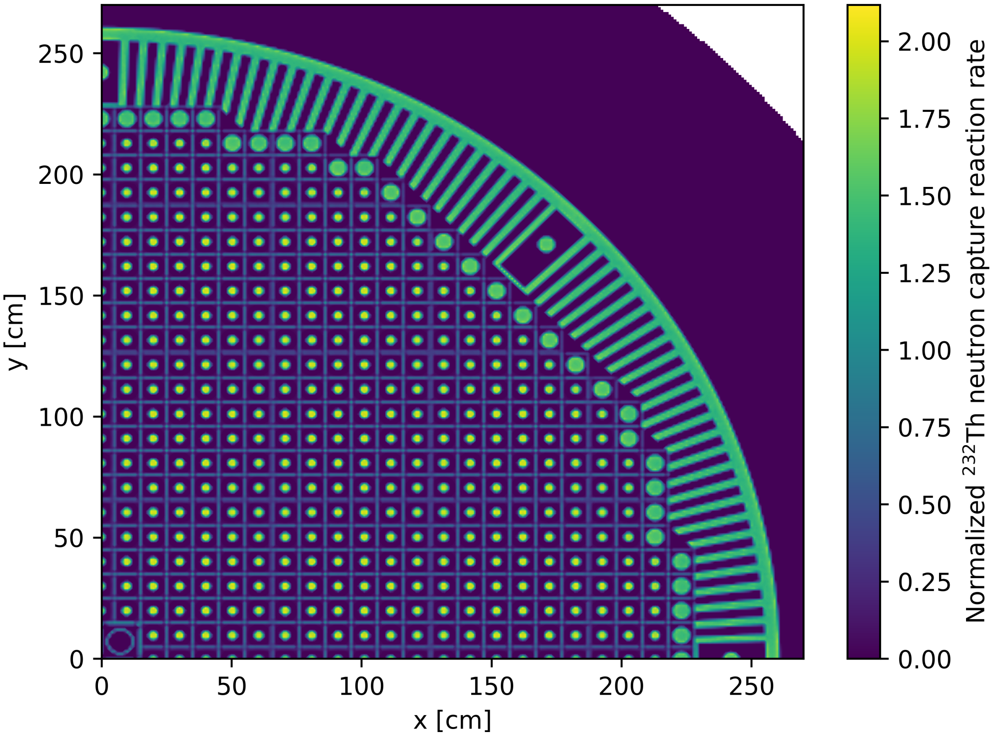

Figure 3.14: ^{232}Th neutron capture reaction rate normalized by total flux for equilibrium fuel salt composition (reproduced from Rykhlevskii *et al.* [88]).

3.3.6 Thorium refill rate

In the MSBR, the only external feed material flow is ^{232}Th. Figure 3.15 shows the ^{232}Th feed rate calculated over 60 years of reactor operation. The ^{232}Th feed rate fluctuates significantly as a result of the batch-wise nature of this online reprocessing approach. Figure 3.16 shows a zoomed thorium feed rate for a short 150-EFPD interval. Note that the large spikes of up to 36 kg/day in a thorium consumption occur every 3435 days. Those spikes happened due to strong absorbers' (Rb, Sr, Cs, Ba) removal at the end of the effective cycle (100% of these elements removing every 3435 days of operation). The corresponding effective multiplication factor increase (Figure 3.6) and breeding intensification leads to additional ^{232}Th consumption.

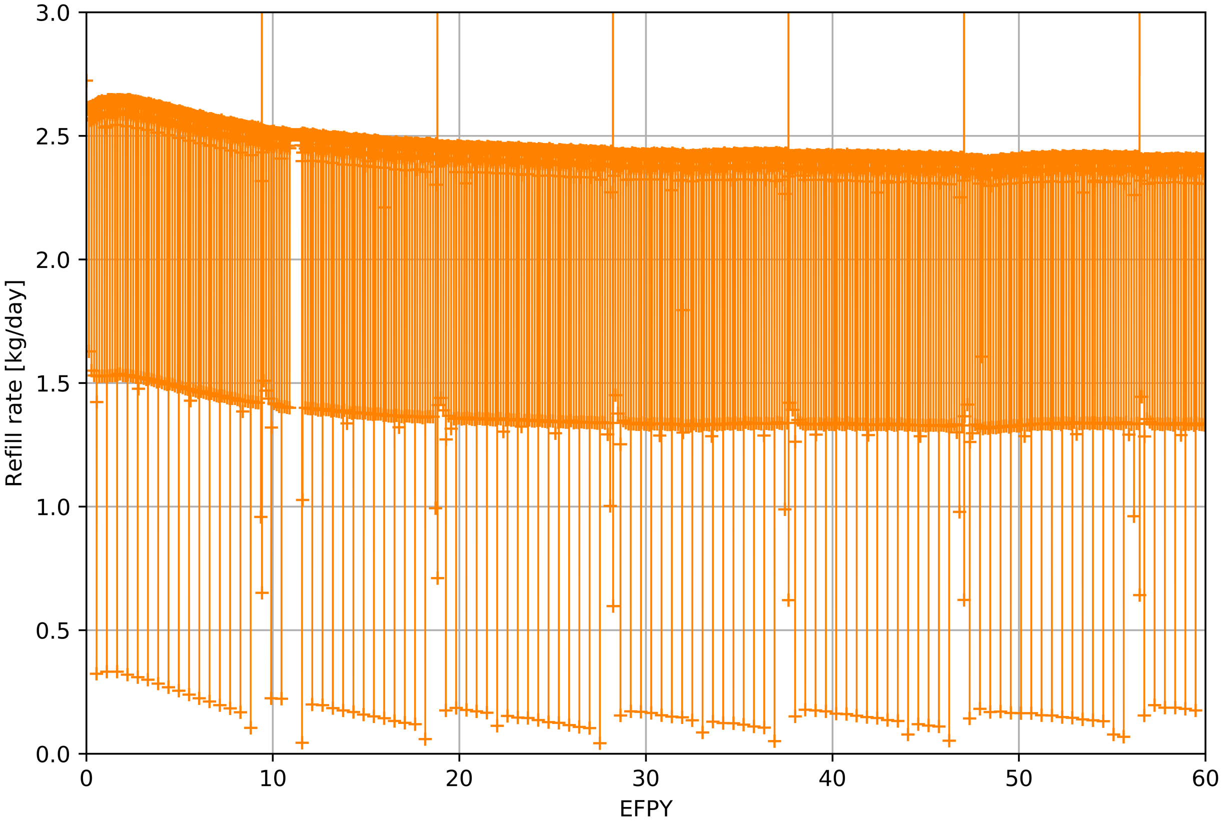

Figure 3.15: ^{232}Th feed rate over 60 years of the MSBR operation (reproduced from Rykhlevskii *et al.* [88]).

The average thorium feed rate increases during the first 500 days of operation and steadily decreases due to spectrum hardening and accumulation of absorbers in the core. As a result, the average ^{232}Th feed rate over 60 years of operation is about 2.40 kg/day which is in a good agreement with a recent online reprocessing study by ORNL (2.45 kg/day, 2% difference) [15, 12]. At equilibrium, the thorium feed rate is determined by the reactor power, the energy released per fission, and the neutron energy spectrum.

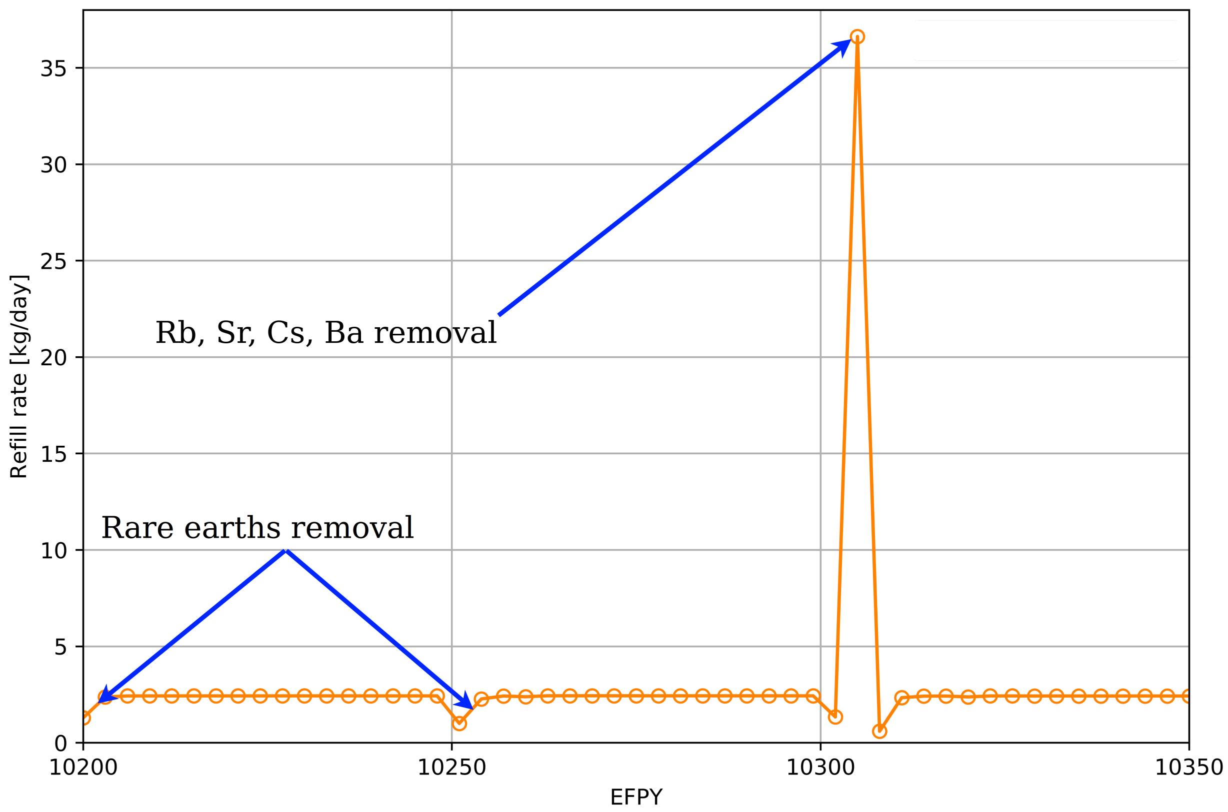

Figure 3.16: Zoomed ^{232}Th feed rate for a 150-EFPD time interval (reproduced from Rykhlevskii *et al.* [88]).

3.4 Operational and safety parameter evolution

In Section 3.3, we reported how fuel salt composition changes during MSBR operation. The number density of the most important heavy isotopes, ^{233}U and ^{232}Th, was stable while transitioning from startup to equilibrium composition (Figure 3.8). At the same time, a number of different actinides is being produced in the reactor core. Most of these nuclides (^{234}U, ^{239}Pu, ^{241}Pu) have a much larger absorption cross section than ^{233}U and ^{232}Th loaded initially into the core, which causes significant neutron energy spectrum hardening. In the current section, we analyze how such neutron spectrum shift affects major operation and safety parameters such as temperature coefficients of reactivity and reactivity worth of the control rods.

3.4.1 Temperature coefficient of reactivity

Table 3.4 summarizes temperature effects on reactivity calculated in this work for both initial and equilibrium fuel compositions, compared to the original ORNL report data [83]. By propagating the k_{eff} statistical error provided by Serpent, uncertainty for each temperature coefficient was obtained and appears in Table 3.4. Other sources of uncertainty are neglected, such as cross section measurement error and approximations inherent in the equations of state, providing both the salt and graphite density dependence on temperature. The main physical principle underlying the reactor temperature feedback is an expansion of heated material. If the fuel salt temperature increases, the density of the salt decreases; at the same time, the total volume of fuel salt in the core remains constant because the graphite bounds it. If the graphite temperature increases, the density of graphite decreases, creating additional space for fuel salt. To determine the temperature coefficients, the cross section temperatures for the fuel and moderator were changed from 900K to 1000K. Three different cases were considered:

1. Temperature of fuel salt rising from 900K to 1000K.
2. Temperature of graphite rising from 900K to 1000K.
3. Whole reactor temperature rising from 900K to 1000K.

Table 3.4: Temperature coefficients of reactivity for the initial and equilibrium states (reproduced from Rykhlevskii *et al.* [88]).

Reactivity coefficient	Initial [pcm/K]	Equilibrium [pcm/K]	Reference [83] (initial) [pcm/K]
Doppler in fuel salt	−4.73 ± 0.038	−4.69 ± 0.038	−4.37
Fuel salt density	+1.21 ± 0.038	+1.66 ± 0.038	+1.09
Total fuel salt	−3.42 ± 0.038	−2.91 ± 0.038	−3.22
Graphite spectral shift	+1.56 ± 0.038	+1.27 ± 0.038	
Graphite density	+0.14 ± 0.038	+0.23 ± 0.038	
Total moderator (graphite)	+1.69 ± 0.038	+1.35 ± 0.038	+2.35
Total core	−1.64 ± 0.038	−1.58 ± 0.038	−0.87

In the first case, changes in the fuel temperature only impact fuel density. In this case, the geometry is unchanged because the fuel is a liquid. However, if the moderator heats up, both the density and the geometry change due to the thermal expansion of the solid graphite blocks and reflector. Accordingly, the new graphite density was calculated using a linear temperature expansion coefficient of $1.3\times10^{-6}K^{-1}$ [83]. A new geometry input for Serpent, which takes into account the displacement of graphite surfaces, was created based on this information. For calculation of displacement, it was assumed that the interface between the graphite reflector and vessel is immobile and the vessel temperature is constant. This is the most reasonable assumption for the short-term reactivity effects because inlet salt cools the graphite reflector and the inner surface of the vessel.

The fuel temperature coefficient (FTC) is negative for both initial and equilibrium fuel compositions due to thermal Doppler broadening of the resonance capture cross sections in the thorium. A small positive effect of fuel density on reactivity increases from +1.21 pcm/K at reactor startup to +1.66 pcm/K for equilibrium fuel composition, which has a negative effect on FTC magnitude during the reactor operation; this is in good agreement with earlier research [83, 73]. The moderator temperature coefficient (MTC) is positive for the startup composition and decreases during reactor operation because of spectrum hardening with fuel depletion. Finally, the total temperature coefficient of reactivity is negative for both cases but decreases in magnitude during reactor operation due to spectral shift. In summary, even after 20 years of operation, the total temperature coefficient of reactivity is relatively large and negative during reactor operation (comparing with conventional PWR which has temperature coefficient about -1.71 pcm/°F ≈ -3.08 pcm/K [40]), despite positive MTC, and affords excellent reactor stability and control.

3.4.2 Reactivity control system rod worth

Table 3.5 summarizes the reactivity control system worth. During normal operation, the control (graphite) rods are fully inserted, and the safety (B_4C) rods are fully withdrawn. To insert negative reactivity into the core, the graphite rods are gradually withdrawn from the core. In an accident, the safety rods would be dropped down into the core. The integral rod worths were calculated for various positions to separately estimate the worth of graphite control rods, the emergency shutdown rods, and the whole reactivity control system. Control rod integral worth is approximately 28 cents and stays almost constant during reactor operation. The emergency shutdown rod integral worth decreases by 16.2% during 20 years of operation because of neutron spectrum hardening and absorber accumulation in proximity to reactivity control system rods. This 16% decline in control system worth must be taken into account in MSBR accident analysis and safety justification.

Table 3.5: Control system rod worth for the initial and equilibrium fuel compositions (reproduced from Rykhlevskii *et al.* [88]).

Reactivity parameter	Initial[¢]	Equilibrium[¢]
Graphite control rod integral worth	28.2 ± 0.8	29.0 ± 0.8
Emergency shutdown rod integral worth	251.8 ± 0.8	211.0 ± 0.8
Total reactivity control system worth	505.8 ± 0.7	424.9 ± 0.8

3.4.3 Six Factor Analysis

The effective multiplication factor can be expressed using the following formula:

$$k_{eff} = \eta f p \epsilon P_f P_t \tag{3.1}$$

where

η = neutron reproduction factor [−]

f = thermal utilization factor [−]

p = resonance escape probability [−]

ϵ = fast fission factor [−]

P_f = fast non-leakage probability [−]

P_t = thermal non-leakage probability [−].

Table 3.6 summarizes the six factors for both the initial and equilibrium fuel salt compositions. Using Serpent and SaltProc, these factors and their statistical uncertainties have been calculated for both the initial and equilibrium fuel salt compositions (see Table 3.1). The fast and thermal non-leakage probabilities remain constant despite the evolving neutron spectrum during operation. In contrast, the neutron reproduction factor (η), resonance escape probability (p), and fast fission factor (ϵ) are considerably different between startup and equilibrium. As indicated in Figure 3.10, the neutron spectrum is softer at the beginning of reactor life. Neutron spectrum hardening causes the fast fission factor to increase through the core lifetime; the opposite is true for the resonance escape probability. Finally, the neutron reproduction factor decreases during reactor operation due to the accumulation of fissile plutonium isotopes.

Table 3.6: Six factors for the full-core MSBR model for the initial and equilibrium fuel compositions (reproduced from Rykhlevskii *et al.* [88]).

Factor	Initial	Equilibrium
Neutron reproduction factor (η)	1.3960 ± .000052	1.3778 ± .00005
Thermal utilization factor (f)	0.9670 ± .000011	0.9706 ± .00001
Resonance escape probability (p)	0.6044 ± .000039	0.5761 ± .00004
Fast fission factor (ϵ)	1.3421 ± .000040	1.3609 ± .00004
Fast non-leakage probability (P_f)	0.9999 ± .000004	0.9999 ± .000004
Thermal non-leakage probability (P_t)	0.9894 ± .000005	0.9912 ± .00005

3.5 Benefits of fission products removal

To investigate how online fuel salt processing described in Chapter 2 affects the reactor performance, the separate effect of each poison group removal was studied in this section.

3.5.1 The effect of removing fission products from the fuel salt

Loading the initial fuel salt composition into the MSBR core leads to a supercritical configuration (Figure 3.17). After reactor startup, the effective multiplication factor for the case with volatile gases and noble metals removal is approximately 7500 pcm higher than for the case without fission product removal. This significant impact on the reactor core lifetime is achieved due to the immediate removal (20 sec cycle time) and the high absorption cross sections of Xe, Kr, Mo, and other noble metals removed. The effect of rare earth element removal is significant in a few months after startup and reached approximately 5500 pcm after 10 years of operation. The rare earth elements were removed at a slower rate (50-day cycle time). Moreover, Figure 3.17 demonstrates that batch-wise removal of strong absorbers every 3 days unnecessarily leads to fluctuation in results, but rare earth element removal every 50 days causes an approximately 600 pcm jump in reactivity.

The effective multiplication factor of the core reduces gradually over operation time because the fissile material (^{233}U) continuously depletes from the fuel salt due to fission while fission products accumulate in the fuel salt simultaneously. Eventually, without fission products removal, the reactivity decreases to the subcritical state after approximately 500 and 1300 days of operation for cases with no removal and volatile gases & noble metals removal, respectively. The time when the simulated core becomes subcritical (k_{eff} <1.0 for full-core model) is called the core lifetime. Therefore, removing fission products provides significant neutronic benefits and enables a longer core lifetime.

3.6 Concluding remarks

This chapter introduces the first ever version of the open-source MSR simulation package SaltProc v0.1. The main goal of this work has been to demonstrate SaltProc's capability to find the equilibrium fuel salt composition (the number densities of major isotopes vary by less than 1% over several years). A secondary goal has been to compare predicted operational

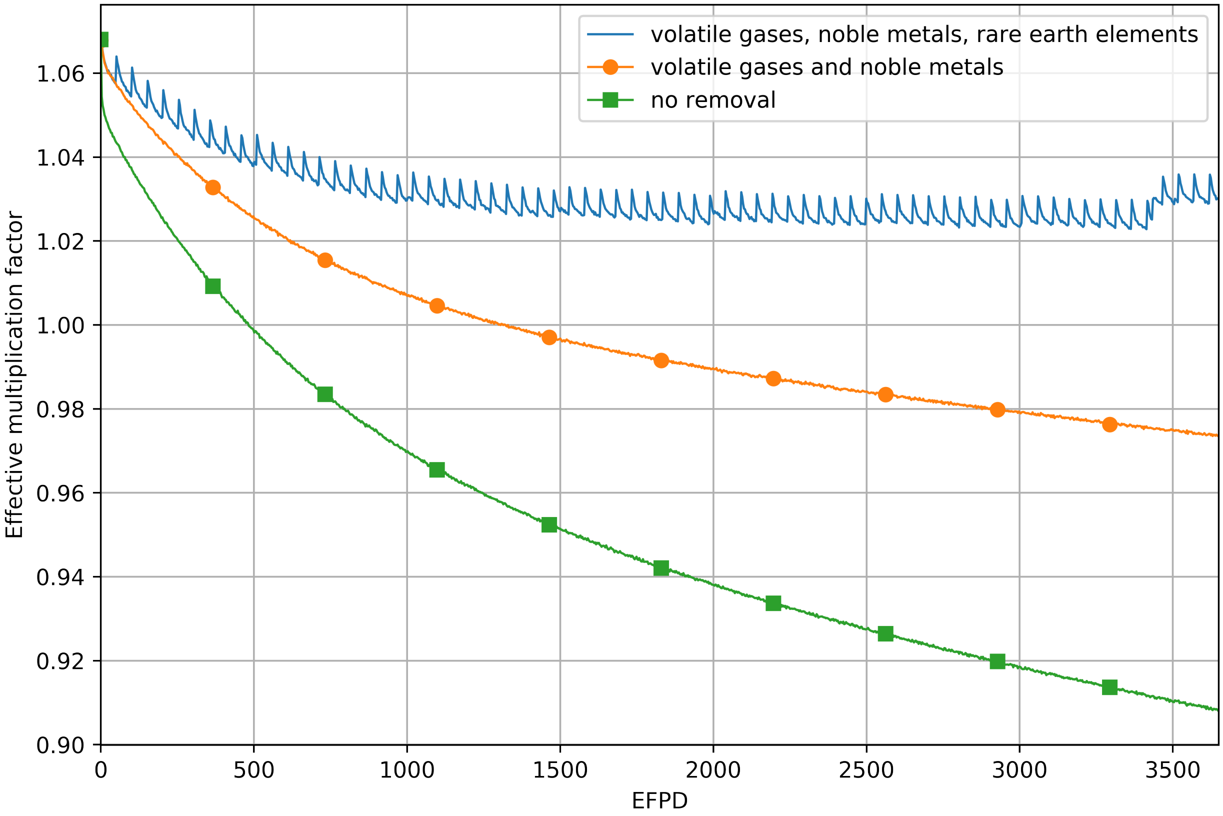

Figure 3.17: Calculated effective multiplication factor for the full-core MSBR model with the removal of various fission product groups over 10 years of operation (reproduced from Rykhlevskii *et al.* [88]).

and safety parameters (e.g., neutron energy spectrum, power and breeding distribution, temperature coefficients of reactivity) of the MSBR at startup and equilibrium states. A tertiary goal has been to demonstrate the benefits of continuous fission product removal for thermal MSR design.

To achieve these goals, a full-core high-fidelity benchmark model of the MSBR was created in Serpent 2. The full-core model was used instead of the simplified single-cell model [15, 93, 18] to precisely describe the two-region MSBR concept design sufficiently to represent breeding in the outer core zone accurately. When running depletion calculations, the most critical fission products and ^{233}Pa are removed, while fertile and fissile materials are added to the fuel salt every 3 days. Meanwhile, the removal interval for the rare earths, volatile fluorides, and semi-noble metals was greater than one month (50 days), which caused significant k_{eff} fluctuation.

The results in this chapter indicate that k_{eff} slowly decreases from 1.075 and reaches 1.02 at equilibrium after approximately 6 years of operation. At the same time, the concentrations of ^{233}U, ^{232}Th, ^{233}Pa, and ^{232}Pa stabilized after approximately 2500 days of operation. Particularly, ^{233}U number density equilibrates[3] after 16 years of operation. Consequently, the core reaches the quasi-equilibrium state after 16 years of operation. However, a wide variety of actinides, including fissile isotopes (e.g., ^{233}U and ^{239}Pu) and non-fissile strong absorbers (^{234}U), continue accumulating in the core.

Those actinides cause neutron energy spectrum hardening as the core approaches equilibrium. Moreover, the neutron energy spectrum in the central core region is much softer than in the outer core region due to the lower moderator-to-fuel ratio in the outer zone, and this distribution remains stable during reactor operation. Finally, the epithermal or thermal spectrum is needed to effectively breed ^{233}U from ^{232}Th because the radiative capture cross section of ^{232}Th monotonically decreases from 10^{-10} MeV to 10^{-5} MeV. A harder spectrum in the outer core region tends to significantly increase resonance absorption in thorium and decrease the absorption in fissile and structural materials.

The spatial power distribution in the MSBR shows that 98% of the fission power is generated in the central zone I, and the neutron energy spectral shift has zero effect on the power distribution. The spatial distribution of neutron capture reaction rate for fertile ^{232}Th, corresponding to breeding in the core, confirms that most of the breeding occurs in an outer, undermoderated, region of the MSBR core. Finally, the average ^{232}Th refill rate throughout 60 years of operation is approximately 2.40 kg/day or 100 g/GWh$_e$.

We compared the safety parameters at startup and equilibrium state using the Serpent Monte Carlo code. The total temperature coefficient is large and negative at startup and equilibrium, but the magnitude decreases throughout reactor operation from −1.64 to −1.58 pcm/K as the spectrum hardens. The moderator temperature coefficient is positive and also

---

[3] fluctuates less than 0.8%

decreases during fuel depletion. The reactivity control system efficiency analysis showed that the safety rod integral worth decreases by approximately 16.2% over 16 years of operation, while the graphite rod integral worth remains constant. Therefore, neutron energy spectrum hardening during fuel salt depletion has an undesirable impact on MSBR stability and controllability and should be taken into consideration in further analysis of transient accident scenarios.

Finally, we proved that the MSBR core performance benefits from the removal of volatile gases, noble metals, and rare earths from the fuel salt. Immediate removal of volatile gases (e.g., xenon) and noble metals increased reactivity by approximately 7500 pcm over a 10-year timeframe. In contrast, the effect of relatively slower removal of rare earth elements (every 50 days cycle instead of 3 days) has less impact (5500 pcm) on the core reactivity after 10 years of operation. An additional study is needed to establish neutronic and economic tradeoffs of removing each element.

This chapter's results also helped identify the main directions of SaltProc v0.1 improvement. Firstly, the poison removal efficiency is not ideal, as was discussed in Chapter 1; consequently, the user should be able to simulate the fuel salt reprocessing system using a variable, non-ideal extraction efficiency. Secondly, SaltProc v0.1 entirely removes elements with longer residence times (semi-noble metals, volatile fluorides, Rb, Sr, Cs, Ba, Eu) at the end of cycle time (e.g., 3435 days for rubidium) which causes significant jumps in k_{eff} due to the removal of large batches of the poison at once. In SaltProc v1.0, this drawback has been eliminated by removing a fraction of the target element with longer residence time at each depletion step. In the following chapters, improved SaltProc v1.0 capabilities will be demonstrated.

Chapter 4

Tool demonstration for lifetime-long depletion: Transatomic Power MSR

This chapter presents a validation demonstration applying SaltProc v1.0 to the TAP MSR. The TAP concept was selected because it is well analyzed in the literature [16, 17] making code-to-code verification with ChemTriton/SCALE possible [17]. This chapter presents the TAP MSR core lifetime-long (25 years) depletion simulation with moderate time resolution (3-day depletion step) and a constant, 100% power level. The results obtained with SaltProc v1.0 are compared with full-core TAP depletion analysis by Betzler *et al.* [17] with assumed ideal removal efficiency (100% of the target isotope is removed). This validation effort showed that the SaltProc v1.0 solution matches the case with *ideal extraction efficiency.*

Finally, this chapter presents a lifetime-long fuel salt depletion simulation for the case with *a realistic, physics-based* mathematical model for noble gas removal efficiency, which provides fuel isotopic composition evolution during 25 years of the TAP MSR operation. Additionally, this chapter presents safety and operational parameters evolution during operation. Detailed insights about fuel salt composition and neutron spectrum dynamics obtained herein will be used in the following chapters to investigate TAP reactor poisoning during load-following.

4.1 Transatomic Power MSR design description

The TAP concept is a 1250 MW_{th} MSR with a LiF-based uranium fuel salt [106]. This concept uses configurable zirconium hydride rods as the moderator, while most MSR designs typically propose high-density reactor graphite. Zirconium hydride offers a much higher neutron moderating density than graphite, so a much smaller volume of zirconium hydride is needed to achieve a thermal energy spectrum similar to one obtained with a graphite moderator. Moreover, zirconium hydride clad in a corrosion-resistant material has a much longer lifespan in extreme operational conditions (e.g., high temperature, large neutron flux, chemically aggressive salt) than reactor graphite [107]. Finally, zirconium hydride is a nonporous material and holds up fewer neutron poisons (e.g., xenon, krypton) than does high-density reactor graphite.

In this section, the design characteristics and reprocessing plant design are based on information presented in the TAP white papers [106, 105] and ORNL technical reports [16, 17].

4.1.1 General design description

Figure 4.1 renders of the primary and secondary loop of the TAP MSR seated inside a concrete nuclear island. Figure 4.2 shows the schematic design of a 520 MW_e, 2-loop nuclear reactor system with an intermediate salt loop.

The TAP core design (Figure 4.3) is very similar to the original MSRE design developed by ORNL [47] but has two significant innovations: the fuel salt composition and the moderator. The MSRE's LiF-BeF_2-ZrF_4-UF_4 salt has been substituted with LiF-UF_4 salt, which allows for an increase in the uranium concentration within the fuel salt from 0.9 to 27.5% while maintaining a relatively low melting point (490°C compared with 434°C for the original MSRE's salt) [16]. The graphite has an extensive thermal scattering cross section which makes it a perfect moderator but has a few major drawbacks:

(a) low lethargy gain per collision requires a large volume of a moderator to be present to reach criticality, which leads to a larger core and obstructs the core power density;
(b) even special reactor-grade graphite has relatively high porosity; thus, it holds gaseous FPs (e.g., tritium, xenon) in pores;
(c) reactor graphite lifespan in a commercial reactor is approximately ten years [83].

As previously mentioned, to resolve these issues, the TAP concept uses zirconium hydride

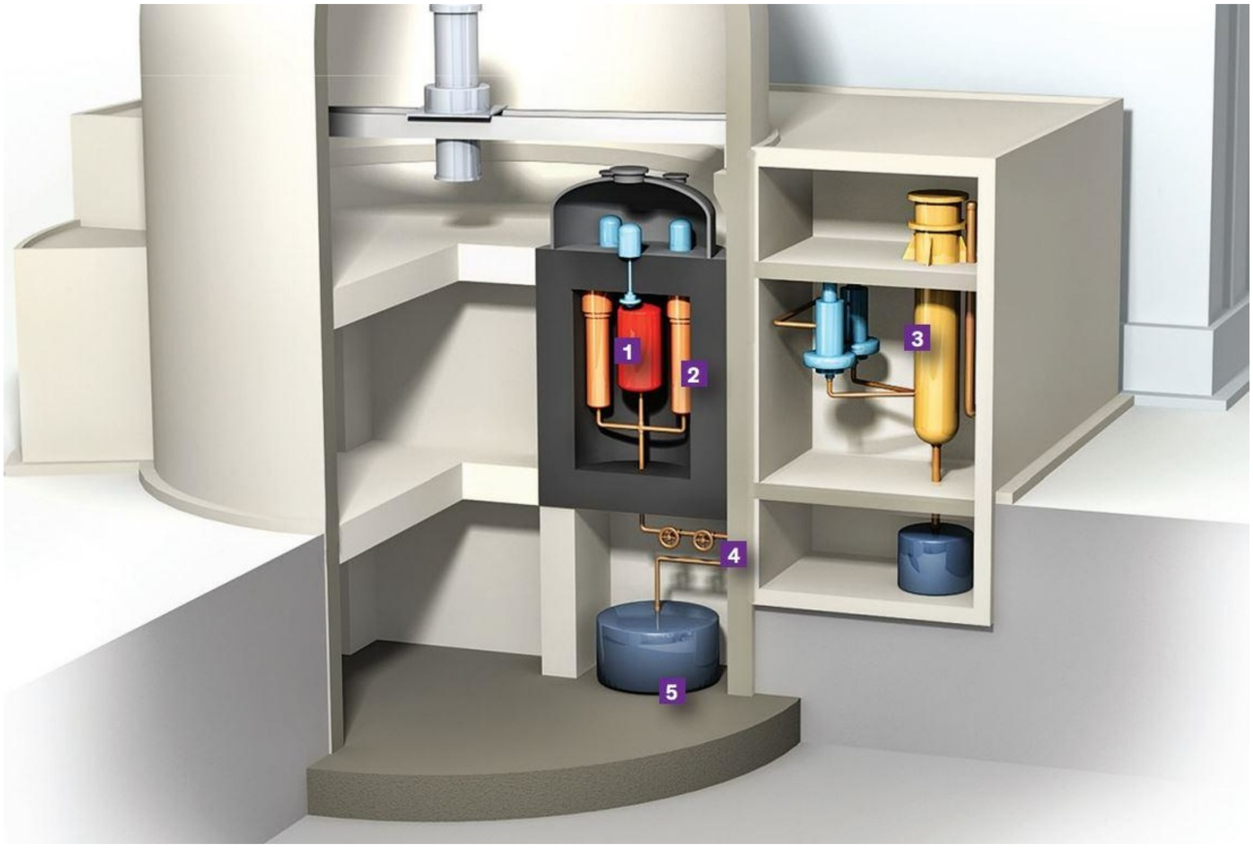

Figure 4.1: Rendering of the TAP MSR. The fission happens in the fuel salt inside the reactor vessel (1). The heat generated by a self-sustaining nuclear fission reaction would be transferred to the secondary salt by heat exchangers (2), which would boil water in the steam generator (3). Valves made of salt with a higher melting point (4) would melt in case of emergency, allowing the salt to drain into a drain tank (5), which can passively dissipate decay heat (reproduced from [100], illustration by Emily Cooper).

instead of graphite, allowing for a more compact core and a significant increase in power density. These two innovative design choices, together with a configurable moderator (the moderator-to-fuel ratio can be changed during operation), facilitate use of commercially available 5% enriched LEU fuel cycle.

The TAP MSR primary loop contains the reactor core volume (including the zirconium hydride moderator rods with silicon carbide cladding), pumps, pipes, and primary heat exchangers. Pumps circulate the LiF-(Act)F_4 fuel salt through the primary loop. The

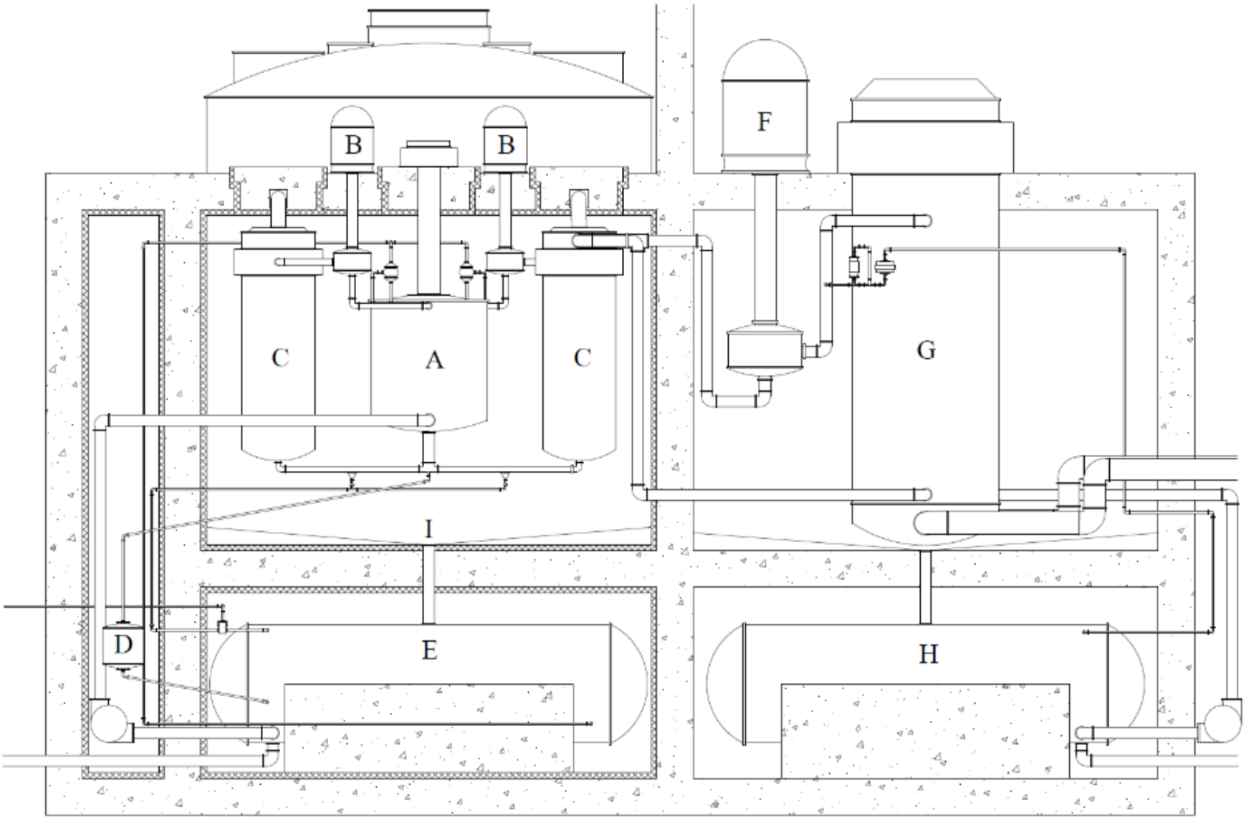

Figure 4.2: Simplified schematic of the TAP MSR primary and secondary loops (reproduced from the Transatomic Power Technical White Paper [106]). Figure legend: A) reactor vessel, B) fuel salt pumps, C) primary heat exchangers, D) freeze plug, E) primary loop drain tank, F) secondary loop salt pump, G) steam generator, H) secondary loop drain tank, I) fuel catch basin.

pumps, vessels, tanks, and piping are made of a nickel-based alloy (similar to Hastelloy-N[1]), which is highly resistant to corrosion in various molten salt environments. Inside the reactor vessel, near the zirconium hydride moderator rods, the fuel salt is in a critical configuration and generates heat. Table 4.1 contains details of the TAP system design, which are taken from a technical white paper [106] and a neutronics overview [105] as well as an ORNL analysis of the TAP design [16, 17].

---

[1] Hastelloy-N is very common in MSR designs now, but was developed at ORNL in the MSRE program that started in the 1950s.

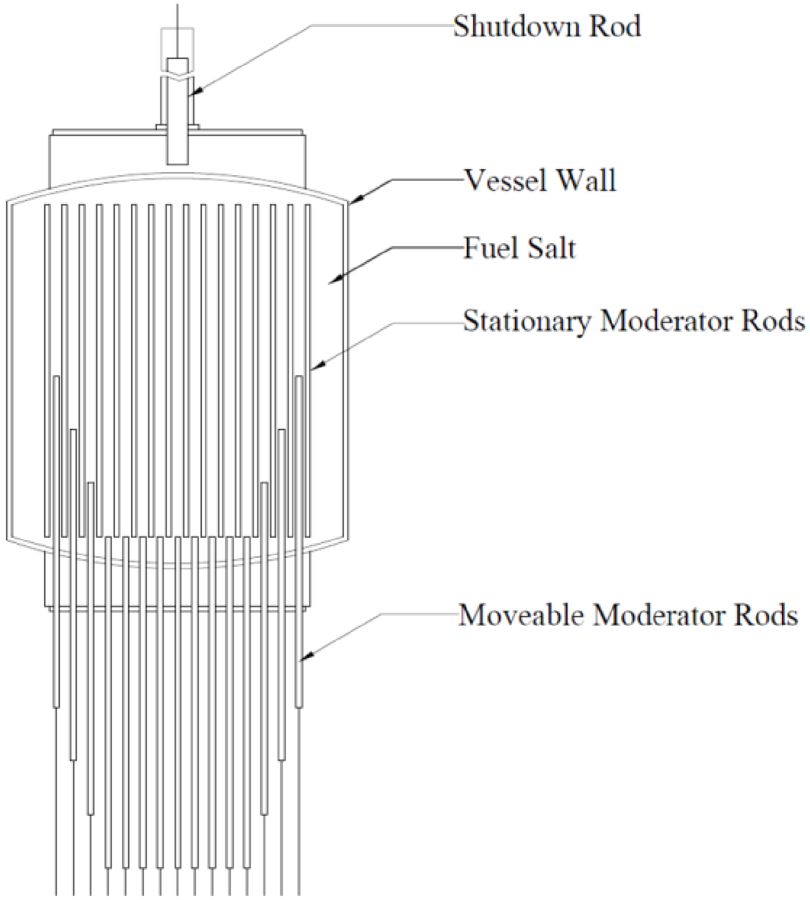

Figure 4.3: The TAP MSR schematic view showing moveable moderator rod bundles and shutdown rod (reproduced from Transatomic Power White Paper [106]).

Table 4.1: Summary of principal data for the TAP MSR (reproduced from [17, 106]).

Thermal power	1250 MW_{th}
Electric power	520 MW_e
Gross thermal efficiency	44%
Outlet temperature	620°C
Fuel salt components	$LiF\text{-}UF_4$
Fuel salt composition	72.5-27.5 mole%
Uranium enrichment	5% ^{235}U
Moderator	Zirconium hydride ($ZrH_{1.66}$) rods (with silicon carbide cladding)
Neutron spectrum	epithermal

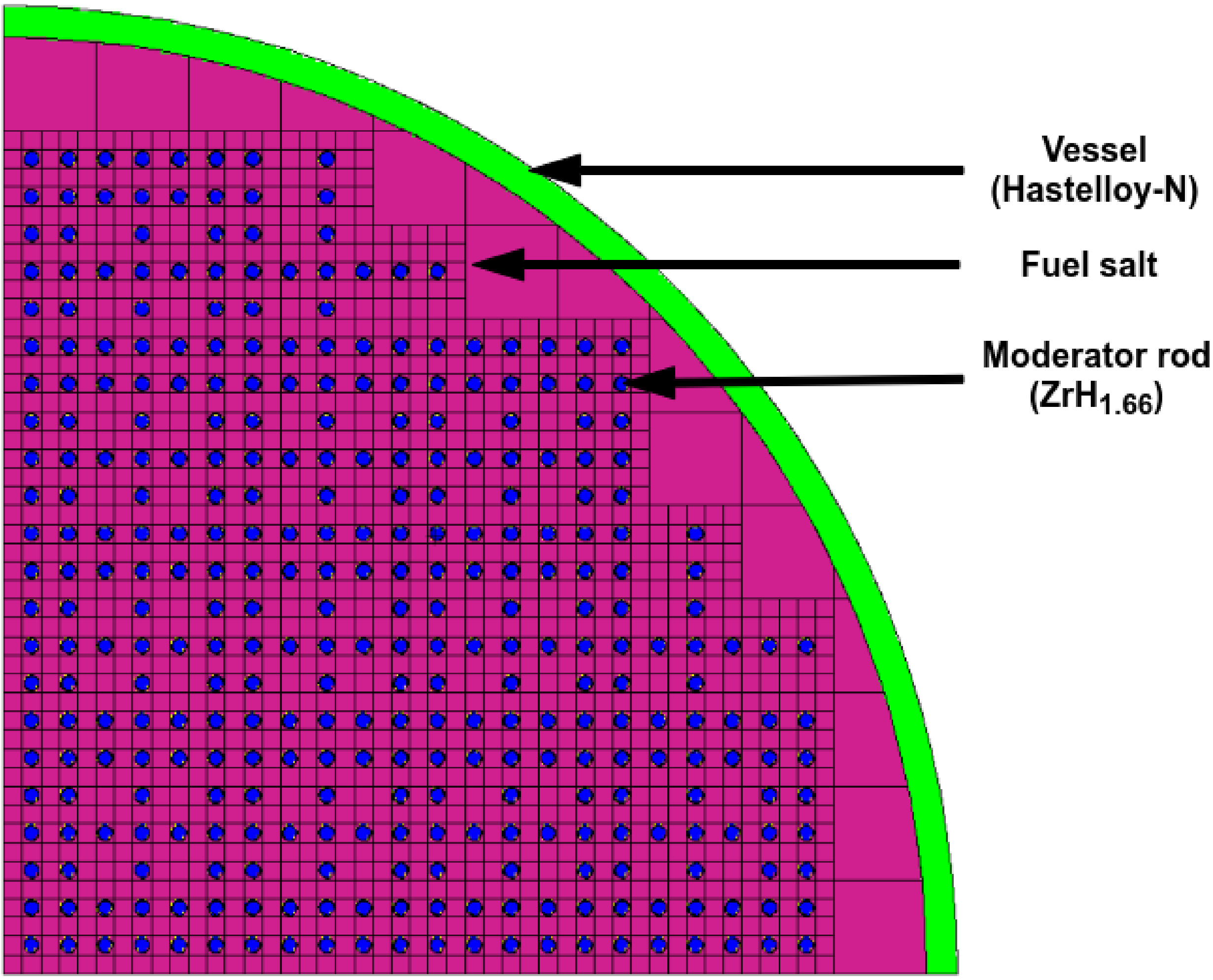

Figure 4.4: The TAP MSR schematic core view showing moderator rods (reproduced from ORNL/TM-2017/475 [17]).

4.1.2 Reactor core design

In the TAP core (Figure 4.4), fuel salt flows around moderator assemblies consisting of lattices of zirconium hydride rods clad in a corrosion-resistant silicone carbide. The TAP reactor pressure vessel is a cylinder made of a nickel-based alloy with an inner radius of 150 cm, a height of 350 cm, and a wall thickness of 5 cm.

The salt volume fraction (SVF) in the core is a parameter similar to the widely-used moderator-to-fuel ratio and can be defined as:

$$SVF = \frac{V_F}{V_F + V_M} = \frac{1}{1 + V_M/V_F} \tag{4.1}$$

where

V_F = fuel volume $[m^3]$

V_M = moderator volume $[m^3]$

V_M/V_F = moderator-to-fuel salt ratio $[-]$.

Figure 4.5 shows the SVF variation during operation that shifts the reactor neutron energy spectrum from intermediate to thermal to maximize fuel burnup. At the BOL, a high SVF results in a relatively hard spectrum and enhances fertile material (^{238}U) conversion into the fissile material (^{239}Pu) when the startup fissile material (^{235}U) inventory is still large. As fissile concentration in the fuel salt declines, additional moderator rods are introduced to maintain criticality, leading to salt volume fraction decrease (see Figure 4.5).

The initial TAP concept suggested varying the SVF by inserting fixed-sized moderator rods via the bottom of the reactor vessel (for safety considerations), similar to moving the control rods in a Boiling Water Reactor (BWR), as shown in Figure 4.3 [105]. The later TAP concept proposes reducing the SVF by reconfiguring the moderator rods during the regular shutdown for reactor maintenance [17]. For the TAP reactor, End of Life (EOL) occurs when the maximum number of moderator rods is inserted into the core and a further injection of fresh fuel salt does not alter criticality. Unmoderated salt flows in the annulus between the core and the vessel wall to reduce fast neutron fluence at the vessel structural material.

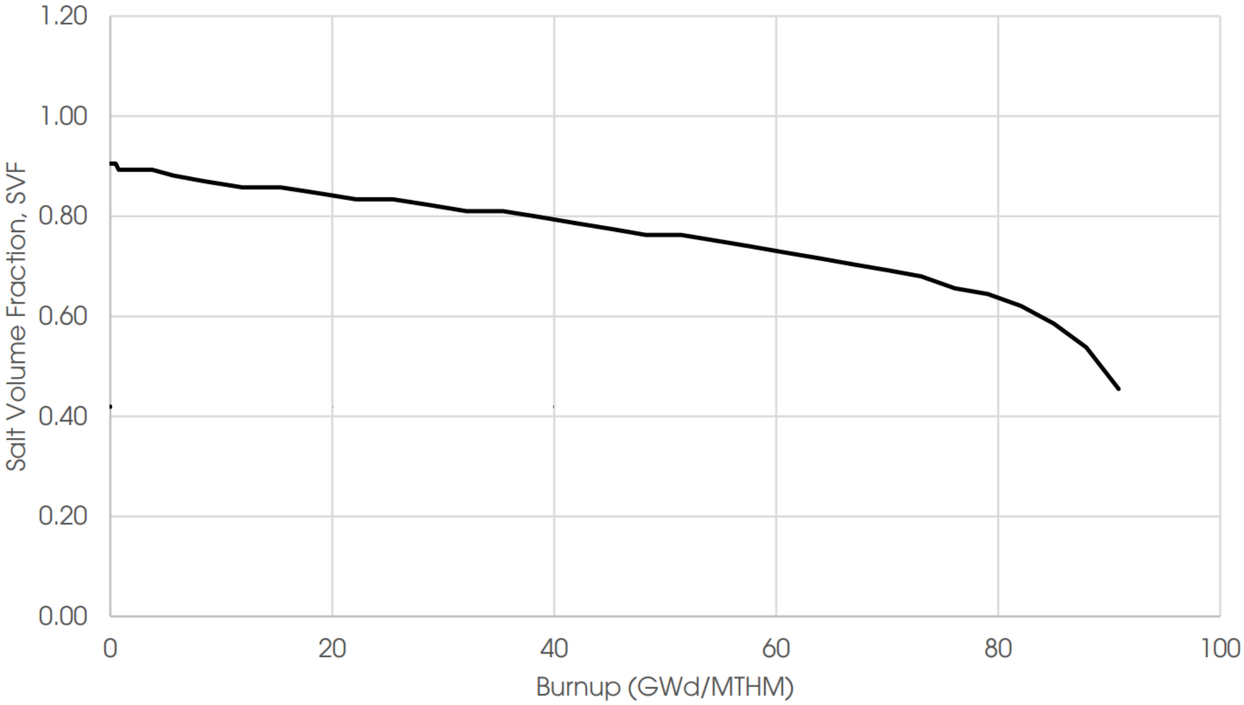

Figure 4.5: The change in SVF as a function of burnup in the TAP reactor (reproduced from Transatomic Power Neutronics Overview [105]).

4.1.3 Fuel salt reprocessing system

The TAP nuclear system contains a fission product removal system. Gaseous FPs are continuously removed using an off-gas system, while liquid and solid FPs are extracted via a chemical processing system. As these byproducts are gradually removed, a small quantity of fresh fuel salt is regularly added to the primary loop. This process conserves a constant fuel salt mass and keeps the reactor critical. In contrast with the MSBR reprocessing system, the TAP design does not need a protactinium separation and isolation system because it operates in a uranium-based single-stage fuel cycle. The authors of the TAP concept suggested three distinct fission product removal methods [105]:

Off-Gas System: The off-gas system removes gaseous fission products such as krypton and xenon, which are then compressed and temporarily stored until they have decayed to the background radiation level. Trace amounts of tritium are also removed and bottled in a liquid form via the same process. Also, the off-gas system directly removes a small fraction of the noble metals.

Metal Plate-Out/Filtration: A nickel mesh filter removes noble and semi-noble metal solid fission products as they plate out onto the internal surface of the filter.

Liquid Metal Extraction: Lanthanides and other non-noble metals stay dissolved in the fuel salt. They generally have a lower capture cross section and thus absorb fewer neutrons than ^{135}Xe, but their extraction is essential to ensure normal operation. In the TAP reactor, lanthanide removal is accomplished via a liquid-metal/molten salt extraction process similar to that developed for the MSBR by ORNL [83]. This process converts the dissolved lanthanides into a well-understood oxide waste form, similar to that of LWR SNF. This oxide waste exits the TAP reprocessing plant in ceramic granules which can be sintered into another convenient form for storage [106].

Figure 4.6 shows the principal design of the TAP primary loop, including an off-gas system, nickel mesh filter, and lanthanide chemical extraction facility. As in the MSBR, the TAP off-gas system is based on helium sparging through the fuel salt with consequent gas bubbles removed before returning the fuel salt to the core (see Section 2.1.1). Nevertheless, one crucial difference must be noted: the MSBR gas separation system suggested helium injection and subsequent transport of the voids throughout the primary loop, including the core for at least ten full loops [83].

In the TAP design the introduction of the void (helium bubbles) during operation is a significant concern for safe, stable operation because the increase of void fraction in the fuel salt when it enters back to the core could cause unpredictable reactivity change. Kedl stated without explanation, "Average loop void fractions as high as 1% are undesirable... it is desirable to keep the average loop void fraction well below 1%."[83] The MSBR design

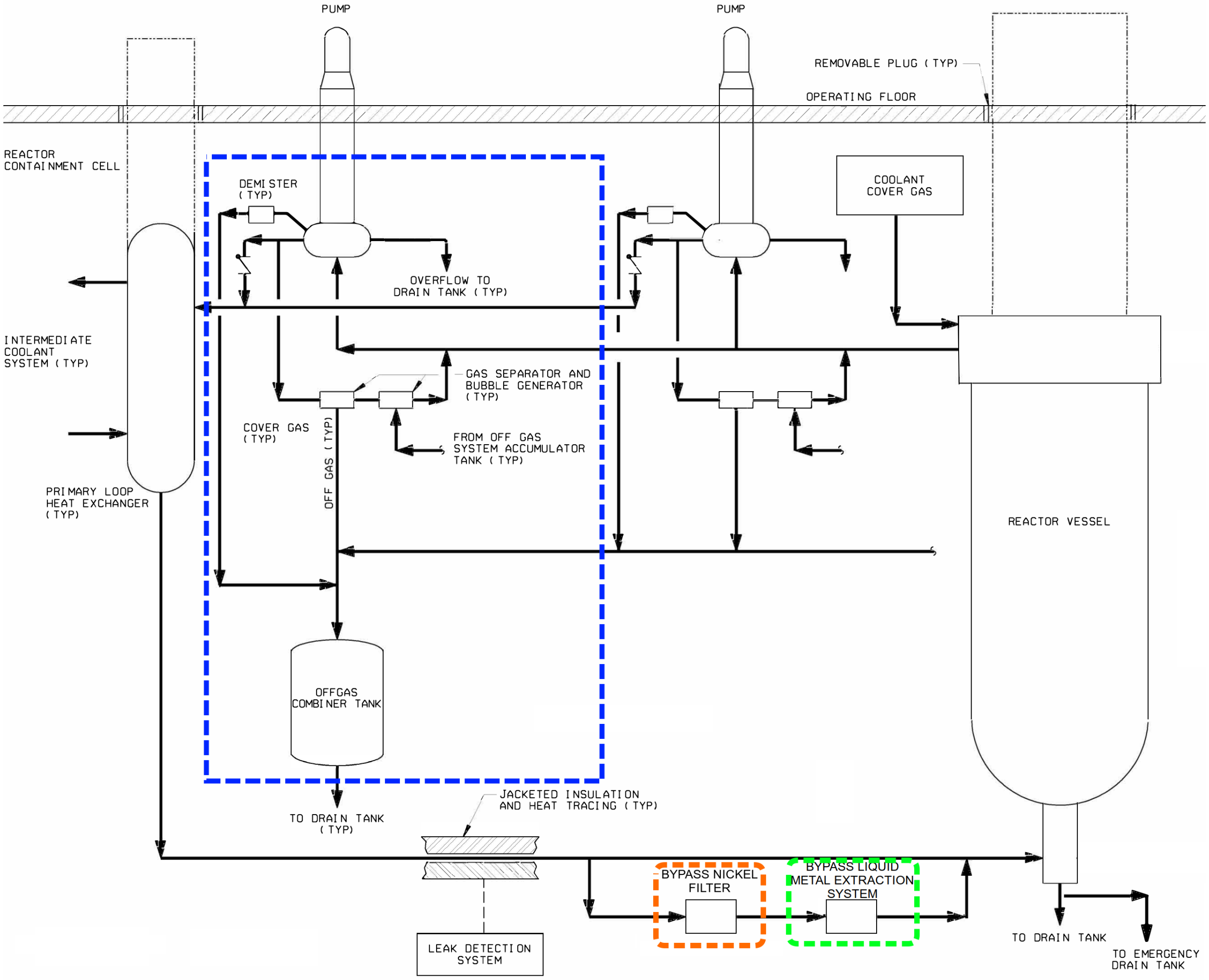

Figure 4.6: Simplified TAP primary loop design including off-gas system (blue), nickel filter (orange), and liquid metal extraction system (green) (reproduced from [76]).

targeted a 0.2% average void in the fuel salt [83] and the MSRE successfully operated with an average void fraction of about 0.7% [31]. The TAP design reduces void fraction in the fuel salt to negligible levels by using an effective gas separator for stripping helium/xenon bubbles before returning the salt to a primary loop (Figure 4.6, blue block).

Noble and semi-noble metal solid fission products tend to plate out onto metal surfaces, including piping, heat exchanger tubes, reactor vessel inner surface, etc. Previous research by ORNL [83] reported that about 50% of noble and semi-noble metals would plate out inside MSBR systems (including the off-gas system) without any special treatment. To improve the extraction efficiency of these fission products, the TAP concept suggested employing a nickel mesh filter located in a bypass stream in the primary loop (Figure 4.6, orange block). The main idea of this filter is to create a large nickel surface area using porous metal (e.g., Inconel fibers). The fuel salt flows throughout the filter and noble metals plate out on the filtering material.

This Liquid Metal Extraction process for the TAP concept has been adopted from the MSRE. The MSRE demonstrated a liquid-liquid extraction process for removing rare earths and lanthanides from fuel salt and estimated efficiency of this process. In fact, due to similarities in reprocessing schemes, the TAP project reported almost the same set of elements for removal and similar effective cycle times[2] as suggested for the MSBR (Table 4.2). The TAP neutronics white paper specifies additional low-probability fission products and gases that should be removed during operation [105]. These elements are categorized into the previously defined processing groups, but the removal rates of most of these elements (except hydrogen) are meager.

Details of gas removal and fuel reprocessing systems have historically been conceptual. Accordingly, liquid-fueled system design, including the TAP concept, usually assumes ideal (rather than realistically constrained) removal efficiencies for reactor performance simula-

---

[2] The MSBR program defined “cycle time” as the time required to remove 100% of atoms of a target nuclide from a fuel salt [83].

tions. In this thesis, I developed a realistic online reprocessing system and reactor model to capture the dynamics of fuel composition evolution during reactor operation. Gas removal efficiency is variable in that model, described using mathematical correlations from Chapter 2 (see Equation 2.1). For the other FPs, a fixed[3], non-ideal extraction efficiency based on cycle time from Table 4.2 was used to inform the fuel reprocessing model.

Table 4.2: The effective cycle times for fission product removal from the TAP reactor (reproduced from [11] and [105]).

Processing group	**Nuclides**	**Removal rate (s^{-1})**	**Cycle time (at full power)**
Elements removed in the MSBR concept and adopted for the TAP [83]			
Volatile gases	Xe, Kr	5.00E-2	20 sec
Noble metals	Se, Nb, Mo, Tc, Ru, Rh, Pd, Ag, Sb, Te	5.00E-2	20 sec
Semi-noble metals	Zr, Cd, In, Sn	5.79E-8	200 days
Volatile fluorides	Br, I	1.93E-7	60 days
Rare earths	Y, La, Ce, Pr, Nd, Pm, Sm, Gd	2.31E-7	50 days
	Eu	2.32E-8	500 days
Discard	Rb, Sr, Cs, Ba	3.37E-9	3435 days
Additional elements removed [105, 11]			
Volatile gases	H	5.00E-2	20 sec
Noble metals	Ti, V, Cr, Cu	3.37E-9	3435 days
Semi-noble metals	Mn, Fe, Co, Ni, Zn, Ga, Ge, As	3.37E-9	3435 days
Rare earths	Sc	3.37E-9	3435 days
Discard	Ca	3.37E-9	3435 days

4.2 TAP system model

In this section, the TAP core and fuel salt reprocessing system models for demonstrating SaltProc v1.0 are described in detail. I used these models for SaltProc demonstration and

---

[3] Published information about dynamics of extraction efficiency during reactor operation for noble-, semi-noble metals, and rare earths is insufficient to inform a variable removal efficiency.

validation in the current and following chapters.

4.2.1 Serpent 2 full-core model

Nested and lattice geometry types, as well as transformation capabilities of Serpent [63], are employed to represent the TAP core. Figure 4.7 shows the *XY* section of the whole-core model at the expected reactor operational level when all control rods are fully withdrawn. Figures 4.8 and 4.9 show a longitudinal section of the reactor. This model contains the moderator rods with their silicon carbide cladding, the pressure vessel, and the inlet and outlet plena (Table 4.3). Fuel salt flows around square moderator assemblies consisting of lattices of small-diameter zirconium hydride rods in a corrosion-resistant material. The salt volume fraction for Figure 4.7 is 0.917204, which means the modeled core is under-moderated and has an intermediate neutron spectrum. Quarter-core configurations of the TAP core with various salt volume fractions, used in the current work to maintain criticality for a reasonable operational period (> 20 years), are listed in Table A.1, Figures A.1, and A.2 in Appendix A.

To represent the reactivity control system, the model has:

(a) control rod guide tubes made of nickel-based alloy;
(b) control rods represented as boron carbide (B_4C) cylinders with a thin Hastelloy-N coating;
(c) air inside guide tubes and control rods.

The control rods must be able to suppress excess reactivity at the BOL when the core configuration is the most reactive, and the neutron spectrum is the hardest. The control rod design shown on Figures 4.7, 4.8, and 4.9 is comprised of a cluster of 25 rods that provide a total reactivity worth of 3922 ± 10 *pcm* at the BOL.

The control rod cluster is modeled using the **TRANS** Serpent 2 feature, which allows the user to change the control rod position during the simulation easily. The current work assumed that all control rods are fully withdrawn from the core (Figure 4.9), but the user

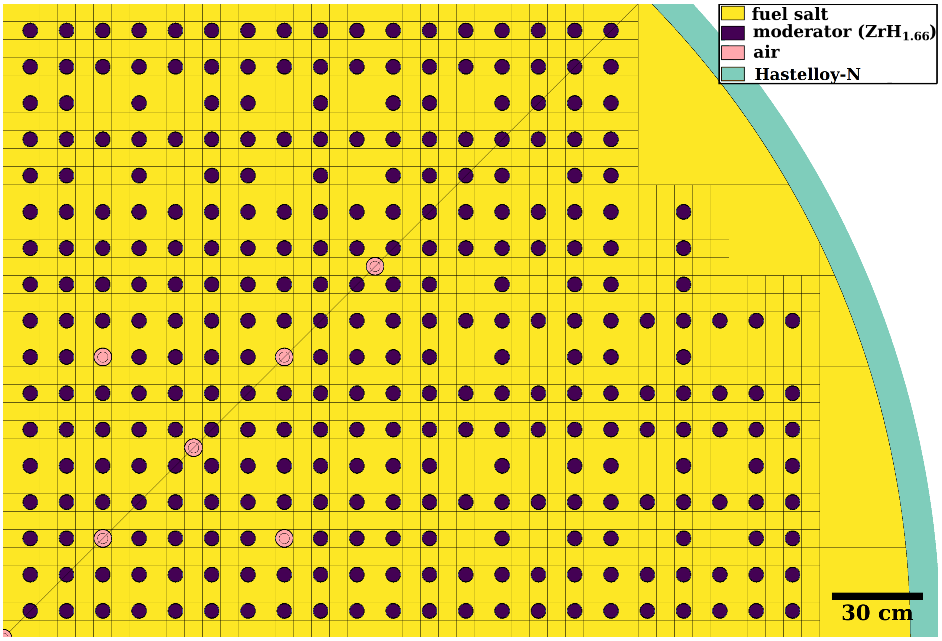

Figure 4.7: An XY section of the TAP model at horizontal midplane with fully withdrawn control rods at BOL (347 moderator rods, salt volume fraction 0.917204) [28, 90].

Table 4.3: Geometric parameters for the full-core 3D model of the TAP (reproduced from Betzler *et al.* [17]).

Component	Parameter	Value	Unit
Moderator rod	Cladding thickness	0.10	cm
	Radius	1.15	cm
	Length	3.0	m
	Pitch	3.0	cm
Moderator assembly	Array	5 × 5	rods×rods
	Pitch	15.0	cm
Core	Assemblies	268	assemblies/core
	Inner radius	1.5	m
	Plenum height	25.0	cm
	Vessel wall thickness	5.0	cm

can use reactivity control capabilities in SaltProc v1.0 to change control rod position during operation. In this dissertation, all figures of the core were generated using the built-in Serpent plotter.

The neutron population per cycle and the number of active/inactive cycles were chosen to obtain a balance between minimizing uncertainty for a transport problem (28 pcm for k_{eff}) and simultaneously minimizing computational time.

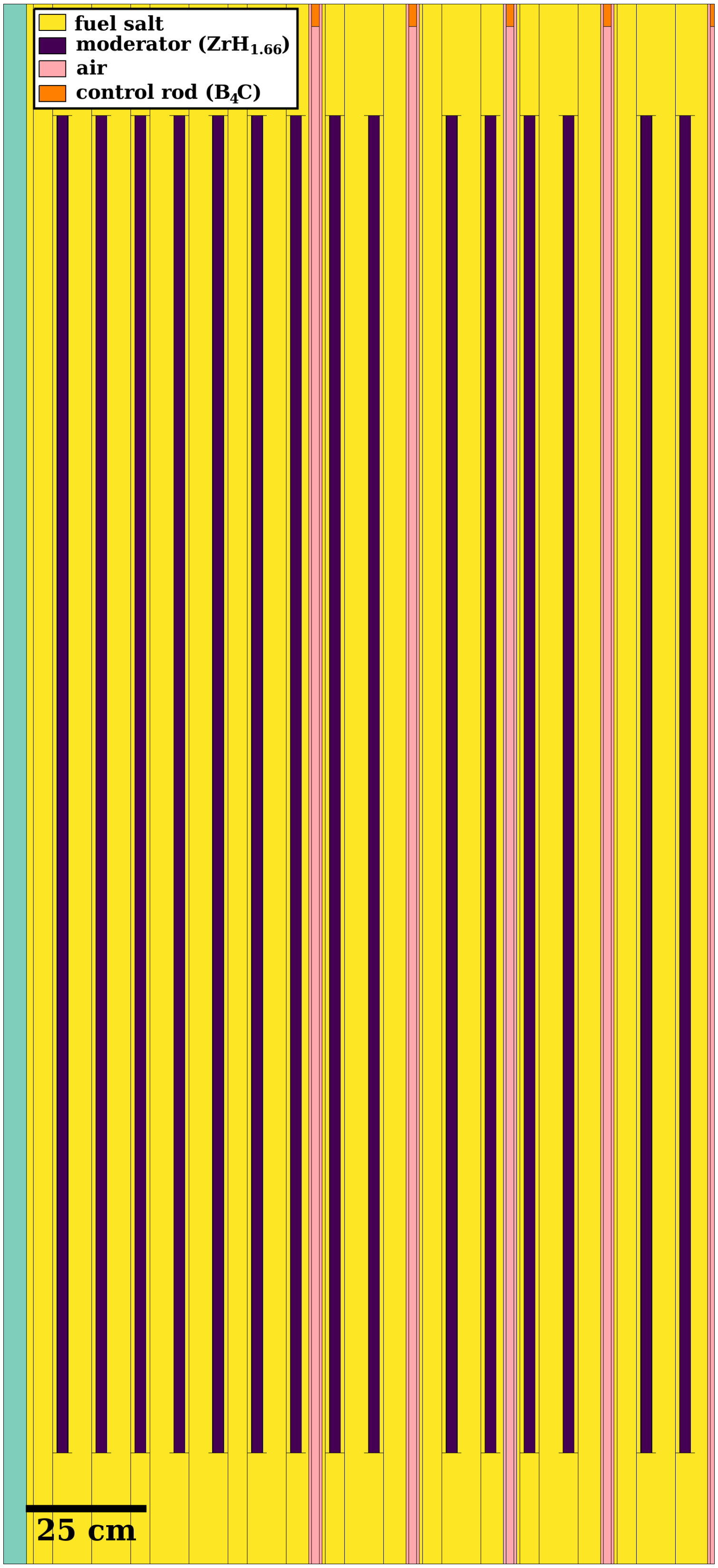

Figure 4.8: 45° XZ section of the TAP core model [28, 90].

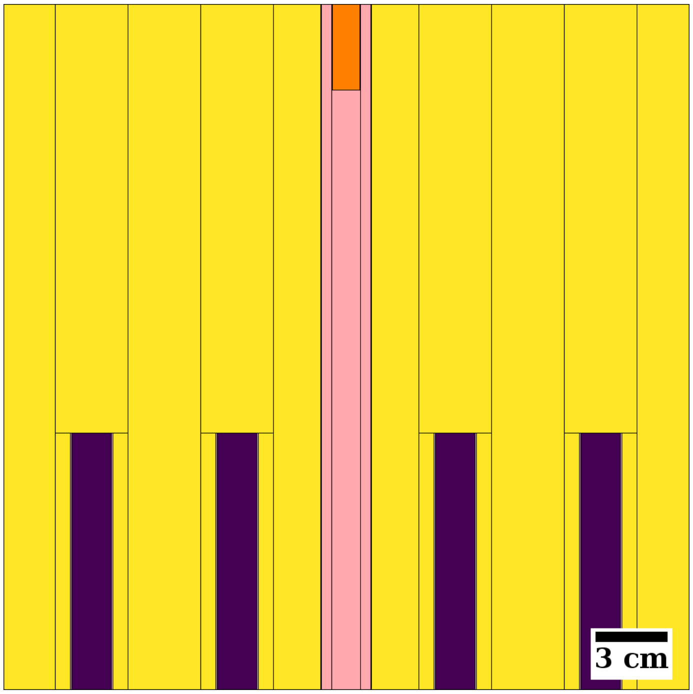

Figure 4.9: Zoomed XZ section of the top of the moderator and control rods in the TAP model.

4.2.2 Model of the fuel reprocessing system

I thoroughly analyzed the original TAP reprocessing system design (Figure 4.6) and neutron poison removal rates (Table 4.2) to determine a suitable reprocessing scheme for the SaltProc v1.0 demonstration (Figure 4.10). This chapter presents two demonstration cases: with ideal (Section 4.3.1) and realistic, non-ideal (Section 4.3.2) gas removal efficiency. Realistic noble gas removal efficiency is based on the physical model for noble gas extraction efficiency discussed in Section 2.1.1.

Arrows on Figure 4.10 represent material flows, percents represent a fraction of total mass flow rates; ellipses represent fuel reprocessing system components; boxes represent waste streams; the diamond shows refuel material flow (UF_4, 5 wt% of ^{235}U). The efficiency of gas migration to helium bubbles (ϵ_m) and efficiency of gas bubbles separation from the salt (ϵ_{es}) are different for various demonstration cases and discussed in more detail in Sections 4.3.1 and 4.3.2. Efficiency of noble metal extraction in the nickel filter (Figure 4.2, orange block)

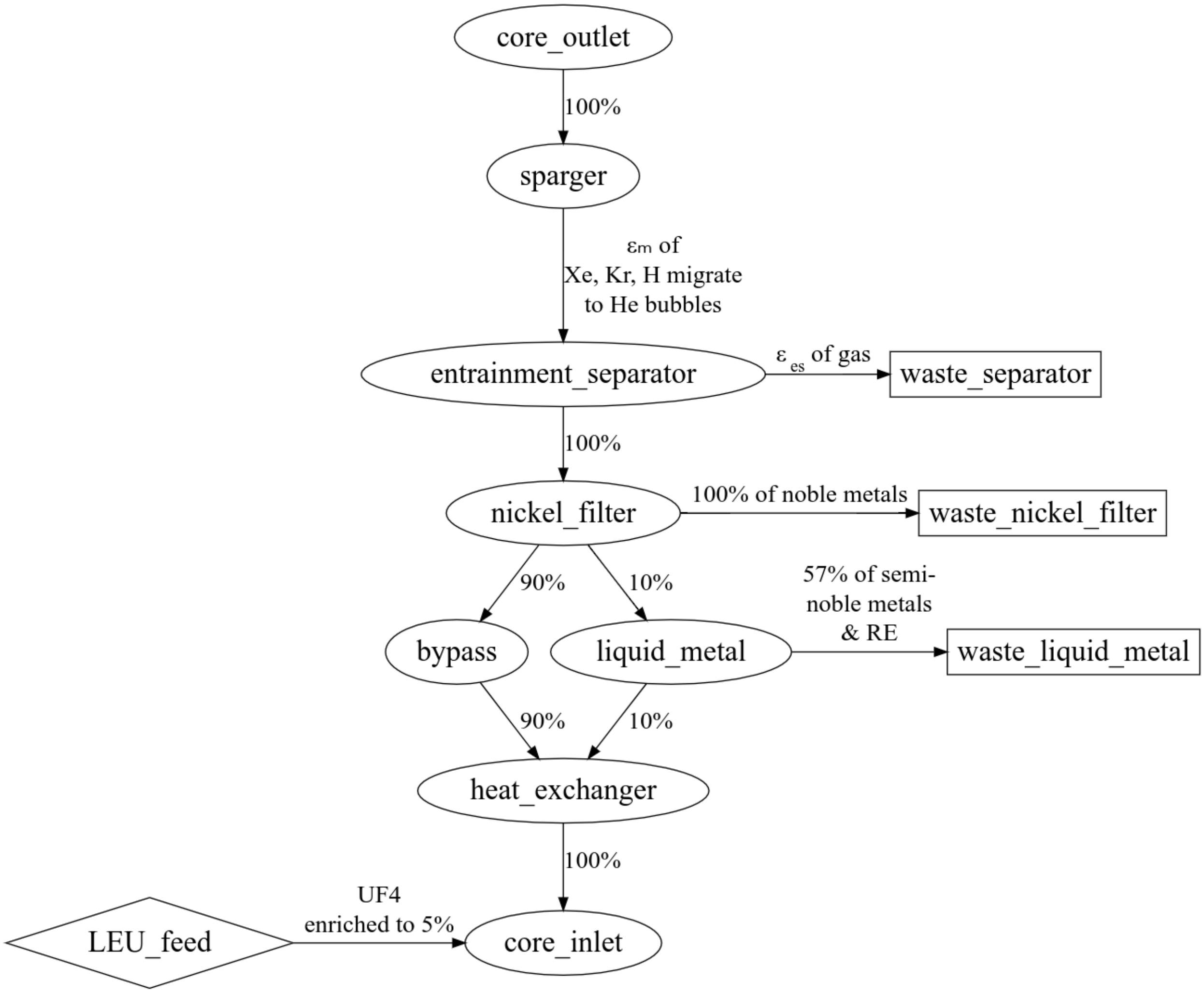

Figure 4.10: TAP reprocessing scheme flowchart used for the demonstration of SaltProc v1.0.

and semi-noble metals/rare earths (RE) in the liquid metal extraction system (Figure 4.2, green block) is assumed fixed and equal 100% and 57%, respectively.

The gas removal components (sparger/contactor and entrainment separator) are located in-line because the estimated full loop time[4] for the fuel salt is about 20 seconds and approximately equal to the cycle time (Table 4.2). To extract volatile gases every 20 seconds, the gas removal system must operate with 100% of the core throughout flow rate (in-line gas removal system). In this chapter, the efficiency of noble gas migration to helium bubbles and the efficiency of bubble removal from the salt by the entrainment separator ($\epsilon_m, \epsilon_{es}$ on Figure 4.10, respectively) are selected separately for each demonstration case.

The nickel filter in the TAP concept is designed to extract noble/semi-noble metals and volatile fluorides (Table 4.2). Similar to volatile gases, noble metals must be removed every 20 seconds and, hence, the filter should operate at 100% of the flow rate through the core. The nickel filter removes a wide range of elements with various effective cycle time (Table 4.2).

Lanthanides and other non-noble metals have a lower capture cross section than gases and noble metals. These elements can be removed via a liquid-metal/molten salt extraction process with relatively low removal rates (cycle time > 50 days). This is accomplished by directing a small fraction of the salt mass flow leaving the nickel mesh filter (10% of the flow rate throughout the core) to the liquid-metal/molten salt component of the reprocessing system, in which lanthanides are removed with a specific extraction efficiency to match the required cycle time (Table 4.2). The remaining 90% of the salt mass flow is directed from the nickel filter to the heat exchangers without performing any fuel salt treatment.

The removal rates vary among nuclides in this reactor concept, which dictate the necessary resolution of depletion calculations. To compromise, a 3-day depletion time step was selected for the long-term demonstration case based on a time step refinement study by Betzler *et al.* [17] A complimentary time step refinement study is presented in Section 4.3.1.4 to determine the impact of temporal resolution on the depleted composition calculation.

---

[4] Full loop time is the time taken by a particle of the coolant to make one full circle in the primary loop.

4.3 Long-term depletion demonstration and validation

4.3.1 Constant, ideal extraction efficiency case

To validate SaltProc v1.0, I performed a lifetime-long depletion calculation with ideal extraction efficiency. This case was selected to repeat fuel salt depletion as close as possible to the ChemTriton simulation for the full-core TAP reactor by Betzler *et al.* [17] Betzler *et al.* made the following assumptions and approximations in their work [17]:

(a) Effective cycle times as prescribed by the Transatomic Power Technical White Paper [106] (Table 4.2) with **100% noble gas removal efficiency**; hence, ϵ_{es} and ϵ_m in the reprocessing model (Figure 4.10) are both set to 1.0.

(b) 5% LEU feed rate is equal to the rate of fission product removal.

(c) 3-day depletion step.

(d) Quarter-core, 3-D model with vacuum boundary conditions.

(e) Delayed neutron precursor drift was neglected.

I adopted these assumptions for code-to-code verification of SaltProc v1.0 against ChemTriton. The ENDF/B-VII.1 [27] nuclear data library is used for this case to be consistent with Betzler's work. Unfortunately, some crucial details have not been reported in [17]: (1) exact core geometries for various moderator rod configurations except startup configuration; (2) the excess reactivity at startup; (3) the library from which S(α, β) tables for thermal scattering in zirconium hydride are obtained. This section presented my best effort to repeat Betzler's simulation using the same input data to validate SaltProc for the TAP concept.

4.3.1.1 Effective multiplication factor dynamics

Figures 4.11 and 4.12 demonstrate the effective multiplication factor obtained using SaltProc v1.0 with Serpent. The k_{eff} was obtained after removing fission products and adding feed material at the end of each depletion step (3 days for this case). SaltProc v1.0 updated the moderator rod configuration to the next configuration (e.g., from 1388 rods per core to 1624 rods per core) once the predicted value of k_{eff} at the end of the next depletion step dropped below 1. This algorithm mimics regular maintenance shutdown when the TAP core excess reactivity is exhausted, and moderator rod assemblies should be reconfigured to operate the next cycle.

An optimal number of moderator configurations (cycles) is found to be 15 (see Appendix A). Fewer cycles would improve capacity factor but need larger excess reactivity at the Beginning of Cycle (BOC), which is strictly limited by reactivity control system worth. More cycles would require more frequent moderator rod reconfigurations, which worsens the capacity factor. The interval between the first and second moderator configuration was only 12 months, the shortest interval between moderator configuration updates. For the operation interval between 2 and 16 years after startup, the intervals between shutdowns for moderator rod updates were 18-26 months. However, towards the EOL, the intervals between moderator rod reconfigurations dropped to 13 months. Overall, the average interval between regular shutdowns for the core reconfiguration was 18 months, which exactly matches the refueling interval for conventional LWRs and is consistent with Betzler *et al.* (≈16 months) [17].

The k_{eff} fluctuates significantly as a result of the batch-wise nature of the online reprocessing approach used. Loading the initial fuel salt composition with 5% LEU into the TAP core leads to a supercritical configuration with an excess reactivity of about 3200 *pcm* (Figure 4.11). Without performing any fuel salt reprocessing and spectrum shifting, the core became subcritical after 30 days of operation [90]. SaltProc calculates an operational lifetime of 22.5 years, after which the fuel salt reached a total burnup of 81.46 MWd/kgU. The end of an operational lifetime is achieved when the minimum SVF is obtained, as restricted by the moderator geometry parameters (e.g., moderator rod diameter, rod pitch, the internal diameter of the reactor vessel). Table 4.4 compares obtained results with Betzler *et al.* [17].

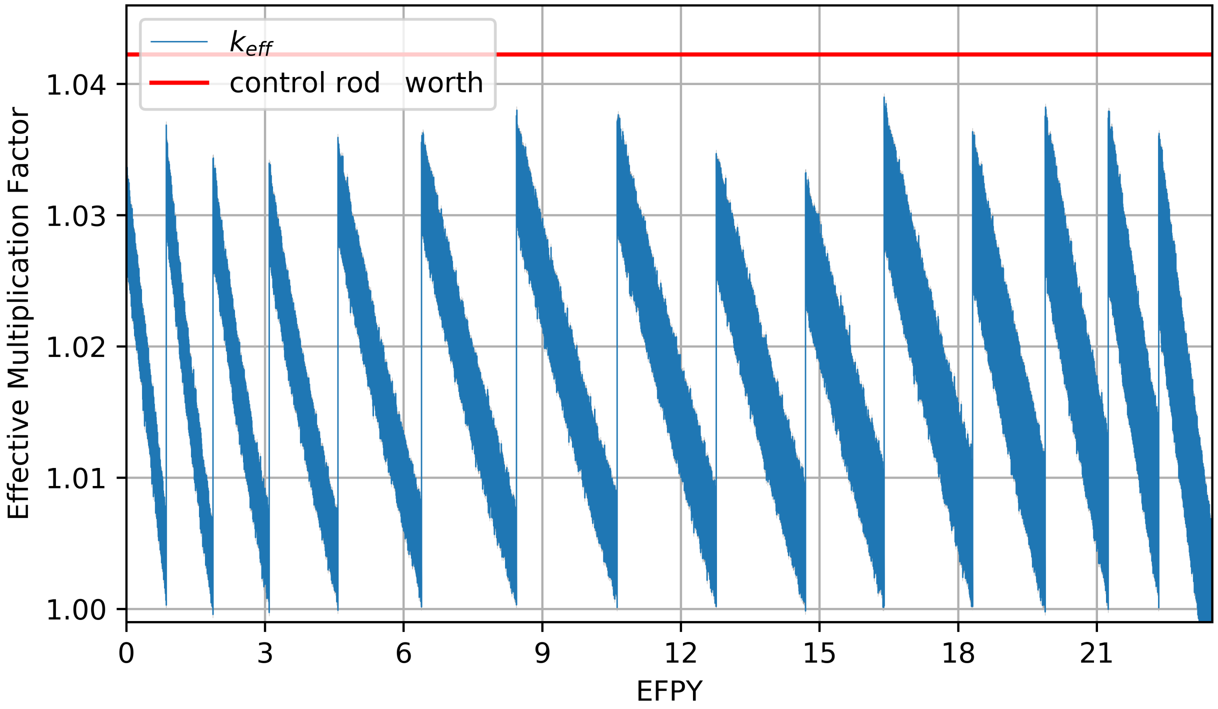

Figure 4.11: Effective multiplication factor dynamics during 23.5 years of operation for the full-core TAP core model for the case with an ideal removal efficiency of fission product. Confidence interval σ = 28 *pcm* is shaded.

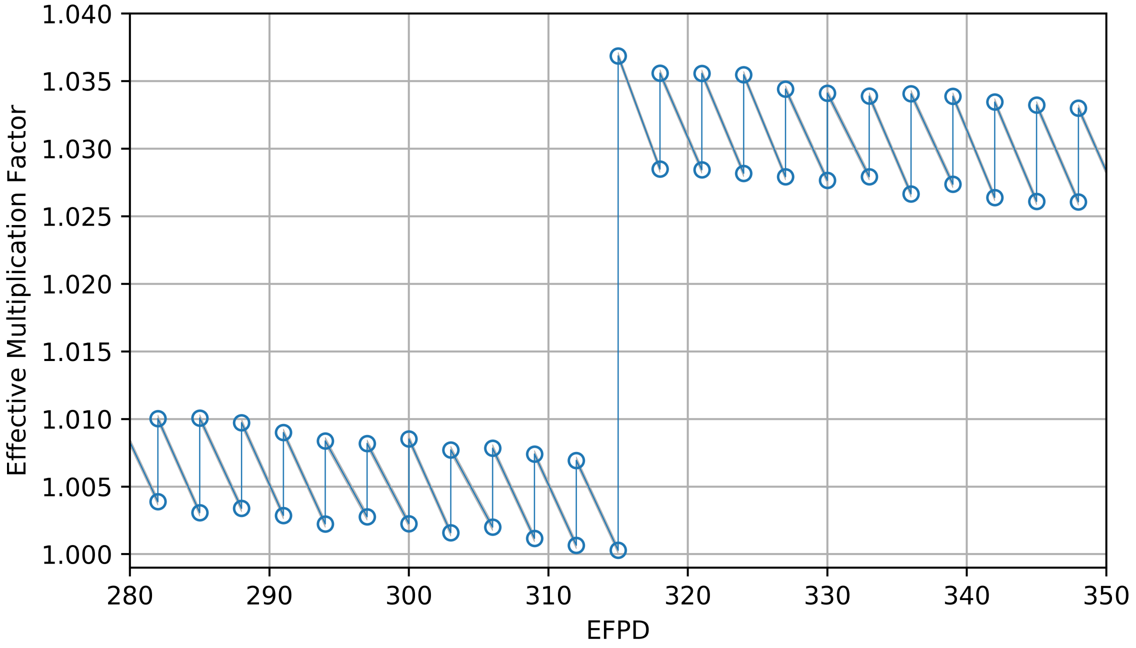

Figure 4.12: Zoomed effective multiplication factor for the interval from 280 to 350 EFPD while transitioning from Cycle #1 (startup geometry configuration, 347 moderator rods, SVF=0.91720353) to Cycle #2 (SVF=0.88694). Confidence interval σ = 28 *pcm* is shaded.

Overall, SaltProc-calculated operational lifetime and burnup are lower than the reference by approximately 22% and 17%, respectively. A better match in the operational lifetime between SaltProc v1.0 and ChemTriton can be obtained if a detailed moderator configuration description of Betzler's model will be available in the future.

Table 4.4: Comparison of main operational parameters in the TAP reactor between the current work and Betzler *et al.* [17].

Parameter	**Current work**	**Betzler, 2017** [17]
Operational lifetime [y]	22.5	29.0
Discharge burnup [MWd/kgU]	76.30	91.9
Average moderator reconfiguration interval [months]	18	16

4.3.1.2 Fuel salt isotopic composition dynamics

Figure 4.13 show that continuous LEU feed into the TAP reactor is not sufficient to maintain the fissile ^{235}U content of the core, as the uranium enrichment steadily decreases from 5% at the BOL to 1% at the EOL. However, during the first 13 years of operation, the TAP MSR breeds fissile ^{239}Pu and ^{241}Pu, reaching a peak of total fissile plutonium inventory of 2.15 t (Figure 4.15). Figure 4.14 shows that a significant amount of non-fissile plutonium (^{238}Pu, ^{240}Pu, and ^{242}Pu) and uranium (^{236}U) builds up in the reactor during operation and negatively impacts criticality of the reactor. ^{239}Pu and ^{241}Pu are major contributors to the fissile material content of the core, keeping it critical during the second half of the operational lifecycle. The total ^{239}Pu inventory in the core rises during the first 11 years of operation due to the harder neutron spectrum. After 11 years, the softer spectrum breeds less ^{239}Pu from ^{238}U, and more of ^{239}Pu is progressively burned. Obtained results are in good agreement with results in ORNL Report by Betzler *et al.* (Table 4.5) [17].

A lifetime-long SaltProc depletion calculation requires a 5% LEU feed rate of 460.8 kg per year to maintain the fuel salt inventory in the primary loop, which is consistent with the reference. Table 4.6 shows the main fuel cycle performance parameters calculated using

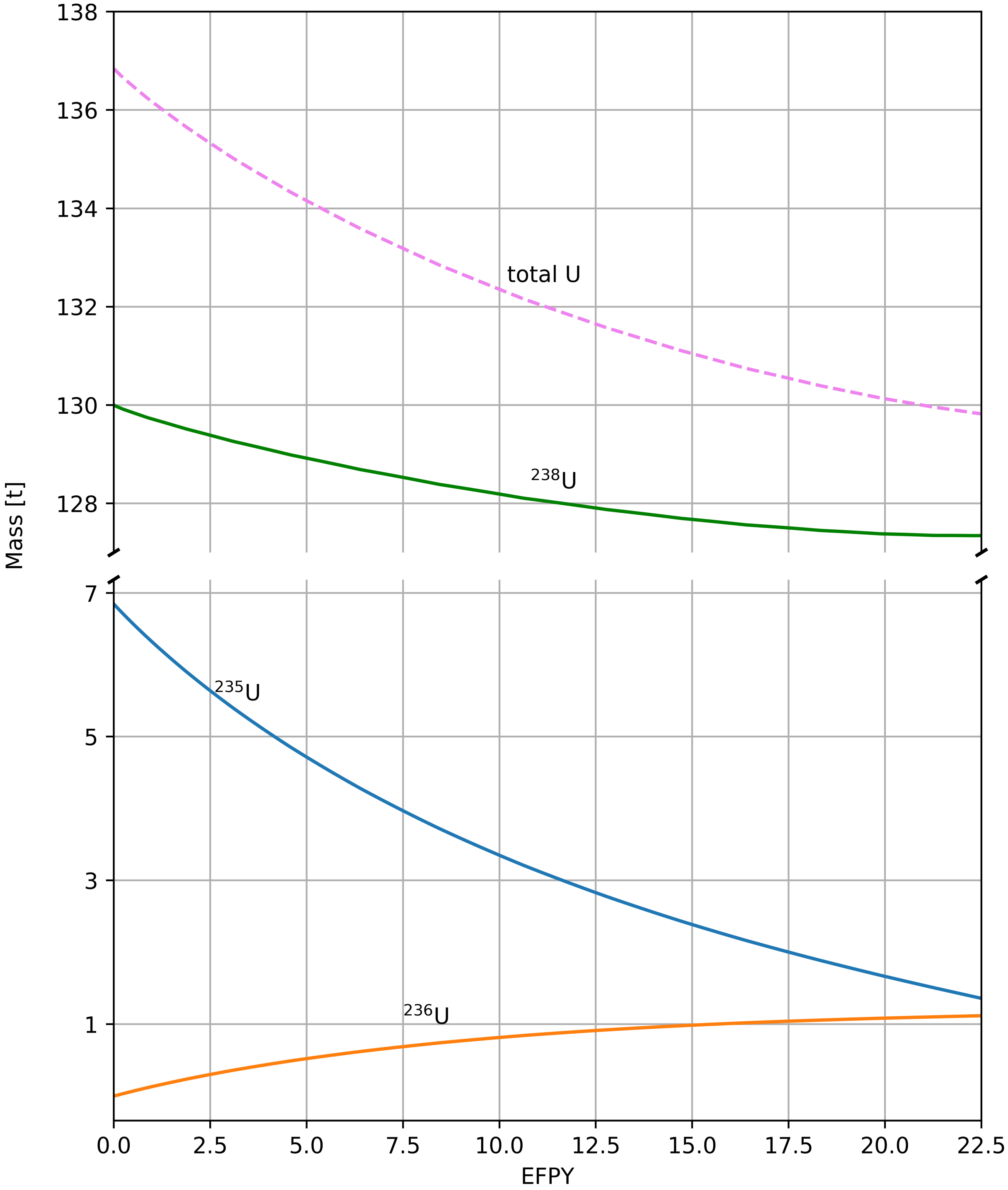

Figure 4.13: SaltProc-calculated uranium isotopic fuel salt content during 22.5 years of operation. Uncertainty of the predicted mass will be estimated and discussed in Chapter 7.

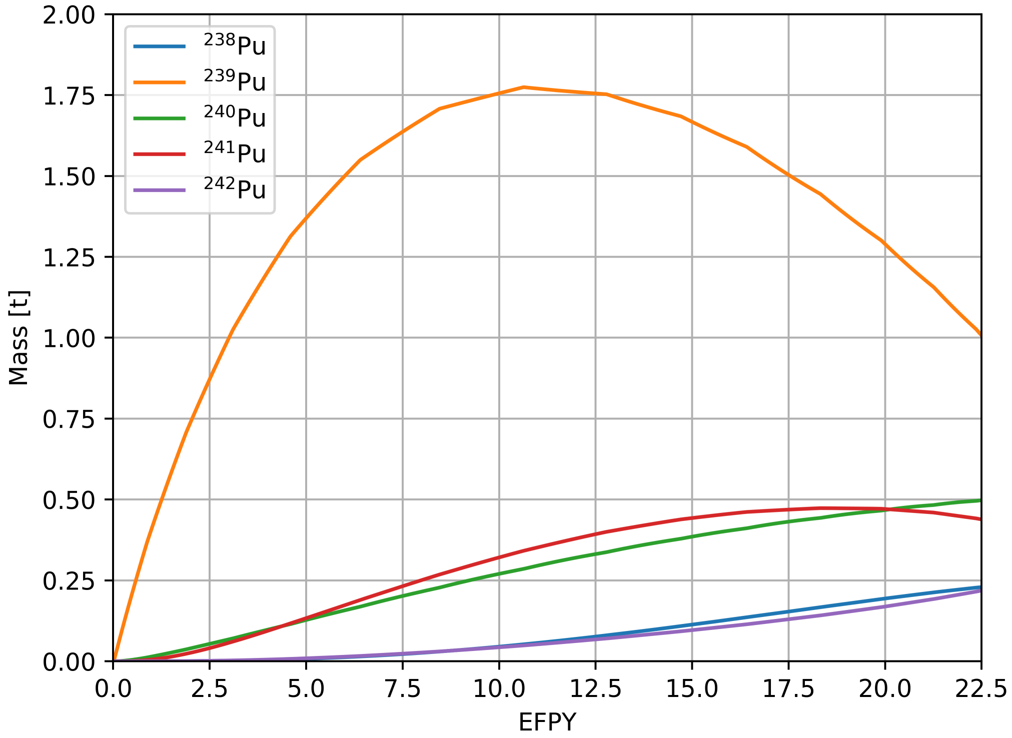

Figure 4.14: SaltProc-calculated plutonium isotopic fuel salt content during 22.5 years of operation.

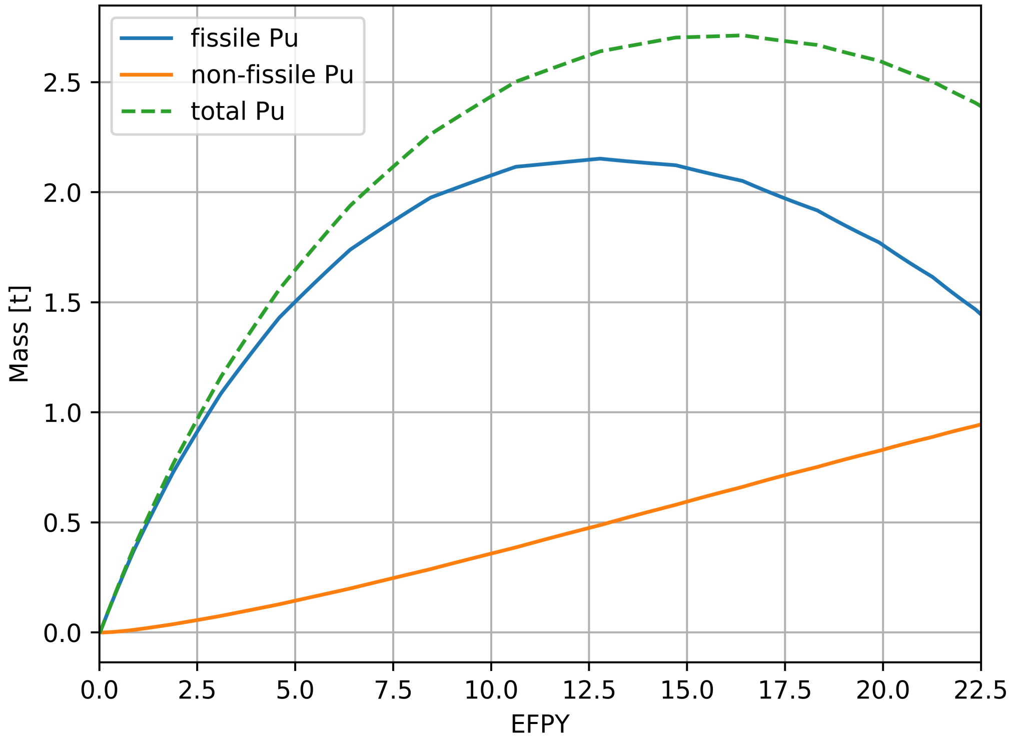

Figure 4.15: SaltProc-calculated fissile and non-fissile plutonium fuel salt content during 22.5 years of operation.

Table 4.5: Comparison of major heavy isotopes inventories at the EOL in the TAP reactor between the current work and Betzler *et al.* [17].

	Isotope	**Current work mass [kg]**	**Betzler, 2017 mass [kg]**	Δm [%]
Fissile	^{235}U	1299	1160	+11%
	^{239}Pu	942	995	−5%
	^{241}Pu	427	435	−2%
	Total	2668	2590	+3%
Non-fissile	^{236}U	1123	1200	−6%
	^{238}U	127,353	132,400	−4%
	^{238}Pu	235	280	−16%
	^{240}Pu	503	1000	−50%
	^{242}Pu	230	310	−26%
	Total	129,444	135,190	+4%

SaltProc and compared with the reference. Normalized per GW$_{th}$-year, the TAP concept requires about 5.23 t of fuel compared with 4.14 t reported by Betzler *et al.* SaltProc-calculated waste production normalized per GW$_{th}$-year is 5% less than reported by ORNL. Potentially, the TAP can operate with LWR SNF as the fissile material feed. The heavy metal component of LWR SNF has a lower fissile material weight fraction than 5% enriched uranium and adds less fertile ^{238}U to the fuel salt, potentially reducing the operational lifetime. Nevertheless, in the case of using waste material (e.g., transuranium elements from LWR SNF) in this fueling scenario, the TAP concept has superior waste reduction metrics.

Table 4.6: Comparison of normalized by GW$_{th}$-year total fuel load and actinide waste from the TAP reactor obtained in the current work and Betzler *et al.* [17].

Parameter	**Current work**	**Betzler, 2017** [17]
5% LEU feed rate [kg/y]	460.8	480.0
Loaded fuel [t per GW$_{th}$-y]	5.23	4.14
Waste [t per GW$_{th}$-y]	3.57	3.74

4.3.1.3 Neutron energy spectrum

Significant thermalization of the neutron spectrum is observed as moderator rods are added into the core configuration (Figure 4.16). At startup, the neutron spectra from the current work and Betzler *et al.* are matched well because the core geometry, its SVF, and initial fuel composition in these two simulations are similar. The Pearson correlation coefficient[5] $r_{BOL} = 0.91115$, which indicates a strong, positive association between the spectra at the BOL (see Figure 4.16, upper plot). At the EOL, SaltProc/Serpent-calculated spectrum is more thermal than reported by Betzler *et al.* [17], but the correlation coefficient $r_{EOL} = 0.90987$ shows that the spectra are still extremely strongly related (see Figure 4.16, lower plot).

The harder spectrum at the BOL tends to significantly increase resonance absorption in ^{238}U and decrease the absorptions in fissile and construction materials. Thus, the softer spectrum in the current work compared with Betzler *et al.* led to fewer resonance captures[6] of neutrons by ^{238}U, hence, less ^{239}Pu bred from ^{238}U. Therefore, the SaltProc/Serpent calculation in the current work underpredicts the destruction (i.e., fission and capture) of ^{235}U and overpredicts the destruction of ^{238}U (see Table 4.5). Finally, the softer neutron spectrum leads to more fissions in fissile plutonium isotopes (^{239}Pu and ^{241}Pu) which also decreases non-fissile plutonium (Table 4.5) and total actinide waste production (Table 4.6).

---

[5] Pearson correlation coefficient is calculated by the following formula:

$$r = \frac{\sum_{i=1}^{N}(\Phi_i^{ref} - \overline{\Phi^{ref}})(\Phi_i - \overline{\Phi})}{\sqrt{\sum_{i=1}^{N}(\Phi_i^{ref} - \overline{\Phi^{ref}})^2 \sum_{i=1}^{N}(\Phi_i - \overline{\Phi})^2}} \tag{4.2}$$

where

Φ_i^{ref}, Φ_i = neutron flux for ith energy bin reported in the reference and the current work $[n/cm^2 \cdot s]$

$\overline{\Phi^{ref}}, \overline{\Phi}$ = neutron flux averaged over N energy bins reported in the reference and current work $[n/cm^2 \cdot s]$

N = number of neutron energy bins [-].

[6] The energy range for ^{238}U resonance neutron capture is between 10^{-5} and 10^{-2} MeV.

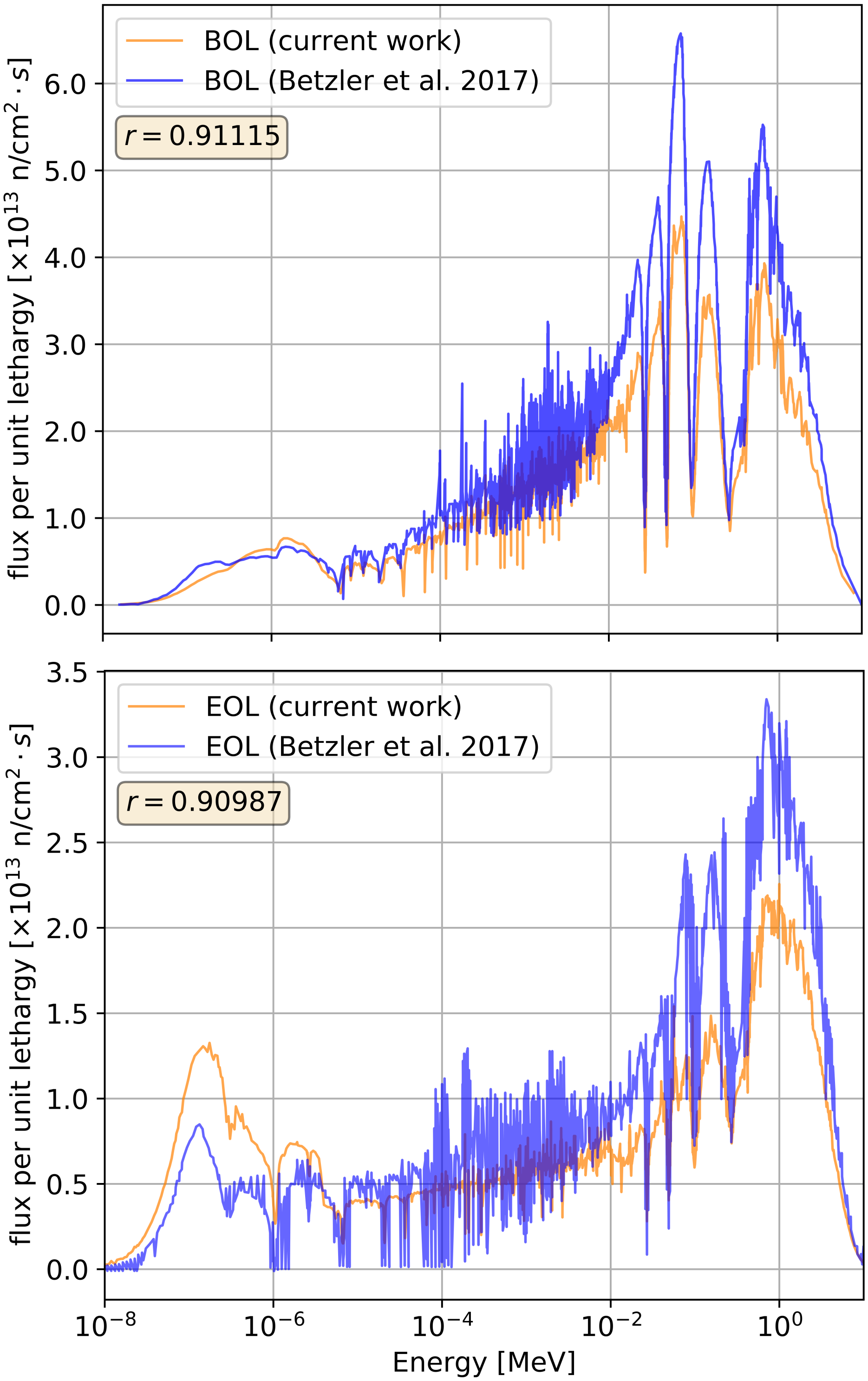

Figure 4.16: Neutron flux energy spectrum at the BOL (upper) and the EOL (lower) obtained using SaltProc/Serpent (orange) compared with ChemTriton/Shift (blue) [17].

4.3.1.4 Time step refinement

The results shown in this chapter are obtained from SaltProc calculations with a uniform depletion time step of 3 days. The duration of the time step was chosen after performing a parametric sweep to determine the longest depletion time step that provides suitable calculation accuracy. A longer time step potentially reduces the SaltProc calculation costs, providing results faster for lifetime-long (25-year) simulations.

Figure 4.17 shows k_{eff} evolution obtained with 3-, 6-, 12-, and 24-day depletion time intervals for a 25-year simulation. The interval between moderator configuration updates was assumed similar for all four cases for consistency. The multiplication factor at the BOC for each moderator configuration reduced with increasing time step duration. At the End of Cycle (EOC) for each geometry, k_{eff} = 1.0 for a 3-day time step but drops below 1.0 to 0.9980, 0.9972, and 0.9948 for 6-, 12-, and 24-day step, respectively. The decrease is because more poisonous FPs (e.g., ^{135}Xe) are produced in the core during longer depletion intervals. With longer time steps, a large concentration of poisons is obtained at the end of the depletion step when those poisons are being removed, resulting in substantial criticality growth.

Figures 4.18 and 4.19 show that the longer time steps appropriately capture uranium depletion (< 1% difference even for a 24-day time step), but the observed difference in fissile ^{239}Pu mass is significant when the depletion interval is 6 days or longer (> 0.5% difference for 6-day step). Using a 6-day depletion interval leads to overprediction of ^{239}Pu production by 5 kg at the EOL (Figure 4.19). The use of a 6-day time step caused an overprediction of total plutonium production by 9.6 kg. Notably, significant quantity for plutonium currently in use by the IAEA is 8 kg (< 80% ^{238}Pu) [30]. Thus, a 6-day depletion interval or longer leads to significant error in the predicted plutonium inventory at the EOL (larger than 1 significant quantity).

Increasing the depletion time interval significantly reduces computational cost but also

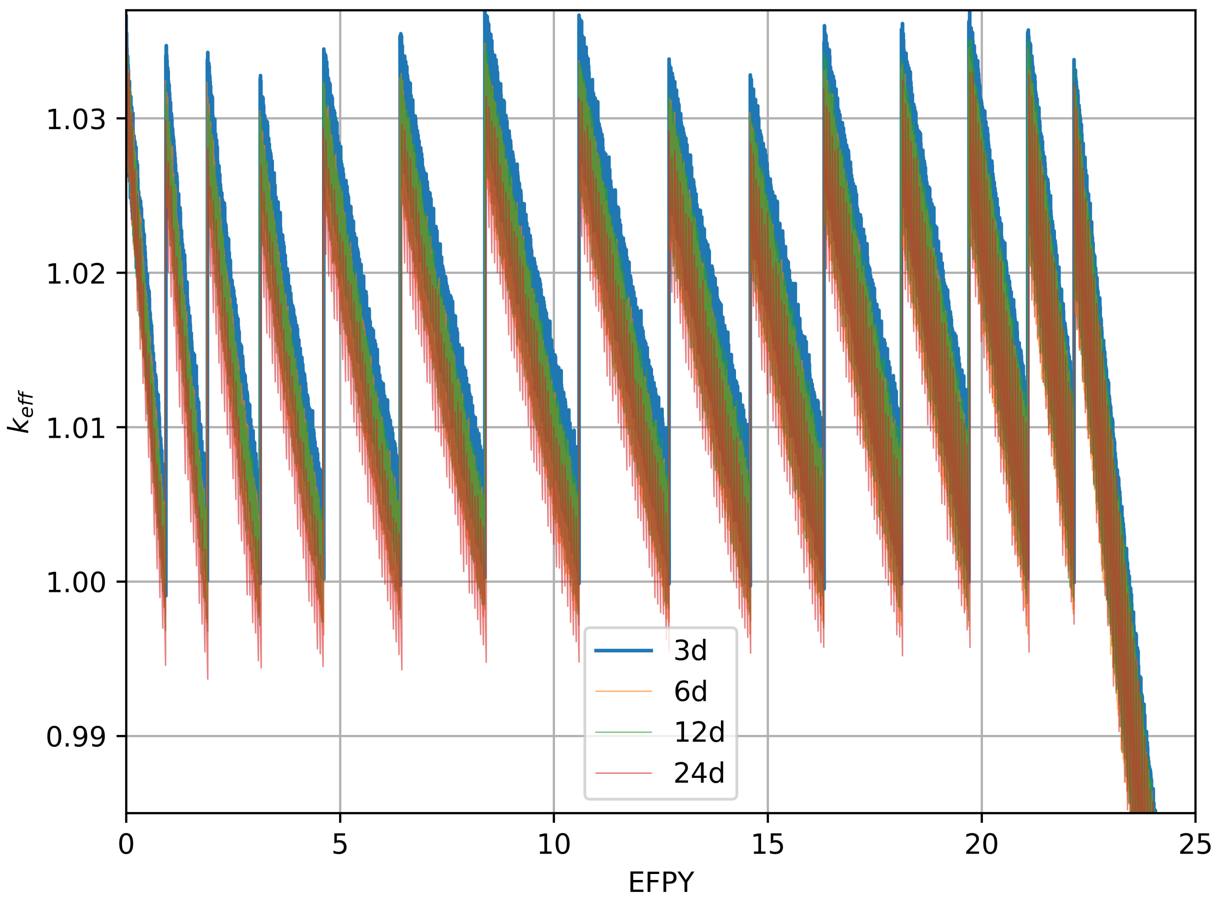

Figure 4.17: SaltProc-calculated effective multiplication factor (k_{eff}) during operation for different depletion time step sizes.

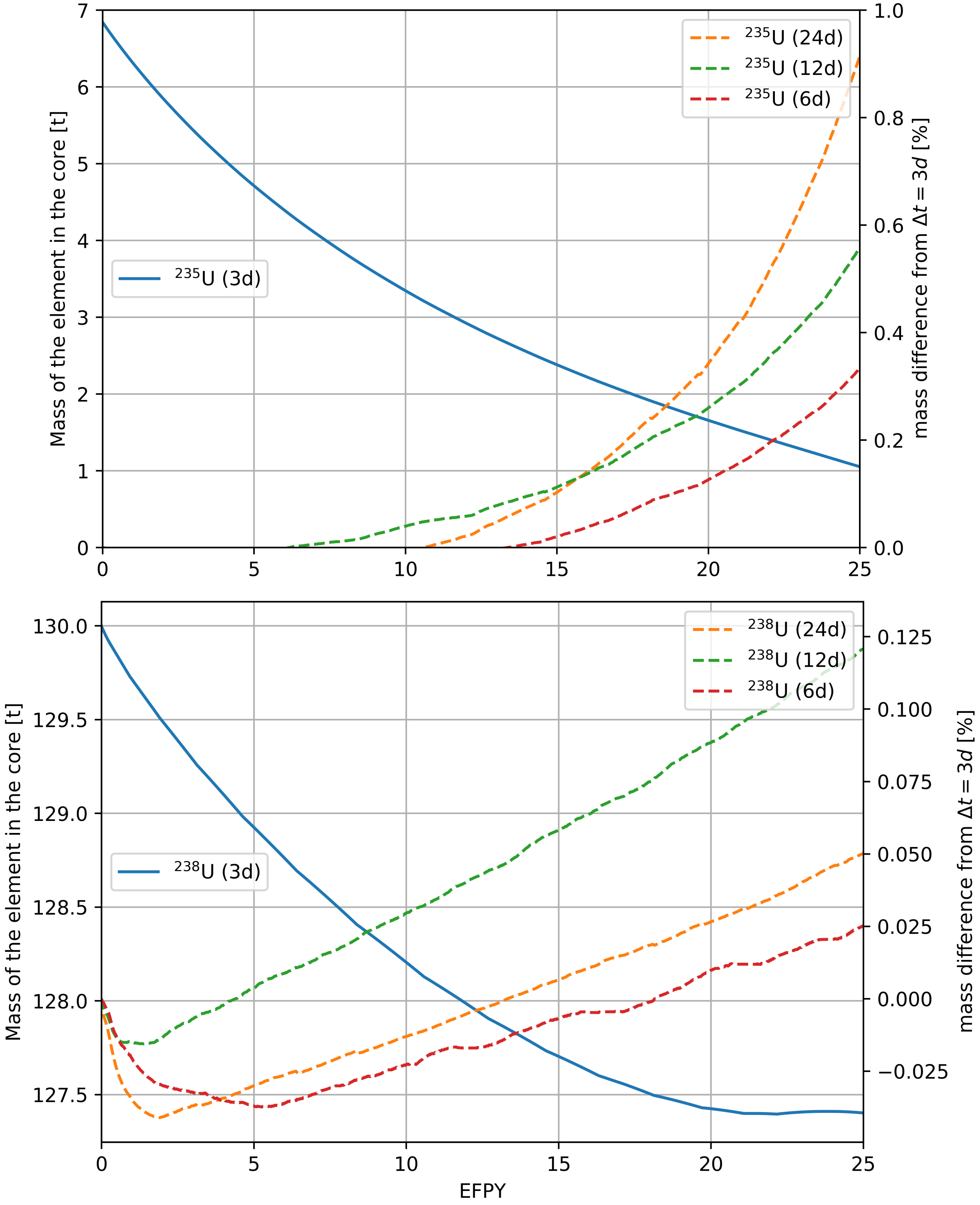

Figure 4.18: SaltProc-calculated ^{235}U (upper) and ^{238}U (lower) content during operation for different depletion time step sizes.

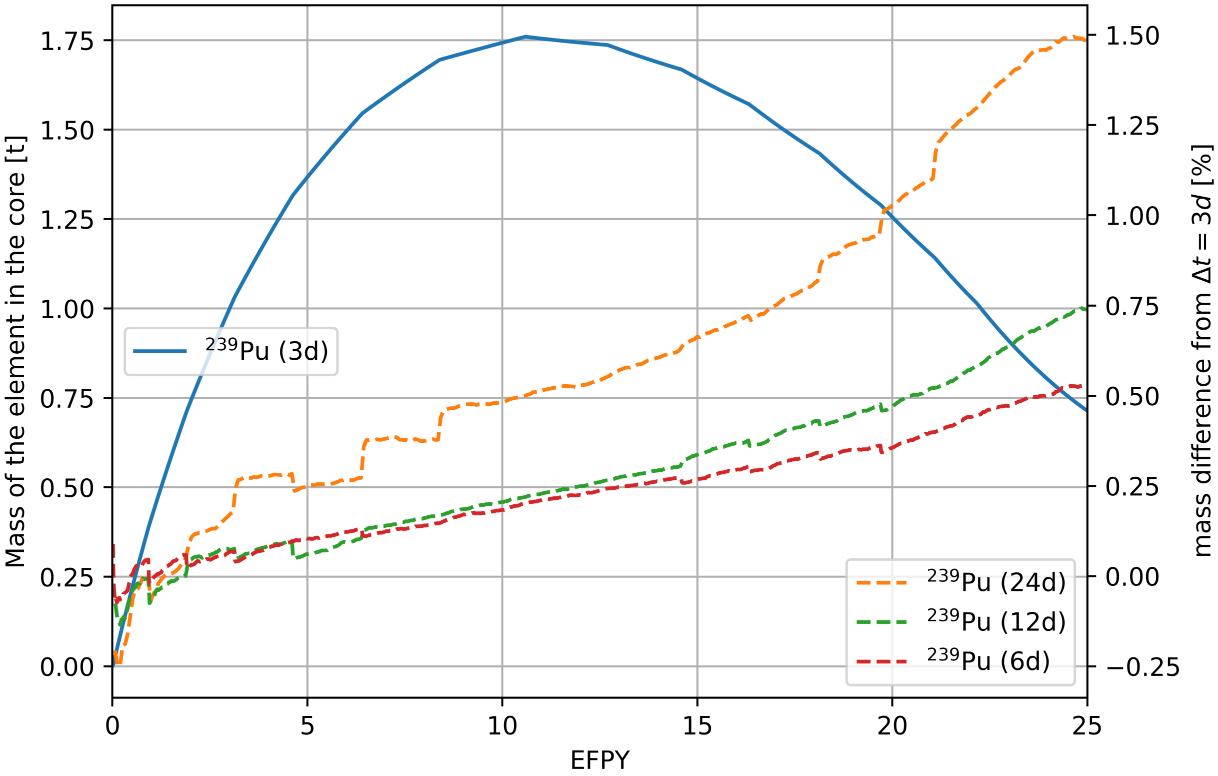

Figure 4.19: SaltProc-calculated ^{239}Pu content during operation for different depletion time step sizes.

deteriorates the accuracy of depletion calculations (i.e., 24-day step gave ×4 speedup but causes about 1.5% error in ^{239}Pu mass prediction). Calculations using a depletion time step of 6 days or more demonstrated a significant difference in calculated k_{eff} (i.e., ≈ 300 *pcm* for 6-day) and depleted mass (e.g., ≈ 0.34% error in ^{235}U predicted mass for 6-day) from those using a 3-day depletion step. *In the current work, a 3-day depletion step was selected to adequately predict the mass of major heavy isotopes in the fuel salt during 25 years of the TAP reactor operation.*

4.3.2 Realistic extraction efficiency case

This section demonstrates SaltProc v1.0 for lifetime-long depletion simulation similar to Section 4.3.1, but with realistic, physics-based correlations for noble gas removal efficiency. For the demonstration case herein, efficiency of xenon, krypton, and hydrogen extraction are determined using the model by Peebles *et al.* (Equation 2.1) discussed earlier in Section 2.1.1. The gas-liquid interfacial area per unit volume (a) to inform Equation 2.1 is a function of salt/gas flow rates and gas bubble diameter [95]:

$$a = \frac{6}{d_b} \frac{Q_{He}}{Q_{He} + Q_{salt}} \tag{4.3}$$

where

Q_{salt} = volumetric salt flow rate $[m^3/s]$

Q_{He} = volumetric helium flow rate $[m^3/s]$

d_b = helium bubble diameter $[m]$.

Additionally, the following parameters inform Equation 2.1 for the prototypic sparger: (1) salt volumetric flow rate throughout the sparger $Q_{salt} = 2\ m^3/s$; (2) sparging gas (helium) volumetric flow rate $Q_{He} = 0.1\ m^3/s$; (3) helium bubble diameter $d_b = 0.508\ mm$ as advised by ORNL [83]; (4) sparger length $L = 11\ m$; (5) sparger diameter $D = 0.4\ m$ (sparger cross section $A_C = 0.126\ m^2$).

The liquid phase mass transfer coefficient (K_L) selection presents a challenge since published information to inform Equation 2.1 is applicable for only laboratory-scale conditions [29]. Peebles *et al.* stated that Equation 2.1 is valid for K_L in a range from 1 to 100 ft/hr (from $0.084\bar{7}$ to $8.47\bar{7}$ mm/s) [74]. For the demonstration case herein, I performed 25-year depletion calculations for K_L of $0.084\bar{7}$, 2.1167, and $8.466\bar{7}$ mm/s to investigate the effect of noble gas removal efficiency on lifetime-long fuel depletion calculations.

The extraction efficiency is gas specific because solubility in the salt (Henry's law constant) is different for various gases. Table 4.7 reports the dimensionless Henry's law constant and corresponding calculated efficiency of noble gas (Xe, Kr, H) migration to the helium bubbles (ϵ_m) in the prototypic sparger for various mass transfer coefficients. Total separation efficiency (Table 4.7, last three columns) refers to the efficiency of extraction target gaseous elements after performing helium sparging in the sparger followed by separation of noble-gas-reach bubbles from the salt in the axial-flow centrifugal bubble separator [42].

Table 4.7: The noble gas extraction efficiency at working temperature T=627°C calculated using Equation 2.1 [74] assuming salt volumetric flow rate $Q_{salt} = 2\ m^3/s$, helium volumetric flow rate $Q_{He} = 0.1\ m^3/s$, helium bubbles diameter $d_b = 0.508\ mm$, and sparger volume $V = 1.4\ m^3$. The liquid phase mass transfer coefficient is varied in validity range $[0.0847, 8.4667]$ mm/s.

Element	**Henry's law constant**	**Efficiency of migration to He bubbles (ϵ_m) for K_L [mm/s]**			**Efficiency of total separation (ϵ)* for K_L [mm/s]**		
	(K_H)[−]	8.4667	2.1167	0.0847	8.4667	2.1167	0.0847
Xe	5.7E-5 [20]	0.9630	0.5639	0.0327	0.9149	0.5357	0.0310
Kr	2.8E-4 [20]	0.9595	0.5630	0.0327	0.9115	0.5349	0.0310
H	3.9E-3[104]	0.9066	0.5499	0.0326	0.8613	0.5224	0.0309

*With axial-flow centrifugal bubble separator by Gabbard *et al.*, which allows the bubble separation efficiency ϵ_{es}=0.95 [42]. Thus, total gas removal efficiency (ϵ) can be calculated as follows: $\epsilon = \epsilon_m \times \epsilon_{es}$.

4.3.2.1 Effective multiplication factor dynamics

Figures 4.20 and 4.21 demonstrate the effective multiplication factor dynamics (k_{eff}) during 25 years of operation with 15 various moderator rod configurations (cycles) described in

Appendix A. SaltProc v1.0 coupled to Serpent calculated k_{eff} after removing fission products and feeding 5% LEU at the end of each depletion step (3 days as was determined in Section 4.3.1.4). Notably, the core went subcritical during the first cycle (startup moderator rod configuration) after 330 and 318 days for K_L = 8.4667 and 0.0847 mm/s, respectively.

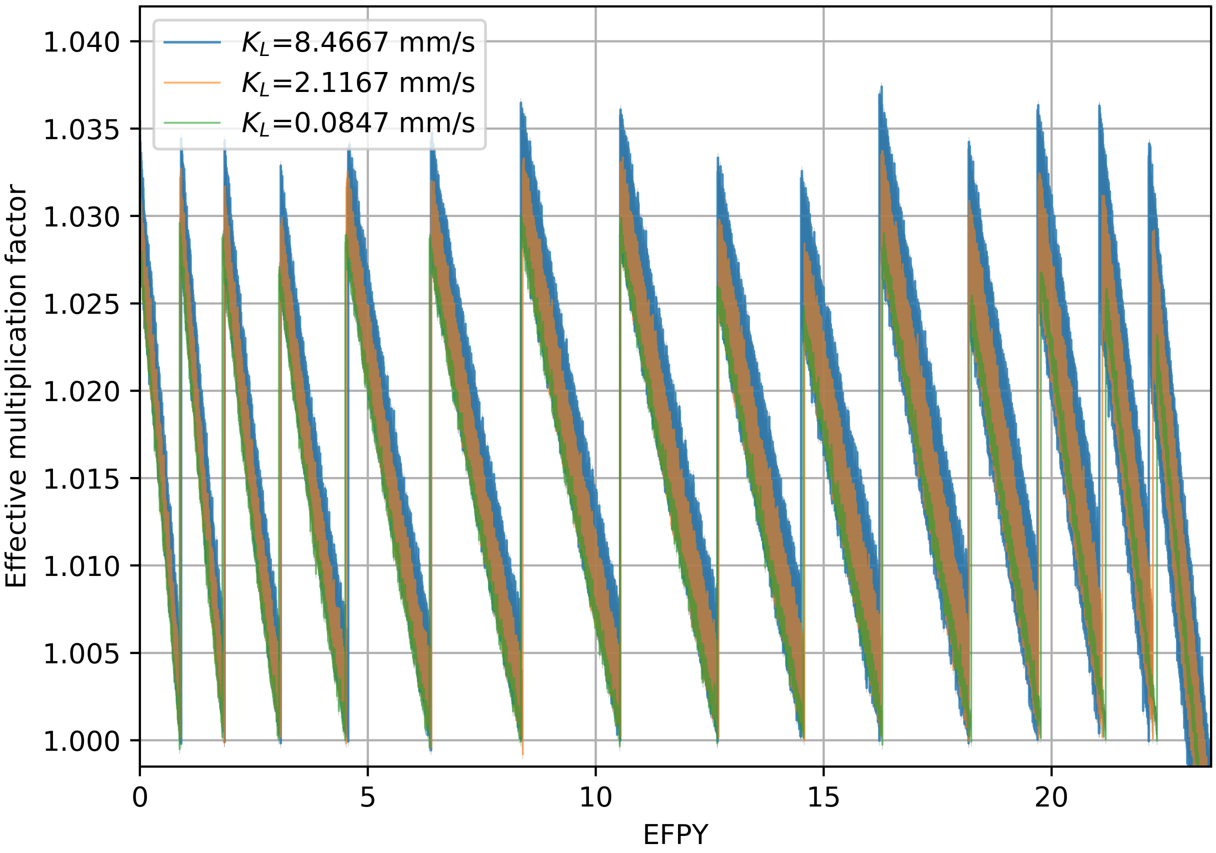

Figure 4.20: Effective multiplication factor dynamics for the full-core TAP core model during 25 years of operation for the case with a realistic removal efficiency of fission product and various mass transfer coefficients. Confidence interval σ = 28 pcm is shaded.

A reduced mass transfer coefficient worsens the neutron poison efficiency, which shortens the interval between shutdowns for moderator rod updates. Additionally, the presence of unremoved poisons in the core suppresses the effective multiplication factor after moderator reconfiguration (≈ 500 pcm lower for K_L = 0.0847 mm/s than for K_L = 8.4667 mm/s at the BOL and ≈ 1100 pcm at the EOL). Overall, noble gas removal provides significant neutronics benefits (fewer neutrons are lost in strong absorbers such as ^{135}Xe), better fuel utilization,

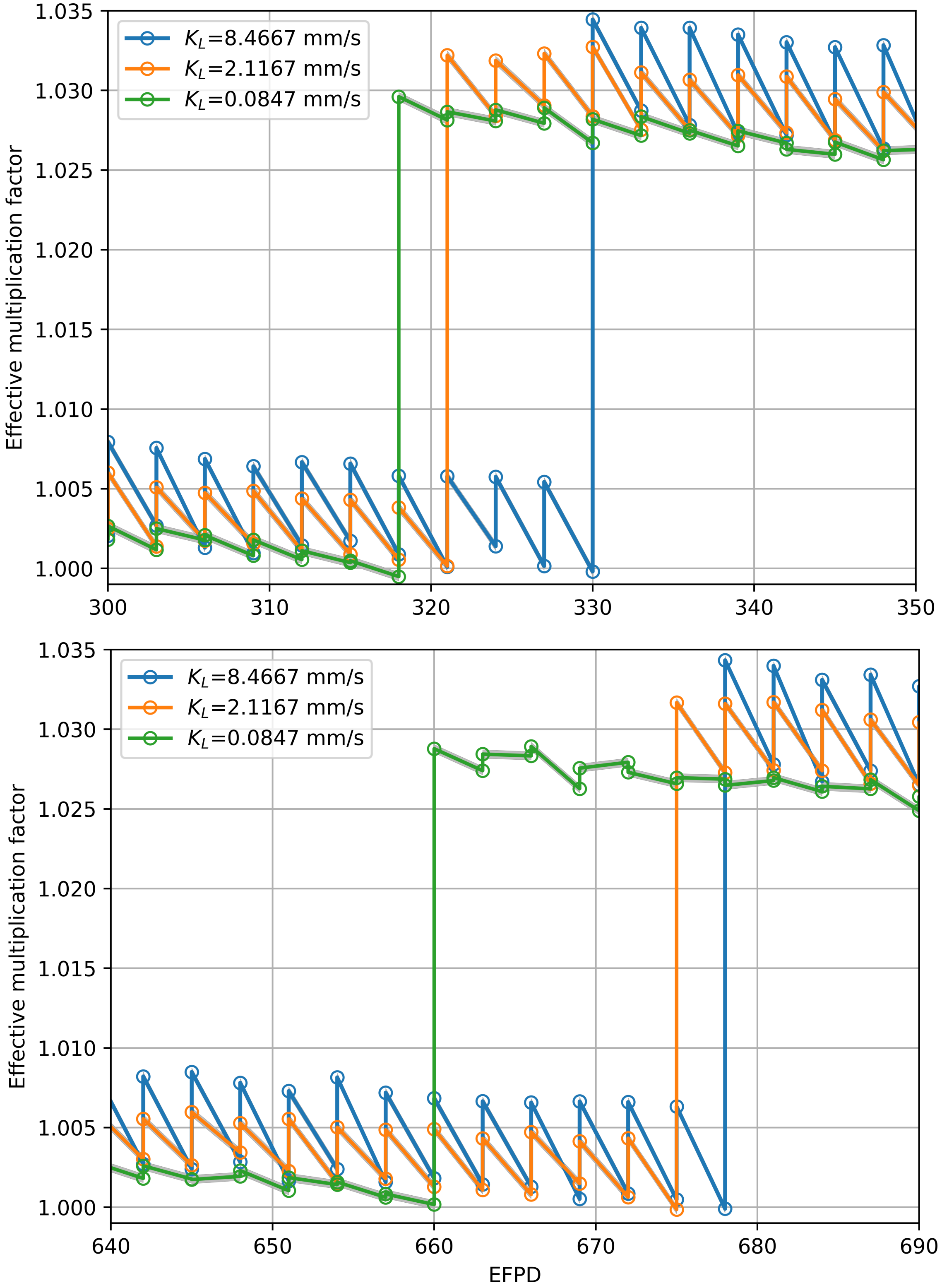

Figure 4.21: Zoomed effective multiplication factor dynamics while switching from Cycle #1 (startup geometry configuration, 347 moderator rods, SVF=0.917) to Cycle #2 (SVF=0.887) (upper panel) and from Cycle #2 to Cycle #3 (SVF=0.881) (lower panel) for various mass transfer coefficients (K_L). Confidence interval $\sigma = 28$ pcm is shaded.

and enables longer moderator rod reconfiguration intervals.

4.3.2.2 Neutron spectrum

Figure 4.22 shows the normalized neutron flux spectrum for the full-core TAP core model in the energy range from 10^{-9} to 15 MeV. The neutron energy spectrum at the EOL is harder than at the BOL due to moderator-to-fuel ratio growth during reactor operation caused by periodic moderator rod reconfigurations. The TAP reactor spectrum is harder than in a typical LWR and correlates well (Pearson correlation coefficient > 0.8) with the TAP neutronics white paper [105] and ORNL reports [17, 16]. The liquid phase mass transfer coefficient (K_L) and, consequently, noble gas removal efficiency (ϵ), has a negligible effect on the spectrum in the fast range (between 10^{-2} and 10 MeV) at the EOL.

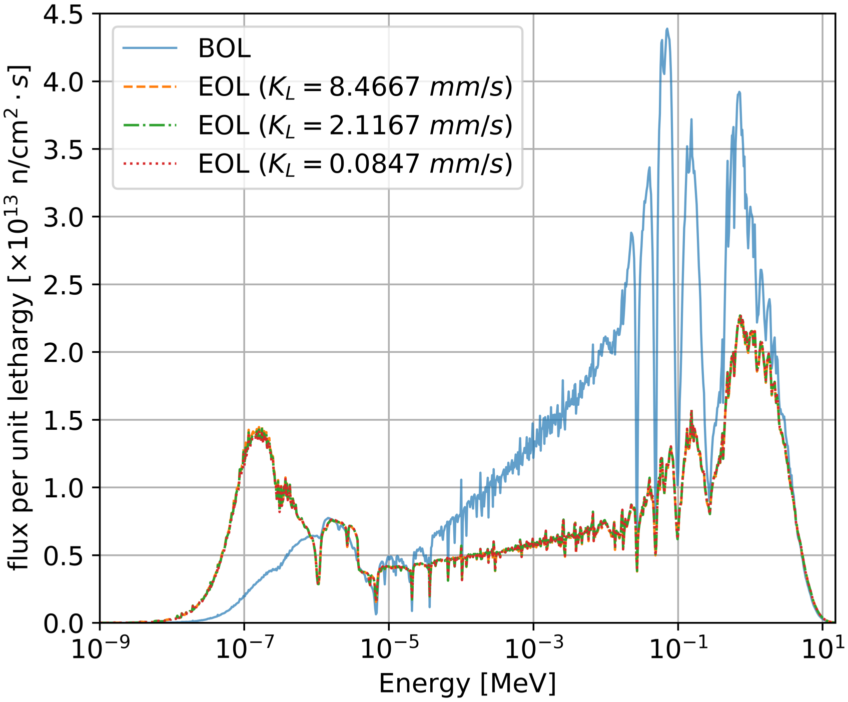

Figure 4.22: The neutron flux energy spectrum normalized by unit lethargy at the BOL and EOL for the case with a realistic removal efficiency of fission product and various mass transfer coefficients.

However, Figure 4.23 demonstrates a notable difference in the thermal range of the spectrum due to the enormous ^{135}Xe absorption cross section ($\sigma_{a,^{135}Xe} = 2.6 \times 10^6$ b). Figure 4.28

shows that ^{135}Xe mass in the core at the EOL for the case with low noble gas removal efficiency ($K_L = 0.0847\ mm/s$) is significantly larger than for the case with high removal efficiency ($K_L = 8.4667\ mm/s$) which leads to higher neutron loss due to absorption in xenon. Overall, noble gas removal from the fuel salt alters the neutron spectrum.

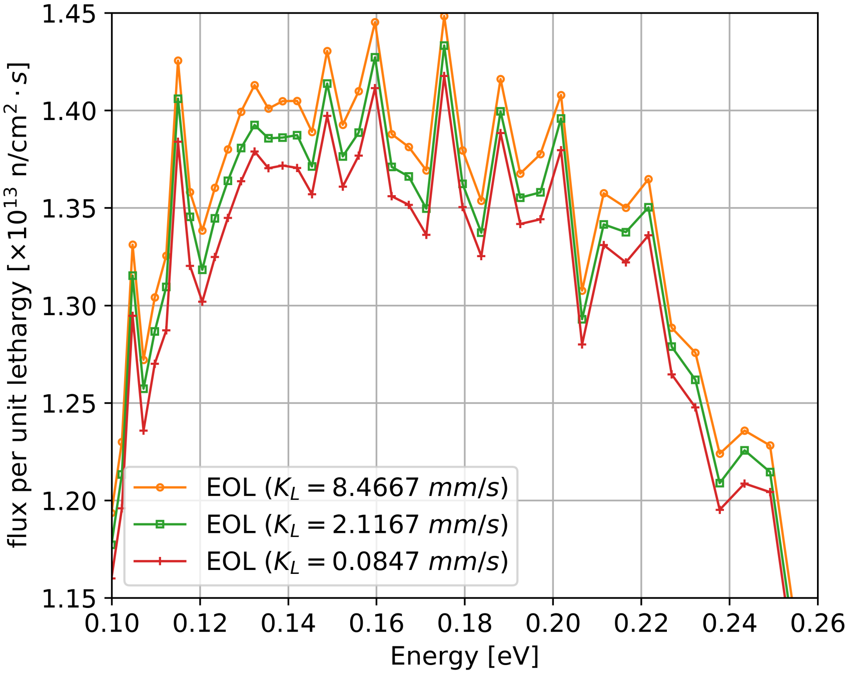

Figure 4.23: The neutron flux energy spectrum normalized by unit lethargy EOL zoomed in the thermal energy range.

4.3.2.3 Fuel salt isotopic composition evolution

The time-dependent isotopic compositions obtained with different noble gas extraction efficiencies behave very similarly. For ^{235}U predicted mass, the difference between $K_L = 8.4667\ mm/s$ (e.g., 91.5% of ^{135}Xe is removed) and $K_L = 0.0847\ mm/s$ (e.g., 3.1% of ^{135}Xe is removed) is within 0.2% for the first 14 years and rises rapidly to 1.15% over the remaining 10 years (Figure 4.24). The simulations with a mass transfer coefficient smaller than 8.4467 mm/s retain more ^{235}U during operation because more neutrons are parasitically absorbed by the noble gas, which leads to a lower fission rate. The relative mass difference in ^{238}U is small (Figure 4.25), but the absolute difference is approximately 50 kg at the EOL, with low removal efficiency corresponding to a reduced EOL inventory of ^{235}U.

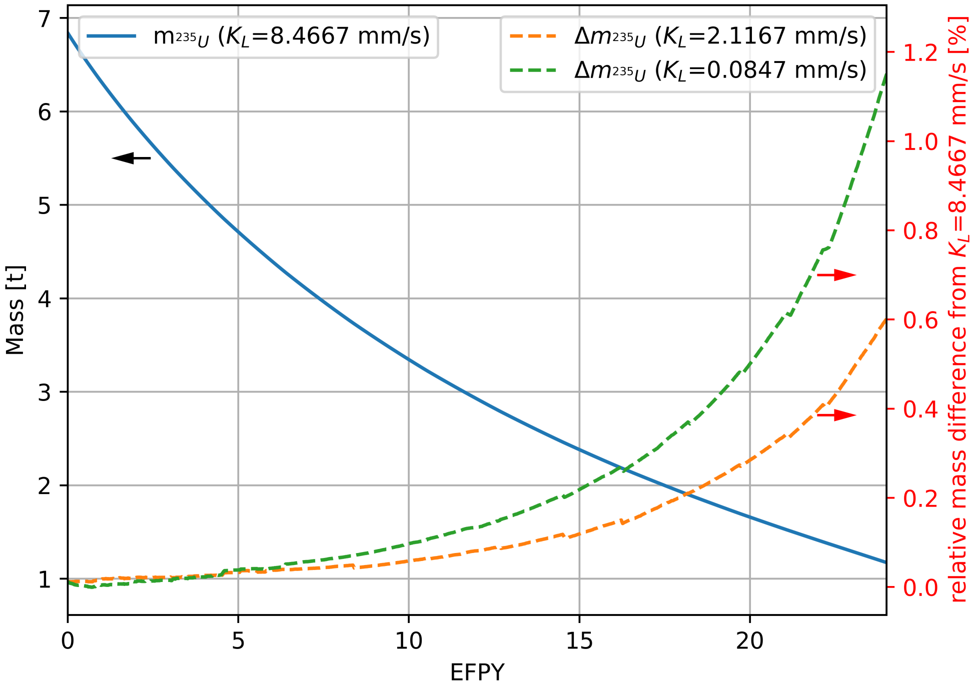

Figure 4.24: SaltProc-calculated mass of ^{235}U in the fuel salt during 25 years of operation for K_L = 8.4667 mm/s compared with less effective noble gas removal.

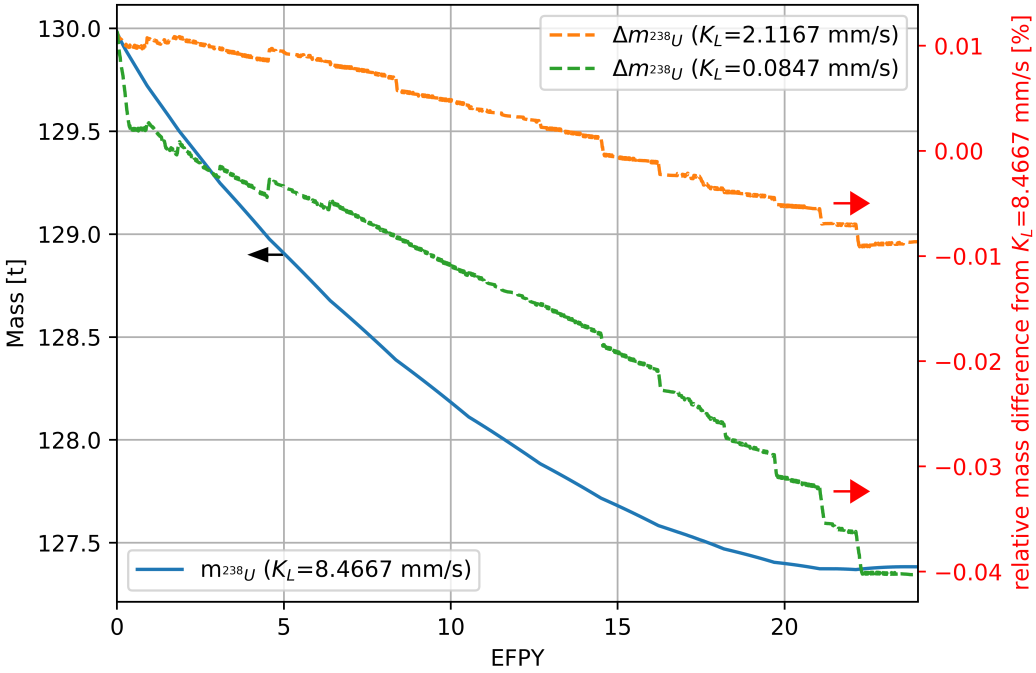

Figure 4.25: SaltProc-calculated mass of ^{238}U in the fuel salt during 25 years of operation for K_L = 8.4667 mm/s compared with less effective noble gas removal.

Differences in the plutonium production between cases with different gas removal efficiencies are much greater. Over 3% more ^{239}Pu mass is generated in the case with K_L = 0.0847 mm/s than with K_L = 8.4667 mm/s (Figure 4.26). The greater mass of neutron poison (^{135}Xe) in the core leads to a harder spectrum (Figure 4.23), which results in a faster rate of destruction of ^{238}U and increased breeding of fissile ^{239}Pu.

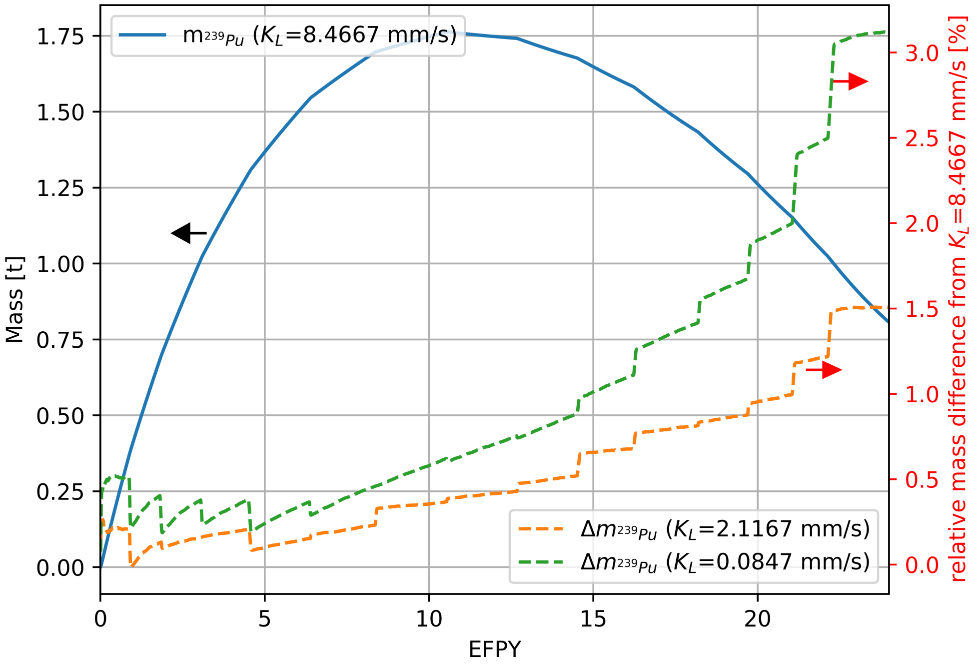

Figure 4.26: SaltProc-calculated mass of ^{239}Pu in the fuel salt during 25 years of operation for K_L = 8.4667 mm/s (91.5% of ^{135}Xe is removed) compared with less effective noble gas removal.

Figure 4.27 demonstrates ^{135}Xe mass dynamics in the TAP core during 25 years of operation for various mass transfer coefficients. Jumps in ^{135}Xe mass every few years reflect the spectral shifts due to moderator rod reconfiguration. In contrast, the mass of ^{135}I, which is the primary direct precursor of ^{135}Xe, is approximately 18 g and stays almost constant over 25 years.

Figure 4.28 shows ^{135}Xe mass at the end of each depletion time step before and after performing the fuel salt reprocessing procedure in SaltProc v1.0. ^{135}Xe concentration in the core after performing FP removals behaves as expected and is consistent with calculated extraction efficiencies in Table 4.7. Notably, the ^{135}Xe production rate increases during the first seven years of operation and then decreases rapidly to 17 g during the remaining 17 years as the spectrum thermalizes during operation.

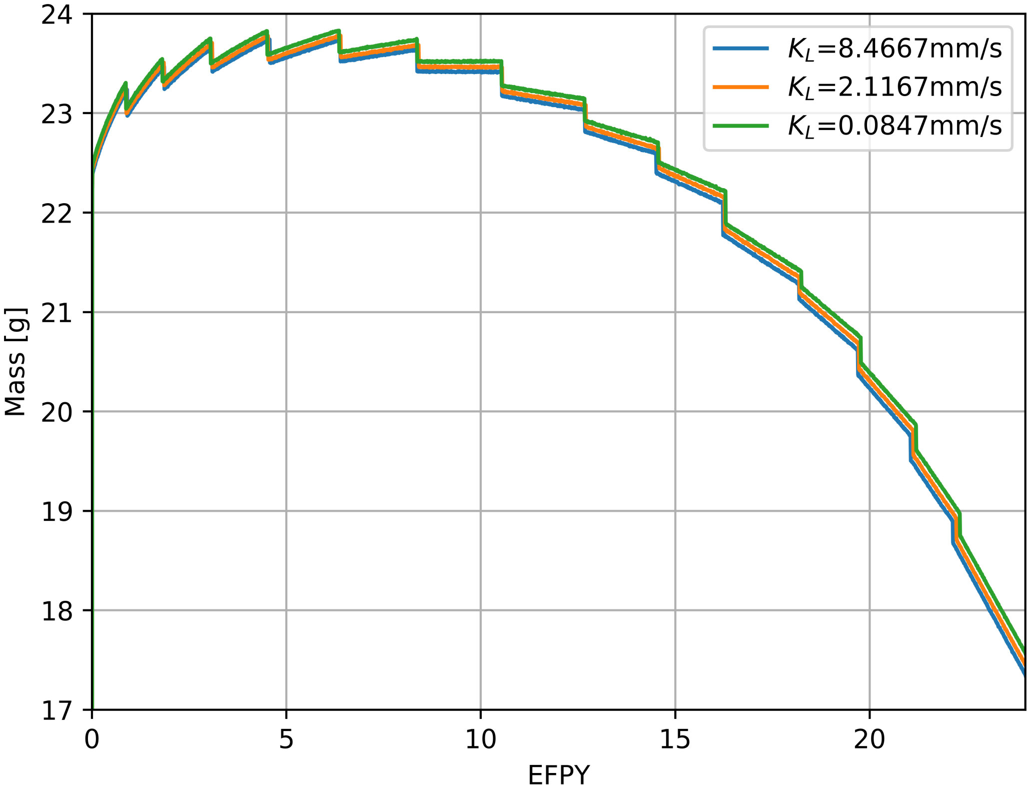

Figure 4.27: SaltProc-calculated mass of ^{135}Xe in the fuel salt during 25 years of operation for the case with a realistic removal efficiency of fission product and various mass transfer coefficients (K_L).

I also performed an analytic verification to confirm SaltProc v1.0 correctness by comparing the mass of ^{135}Xe to the expected mass after performing removals after each depletion step with realistic efficiency (Table 4.7). The expected mass of a reprocessed isotope is calculated as follows:

$$m_a = m_b \times (1 - \epsilon_m) \times (1 - \epsilon_{es}) \tag{4.4}$$

where

m_a = mass of the isotope after applying removals and feeds $[g]$

m_b = mass of the isotope right before reprocessing $[g]$

ϵ_m = efficiency of the isotope migration to helium bubbles $[-]$

ϵ_{es} = entrainment separator extraction efficiency $[-]$.

This simple check showed that the SaltProc-calculated mass of ^{135}Xe (Figure 4.28) matches the expected mass exactly. Thus, SaltProc v1.0 extraction module correctly removes target isotopes with a specified extraction efficiency. Finally, I added this correctness check as SaltProc v1.0 unit test.

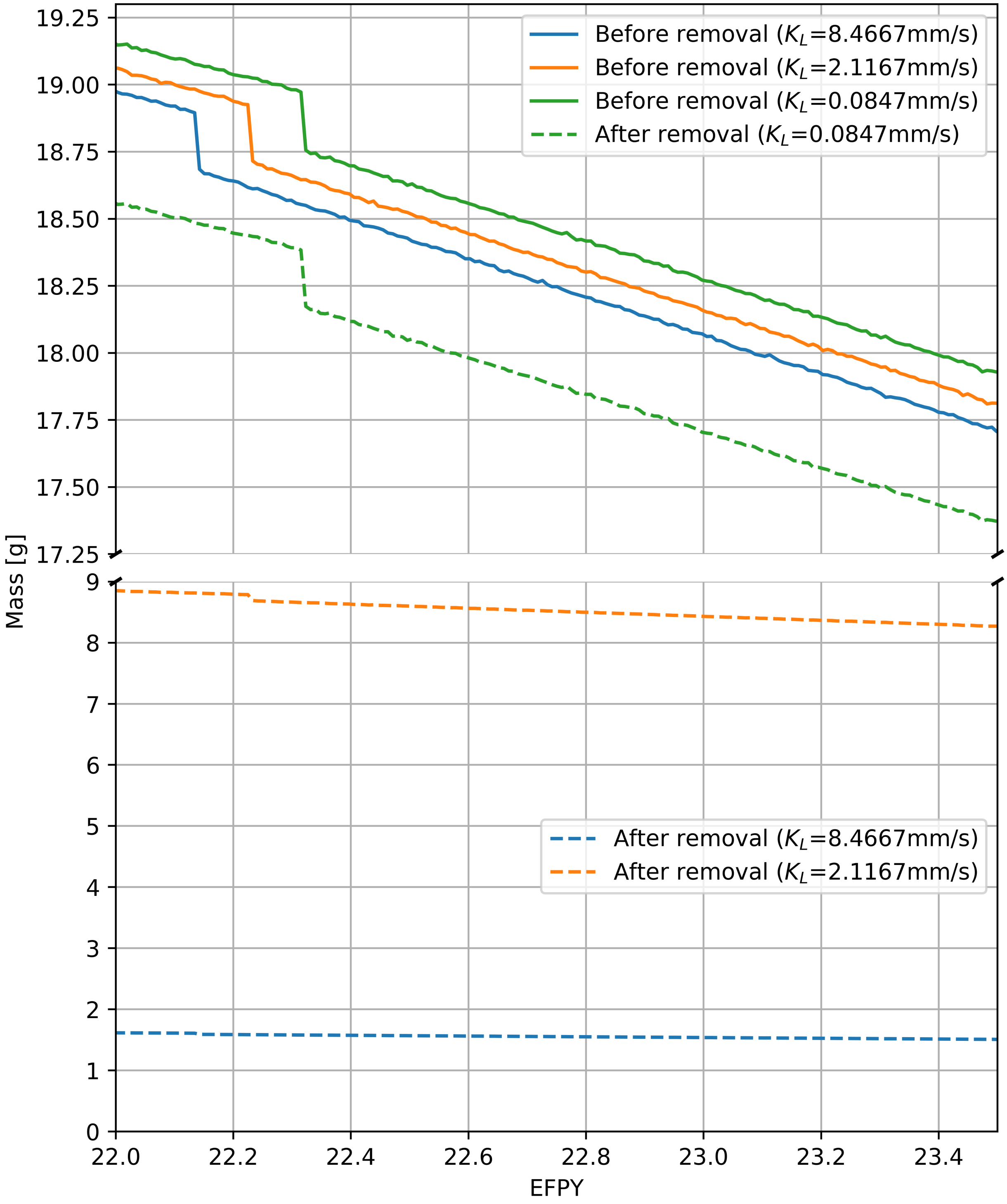

Figure 4.28: SaltProc-calculated mass of ^{135}Xe in the fuel salt during the last 18 months of operation for various mass transfer coefficients (K_L) at the end of each depletion step before and after performing the salt treatment.

4.4 Safety and operational parameters

The previous section (Section 4.3) reported fuel salt composition evolution during 25 years of TAP MSR operation. The inventory of fissile ^{235}U decreased with time, while the inventories of fissile, ^{239}Pu and ^{241}Pu, increased. At the same time, many poisonous actinides (e.g., ^{236}U, ^{240}Pu, ^{242}Pu) built up in the core, shifting the neutron energy spectrum. Moreover, the TAP design assumes an intentional spectrum shift by adding more moderator rods during operation. In this section, I analyze how such neutron spectrum shift affects major safety and operational parameters such as temperature and void coefficients of reactivity, total control rod worth, and other reactor kinetic parameters.

4.4.1 Temperature coefficient of reactivity

The main physical principle underlying reactor temperature feedback is an expansion of heated material. When the fuel salt temperature increases, the density of the salt decreases, but at the same time, the total volume of fuel salt in the core remains constant because it is bounded by the vessel. When the moderator rod temperature increases, the density of zirconium hydride decreases, reducing space between moderator rods and displacing fuel salt from the core. Another physical principle underlying temperature feedback is the Doppler broadening of the resonance capture cross section of the ^{238}U due to thermal motion of target nuclei in the fuel. The Doppler effect arises from the dependence of the capture cross sections on the relative velocity between neutron and nucleus. The Doppler coefficient of reactivity of thermal reactors is always negative and instantaneous.

The temperature coefficient of reactivity, α, quantifies reactivity changes due to temperature change in fuel and moderator component of a reactor core. The $\alpha_{T,j}$ represents the temperature coefficient of reactivity of a component j (fuel, moderator, or isothermal) and can be calculated as:

$$\alpha_{T,j} = \frac{\partial \rho}{\partial T_j} \quad [pcm/K] \tag{4.5}$$

where

$$\rho = \frac{k_{eff} - 1}{k_{eff}} \times 10^5 \quad [pcm] \tag{4.6}$$

k_{eff} = effective multiplication factor corresponding to T of component j $[-]$

∂T_j = change in average temperature of component j $[K]$.

If the temperature change is assumed to be uniform throughout the core, the temperature coefficient of reactivity is usually called Total or Isothermal Temperature Coefficient (ITC), $\alpha_{T,ISO}$, and can be defined as the change in reactivity per unit of temperature change:

$$\alpha_{T,ISO} = \frac{\Delta \rho}{\Delta T} \quad [pcm/K] \tag{4.7}$$

where

$\Delta \rho$ = change in reactivity $[pcm]$

ΔT_j = change in average temperature of the core $[K]$.

However, fuel and moderator temperature are rarely equal because fuel heats up much faster than the moderator; thus, the fuel temperature coefficient ($\alpha_{T,F}$ or FTC) and the moderator temperature coefficient ($\alpha_{T,M}$ or MTC) must be calculated separately. In the base case simulation in this work, the fuel salt and the moderator temperatures are fixed at 900K. To determine $\alpha_{T,F}$, I perturbed the fuel salt temperature from 800K to 1000K in increments of 50K while fixing the moderator temperature at 900K (base case). Likewise, I calculated $\alpha_{T,M}$ by perturbing the moderator temperature from 800K to 1000K with 50K increments, while fixing the fuel temperature at 900K.

The range of temperature perturbation for the temperature coefficient calculation has been selected based on operational parameters. The TAP MSR operates in the range of 773-973K (500-700°C), which is far below the salt boiling point of approximately 1473K [106]. The salt freezes below 773K [7]. At the other end of the temperature spectrum, the temperature higher than 973K passively melts a freeze plug, which drains the fuel salt from the reactor vessel to the drain tanks. The drain tanks have a subcritical configuration with a large free surface area to readily dissipate heat by passive cooling [106]. Thus, calculating temperature coefficients in the temperature range from 800 to 1000K captured the outcomes of most accident transients.

To determine the temperature coefficients, the cross section temperatures for the fuel and moderator were changed in the range of 800-1000K. For $\alpha_{T,F}$ calculation, changes in the fuel temperature impact cross section resonances (Doppler effect) as well as the fuel salt density. The density of fuel salt changes with respect to temperature as follows [53]:

$$\rho_{salt}(T) = 6.105 - 12.720 \times 10^4 T[K] \quad [g/cm^3] \tag{4.8}$$

The uncertainty in the salt density calculated using Equation 4.8 is approximately 0.036 g/cm^3 at 900K. In contrast, when the moderator temperature changes, the density, cross section temperature, and the geometry also change due to thermal expansion of the solid zirconium hydride ($ZrH_{1.66}$) rods. Accordingly, the new moderator density and sizes are calculated using a linear temperature expansion coefficient [115]:

$$\alpha_L = 2.734 \times 10^{-5} \quad [K^{-1}] \tag{4.9}$$

Using this thermal expansion data, I took into account the displacement of the moderator surfaces by generating corresponding geometry definitions for each Serpent calculation. That is, $\alpha_{T,M}$ calculation takes into account the following factors:

- thermal Doppler broadening of the resonance capture cross sections in $ZrH_{1.66}$;
- hydrogen S(α, β) thermal scattering data shift due to moderator temperature change;
- density change due to moderator thermal expansion/contraction;
- corresponding geometric changes in the moderator rod diameter and length.

By propagating the k_{eff} statistical error provided by Serpent 2, the corresponding uncertainty in each temperature coefficient is obtained using the formula:

$$\delta\alpha_T = \left|\frac{1}{T_{i+1} - T_i}\right| \sqrt{\frac{\delta k_{eff}^2(T_{i+1})}{k_{eff}^4(T_{i+1})} + \frac{\delta k_{eff}^2(T_i)}{k_{eff}^4(T_i)}} \tag{4.10}$$

where

k_{eff} = effective multiplication factor corresponding to T_i [-]

δk_{eff} = statistical error for k_{eff} from Serpent output [pcm]

T_i = perturbed temperature in the range of 800-1000K.

Notably, other sources of uncertainty are neglected, such as design parameter uncertainty, cross section measurement error[7], and approximations inherent in the equations of state providing both the salt and moderator density dependence on temperature.

Figure 4.29 shows reactivity as a function of fuel, moderator, and total temperature for the TAP MSR at the BOL and EOL. At startup, reactivity change with temperature clearly fits linear regression (R-squared[8] is 0.9, 0.99, and 0.98 for fuel, moderator, and isothermal case, respectively). Also, while the linear relationship between reactivity and moderator

---

[7] Chapter 7 of the current work presents uncertainty quantification method for propagating cross section measurement uncertainty throughout depletion calculations. While it is out of scope of this work to estimate nuclear-data related uncertainty of the temperature feedback coefficient, method from Chapter 7 can be adopted for the future work to perform such calculations.

[8] Coefficient of determination (R^2) is a statistical measure of how good measured data fitted linear regression line.

temperature worsens toward the EOL, an $R^2 > 0.7$ still indicates a strong linear association between ρ and T (R^2 is 0.99, 0.87, and 0.74 for fuel, moderator, and total case, respectively). I determined the temperature coefficient of reactivity separately for each component (fuel, moderator, and isothermal) using the slope of the linear regression for each.

Table 4.8 summarizes temperature coefficients of reactivity in the TAP core calculated at the BOL and EOL. The fuel temperature coefficient is negative throughout operation and becomes stronger toward the EOL as the spectrum thermalizes due to additional, retained fission products and actinides building up in the fuel salt. The MTC and ITC are both strongly negative at startup. However, the MTC became weakly positive toward the EOL due to the same spectral shift. To better understand the dynamics of temperature coefficient evolution, I calculated temperature coefficients for 15 distinct moments during operation to cover all moderator rod configurations described in Appendix A.

Table 4.8: Temperature coefficients for the TAP reactor at the BOL and EOL.

Coefficient	**BOL [pcm/K]**	**EOL [pcm/K]**
FTC	−0.350 ± 0.050	−0.868 ± 0.045
MTC	−1.134 ± 0.050	+0.746 ± 0.045
ITC	−1.570 ± 0.050	−0.256 ± 0.045

Figure 4.30 shows temperature coefficient evolution for the TAP reactor during 25 years of operation and takes into account the spectral shift due to moderator rod reconfigurations. The fuel temperature coefficient is almost constant for 19 years but decreases for the last 6 years (configurations with 1498 and 1668 moderator rods in the core). In contrast, the moderator temperature coefficient decreases from −1.134 pcm/K to −2.280 pcm/K during the first 11 years and then increases up to +0.746 pcm/K at the EOL. The moderator temperature increase at startup pushes thermal neutrons to higher energies, nearly up to the lowest ^{238}U resonances in the capture cross section. After 11 years, similar moderator temperature increase shifts neutrons into the same energy region, but this time that energy range is populated not only with ^{238}U but also with low-lying resonances from the actinides

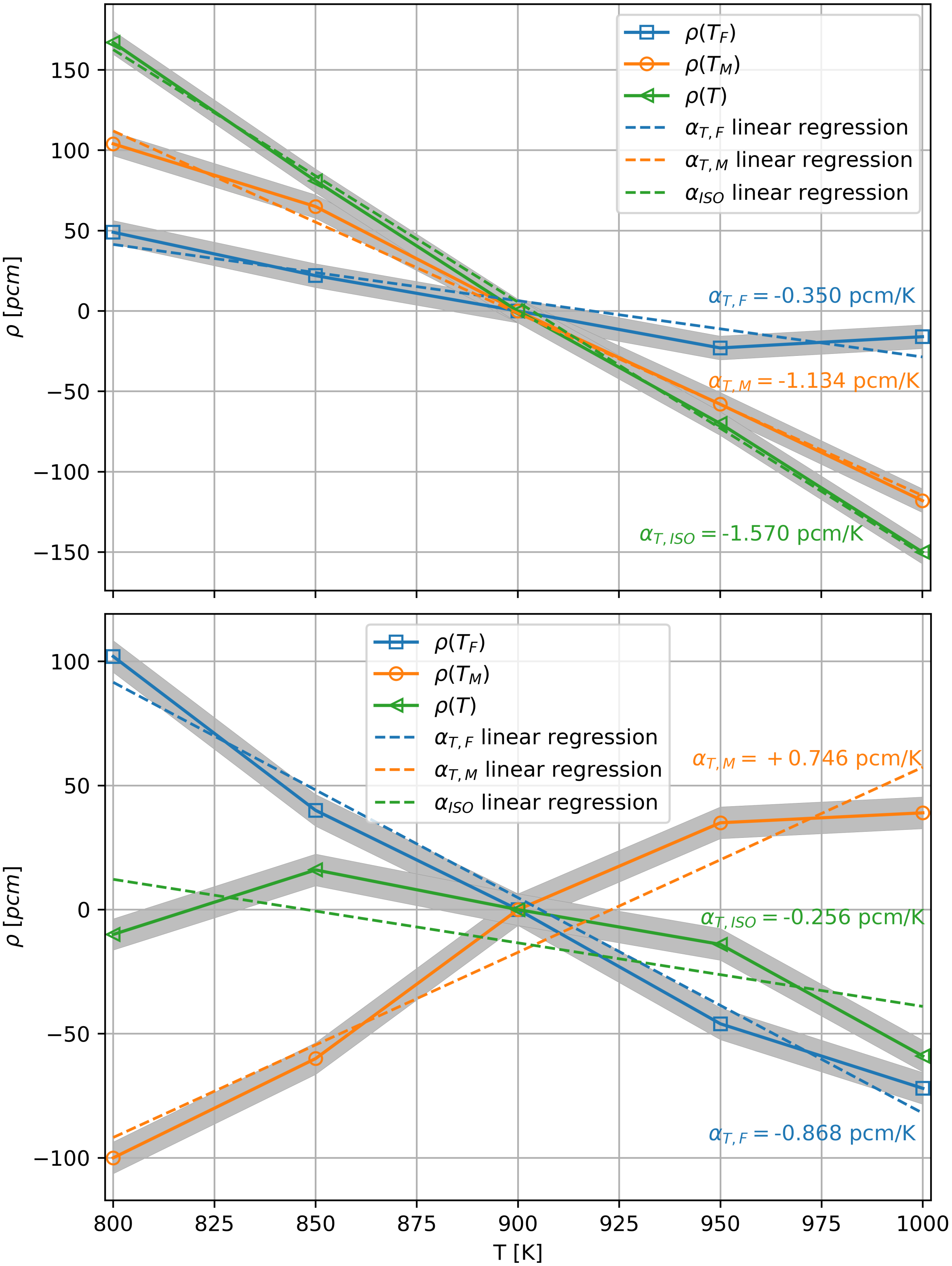

Figure 4.29: Serpent-calculated reactivity as a function of fuel salt (blue), moderator (orange), and both fuel/moderator (green) temperature at BOL (upper) and EOL (lower). The uncertainty ±σ region is shaded.

and fission products.

Additionally, the moderator temperature coefficient increases after 11 years of operation because there is twice as much moderator in the core at 11 years compared to the BOL. The moderator temperature increase causes fuel salt displacement due to the thermal expansion of the moderator rods, which has a particularly strong effect when the salt volume fraction is less than 75%. That is, when moderator heats up, the moderator-to-fuel ratio increases due to thermal expansion of zirconium hydride, which in turn leads to positive change in reactivity.

Finally, the isothermal temperature coefficient dynamics are similar to the MTC: the ITC decreases from -1.57 pcm/K to -2.66 pcm/K first 13 years of operation. After that, the ITC grows rapidly up to -0.256 pcm/K at the EOL. Overall, the ITC remains negative throughout operation but became relatively weak after 25 years of operation (comparing with conventional Pressurized Water Reactor (PWR), which has an isothermal temperature coefficient of $\alpha_{T,ISO} \approx -3.08$ pcm/K [40]).

4.4.2 Void coefficient of reactivity

The effect of fuel voids (i.e. bubbles) on reactivity is evaluated by reducing the fuel salt density from the base value (0% void) assuming helium volume fraction in the salt varies between 0 and 2%. The temperatures of both the fuel salt and the moderator are held constant at 900K. Because a decrease in the salt density causes an increase of moderator-to-fuel ratio, an increase in the helium volume fraction (voids) increases reactivity as shown in Figure 4.31. However, the slope of the line (void coefficient of reactivity (α_V)) decreases toward EOL due to the gradually increasing volume of moderator in the core (the volume fraction of the fuel salt at the EOL is less than 54%).

Figure 4.32 shows the void coefficient evolution during 25 years of operation, taking into account 15 moderator rod reconfigurations. The positive void coefficient of reactivity, though not ideal, does not compromise the reactor safety, if fuel density change resulted be coupled

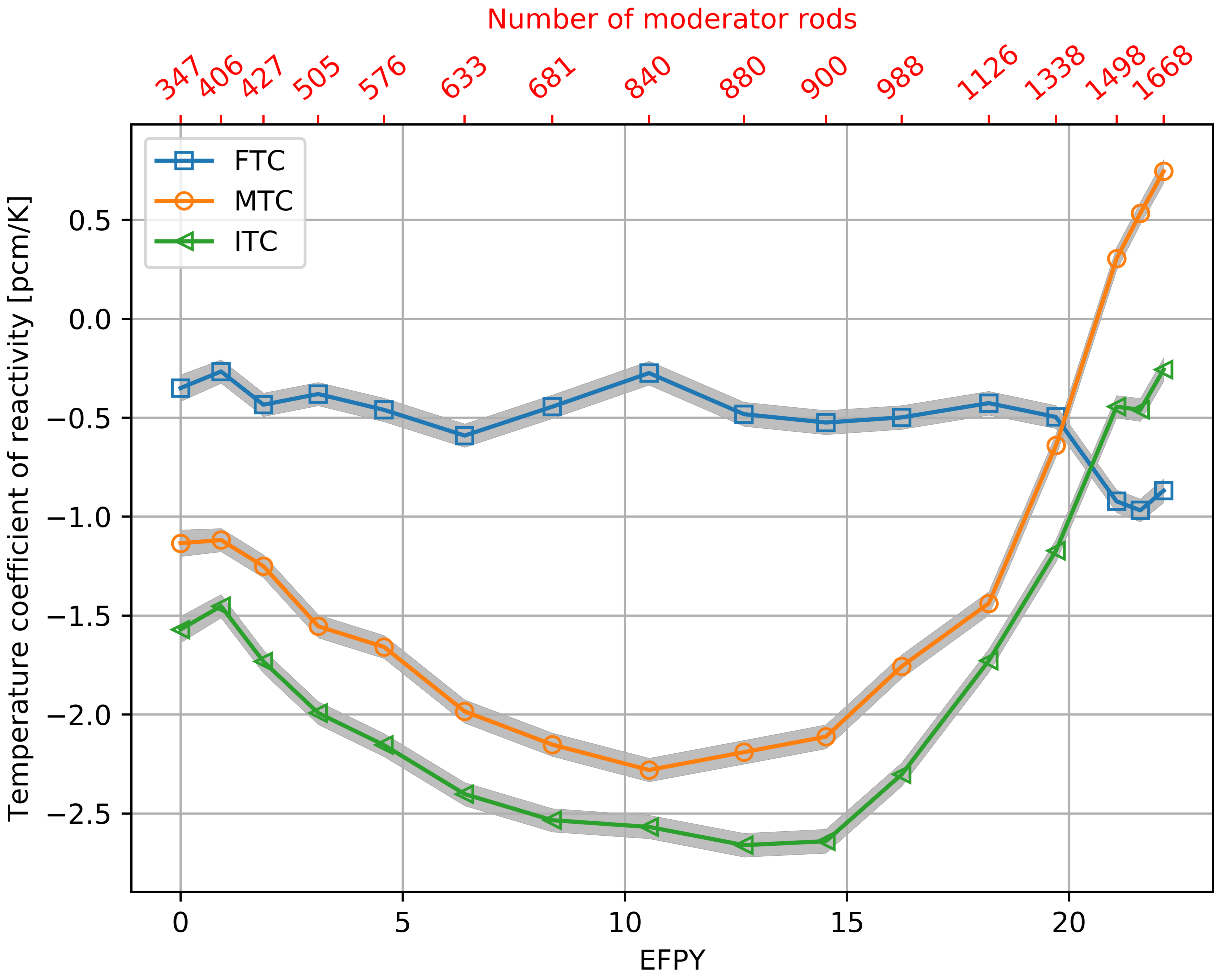

Figure 4.30: Serpent-calculated fuel, moderator, and isothermal temperature coefficients of reactivity as a function of time and number of moderator rods in the TAP core. The uncertainty $\pm\sigma$ region is shaded.

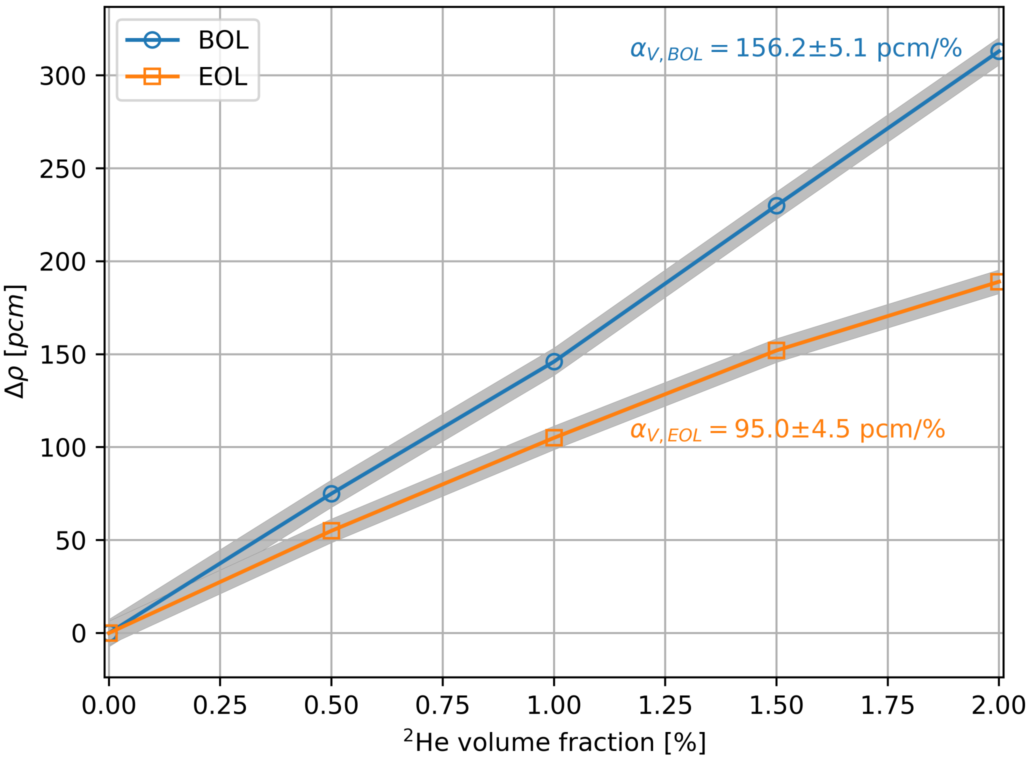

Figure 4.31: Serpent-calculated reactivity as a function of void volume fraction [%] in the fuel salt. The uncertainty ±σ region is shaded.

to a change in temperature. And, while some void fraction fluctuations may happen due to gaseous fission product production, their generation rates are usually almost constant. However, a large volume of sparging gas (helium) can be accidentally introduced into the TAP core in case of the bubble separator malfunction. Thus, *the bubble separator must have backup safety mechanism* to avoid sudden positive negativity insertion in case of the separator failure, particularly at the BOL. These observations from calculating reactivity coefficients should be taken into account in the TAP MSR accident analysis and safety justification.

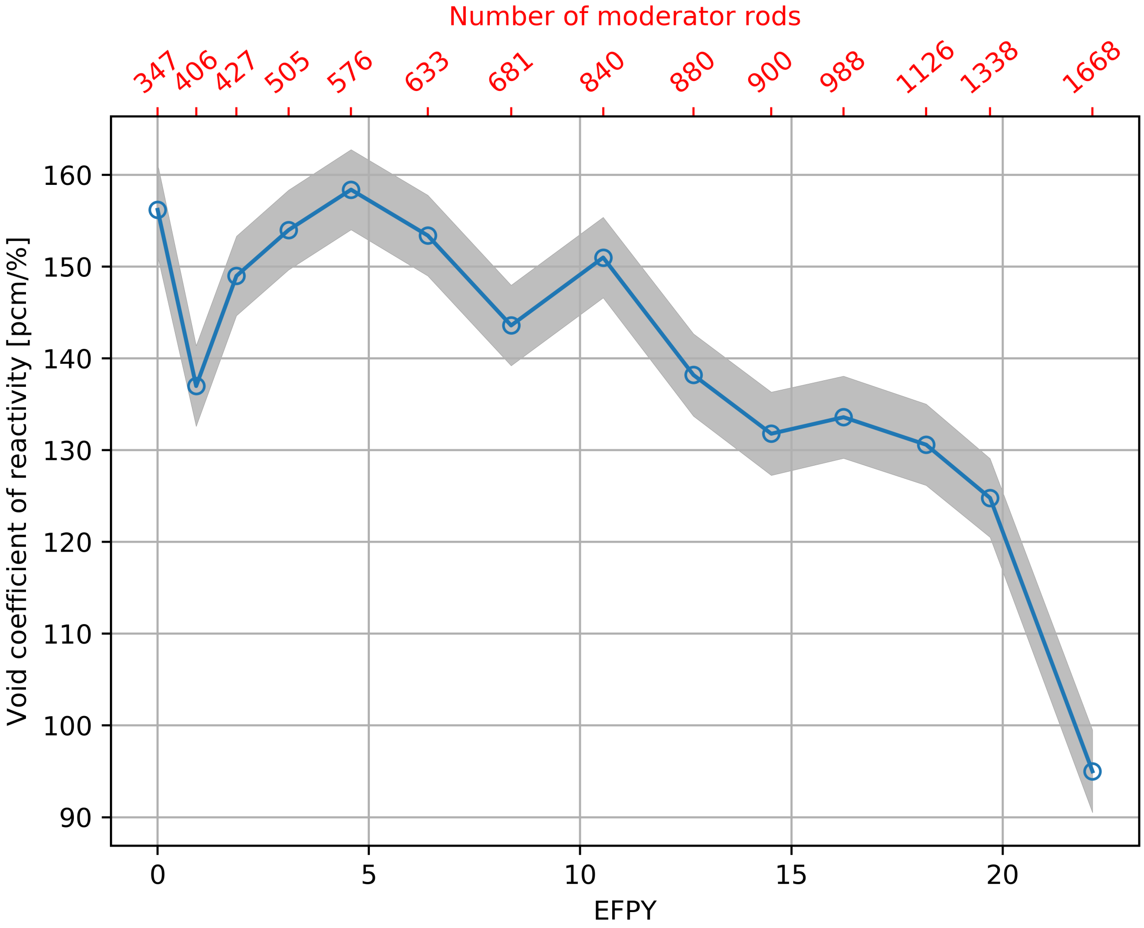

Figure 4.32: Serpent-calculated void coefficient of reactivity as a function of time and number of moderator rods in the TAP core. The uncertainty ±σ region is shaded.

4.4.3 Reactivity control rod worth

In the TAP concept, control rods perform two main functions: to shut down the reactor at any point during operation by negative reactivity insertion and to control the excess of reactivity after moderator rod reconfiguration during regular maintenance. In an accident, the control rods would be dropped down into the core. The total control rod worth (ρ_{CRW} or CRW) is calculated for various moments during 25 years of operation to evaluate neutron spectrum shift influence on the CRW.

The reactivity worth of all control rods is defined as:

$$\rho_{CRW}(pcm) = \frac{k_{eff}^{W} - k_{eff}^{I}}{k_{eff}^{W} k_{eff}^{I}} \times 10^5 \tag{4.11}$$

$$\rho_{CRW}(\$) = \frac{1}{\beta_{eff}} \frac{k_{eff}^{W} - k_{eff}^{I}}{k_{eff}^{W} k_{eff}^{I}} \tag{4.12}$$

where

k_{eff}^{W} = effective multiplication factor when all rods are fully withdrawn

k_{eff}^{I} = effective multiplication factor when all rods are fully inserted

β_{eff} = effective delayed neutron fraction.

The statistical error of the reactivity worth are obtained using formula:

$$\delta\rho_{CRW}(pcm) = \sqrt{\frac{(\delta k_{eff}^{W})^2}{(k_{eff}^{W})^4} + \frac{(\delta k_{eff}^{I})^2}{(k_{eff}^{I})^4}} \tag{4.13}$$

$$\delta\rho_{CRW}(\$) = \frac{1}{\beta_{eff}} \sqrt{\frac{(\delta k_{eff}^{W})^2}{(k_{eff}^{W})^4} + \frac{(\delta k_{eff}^{I})^2}{(k_{eff}^{I})^4} + \frac{(\delta\beta_{eff})^2 (k_{eff}^{W} - k_{eff}^{I})^2}{\beta_{eff}^2 (k_{eff}^{W} k_{eff}^{I})^2}} \tag{4.14}$$

where

$\delta k_{eff}^{W}, \delta k_{eff}^{I}, \delta\beta_{eff}$ = statistical errors from Serpent output.

Figure 4.33 demonstrates control rod worth evolution during 25 years of the TAP reactor operation. The cluster of 25 control rods made of boron carbide (B_4C) provided a reactivity worth of 5.059 ± 0.014 \$ at the BOL. However, spectral shift due to additional moderator rods toward the EOL leads to significant change in ρ_{CRW}. Adding more moderation near control rods increases ρ_{CRW} due to the local neutron spectrum thermalization (see transition from 347 to 427 moderator rods, Figure A.1). In contrast, adding moderator rods far away from the control rod positions leads to ρ_{CRW} degradation (see transition from 427 to 505 moderator rods, Figure A.1). On the one hand, the spectrum thermalizes and many fission product poisons exhibit larger absorption cross sections in the thermal energy range. On the other hand, higher actinides (particularly, isotopes of plutonium) are accumulated in the fuel salt which deteriorates control rod worth. Overall, ρ_{CRW} decreases to 4.472 ± 0.015 \$ at the EOL.

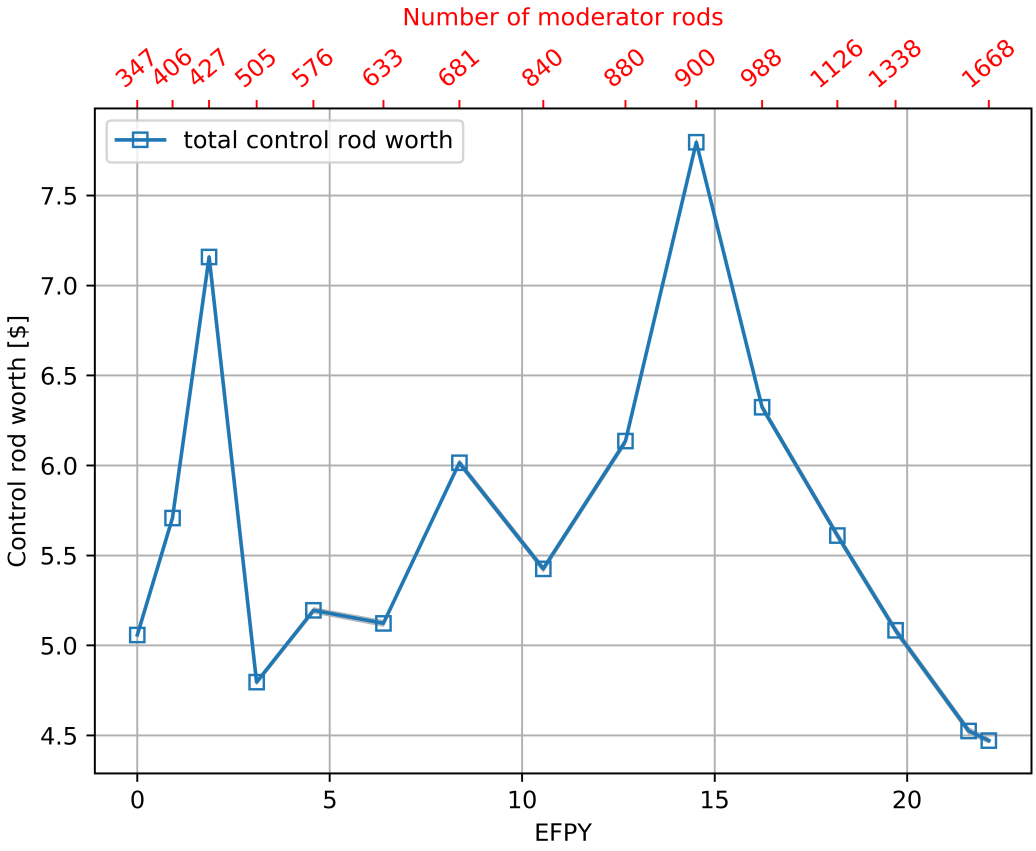

Figure 4.33: Serpent-calculated total control rod worth as a function of time and number of moderator rods in the TAP core. The uncertainty $\pm\sigma$ region is shaded.

Overall, the design of the reactivity control system is sufficient to shut down the TAP reactor at the BOL. However, the spectral shift, moderator rod reconfigurations, and the change in the salt composition during operation drive the total control rod worth below excess reactivity, violating reactor safety (insufficient shutdown margin). Thus, the number of control rods, their position, or material selection must be revised to make sure that the TAP reactor could be safely shut down at any moment during operation. For example, europium oxide (Eu_2O_3) might be a better absorbing material for the control rods [4].

4.4.4 Reactor kinetic parameters

Most of the neutrons produced in fission are prompt (> 99%). But less than 1% of neutrons are later emitted by fission products that are called the delayed neutron precursors (DNP). The term "delayed" means, that the neutron is emitted due to β-decay with half-lives in the range from few milliseconds up to 1 minute. Even though, the number of delayed neutrons per fission neutron is quite small (< 1% for most fissile isotopes), they play an essential role in the nuclear reactor control. Delayed neutrons presence changes the dynamic time response of a reactor to reactivity change from 10^{-7} s to 10 s, making it controllable by reactivity control system such as control rods. In nuclear library JEFF-3.1.2, delayed nuclear precursors are divided into 8 groups, each with different characteristic half-life, λ_i. The delayed neutron fraction, β_i, is defined as the fraction of all fission neutrons that appears as delayed neutrons in the i^{th} group.

It is crucial to study kinetic parameter dynamics because the fuel salt composition changes with time and new actinides appear in the fuel, which alters the emission of delayed neutrons. Figures 4.34 and 4.35 show precursor-group-wise delayed neutron fraction (DNF, β_i) and decay constant (λ_i) evolution during 25 years of TAP MSR operation. The effective delayed neutron fraction (β_{eff}) in the TAP core decreased dramatically from $7.245 \times 10^{-3}(\pm 0.5\%)$ at the BOL to $4.564 \times 10^{-3}(\pm 0.6\%)$ at the EOL (−37%).

Similarly, the effective precursor decay constant (λ_{eff}) slipped slightly from 0.481 $s^{-1}(\pm 0.8\%)$

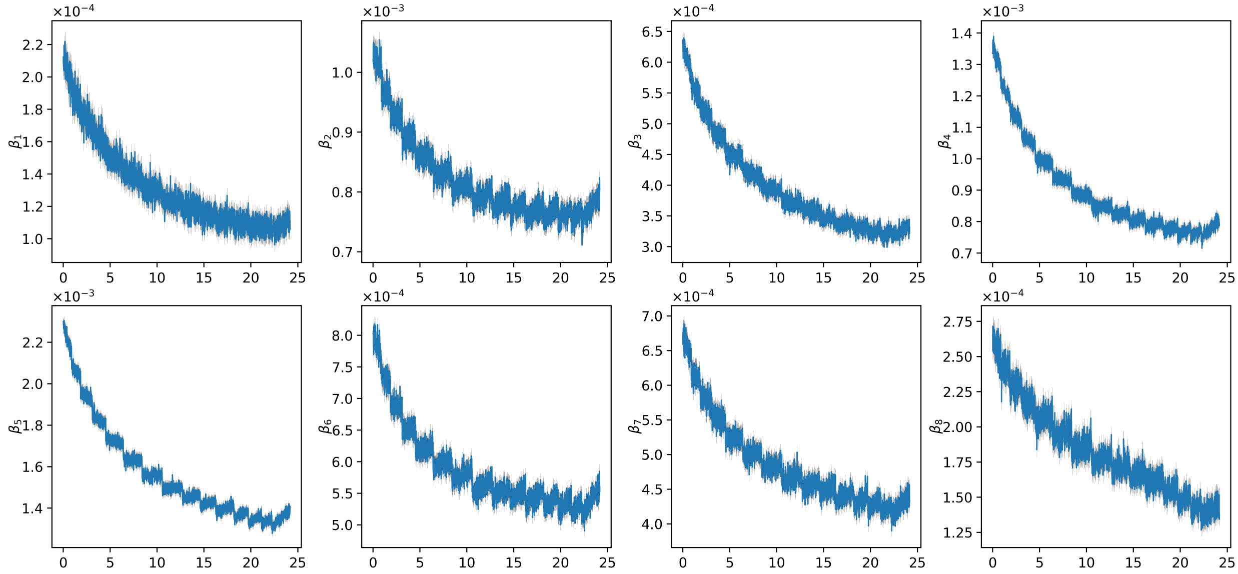

Figure 4.34: Evolution of the precursor-group-wise delayed neutron fraction (β_i) as a function of time for the TAP MSR. The uncertainty $\pm\sigma$ region is shaded.

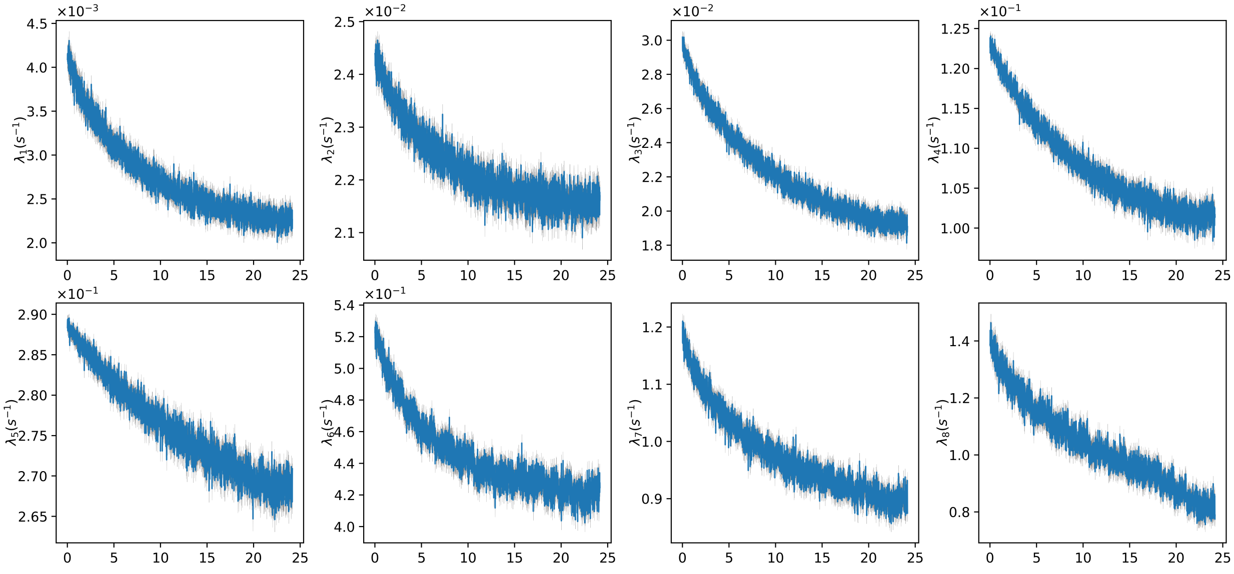

Figure 4.35: Evolution of the precursor-group-wise decay constant (λ_i) as a function of time for the TAP MSR. The uncertainty $\pm\sigma$ region is shaded.

to 0.468 s^{-1}(±1.1%) during 25 years of operation. During operation, the concentration of ^{235}U decreases, and the concentration of fissile plutonium isotopes (e.g., ^{239}Pu) increases. Notably, ^{239}Pu emits about 2.5 times fewer delayed neutrons than ^{235}U; delayed neutron yields are 0.00664 and 0.01650 for the ^{239}Pu and ^{235}U, respectively. Thus, as fuel salt burnup increases, delayed neutron emission is controlled by plutonium isotopes (e.g., ^{239}Pu and ^{241}Pu) and decreases with time. All decay constants show a slight decrease toward the EOL due to the reactor spectrum hardening. This 37% decline in the effective delayed neutron fraction and 3% decline in the effective precursor decay constant must be taken into account in the TAP design accident analysis and safety justification.

4.5 Concluding remarks

This chapter demonstrated SaltProc v1.0 capabilities for lifetime-long fuel salt depletion simulations applied to the TAP MSR. Section 4.1 summarized the TAP MSR core and fuel salt reprocessing system details that inform the SaltProc model (Section 4.2).

Section 4.3.1 presented lifetime-long depletion simulations with SaltProc v1.0. The 25-year simulation assumed ideal removal efficiency (e.g., 100% of target neutron poison is being removed at the end of each depletion step). This validation effort demonstrated good agreement with a reference ORNL report [17]. Full-core 3D SaltProc/Serpent analysis showed that spectrum hardening over the first 13 years of operation produces a sufficient amount of fissile plutonium to achieve the fuel salt burnup of 76.3 MWd/kgU after 22.5 years of operation. SaltProc-calculated inventories of major heavy isotopes at the EOL are consistent with results in the literature. The difference in mass between SaltProc and the reference was only 3% and 4% for fissile (^{235}U, ^{239}Pu, ^{241}Pu) and non-fissile (^{236}U, ^{238}U, ^{238}Pu, ^{240}Pu, ^{242}Pu) isotopes, respectively. Finally, the SaltProc-calculated feed rate is 460.8 kg of UF_4 per year, which consistent with 480 kg/y reported by Betzler *et al.* [17]

The time step refinement study in Section 4.3.1.4 showed that accurate uranium isotopic content predictions could be obtained with a relatively long depletion time step (6- or 12-day). However, the significant absolute difference in plutonium mass at the EOL ($\approx$ 10 kg for a 6-day step) could be a safeguards issue, as this represents more than one significant quantity (8 kg) over the reactor lifetime. Overall, to get accurate plutonium isotopic content without raising proliferation issues, a 3-day depletion time step must be used.

Section 4.3.2 of this chapter demonstrated SaltProc v1.0 for a 25-year depletion simulation with a realistic, physics-based noble gas removal efficiency. When identifying a reasonable mathematical model for realistic gas removal efficiency (ϵ), the liquid phase mass transfer coefficient (K_L) demonstrated a strong correlation with ϵ. Thus, SaltProc simulations using different K_L in validity range from 0.0847 to 8.4667 mm/s (corresponding ^{135}Xe removal efficiency $\epsilon \in [0.031, 0.915]$) showed that the larger liquid phase mass transfer coefficient and corresponding higher noble gas extraction efficiency provided significant neutronics benefit, better fuel utilization, and longer time between shutdowns for moderator rod reconfiguration. Notably, the larger mass transfer coefficient also provides a slightly more thermal neutron spectrum because poisonous FPs (^{135}Xe) absorb fewer thermal neutrons. In the following chapters, the results of these realistic depletion simulations will be used for short-term transient simulations and safety parameter analysis.

Finally, this chapter demonstrated safety and operational parameter evolution during 25 years of the TAP MSR operation. In general, the safety of the reactor worsens with time due to actinides and FPs accumulating in the fuel salt. Shifting neutron spectrum from epithermal to thermal by periodically adding more moderator rods also has a negative influence on crucial safety an operational characteristics. These observations must be taken into account in the TAP MSR designing, accident analysis, and safety justification.

Chapter 5

Tool demonstration for load-following and safety analysis: Transatomic Power MSR

In order to be competitive in the current domestic energy market, MSRs may need the flexibility to follow net load on the grid. Such load-following operation has the potential to increase the commercial competitiveness of nuclear power dramatically. Due to the increasing penetration of renewables into the electric grid, base-load operation carries the risk of correspondingly frequent negative electric energy pricing. Thus, responsiveness to net electricity demand is essential to market relevance for new designs [37]. This chapter presents a validation demonstration applying SaltProc v1.0 to simulate fuel salt depletion with online reprocessing during short-term transient to evaluate load-following capabilities of the TAP MSR.

5.1 Technical aspects of load following with nuclear reactors

The physical constraints limiting power variations in conventional LWRs include [67]:

- thermal strain and stress to fuel materials[1];
- fuel burnup (low excess reactivity at the EOC);
- ^{135}*Xe poisoning (iodine pit)*;
- reactivity thermal feedback (change in the temperature of the primary coolant and fuel causes negative reactivity insertion which limits power regulation capabilities).

Each of these physical effects is currently under active international research.

---

[1] This constrain does not apply to circulating-fuel MSRs because the fuel is into a liquid form.

This chapter focuses only on the fission product poisoning, especially the "iodine pit". The "iodine pit", also called the "iodine hole" or "xenon pit", is the reactor's inability to start a few hours after the reactor power decreases due to peak of ^{135}Xe concentration in the core. The ^{135}Xe is the strongest known neutron absorber ($\sigma_{a,^{135}Xe} = 2.6 \times 10^6$ barns) with a half-life $\tau_{1/2} = 9.17h$ and yield for ^{235}U fission about 6.6%. Figure 5.1 shows the entire decay chain, which characterizes ^{135}Xe gain and loss channels. The vast majority of ^{135}Xe (6.4%) is produced from ^{135}I decay ($\tau_{1/2} = 6.6h$). About half of ^{135}I is produced directly from fission and half from ^{135}Te decay ($\tau_{1/2} = 19s$) [75].

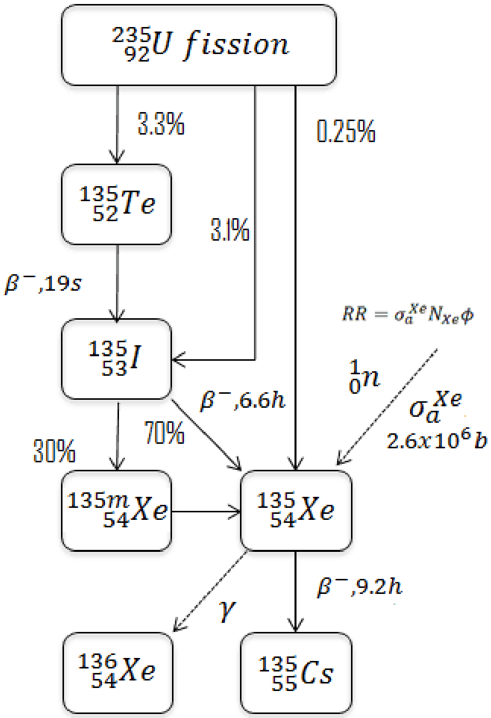

Source: www.nuclear-power.net
Data: JANIS 4.0 / NEA

Figure 5.1: Mechanisms of ^{135}Xe gain and loss in the reactor core (reproduced from [75]).

Under normal operating conditions, ^{135}Xe is transmuted to ^{136}Xe ('burned out') in the reactor core as it is produced. So, while it harms the neutron economy, balancing the reactor controls can compensate for its effect. The burnout of ^{135}Xe for an operating reactor can be described as follows:

$$^{135}\mathrm{Xe} + {}^{1}\mathrm{n} \rightarrow {}^{136}\mathrm{Xe}\ (stable) \tag{5.1}$$

Because ^{135}Xe is produced partially from the ^{135}I decay, the ^{135}Xe concentration directly depends on the ^{135}I concentration. Therefore, the iodine and xenon rate of change can be described as follows

$$\frac{dI(t)}{dt} = \gamma_I \Sigma_f \phi - \lambda_I I \tag{5.2}$$

$$\frac{dX(t)}{dt} = \lambda_I I + \gamma_X \Sigma_f \phi - \lambda_X X - \sigma_{a,X} \phi X \tag{5.3}$$

where

I, X = number density of ^{135}I, ^{135}Xe [cm^{-3}]

γ_I, γ_X = effective yield of ^{135}I, ^{135}Xe [fission^{-1}]

λ_I, λ_X = decay constant of ^{135}I, ^{135}Xe [s^{-1}]

Σ_f = macroscopic fission cross section of ^{235}U [s^{-1}]

$\sigma_{a,X}$ = microscopic absorption cross section of ^{135}Xe [b]

ϕ = neutron flux [$cm^{-2}s^{-1}$].

The difficulty comes when the reactor power is reduced, and there are fewer neutrons to burn the ^{135}Xe out, so its concentration increases and further suppresses reactor power. In this case, the core takes some time to recover from the power reduction impact of ^{135}Xe. This response to changing power levels, particularly from higher to lower power, dramatically slows the reactor's response to power demand [66].

In a liquid-fueled MSR, gaseous fission products (e.g., xenon) can be dynamically removed from the fuel salt by the gas separation system (see Section 2.1.1). Thus, xenon gas, including problematic ^{135}Xe, can be removed from the fuel salt outside the reactor core to eliminate its negative impact on the core neutronics. If the gas separation system can remove the vast majority of xenon, it is possible to alter the reactor power output in a wide range with very brief required recovery time. Overall, ^{135}Xe removal during reactor operation would potentially allow precise and flexible dynamic control of the reactor power level to follow power demands, typically referred to as 'load following.'

This chapter presents modeling and simulation of load following transient operation of the TAP MSR. This study focuses on the ^{135}Xe/^{135}I balance in the TAP core and its effect on reactor performance. In this chapter, I simulated short-term (< 24 hours) depletion with the core power changing in the [0,100%] range for xenon removal efficiency (ϵ_{Xe}) varied between 0 and 0.915 (see Table 4.7).

This chapter also demonstrates an analysis of reactor load-following capability for various moderator configurations and fuel salt compositions to bound the necessary efficiency of the gas removal system to ensure load-following operation.

5.2 TAP MSR load following analysis

All of the analysis herein used SaltProc v1.0 with the full-core 3-D model of the TAP MSR developed using Serpent 2 (see Section 4.2). The multi-component, online reprocessing system model with realistic noble gas removal efficiency described in Section 4.2.2, is used to simulate fission product removal and fresh fuel injection during the anticipated transient. To simulate transients with time-dependent power generation, I added to SaltProc v1.0 a new capability to perform fuel salt depletion with variable time step size and power level[2] during each depletion step. The depletion calculation in the load following regime captures the effects of ^{135}Xe poisoning and illuminates the benefit of using an online gas removal

---

[2] For simplicity, the reactor power level is adjusted by changing the normalization factor in Serpent (*set power P[W]*). This simplification assumes that spatial and energy distribution of the neutron flux remains constant and only the magnitude of the flux changes with time. That is, control rod movement and the corresponding change in the flux spatial and energy distribution are not treated here.

system in the TAP concept.

5.2.1 Power load curve selection approach

The load and generation must be continuously and almost instantly balanced in an electric power system. This is a physical requirement independent of the market structure. Regulation and load following (in the real-time energy market they are provided by the intra-hour workings) are the two services required to maintain a balance between power generation and power load. Figure 5.2 demonstrates the morning ramp-up decomposed into the total load (green), smooth load-following ramp (blue), and regulation (red). The smooth load-following slowly rises from 3566 MW to 4035 MW over 3 hours. Regulation compensates for high-frequency fluctuations in the load around the underlying trend within the ±55MW range. In the PJM region (Delaware, Illinois, Indiana, Kentucky, Maryland, Michigan, New Jersey, North Carolina, Ohio, Pennsylvania, Tennessee, Virginia, West Virginia, and the District of Columbia), New York, and New England, the 5-min ramping capability of a generator is required for the regulation, while in Texas and California it is 15-min and 10-min, respectively [56].

In this context *regulation* refers to the use of online generation or storage that is equipped with automatic generation control and can change output quickly (MW/min ramp rate) to compensate for the minute-to-minute fluctuations in customer loads and correct for unintentional fluctuations in power generation [56]. Typical natural gas peaking plants can ramp at or above 10% of their capacity per minute [50]. Elite combustion engine peakers (Wärtsilä) can ramp up from 10% to 100% load (or down) in less than one minute [110]. Hydropower plants also typically have accurate, high-speed ramping capability suitable for regulation [56].

Conventional nuclear power plants (Generation III/III+) can be used for load-following (blue curve on Figure 5.2) but have limited maneuverability. For example, the German Konvoi reactors are designed for 15,000 cycles with daily power variations from 100% to

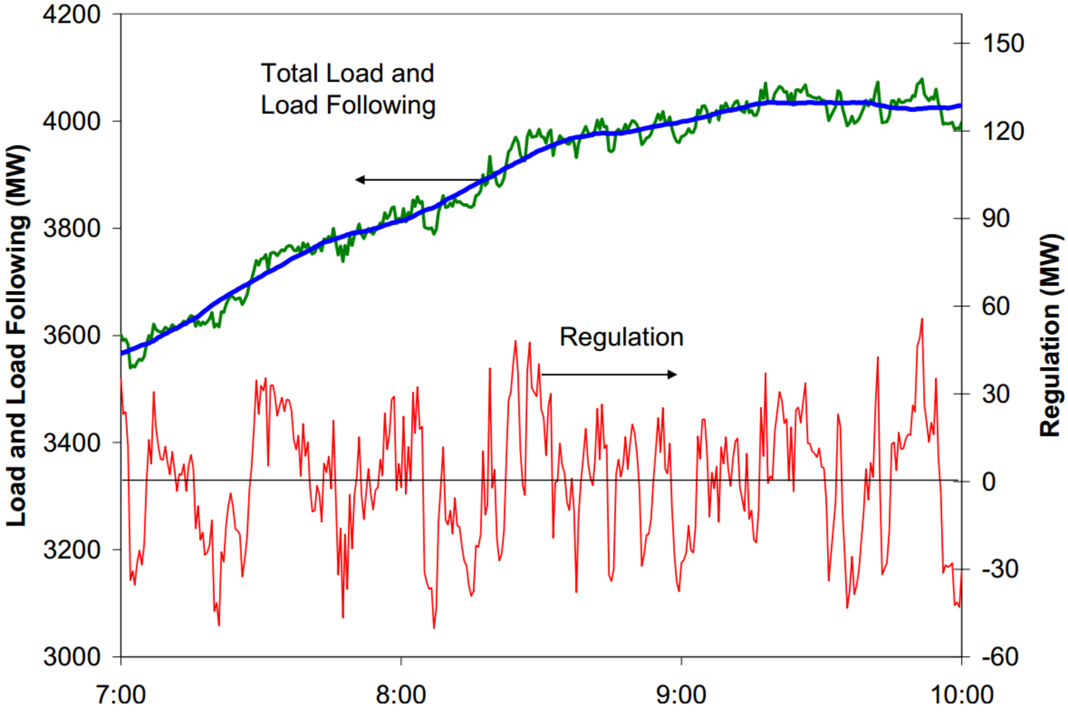

Figure 5.2: Regulation (red) compensates for minute-to-minute fluctuations in system total load (green), load following (blue) compensates for the inter- and intra-hour ramps (reproduced from [56]).

60% power level with ramp rate up to 2%/min [68], which is by order of magnitude slower than fossil-fueled plants. The MSRs must enable daily power variation with a much more flexible range (from 100% to 0% and from 0% to 100%) and ramp rate up to 10%/min to compete with these generators. The physical constrains limiting power variation range and ramp rate in nuclear reactors was listed in Section 5.1. *The current chapter of the dissertation focuses only on the* ^{135}Xe *poisoning effect.* Other physical effects, such as thermal strain and stress in structural materials are not treated here.

Performing a depletion calculation with SaltProc v1.0 to mimic the load-following maneuvering shown in Figure 5.2 would require a very fine time step (e.g., 15-minute step). To simulate power change with the desired rump rate (0.1 Hot Full Power (HFP)/min), depletion time step resolution of less than a 1-minute is needed. Such fine resolution requires thousands of depletion time steps to simulate 12-hour transient involving unreasonable computational costs. Instead, this chapter presents simulations with a 1-hour time step to investigate the impact of gaseous fission product removal on the reactor response to power demands.

The most challenging power transient for conventional LWRs from the viewpoint of xenon poisoning is well-defined in the literature. If after the ^{135}Xe concentration reaches equilibrium (40-50 hours after startup with fresh fuel), the reactor power was decreased from 100% to 0% (e.g., the reactor is tripped), the ^{135}Xe concentration and corresponding negative reactivity insertion would reach maximum in about 10-11 hours after shutdown [58, 9]. Notably, the time after shutdown when ^{135}Xe concentration reaches a maximum strongly depends on the reactor neutron energy spectrum.

Thus, to demonstrate SaltProc v1.0 capabilities for a short-term transient with the reactor power change and to investigate load-following capabilities of the TAP reactor with a focus on the xenon poisoning, I selected following worst-case power load profile:

(a) operate on 100% of HFP long enough to reach ^{135}I/^{135}Xe equilibrium;
(b) instantaneous power drop from 100% to 0%;
(c) shutdown for t_X^{max} [hours] to reach the ^{135}Xe concentration extremum;
(d) restart the reactor instantly from 0% to 100% power level and operate on 100% for a few hours.

Or in math formulation:

$$P(t) = \begin{cases} 100\%, & t < t_{eq} \\ 0\%, & t_{eq} \leq t \leq t_{eq} + t_X^{max} \\ 100\%, & t > t_{eq} + t_X^{max} \end{cases} \tag{5.4}$$

where

$P(t)$ = reactor power level [%]

t_{eq} = time after startup to reach ^{135}Xe equilibrium concentration [h]

t_X^{max} = time after shutdown when ^{135}Xe concentration peaks [h].

This postulated worst-case transient could be considered as backing up solar power with nuclear on a high-solar-penetration grid (e.g., in California). Any other power load profile (i.e., blue load-following line shown in Figure 5.2) would demonstrate a significantly milder xenon poisoning effect because of the power demand change in the [0,100%] range realistically is not instantaneous. That is, if the TAP MSR would be able to maintain criticality in the described stress test (e.g., $k_{eff} > 1.0$ during all stages of the transient), then it is capable of following a realistic load curve.

The local extremum of xenon concentration can be described as follows

$$\frac{dX(t)}{dt} = 0 \tag{5.5}$$

The system of Ordinary Differential Equations which consist of Equations 5.2, 5.3, and 5.5 must be solved to calculate when the ^{135}Xe concentration reaches maximum.

If the ^{135}I and ^{135}Xe concentrations at shutdown is I_0 and X_0, respectively, the time after shutdown when the ^{135}Xe concentration peaks is given by:

$$t_X^{max} = \frac{1}{\lambda_X - \lambda_I} log\left(\frac{\lambda_X(\lambda_I[X_0 + I_0] - \lambda_X X_0)}{\lambda_I^2 I_0}\right) \tag{5.6}$$

Since the ^{135}I and ^{135}Xe concentrations at shutdown in the TAP core are expected to be different at the BOL and EOL due to significant spectral shift, t_X^{max} is recalculated for each case to obtain the worst possible xenon poisoning effect. The ultimate goal of this effort is to evaluate the timing and impact of problematic fission product removal (i.e. xenon removal) on maximum negative reactivity insertion.

5.2.2 Results and Analysis

The TAP full core depletion analysis was performed using SaltProc v1.0. A 1-hour depletion time step captures rapid changes in reactivity and isotopic composition during the transient. Figure 5.3 demonstrated the effective multiplication factor evolution during postulated worst-case transient when the reactor is tripped for 11 hours (typical time to reach maximum ^{135}Xe concentration in conventional LWRs) and then restarted. *The gas removal system for that demonstration case was inactive to enhance the xenon poisoning effect.* At the beginning of the transient (initial conditions), the reactor operated for 8448 days ($\approx$ 23 years), and all moderator rods are inserted in the core (see 1668 rods configuration in Figure A.2). The negative effect of xenon poisoning is expected to be the greatest at the EOL when the core has the most thermal neutron spectrum. The multiplication factor decreases by 64 *pcm* during the first two hours after shutdown (^{135}Xe concentration reached its maximum) and then increases by 242 *pcm* because ^{135}Xe loss due to decay overcame its gain from ^{135}I decay. The k_{eff} increase accelerated after reactor power turned back to 100% due to ^{135}Xe burnout. Figure 5.3 clearly indicates that the time after shutdown when the ^{135}Xe reaches its extremum (t_X^{max}) is significantly shorter for the TAP reactor than for LWRs (11 hours).

Using ^{135}I and ^{135}Xe number densities at the 8448^{th} day of operation (the 10^{th} day before the EOL) from long-term realistic analysis (see Section 4.3.2) and Equation 5.6, I calculated the xenon peak time for the TAP MSR with all moderator rods inserted: $t_X^{max} = 2.76h$. To estimate maximum negative reactivity insertion due to xenon poisoning, the transient simulation is repeated with the finer time resolution (15 minutes instead of 1 hour) and shutdown time of 2.75 hours (e.g., the time between the shutdown and power ramp-up to 100% is equal t_X^{max}).

Figure 5.4 shows that the effective multiplication factor dropped by 70 *pcm* during the first 2.75 hours after shutdown as predicted by Equation 5.6. After power ramps up from 0% to

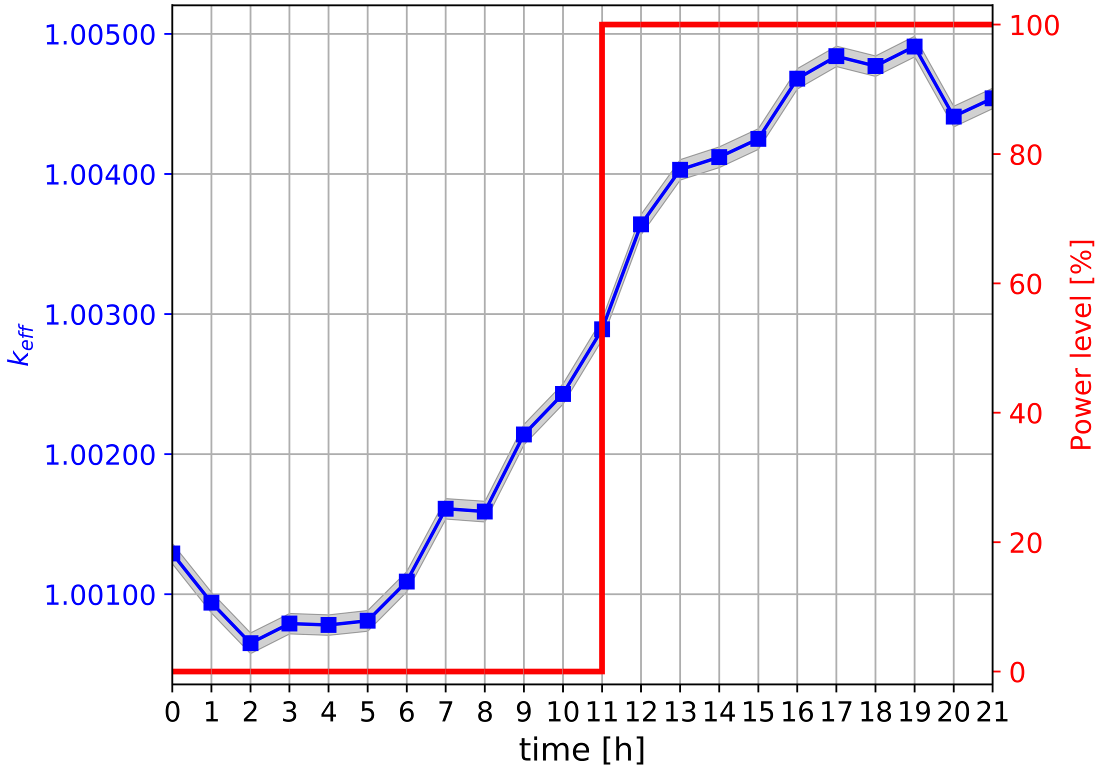

Figure 5.3: The effective multiplication factor dynamics for an 11-hour shutdown (well-known xenon peak time for LWRs) for the TAP reactor, 10 days before the EOL (all moderator rods inserted), the gas removal system is turned off. Uncertainty ($\sigma \pm 7$ pcm) is shaded.

100%, k_{eff} returned to its initial value (1.00151) in 75 minutes. The imbalance between ^{135}I production and ^{135}Xe burnout is the main reason for this positive reactivity boost. Notably, maximum negative reactivity insertion due to ^{135}Xe buildup after shutdown in the PWR (-1500 pcm) is two orders of magnitude greater than in the TAP MSR (-70 pcm). Thus, the TAP reactor with inactive gas removal system remains critical throughout worst-case power change even during the 8448^{th} of operation (the 10^{th} day before k_{eff} drops below 1) when operative excess reactivity is low ($151\ pcm > 70\ pcm$). If the shutdown happens during the last 9 days of the TAP reactor operation, then the operator would not be able to restart it until $t_X^{max} = 2.76h$ after shutting down.

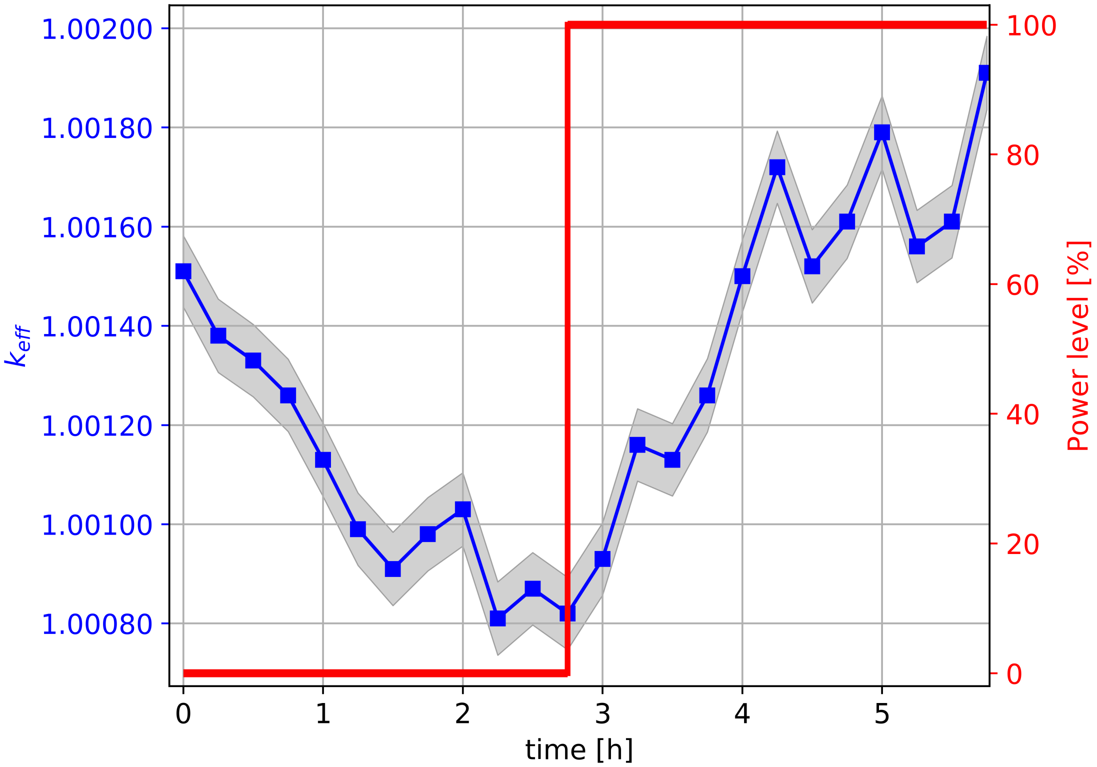

Figure 5.4: The effective multiplication factor dynamics for the worst-case load curve (2.75-hour shutdown) for the TAP reactor, 10 days before the EOL (all moderator rods inserted), the gas removal system is turned off. Uncertainty ($\sigma \pm 7$ pcm) is shaded.

The analysis of the fuel composition evolution provides clearer information about the ^{135}Xe/^{135}I equilibrium and the core state. Figure 5.5 shows changes in the number density of isotopes influential to the TAP core neutronics throughout the transient. The ^{135}I/^{135}Xe number density ratio after reaching xenon equilibrium is equal to 1.0. After shutdown, ^{135}I decays to ^{135}Xe that is not burned up. The ^{135}I decay caused xenon concentration to increase by 4% from equilibrium after 2.75 hours due to a shorter ^{135}I half-life ($\tau_{1/2}(^{135}I) = 6.6h$ vs. $\tau_{1/2}(^{135}Xe) = 9.17h$). Thus, during the first 2.75 hours, ^{135}Xe gain from ^{135}I decay slightly overcame ^{135}Xe decay loss. In sum, the ^{135}Xe peak is almost negligible (+4%) even in the worst-case load profile scenario due to a lower ^{135}I/^{135}Xe concentration ratio at the equilibrium: 1.0 and 2.3 for the TAP reactor and PWR, respectively [94].

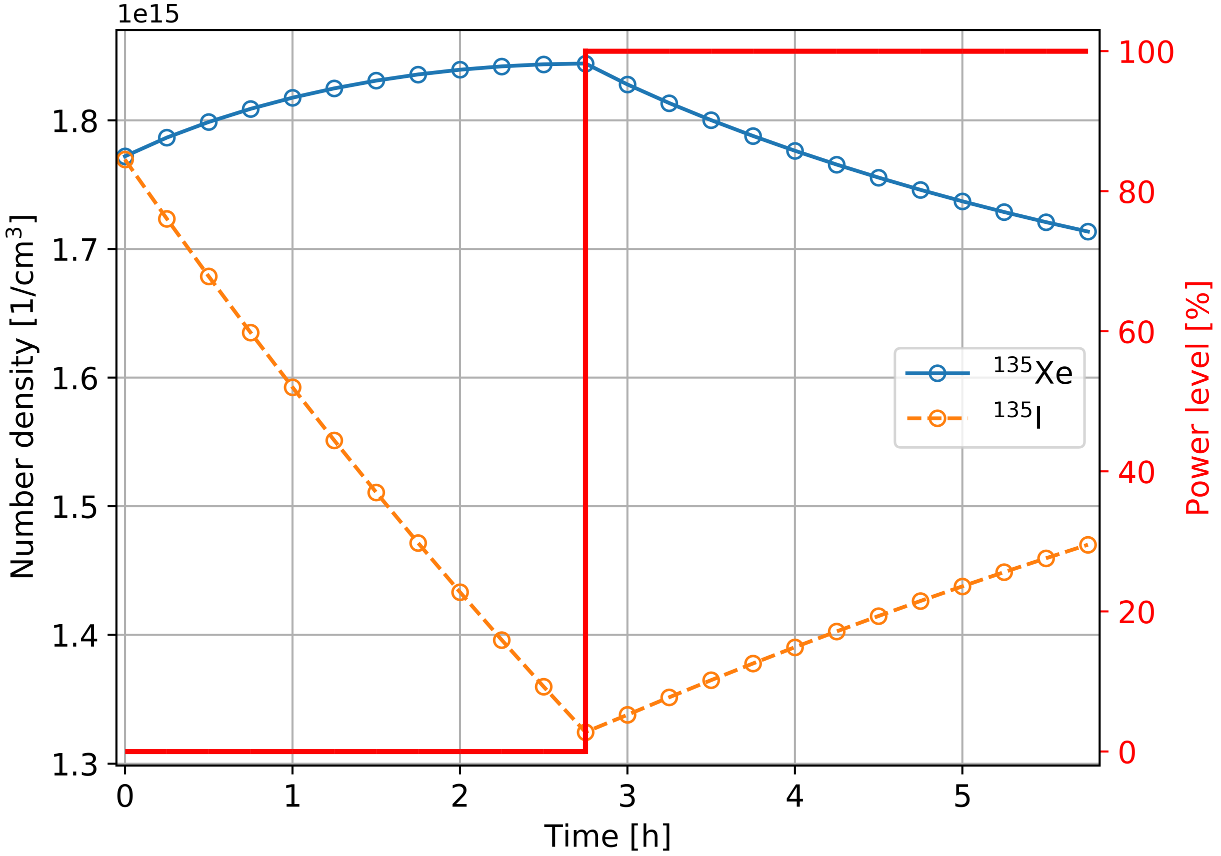

Figure 5.5: Number density of ^{135}Xe and its direct precursor ^{135}I for the worst-case load curve (2.75-hour shutdown) for the TAP reactor, 10 days before the EOL (all moderator rods inserted), the gas removal system is turned off.

Table 5.1 shows that *even without gas removal* the TAP reactor experienced *insignificant effect of xenon poisoning* during the transient, however, the effect worsened toward the

EOL. I repeated the fuel composition and multiplication factor evolution analysis described earlier to evaluate impact of the reactor spectrum (geometry #1 has a significantly harder spectrum than geometry #15) and the fuel salt composition on the effect of xenon poisoning and on the reactor's potential ability to follow load. The effect of xenon poisoning worsens toward the EOL because the ^{135}Xe concentration peak is larger for the most thermal core configuration (all moderator rods inserted, the largest moderator-to-fuel ratio). Right after the final moderator configuration update (switch from geometry #14 to #15), the xenon concentration peak is slightly larger than at the 297^{th} day of the cycle. The fissile ^{235}U, ^{239}Pu, and ^{241}Pu concentration decreasing during last cycle due to burnup, while poisonous actinides (e.g., ^{238}Pu, ^{240}Pu, ^{242}Pu, ^{236}U) concentration increases which impacts ^{135}I/^{135}Xe number density ratio and, consequently, ^{135}Xe concentration peak value. Notably, such phenomena are not observed for the BOL (geometry #1, SVF=0.903) or Middle of Life (MOL) (geometry #8, SVF=0.766).

Table 5.1: Effect of ^{135}Xe poisoning after shutdown for the TAP reactor operation with inactive gas removal system ($\epsilon_{Xe} = 0$). Stochastic uncertainty $\sigma_\rho = 7$ *pcm*.

Geometry	SVF [-]	Time after moderator configuration update [d]	Operative excess reactivity (ρ_0) [*pcm*]	Analytically predicted ^{135}Xe peak time (t_X^{max}) [h]	Maximum relative ^{135}Xe concentration change [%]	Maximum reactivity change after shutdown ($\Delta\rho$) [*pcm*]
1	0.903	3	3542	0.749	+0.33	-10
1	0.903	288	405	0.500	+0.14	-15
1	0.903	315	165	0.484	+0.13	-4
8	0.766	3	3014	0.688	+0.36	-10
8	0.766	390	1529	0.722	+0.39	0
8	0.766	777	204	0.751	+0.42	0
15	0.536	3	2263	2.528	+3.32	-57
15	0.536	153	1160	2.647	+3.69	-60
15	0.536	297	129	2.758	+4.07	-70

Overall, the TAP MSR could be restarted after shutdown *even without gas removal* in worst-case initial conditions: the most thermal moderator configuration, low operative excess reactivity at the end of the burnup cycle, instantaneous power drop, and ^{135}Xe concentration at its extremum. To investigate the benefits of online fission gas removal on the xenon poisoning effect, I repeated the postulated transient simulation for different moments in time (e.g., BOL, MOL, EOL) with a fully operational gas removal system ($\epsilon_{Xe} = 0.915$).

Figure 5.6 demonstrates a more notable xenon poisoning effect for the case with high gas removal efficiency than for the no-removal case. The reactivity drops by 100 *pcm* during the first hour after shutdown. The gas removal system keeps ^{135}Xe concentration very low by continuously extracting 91.5% of xenon isotopes. Simultaneously, the online reprocessing system extracts ^{135}I very slowly (cycle time is 60 days); hence, ^{135}I/^{135}Xe concentration ratio is significantly greater than for the no-removal case (11.0 vs. 1.0). According to Equation 5.6, ^{135}Xe concentration should reach local extremum in about 11 hours after shutdown, but this equation disregards online reprocessing. The depletion simulation performed using SaltProc v1.0 demonstrated that ^{135}Xe concentration peaked in one hour after the shutdown and caused the reactivity drop by 100 *pcm* (see Figure 5.6). Afterward, the reactivity restored quickly (< 2 hours) to its initial value because the gas removal system extracts 91.5% of xenon every hour. Overall, ^{135}Xe loss due to its decay and online gas extraction is more significant than ^{135}Xe gain due to ^{135}I decay throughout the transient.

Table 5.2 shows that the TAP reactor with high gas removal efficiency experienced *small effect of xenon poisoning* during the transient, and it also worsened toward the EOL. Similar to the analysis with inactive gas removal system, maximum negative reactivity insertion due to xenon poisoning worsens toward the EOL because ^{135}Xe absorption cross section drops dramatically as energy grows. Notably, the maximum ^{135}Xe concentration peak is significantly greater for an excellent gas removal efficiency ($\epsilon_{Xe} = 0.915$) than for the no-removal case ($\epsilon_{Xe} = 0$): +197% and +4%, respectively. Despite greater ^{135}Xe concentration peak, negative change of reactivity after shutdown for the $\epsilon_{Xe} = 0.915$ case is slightly deeper than for the $\epsilon_{Xe} = 0$ case: -100 *pcm* and -70 *pcm*, respectively. The reason for this is the neutron energy spectrum in the TAP MSR, which is harder than in conventional light-water thermal reactors. As we know, fast reactors are unaffected by xenon poisoning because the

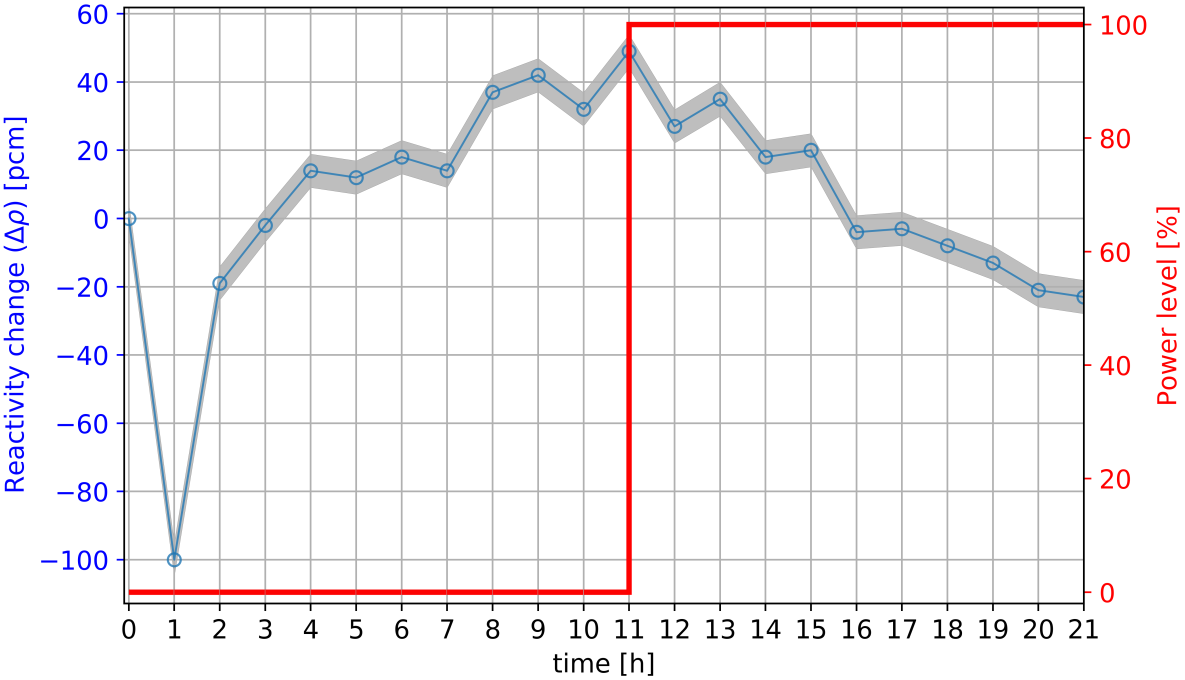

Figure 5.6: Reactivity dynamics during an 11-hour shutdown for the TAP reactor, 10 days before the EOL (all moderator rods inserted), the gas removal system operates with efficiency $\epsilon_{Xe} = 0.915$. Uncertainty ($\sigma \pm 5$ pcm) is shaded.

absorption cross section of ^{135}Xe in the fast spectrum is insignificantly larger than absorption cross section of other fission products [9, 101]. The TAP concept has intermediate spectrum which softens towards the EOL. Finally, the effect of xenon poisoning in TAP MSR is almost negligible and can be easily compensated by control rod movement, while in well-studied PWR it presents a challenge (-1500 pcm) [94].

Additionally, I analyzed the neutron spectrum of both reactors to understand the difference between ^{135}I/^{135}Xe gain and loss for the TAP MSR and PWR. Figure 5.7 demonstrates the neutron flux energy distribution normalized by unit lethargy for both reactors. The TAP reactor spectrum at the BOL (SVF=0.903) is much harder than for the PWR due to a lack of moderation in the TAP core and its type ($ZrH_{1.66}$ instead of light water). The harder neutron spectrum leads to weaker ^{135}Xe transmutation because the capture cross section declines rapidly with energy (see Figure 5.7, lower plot, solid red line, energy range from 10^{-7} to 10^{-4} MeV). As a result, the ^{135}I/^{135}Xe number density ratio is 0.78 for the TAP

Table 5.2: Effect of ^{135}Xe poisoning after shutdown for the TAP reactor operation with the high ^{135}Xe removal efficiency ($\epsilon_{Xe} = 0.915$). Stochastic uncertainty $\sigma_\rho = 5$ pcm.

Geometry	SVF [-]	Time after moderator configuration update [d]	Operative excess reactivity (ρ_0) [pcm]	^{135}I/^{135}Xe concentration ratio before shutdown [-]	Maximum relative ^{135}Xe concentration change [%]	Maximum reactivity change after shutdown ($\Delta\rho$) [pcm]
1	0.903	9	3344	8.96	+174	-50
1	0.903	171	1930	8.76	+173	-40
1	0.903	324	570	8.66	+172	-38
8	0.766	3	3570	8.87	+175	-61
8	0.766	366	2150	8.90	+174	-40
8	0.766	762	762	8.93	+175	-33
15	0.536	9	3370	11.07	+194	-105
15	0.536	90	2771	11.17	+195	-108
15	0.536	303	1265	11.42	+197	-100

MSR at the BOL, which is significantly lower than that for the PWR with fresh fuel (2.3). Thus, ^{135}Xe gain from ^{135}I decay cannot overcome ^{135}Xe loss due to decay, and no xenon concentration peak is observed at the BOL (Table 5.1, first three rows).

The TAP MSR neutron spectrum thermalizes toward the EOL due to additional moderator rod insertion. Figure 5.7 shows that the TAP core spectrum at the EOL (after 23 years of operation, all moderator rods inserted into the core) is thermal and similar to the PWR spectrum. However, the ^{135}I/^{135}Xe inventory ratio for the PWR with fresh fuel is significantly greater than for the TAP core at the EOL despite similar spectra (2.3 and 1.0, respectively). The reason for that difference is the different fissile content. Results in Section 4.3 shown that toward the EOL fissile ^{235}U is being substituted with fissile ^{239}Pu and ^{241}Pu. More specifically, instead of 6.8 t of ^{235}U at startup, at the EOL, the fuel salt contains 1.3 t of ^{235}U, 1 t of ^{239}Pu, and 0.5 t of ^{241}Pu. That is, the fuel salt fissile inventory in the TAP MSR at the EOL contains 46 wt% of ^{235}U, 36 wt% of ^{239}Pu, and 18 wt% of ^{241}Pu.

Table 5.3 shows ^{135}I and ^{135}Xe yields from thermal fission for all fissile isotopes contained in the fuel salt. At the BOL, ^{135}I and ^{135}Xe in the TAP reactor and PWR are produced from ^{235}U fission. The ^{135}I isotope production rate per thermal fission stays approximately

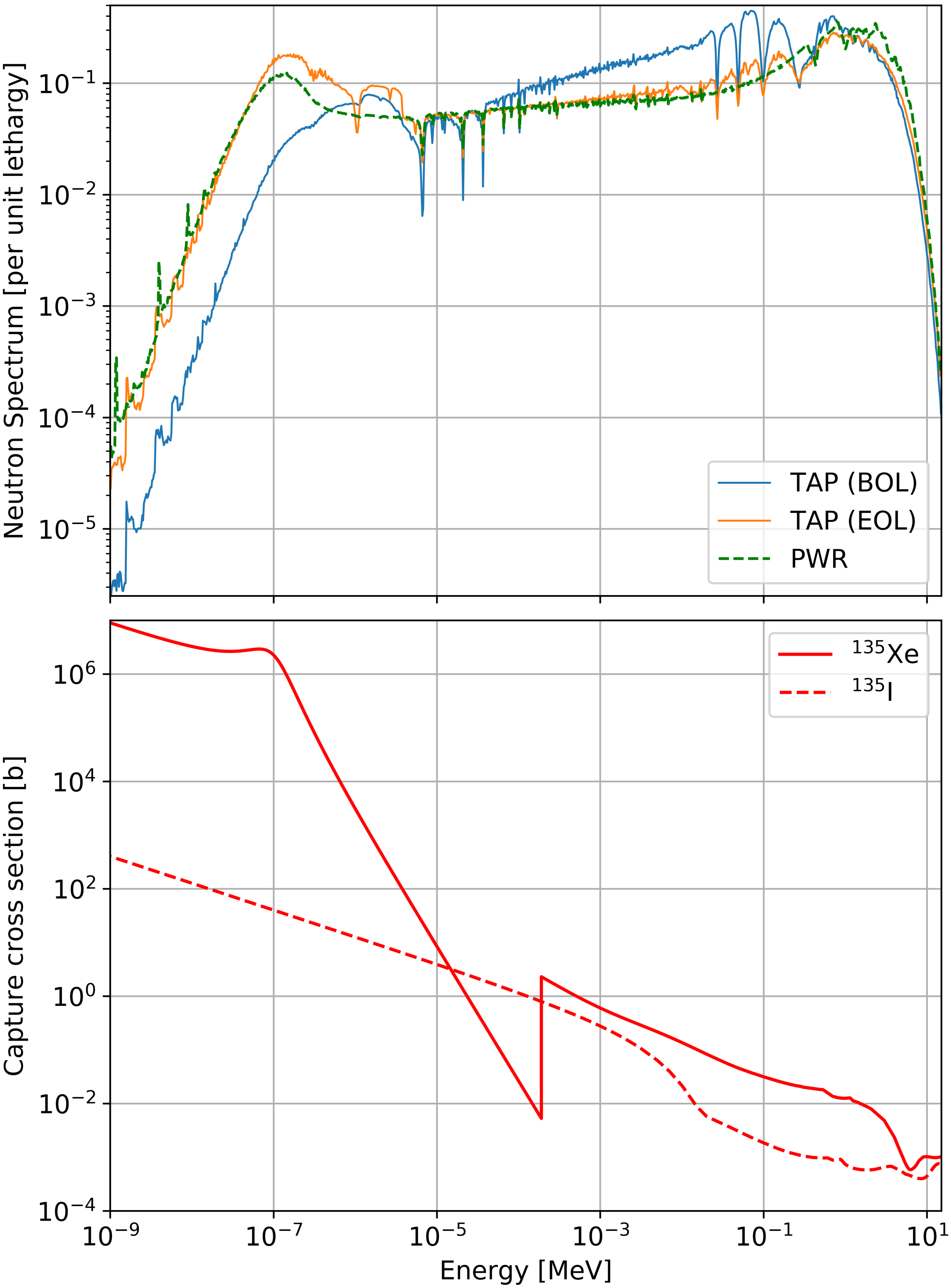

Figure 5.7: Neutron spectra normalized by lethargy for the PWR and TAP (upper) and ^{135}I, ^{135}Xe caption cross section (lower) [94].

the same during 23 years of operation because ^{135}I yield is very close for all considered fissile isotopes. However, the rate of ^{135}Xe production directly from fission for fissile plutonium isotopes is significantly greater than for the ^{235}U (e.g., ≈ 5 times greater for ^{239}Pu and ≈ 8 times greater for ^{241}Pu). Thus, a greater ^{135}Xe production rate toward EOL with approximately the same ^{135}I production rate leads to a smaller ^{135}I/^{135}Xe concentration ratio. Overall, ^{135}I/^{135}Xe number density ratio increasing from 0.78 to 1.0 during 25 years of the TAP MSR operation, which leads to a more massive ^{135}Xe concentration peak after shutdown and worsens xenon poisoning effect.

Table 5.3: Fission product yields (isotopes per fission) from thermal fission [70].

Isotope	^{235}**U**	^{239}**Pu**	^{241}**Pu**
^{135}I	0.0639	0.0633	0.0684
^{135}Xe	0.0022	0.0103	0.0017

In conclusion, I observed a negligible xenon poisoning in the TAP reactor during the anticipated transient because it has a relatively hard neutron energy spectrum even at the most thermal core configuration (all moderator rods are inserted into the core). The harder spectrum gives a small ^{135}I/^{135}Xe concentration ratio which leads to a low ^{135}Xe concentration peak after the shutdown. Notably, the fission gas removal with high efficiency did not significantly change the xenon poisoning effect because the ^{135}Xe absorption cross section fell dramatically as neutron energy grows. Overall, the TAP reactor can effectively load-follow even without fission gas removal.

5.3 Safety and operational parameters evolution during load following

To analyze the impact of the load-following transient on the TAP concept safety, I calculated safety and operational parameters at various moments during postulated earlier worst-case power change transient (0% power level for 11 hours, instantaneous power boost to 100%, and then 10 hours on 100% power level) using methodology from Section 4.4. The combination of fuel and moderator temperature feedback coefficients must remain negative, and the reactivity worth of control rods must be sufficient to shut down the reactor throughout the transient. Ideally, the reactor is more controllable if major safety and operational parameters remain stable and unaffected by the substantial power level change.

5.3.1 Temperature coefficient of reactivity

Figure 5.8 shows the temperature feedback coefficient evolution for the TAP reactor during the power change transient. The Fuel Temperature Coefficient ($\alpha_{T,F}$) became less negative during the first hour of the transient due to a slight spectrum hardening because the ^{135}Xe concentration peak changes the Doppler effect in the fuel salt. After turning the power back on, all three temperature coefficients of reactivity remains stable because the fuel salt composition remain almost unchanged. Overall, the isothermal temperature coefficient, $\alpha_{T,ISO}$ remains negative and strong throughout the postulated transient and fluctuates slightly within stochastic error range $\sigma_{\alpha_{T,ISO}} \pm 0.043\ pcm/K$.

5.3.2 Void coefficient of reactivity

Figure 5.9 demonstrates the void coefficient of reactivity evolution during the postulated transient. The α_V remains almost constant throughout the postulated transient. All observed changes in the void coefficient of reactivity are due to the stochastic nature of the Monte Carlo method ($\sigma_{\alpha_V} \pm 4\ pcm/\%$).

5.3.3 Reactivity control rod worth

Figure 5.10 demonstrates the control rod worth evolution during the power change transient. The control rod worth remains almost constant and sufficient to shut down the reactor throughout the postulated transient. During the first three hours of the transient, the

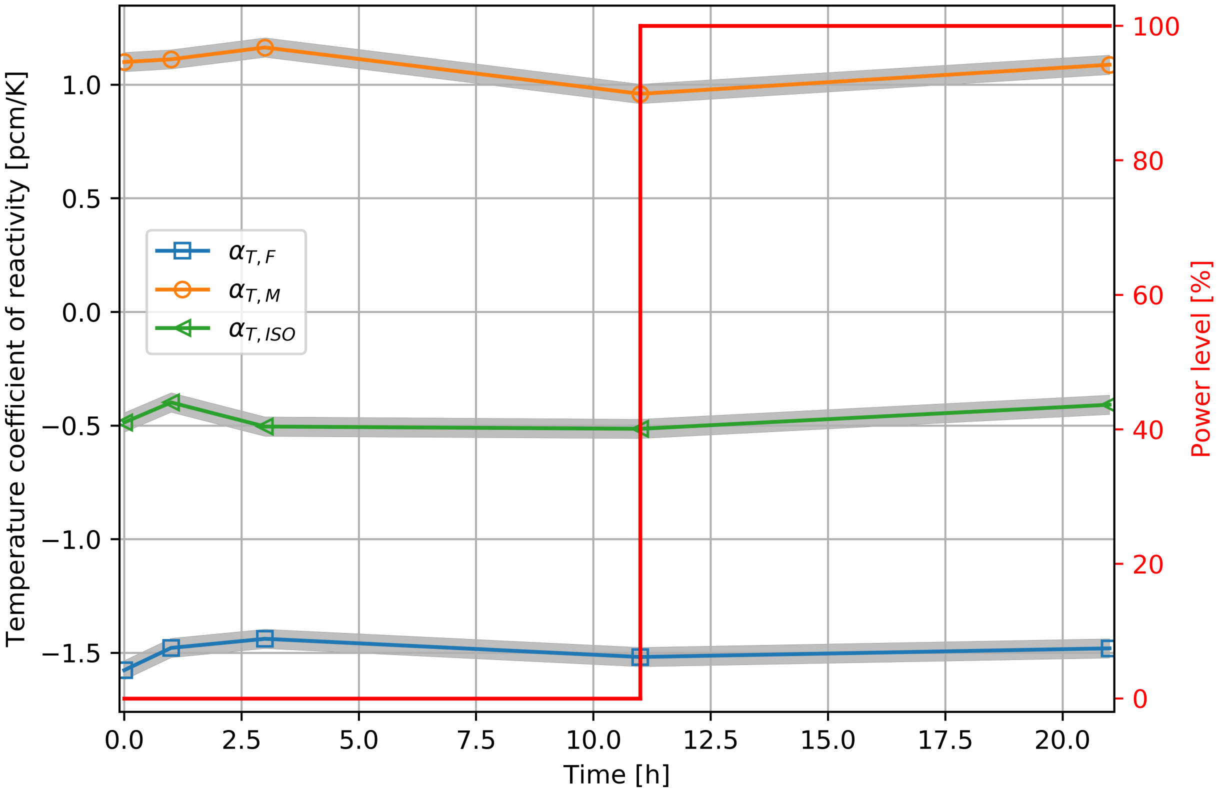

Figure 5.8: Temperature feedback coefficients during the postulated transient for the TAP reactor, 10 days before the EOL (all moderator rods inserted), the gas removal system operates with efficiency $\epsilon_{Xe} = 0.915$. The uncertainty, $\pm\sigma$, is shaded.

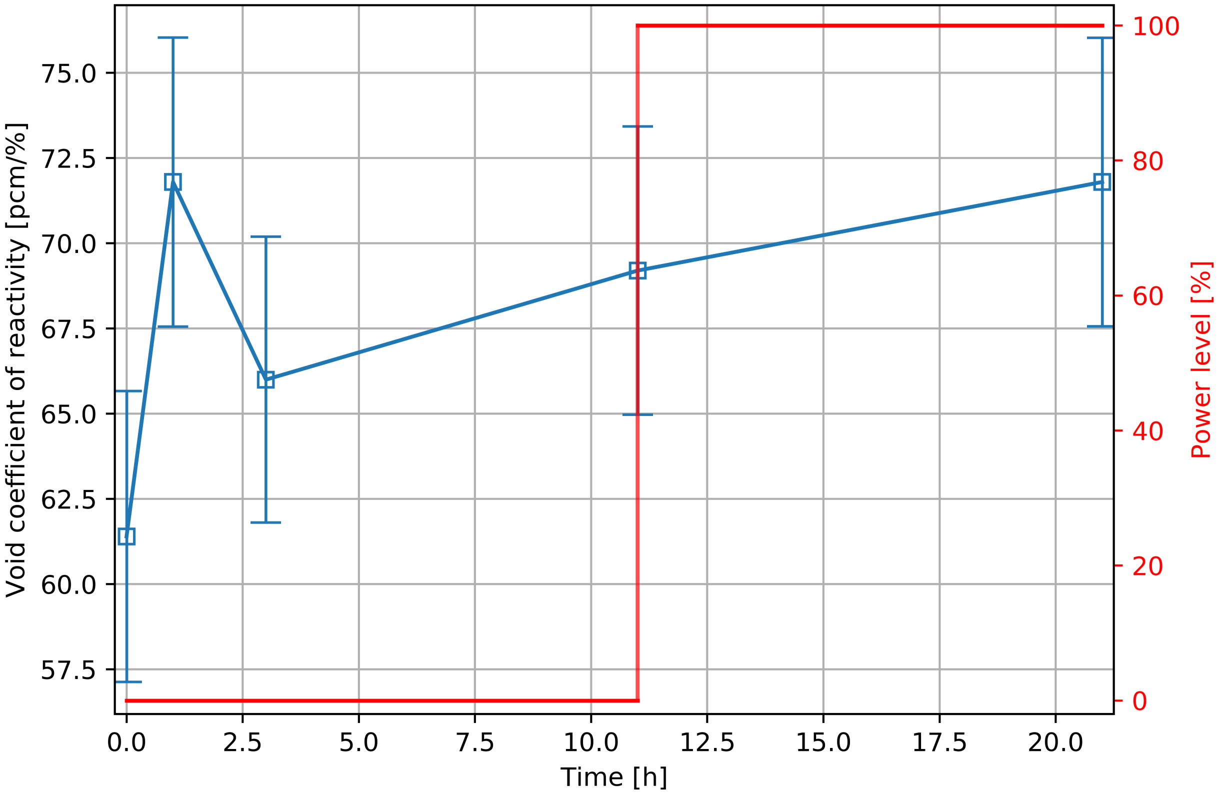

Figure 5.9: Void coefficient of reactivity as a function of time during postulated transient for the TAP reactor, 10 days before the EOL (all moderator rods inserted), the gas removal system operates with efficiency $\epsilon_{Xe} = 0.915$.

control rod worth decreases from 1998.9±8.9 *pcm* to 1988.3±8.9 *pcm* due to a slight spectrum hardening caused by ^{135}Xe concentration raise. Overall, the control rod worth changes are insignificant and lie within the stochastic error range ($\sigma_{CRW} \pm 8.9\ pcm$).

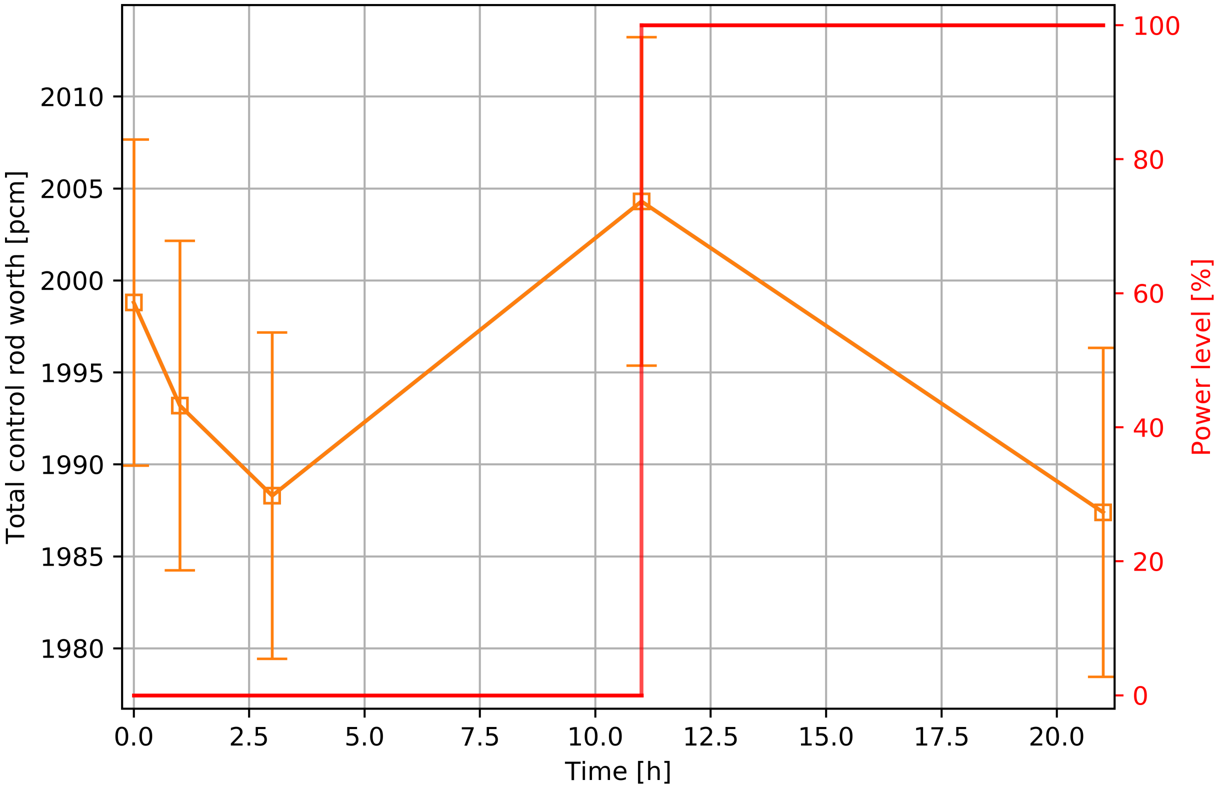

Figure 5.10: Total control rod worth as a function of time during postulated transient for the TAP reactor, 10 days before the EOL (all moderator rods inserted), the gas removal system operates with efficiency $\epsilon_{Xe} = 0.915$.

5.4 Concluding remarks

This chapter demonstrated the short-term depletion simulations for the TAP reactor with the core power level variation in the range of [0, 100%] using SaltProc v1.0 and Serpent. I considered two different noble gas removal scenarios: (1) no gas removal (e.g., $\epsilon_{Xe} = 0$), and (2) fully operational gas removal system (e.g., $\epsilon_{Xe} = 0.915$). The results in the literature reported that negative xenon poisoning effect for conventional LWRs reaches its extremum

$\Delta\rho \approx -1500$ *pcm* in approximately 11 hours after shutdown. Such a vast reactivity drop complicates the LWRs load-following.

For the case with no gas removal ($\epsilon_{Xe} = 0$), ^{135}Xe concentration peaks about 45 and 165 min after the shutdown at the BOL and EOL, respectively. The xenon concentration peaks sooner for the harder core configuration (e.g., at the BOL, SVF=0.9) because ^{135}Xe absorption cross section drops dramatically as neutron energy grows above 0.1 eV, thus, ^{135}Xe burn out faster in a harder spectrum. Thus, the harder spectrum leads to a smaller ^{135}I/^{135}Xe concentration ratio and, consequently, lower xenon concentration peak after shutdown. Without gas removal (e.g., ^{135}Xe loss after shutdown due to decay only) xenon concentration at the BOL remains almost constant ($\Delta N_{^{135}Xe} = +0.33\%$), and no effect of xenon poisoning was observed ($\Delta\rho = -10 \pm 7$ *pcm*). However, at the EOL, when all moderator rods are in and the neutron spectrum is more thermal, I observed a more significant effect of poisoning: ^{135}Xe concentration increased by 4% with corresponding negative reactivity insertion of −70 *pcm*.

For the case with very effective noble gas removal ($\epsilon_{Xe} = 0.915$), the time when ^{135}Xe concentration peaks cannot be predicted analytically, because, after shutdown, the gas removal system removes a major fraction of xenon gas at the end of each depletion step. Moreover, the ^{135}I/^{135}Xe ratio is significantly greater (e.g., between 8.66 and 11.42) than for the non-removal ($\epsilon_{Xe} = 0$) case. Thus, ^{135}I decay leads to a substantial increase in ^{135}Xe concentration right after shutdown (up to +200% at the EOL), and corresponding reactivity drop (-108 ± 5 *pcm* at the EOL). However, after the first hour, reactivity increases quickly because the gas removal system extracts most of the xenon every 1 hour (the selected SaltProc v1.0 depletion time step). The true effect of xenon poisoning for the TAP reactor with active gas removal is expected to be even less severe because the real system would remove noble gases continuously, not discretely as simulated by SaltProc (e.g., xenon would be removed with $\epsilon_{Xe} = 0.915$ every moment, not once per hour). Overall, more realistic results for load-following transients can be obtained with better time resolution. Though the ideal depletion time step should be closer to full loop time (20 seconds), such fidelity would require an enormous computation burden.

Finally, this chapter demonstrated that the TAP reactor maintains required safety margins during postulated transients. The temperature feedback coefficients, void coefficient of reactivity, and control rod worth all remain within stochastic uncertainty throughout the transient. Small elevation in total temperature coefficient and void coefficient of reactivity during the first hour after shutdown is due to the ^{135}Xe concentration raise and corresponding short-term neutron spectrum hardening. In conclusion, the TAP MSR, even without gas removal, is capable of the safe restart after reducing power from 100% to 0% even when ^{135}Xe concentration peaks. While this work has confirmed neutronics feasibility of resilience against the iodine pit, separate thermomechanical structural analysis is needed to confirm that structural materials could withstand such dramatic core power fluctuations.

Chapter 6

Tool demonstration for load-following and safety analysis: Molten Salt Breeder Reactor

The previous chapter has shown that the TAP MSR is unaffected by xenon poisoning during power variation because it has a relatively fast neutron energy spectrum. While long-term performance metrics such as fuel utilization would definitely benefit from online removal of poisonous fission products, the gas removal system is not necessary to ensure safe TAP system operation during a short-term power drop and restart transient. However, Chapter 5 clearly demonstrated a strong impact of the noble gas removal on the reactor neutronics during power adjustments. Thus, another liquid-fueled MSR design with thermal spectrum (not epithermal like in the TAP core) was considered to investigate the benefits of the online gas removal for load-following operation.

This chapter presents fuel salt depletion analysis with SaltProc during a short-term power transient to evaluate load-following capabilities of the graphite-moderated molten salt reactor design with a thermal neutron energy spectrum - Molten Salt Breeder Reactor (MSBR). The details of the MSBR design, the full-core Serpent model, and the results of long-term depletion simulation with SaltProc were described in Chapter 3. I simulated the load-following transient postulated in Section 5.2.1 using the methodology described in Chapter 5. To investigate the effect of noble gas removal efficiency on the load-following operation, I considered three various regimes of the gas removal system operation:

(a) no gas removal ($\epsilon_{Xe} = 0.0$);
(b) moderate gas removal efficiency ($\epsilon_{Xe} = 0.536$);
(c) high gas removal efficiency ($\epsilon_{Xe} = 0.915$).

I then calculated a major safety and operational parameters for all three regimes at various moments of the transient to ensure that the critical safety margins are maintained. Finally, I compared the TAP MSR and MSBR behavior during the postulated load-following transient.

6.1 Depletion analysis results

I used the methodology described previously in Chapter 5 for the MSBR full-core depletion analysis with SaltProc v1.0 with a 30-minute depletion time step to capture rapid changes in reactivity. Equation 5.6 predicted the time after shutdown when ^{135}Xe concentration peaks (t_X^{max}) in the range from 6.8h (ϵ_{Xe} = 0.0, 30 years after startup) to 7.5h (ϵ_{Xe} = 0.915, BOL). The t_X^{max} for the MSBR is longer than for the TAP reactor (2.75h) due to a much more thermal neutron energy spectrum. To be consistent throughout different gas removal regimes while investigating load-following capabilities of the MSBR, I selected a following transient (power load profile) very similar to the transient chosen in Chapter 5:

(a) operate on 100% of HFP to reach ^{135}I/^{135}Xe equilibrium (at least 3 days from the startup);
(b) instantaneous power drop from 100% to 0%;
(c) shutdown for $t_X^{max} = 7.5h$ to reach the ^{135}Xe concentration extremum;
(d) instant restart from 0% to 100% power level and operate on 100% for 5 hours.

6.1.1 Reactivity dynamics

Figures 6.1 and 6.2 show the effective multiplication factor and reactivity dynamics for the various gas removal efficiencies in the MSBR during the transient, described earlier. For the no-removal case (Figure 6.1, upper panel), the effective multiplication factor dropped after $t_X^{max} = 7.5h$ by 1457 *pcm* and 1035 *pcm* at BOL and after 15 years of full-power operation, respectively. Thus, the Equation 5.6 correctly predicted the moment when the xenon poisoning effect maximized in the no-removal case ($\epsilon_{Xe} = 0$). After the power ramp-up from 0% to 100%, the effective multiplication factor returned to its initial value in about

3 hours. Notably, maximum negative reactivity insertion due to ^{135}Xe buildup after the MSBR shutdown is very similar to the PWR (both at startup): 1457 *pcm* and 1500 *pcm* [94], respectively. Additionally, the xenon poisoning effect diminished toward the EOL because the ^{135}Xe concentration peak is more significant for the softer thermal spectrum (the MSBR spectrum becomes *harder* during operation due to plutonium and other strong neutron absorbers accumulation in the fuel salt). Finally, the effect of ^{135}Xe poisoning is almost the same after 15 and 30 years of operation because the fuel salt composition reaches its equilibrium after about 16 years of full-power operation (see Section 3.3.2).

The middle and lower plots in Figure 6.2 show reactivity change during the MSBR shutdown for 7.5 hours and following power ramp up to 100% for moderate ($\epsilon_{Xe} = 0.536$) and high ($\epsilon_{Xe} = 0.915$) removal efficiency, respectively. In contrast with no gas removal, reactivity dropped during the 30-minutes interval after shutdown by 161 *pcm* and 189 *pcm* for moderate and high removal efficiency, respectively. Afterward, the reactivity boosts by 1494 *pcm* and 2608 *pcm* for $\epsilon_{Xe} = 0.536$ and 0.915, respectively. Such reactivity change happens because the gas removal system extracted 53.6% and 91.5% of xenon mass at the end of the 30-minute depletion step. The more effective xenon removal leads to greater positive reactivity jump, as expected. Notably, the reactivity stabilizes at approximately +2500 *pcm* level about 5 hours after the shutdown because the ^{135}Xe loss due to its decay and online gas removal equalizes ^{135}Xe gain from ^{135}I decay. Overall, the online gas removal from the fuel salt even with moderate efficiency is beneficial to the core neutronics and significantly reduces the xenon poisoning effect (-161 ± 10 *pcm* instead of -1494 ± 10 *pcm*). Moreover, the very high removal efficiency ($\epsilon_{Xe} = 0.915$) is unnecessary to significantly reduce the effect of xenon poisoning and enable the load-following capability of the MSBR.

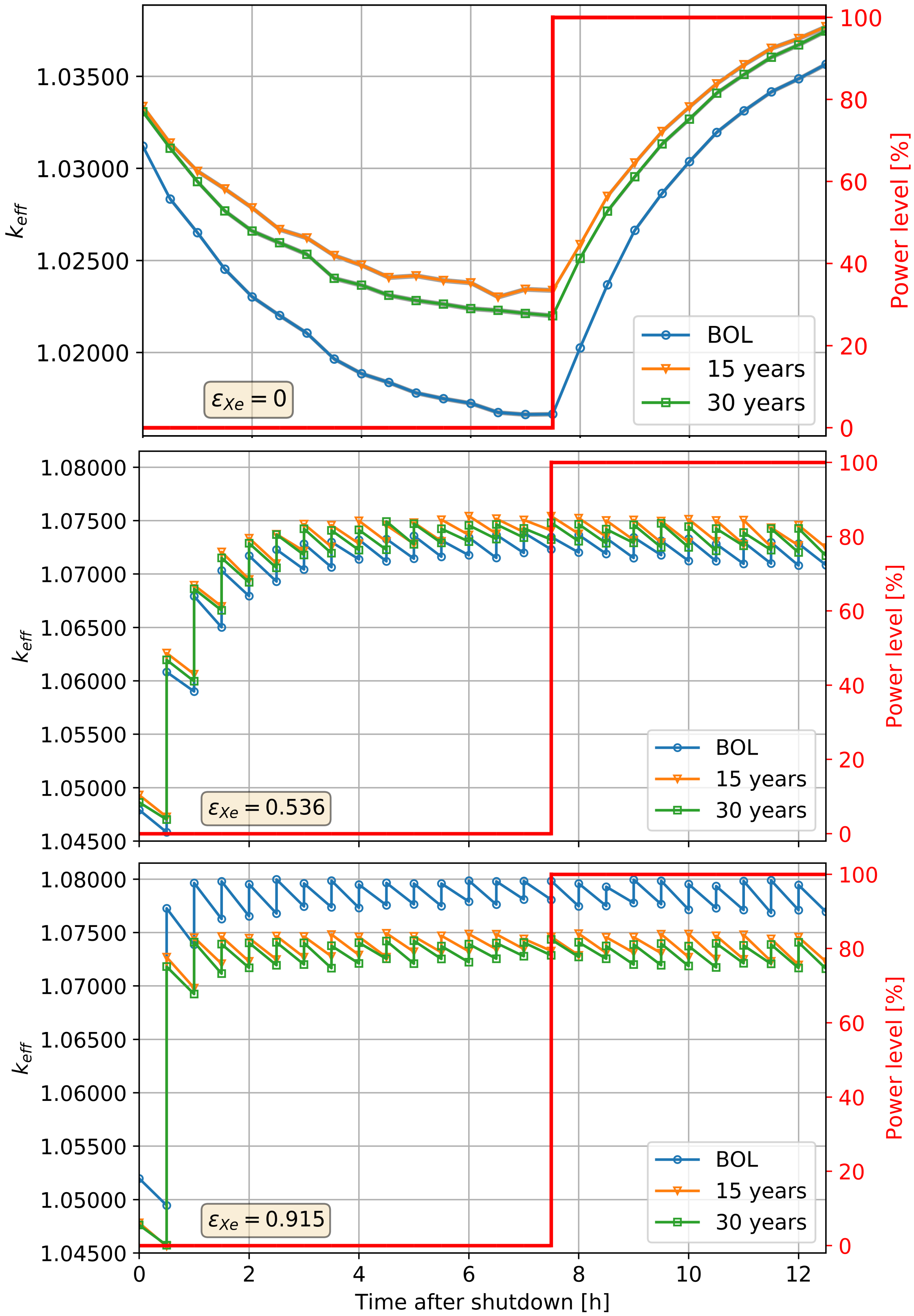

Figure 6.1: SaltProc-calculated evolution of the effective multiplication factor during the postulated load-following transient for various regimes of the gas removal system operation. The uncertainty ($\pm\sigma = 10\ pcm$) is shaded.

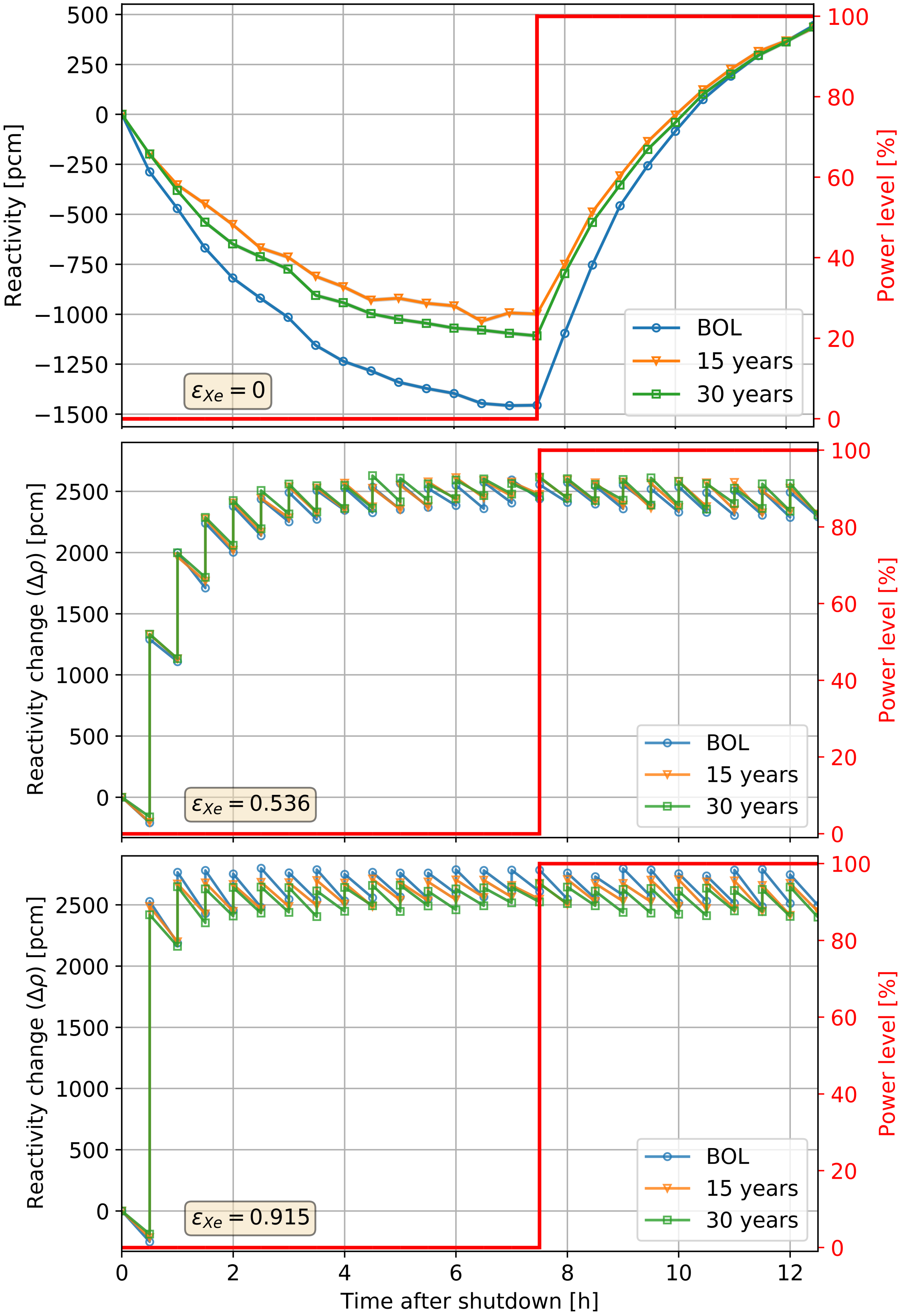

Figure 6.2: SaltProc-calculated evolution of the reactivity during the postulated load-following transient for various regimes of the gas removal system operation. The uncertainty ($\pm\sigma = 10\ pcm$) is shaded.

6.1.2 Fuel salt composition evolution

Figure 6.3 shows ^{135}Xe and ^{135}I mass dynamics evolution during the postulated transient for various gas removal efficiencies. The ^{135}I/^{135}Xe concentration ratio at the beginning of the transient for the no-removal case is 2.45 and 2.03 at the BOL and after 30 years of full-power operation, respectively. Because the ^{135}I/^{135}Xe concentration ratio is greater at startup, the ^{135}Xe concentration peak is 11% higher than at the EOL, which is consistent with the TAP MSR results. However, a larger ^{135}Xe concentration does not necessarily worsen the xenon poisoning effect (Figure 6.2) because the spectrum hardens toward EOL and the ^{135}Xe absorption cross section slumps with higher neutron energy (see Figure 5.7).

For the high gas removal efficiency regime, the ^{135}I/^{135}Xe concentration ratio is 2.47 and 2.08 at the BOL and after 30 years of full-power operation, respectively. For the BOL and a 30-year case, the ^{135}Xe concentration peaked only by 8% at the end of a first 30-minute depletion step, which caused a 189-*pcm* negative reactivity insertion. Afterward, the concentration of ^{135}Xe dropped quickly because the gas removal system extracted most of the fission gas. The ^{135}Xe concentration in the fuel salt before the shutdown is approximately 7 times greater than after the power turned back on, which caused significant reactivity growth by ≈ 2550 *pcm*. Surprisingly, the removal of 12 g of ^{135}Xe from $t = 30min$ to $t = 60min$ caused an impressive 2600-*pcm* positive reactivity insertion (217 pcm/g^{135}Xe reactivity worth).

Such large fluctuations in the ^{135}Xe concentration are observed due to the batch-wise nature of SaltProc simulations (e.g., the fraction of target poison is being removed discretely at the end of each depletion step). Realistically, the gas removal system would extract gas from the fuel salt continuously, which would result in a much smoother change in the concentration and, accordingly, in the reactivity. Notably, for both BOL and EOL, the ^{135}Xe mass stabilized at 1 g in about 3-4 hours after the shutdown and then inclined slowly (60 $mg/EFPH$) after power ramp-up from 0 to 100%. That is, when the reactor returns to a full-power level, the ^{135}Xe concentration during a few days will be significantly lower

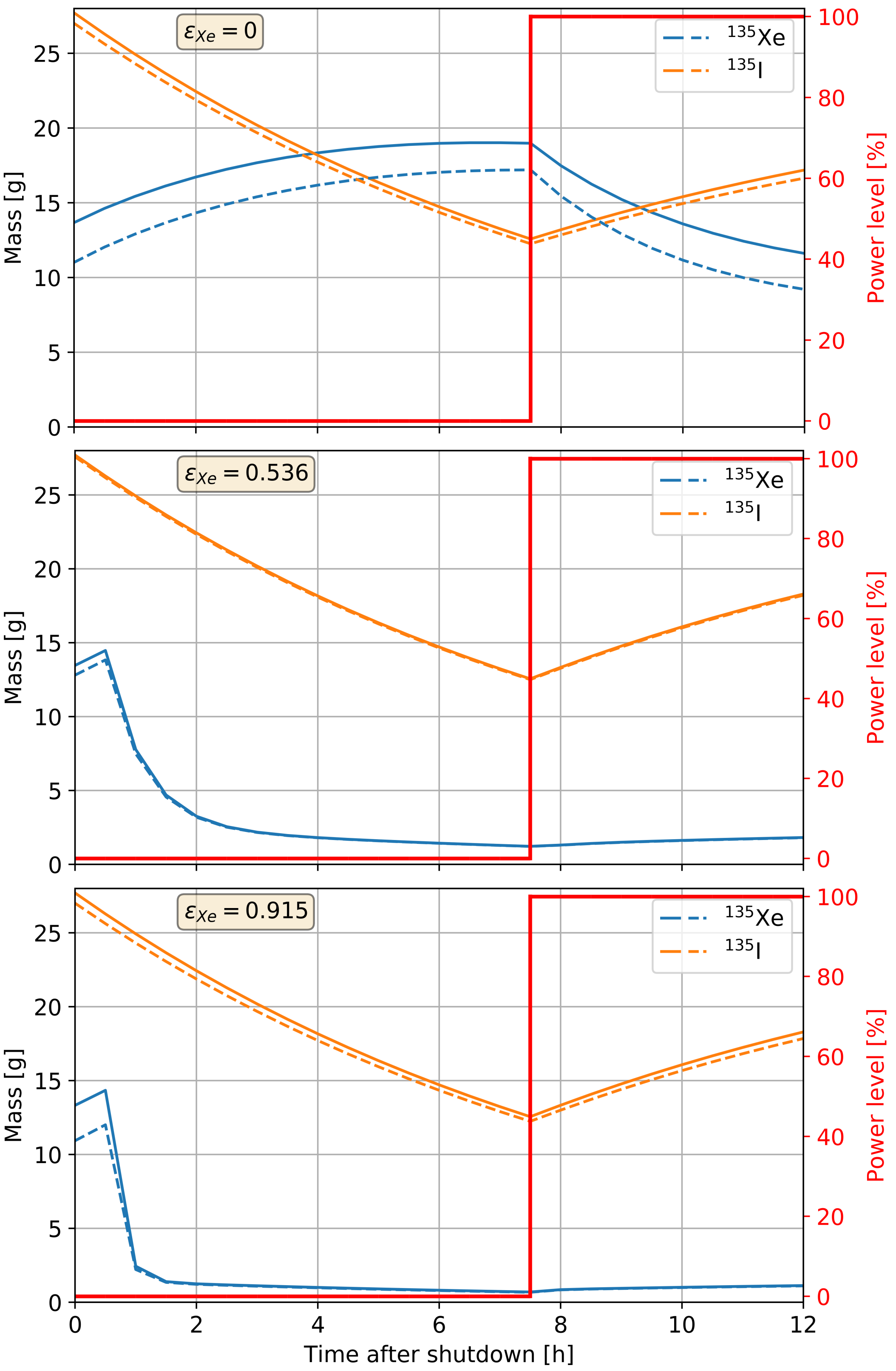

Figure 6.3: Comparison of ^{135}Xe and ^{135}I isotopic content at the BOL (dashed line) and after 30 years of operation (solid line) for various gas removal regimes. Uncertainty of the predicted mass will be estimated and discussed in Chapter 7.

than before the load-following transient. Thus, fewer thermal neutrons will be parasitically absorbed in the fission gas. As a result, long-term fuel cycle performance metrics such as fuel utilization and core lifetime would benefit enormously from a very low ^{135}Xe concentration in the core after the postulated transient. In other words, the transient cleans up the fuel salt, but more analyses are required to evaluate all benefits of this finding.

In the case of moderate gas removal efficiency, the fission product concentration changes very similarly to a high removal efficiency case. The ^{135}I/^{135}Xe concentration ratio is 2.15 and 2.06 at the BOL and after 30 years of full-power operation, respectively, and caused a 7.5% hike in ^{135}Xe concentration. Surprisingly, a significantly lower gas removal efficiency (ϵ_{Xe} = 0.536 instead of 0.915) provided comparable benefits to the core neutronics during the postulated load-following transient. Similarly to the ϵ_{Xe} = 0.915 case, the ^{135}Xe mass stabilized at 1.5 g about 5 hours after the shutdown and then increased slowly (165 $mg/EFPH$) after power ramp-up from 0 to 100%. In conclusion, a simpler and cheaper gas removal system with extraction efficiency ϵ_{Xe} = 0.536 is sufficient to suppress the xenon poisoning effect to an acceptable level (-161 pcm) and improve the load-following capability of the MSBR.

6.1.3 Neutron spectrum

Figure 6.4 shows that the MSBR spectrum after 30 years of operation (solid line) is harder than at the startup (dashed line). Compared with the MSBR, the TAP MSR spectrum is significantly harder even when all moderator rods are inserted to the core. Notably, the MSBR spectrum has a clear peak in the thermal energy region, but flat neutron energy dependence in intermediate and fast energy region, which is quite common for thermal reactors. In contrast, the TAP core spectrum at the EOL has a high peak in the fast and lower peak in the thermal energy region, which is typical for epithermal/intermediate reactors. This is the main reason why for the postulated load-following transient, I observed a significant xenon poisoning effect in the MSBR and negligible xenon impact in the TAP

MSR (see Chapter 5).

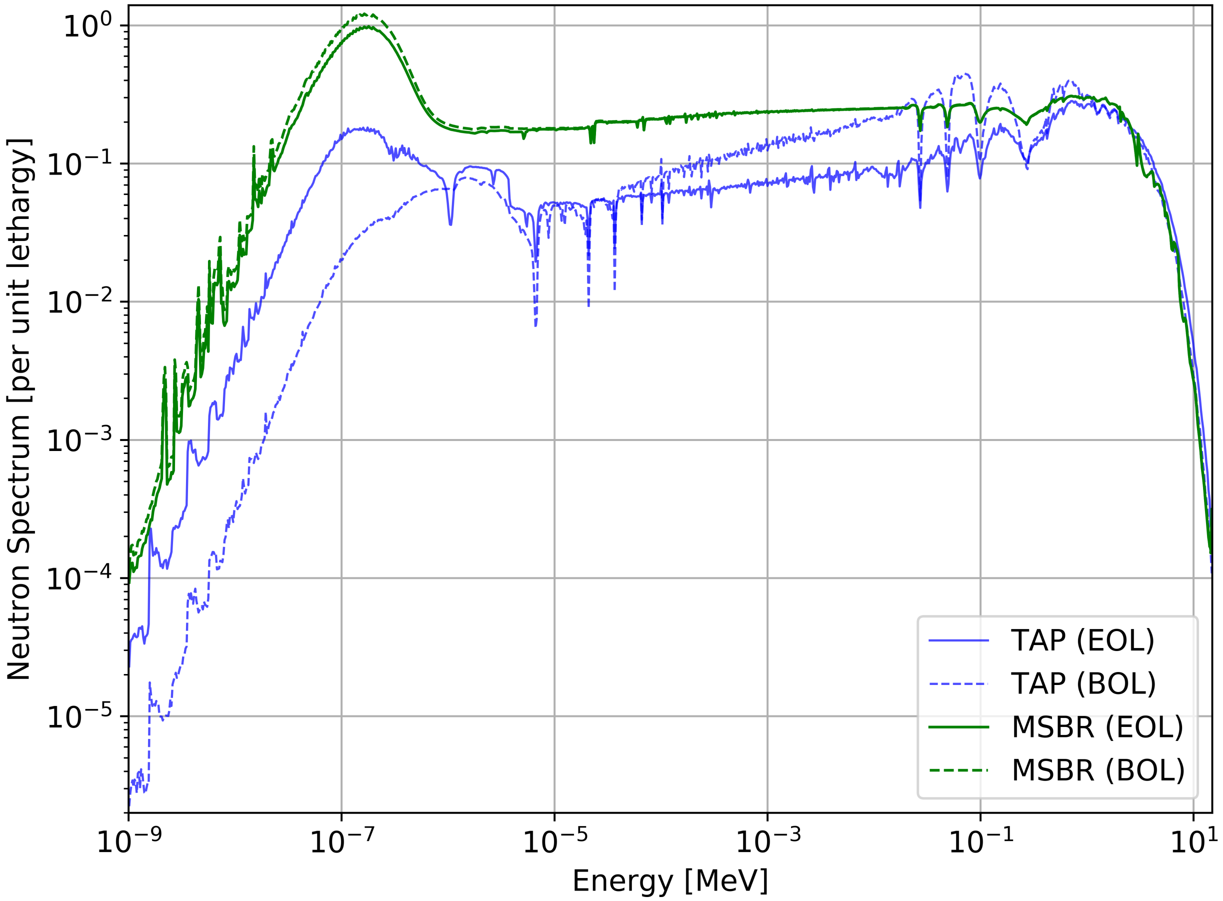

Figure 6.4: Neutron spectra normalized by lethargy for the MSBR and TAP at various moments during operation. The neutron flux uncertainties σ_Φ are 0.6% and 0.18% for the TAP reactor and MSBR, respectively.

Any graphite-moderated liquid-fueled MSR conceptual design[1] would potentially demonstrate similar benefits from an online noble gas removal from the fuel salt.

6.2 Safety and operational parameters

The significant change of strong absorber concentrations in the fuel slightly shifts the core spectrum, potentially impacting the reactor's safety. Since rapid changes in the fuel salt

---

[1] Integral Molten Salt Reactor (IMSR) from Terrestial Energy [60], Molten Salt Demonstration Reactor (MSDR) from Oak Ridge National Laboratory [10], Liquid fluoride thorium reactor (LFTR) from Flibe energy [99], etc.

composition cannot be allowed to compromise critical safety margins, I calculated major safety and operational parameters at various moments throughout the postulated transient using approaches from Sections 4.4 and 5.3. The total temperature coefficient of reactivity (α_{ISO}) must remain negative, and the total control rod worth (CRW) must be sufficient to trip the reactor throughout the postulated transient. Ideally, we want major safety and operational parameters to stay almost constant because the changes in those parameters would require fast response from the reactor control systems (i.e., control rod jerk in response to a CRW change).

6.2.1 Temperature coefficient of reactivity

Figure 6.5 shows the temperature feedback coefficient dynamics for the MSBR during the transient for various gas removal efficiencies (ϵ_{Xe} = 0.536 and 0.915). The Fuel Temperature Coefficient ($\alpha_{T,F}$) becomes less strong at the beginning of the transient for all cases. The reason for this is a slight spectrum hardening due to the ^{135}Xe concentration peak that changed the Doppler broadening of resonances. After that, the magnitude of $\alpha_{T,F}$ slowly increased due to a steady incline in the ^{135}Xe concentration.

The isothermal temperature coefficient, α_{ISO}, is -0.36 ± 0.09 pcm/K at the beginning and remains stable during the first 30 minutes of the transient for the moderate removal efficiency case. Then, as the gas removal system reduces ^{135}Xe concentration in the core, α_{ISO} becomes even more negative: -1.52 ± 0.09 pcm/K when the ^{135}Xe mass stabilized at 1.5 g in about 5 hours after the shutdown. After power ramp-up from 0% to 100%, α_{ISO} also remains stable since the ^{135}Xe mass increasing very slowly. On the whole, another exciting benefit from the online gas removal is improved passive safety (more powerful temperature feedback coefficient) throughout and, possibly, a few days after the postulated transient due to low concentration of the ^{135}Xe in the fuel salt.

For the high gas removal efficiency regime (ϵ_{Xe} = 0.915), the isothermal temperature coefficient worsens from -0.54 ± 0.09 pcm/K to approximately -0.22 ± 0.09 pcm/K during

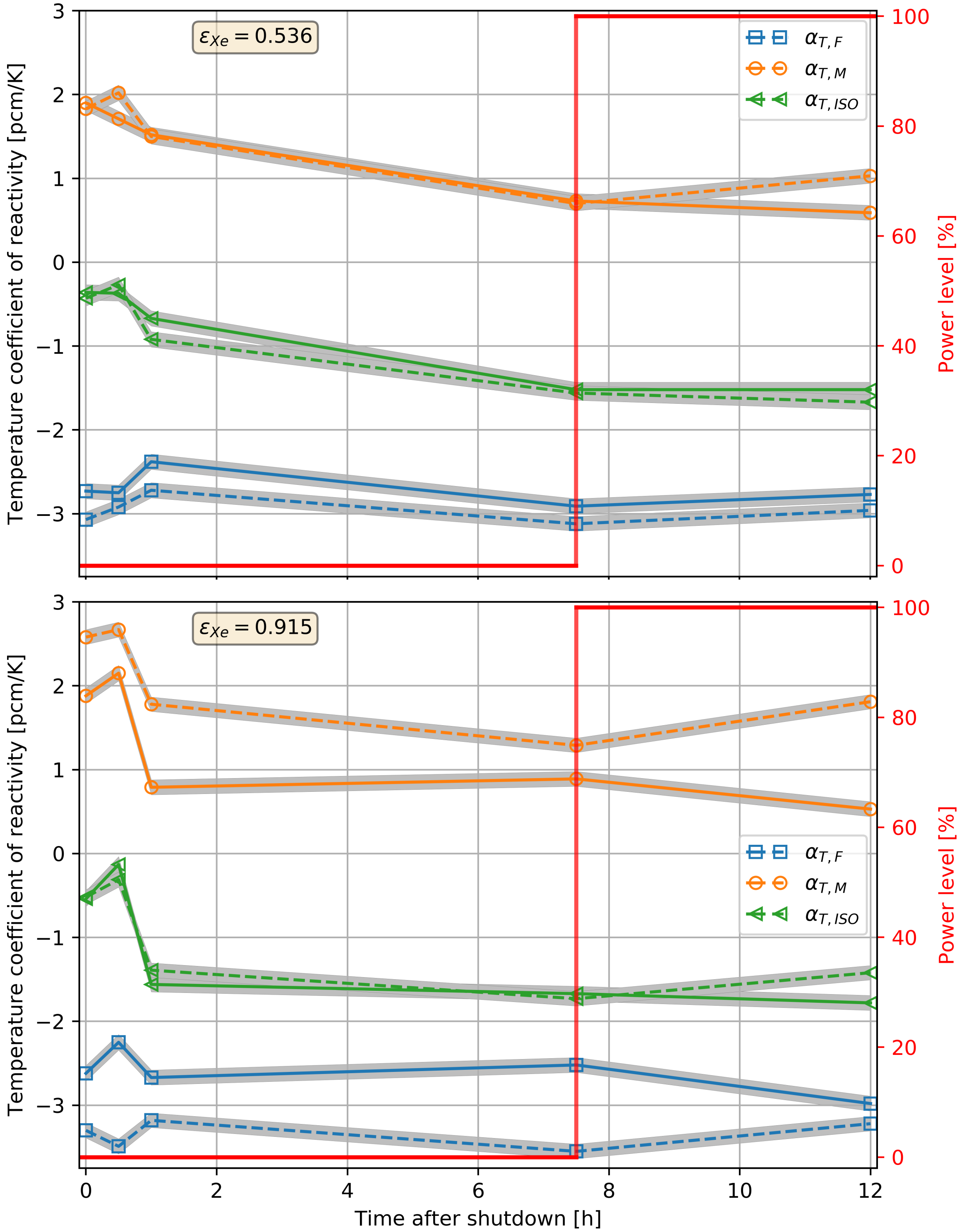

Figure 6.5: Temperature feedback coefficients during the postulated transient for the MSBR operating with moderate ($\epsilon_{Xe} = 0.536$, upper) and high ($\epsilon_{Xe} = 0.915$, lower) gas removal efficiency at the BOL (dashed line) and after 30 years of operation (solid line). The uncertainty, $\pm\sigma$, is shaded.

first the 30 minutes after shutdown. Afterward, however, once the gas removal system extracted a significant fraction of the ^{135}Xe from the fuel salt, α_{ISO} recovered, becoming significantly more negative (−1.39 and −1.56 pcm/K at the BOL and after 30 years of operation, respectively) due to the spectrum softening. In brief, *the temperature feedback in the MSBR becomes stronger when neutron poisons concentration in the fuel decreases.* As a result, flattening the ^{135}Xe concentration curve improves the MSBR passive safety.

Overall, the combination of fuel and moderator thermal feedback coefficients, α_{ISO}, remains negative throughout the postulated transient. Moreover, a simpler and cheaper gas removal system with extraction efficiency $\epsilon_{Xe} = 0.536$ provided more predictable thermal feedback coefficient dynamics throughout the transient due to a more gradual change in the ^{135}Xe concentration.

6.2.2 Void coefficient of reactivity

Figure 6.6 demonstrates the void coefficient of reactivity evolution during the postulated transient. In contrast with the TAP MSR, the void coefficient of reactivity after 30 years of full-power operation is substantially higher than at the startup for both gas removal regimes. The reason for this is the hardening of the MSBR spectrum toward EOL, which is the opposite of the TAP MSR spectrum evolution. Thus, an unexpected void insertion due, for example, to a gas separation system failure in the MSBR would have more severe consequences for the EOL.

For the high gas removal efficiency, α_V fluctuates during the postulated transient between 42 and 61 pcm/void% at the BOL and between 87 and 102 pcm/void% after 30 years of operation. The ^{135}Xe concentration spike caused corresponding α_V drop due to the short-term spectrum hardening. Then, α_V quickly recovers to its initial value. Similarly to the temperature feedback coefficient, the moderate gas removal efficiency provided more predictable α_V dynamics throughout the transient. Additionally, a small α_V fluctuation during the transient at the EOL for the case with $\epsilon_{Xe} = 0.536$ ($\Delta\alpha_V \approx 25$ pcm/void%) would simplify the

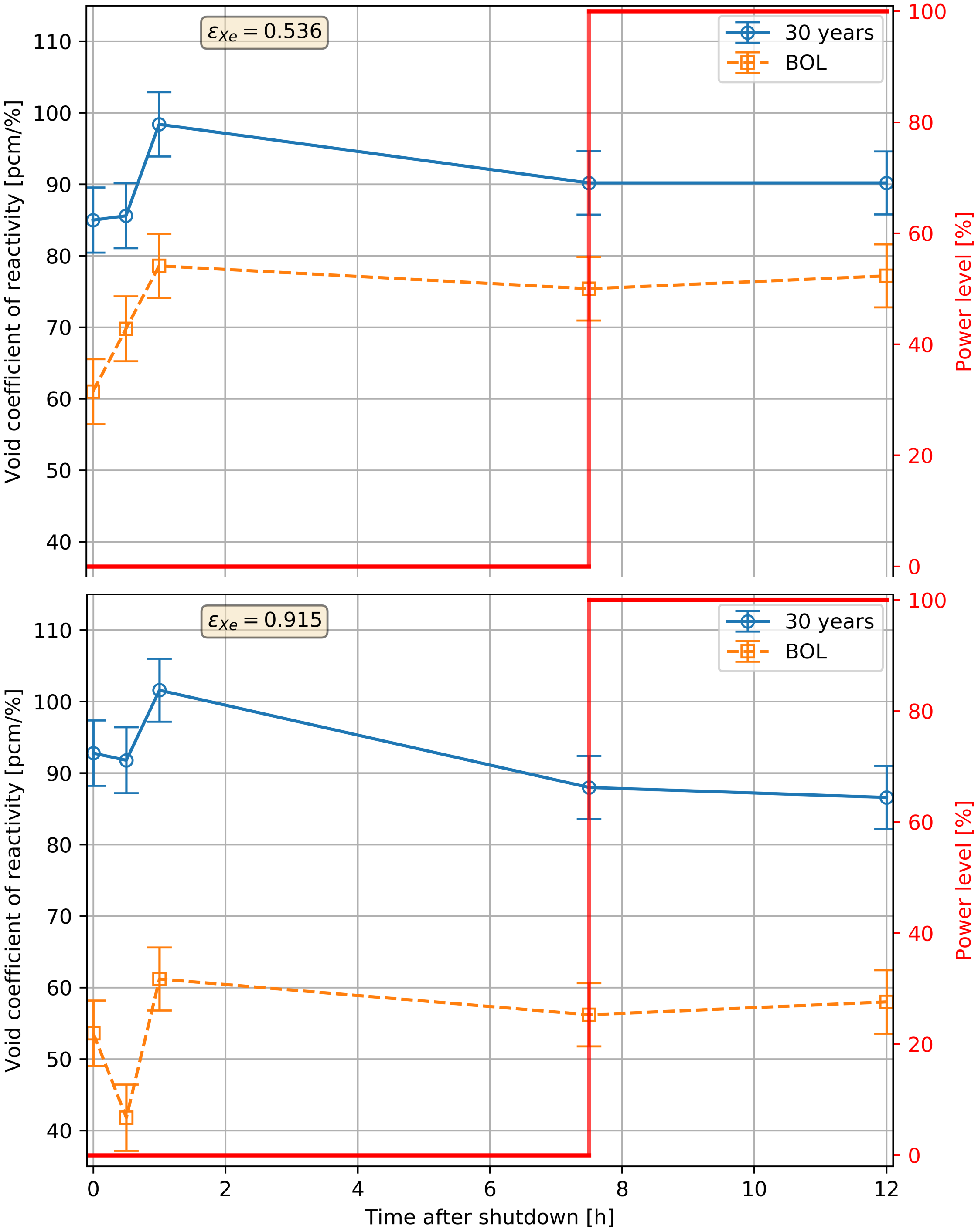

Figure 6.6: Void coefficient of reactivity as a function of time during postulated transient for the MSBR operating with moderate ($\epsilon_{Xe} = 0.536$, upper) and high ($\epsilon_{Xe} = 0.915$, lower) gas removal efficiency at the BOL (dashed line) and after 30 years of operation (solid line).

gas separator backup safety mechanism. Overall, all observed changes in the void coefficient of reactivity throughout the load-following transient for all cases are within the 3-σ range ($\sigma_{\alpha_V} \pm 5$ *pcm*/%). These observations should be taken into account in the MSBR accident analysis and safety justification.

6.2.3 Reactivity control rod worth

Figure 6.7 shows the control rod worth evolution during the postulated transient. For the high gas removal efficiency regime after 30 years of full-power operation, the control rod worth dropped by 46 ± 9 *pcm* during the first 30 minutes after the shutdown. This happens due to a short-term spectrum hardening related to the ^{135}Xe concentration peak. In the next 30 minutes, the CRW recovers to its initial value and keeps increasing throughout the transient because the gas removal system steadily reduces the ^{135}Xe concentration in the core. Notably, the control rod worth is greater at the BOL because the absorption cross section of ^{10}B (used as an absorber in the control rods) declines rapidly with energy. Overall, the control rod worth benefits from the MSBR spectrum softening toward EOL.

For the moderate gas separation efficiency regime, the control rod worth remains almost constant during the first hour after shutdown. Afterward, the CRW increased by 4% due to the spectrum softening caused by the increased ^{135}Xe concentration. As for other safety parameters, the control rod worth also benefits from a less effective gas removal system due to smother xenon concentration dynamics and a more predictable neutron spectrum shift.

Unfortunately, the total control rod worth is insufficient to shut down the reactor throughout the postulated transient for both medium and high removal efficiency ($\epsilon_{Xe} = 0.536$ and $\epsilon_{Xe} = 0.915$). The reactivity change during the transient is up to 2600 *pcm*, while the total control rod worth is only about 1250 – 1425 *pcm*. The MSBR was designed with only two graphite and two boron-carbide rods located in the center of the core (see Figure 3.1) for operative reactivity control and relied heavily on fissile feed adjustment as a primary reactivity control mechanism. However, the fissile feed cannot be adjusted quickly, and nuclear

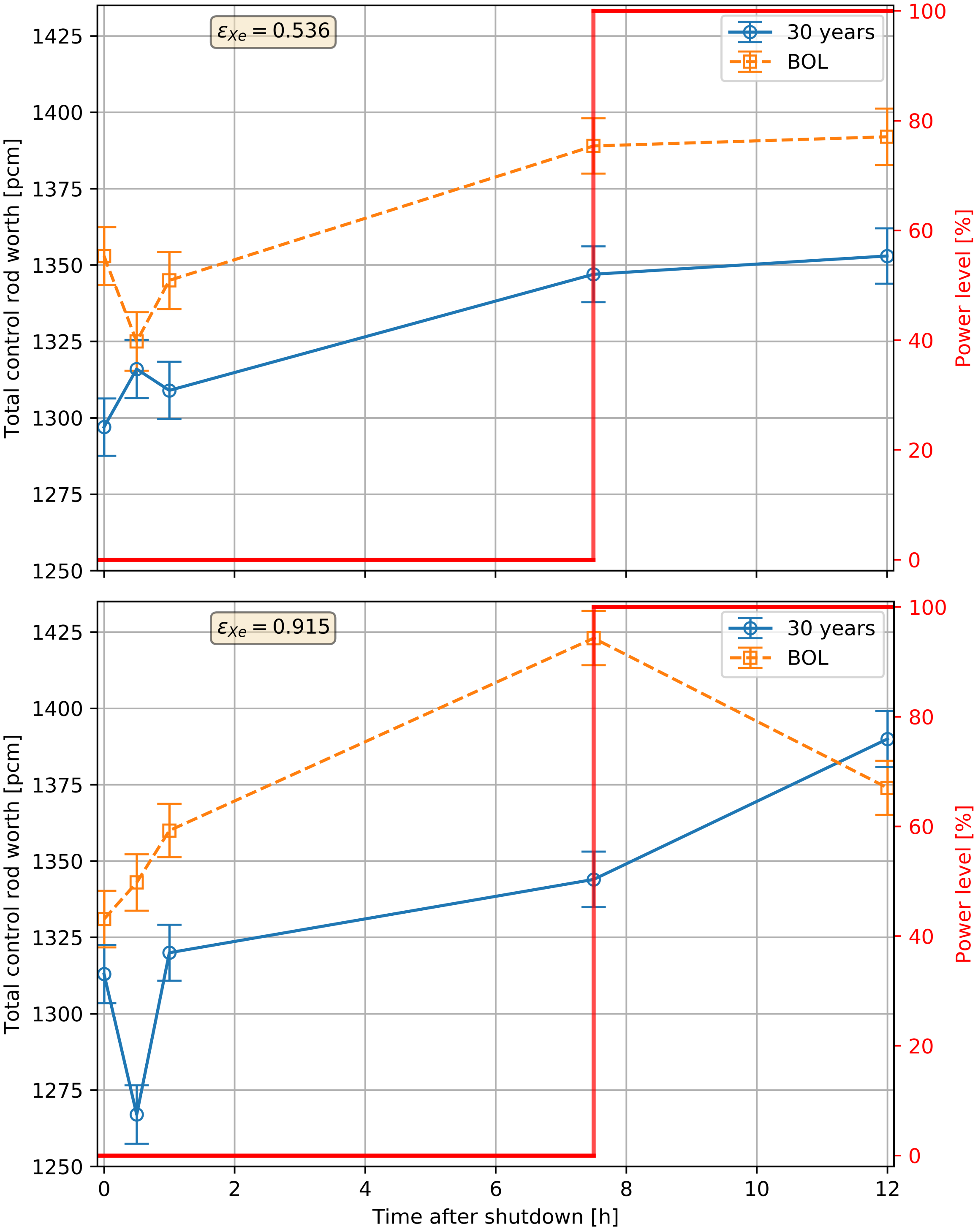

Figure 6.7: Total control rod worth as a function of time during postulated transient for the MSBR operating with moderate ($\epsilon_{Xe} = 0.536$, upper) and high ($\epsilon_{Xe} = 0.915$, lower) gas removal efficiency at the BOL (dashed line) and after 30 years of operation (solid line).

regulations require control rods to have sufficient worth to shut down the reactor safely at any time. Therefore, the control rod design in the MSBR must be reexamined to ensure the total control rod worth of at least 3000 *pcm* to ensure safety during the transient with rapid power change.

6.3 Concluding remarks

This chapter demonstrated SaltProc v1.0 capabilities to simulate the short-term depletion with the power variation from 0% to 100% for the MSBR. I applied methodology from Chapter 5 to investigate the xenon poisoning effect in the MSBR for three various gas removal system regimes: (1) no gas removal, (2) moderate gas removal efficiency, and (3) high gas removal efficiency.

When the gas removal system is inactive, the ^{135}Xe concentration peaked in about 7.5 hours after shutdown, which caused the reactivity drop by 1457 and 1035 *pcm* for the startup and equilibrium fuel salt composition. Such a negative effect of the xenon poisoning is consistent with other thermal reactor designs (i.e., -1500 *pcm* for PWR [94]). In contrast with results for the TAP MSR in Chapter 5, the MSBR demonstrated a significant negative impact of the ^{135}Xe concentration spike on the core neutronics after shutdown. The reason for that is significantly greater initial ^{135}I/^{135}Xe concentration ratio: 2.45 and 1.0 for the MSBR and TAP reactor at the BOL, respectively. Thus, the ^{135}Xe peak is significantly higher for the MSBR than for the TAP reactor: +56% and +0.33%, respectively. Finally, the ^{135}Xe parasitically absorbs substantially more neutrons in the thermal (MSBR) than in the epithermal (TAP MSR) neutron spectrum, which amplifies the xenon poisoning effect when the spectrum softens. In contrast with the spectrum thermalization toward EOL in the TAP reactor, in the MSBR, the neutron spectrum hardens toward EOL due to plutonium and other strong absorbers accumulation in the fuel salt. Thus, for the MSBR, the xenon poisoning effect becomes less severe toward EOL.

The online gas removal in the MSBR demonstrated an impressive positive impact on the core neutronics. The gas removal system operation almost eliminated the effect of xenon poisoning by removing the vast majority of ^{135}Xe during the first hour after the shutdown. During the first 30-minute interval, the reactivity dropped by 161 and 189 *pcm* for moderate and high removal efficiency, respectively. Afterward, the reactivity raised by 2700 *pcm* for both efficiencies in a few hours because the ^{135}Xe inventory fell from 14 to 1-2 g. Indeed, the ^{135}Xe loss due to decay and active gas removal significantly overcame its gain from the ^{135}I decay only (no fission happens; thus, no new ^{135}I is produced). Notably, the amplitude of the reactivity swing after shutdown is more significant for the BOL when the xenon reactivity worth is greater due to the softer neutron spectrum. Finally, significantly lower gas removal efficiency (ϵ_{Xe} = 0.536 instead of 0.915) provided comparable benefits to the MSBR core neutronics during the postulated load-following transient.

Finally, this chapter demonstrated that the MSBR maintains necessary safety margins throughout the postulated load-following transient. Thus, the temperature coefficient of reactivity and the total control rod worth worsen slightly during the first 30 minutes of the transient when the ^{135}Xe concentration peaked, causing corresponding neutron spectrum hardening. After that, the fast ^{135}Xe concentration decline improved all safety and operational parameters among the cases. Unfortunately, the reactivity worth of two control rods made of boron carbide (B_4C) is insufficient to compensate for huge reactivity change after the shutdown. Even though the total control worth rises throughout the transient, the reactivity system design is unfeasible for load-following and must be redesigned.

In conclusion, the xenon poisoning impact on the core neutronics is much stronger in the MSBR than in the TAP MSR. Thus, the MSBR without gas removal is incapable of flexible restart after reducing power from 100% to 0%. However, online gas removal, even with moderate separation efficiency, helps eliminate the iodine pit problem and enable the load-following capability of the MSBR without compromising its safety. Another benefit from the online gas removal is a stronger thermal feedback.

The work determined that the gas removal system should have a smart control coupled with reactivity control and power regulation systems. Such a system must boost the separation efficiency right before and during the first few minutes after power drop to flatten the ^{135}Xe peak. Then, the control system should reduce the removal efficiency to avoid a sizeable positive reactivity insertion due to a fast ^{135}Xe concentration drop. Finally, a more detailed study of power-changing transients must be performed using SaltProc v1.0 with better time resolution (i.e., a 1-min interval) to understand better how to adjust the gas removal efficiency during power adjustments.

Chapter 7

Error propagation in depletion calculations

In the Monte Carlo (MC) depletion analyses, the uncertainties on predicted isotopic composition are caused by two primary factors: stochastic uncertainty in the computed flux and uncertainty in the nuclear data (e.g., cross sections, fission yields, decay constants). In MC reactor physics software, the stochastic uncertainty of a single burnup step is superposed with errors, propagated throughout calculations from previous steps. Over time, these errors accumulate, and cumulative error in the predicted number density might be significant for the lifetime-long fuel depletion calculations.

Takeda *et al.* [102] first proposed a method to evaluate the uncertainty of the number density in the MC simulations applying the sensitivities of the burnup matrix to number densities [102]. Takeda and colleagues propagated covariances of the cross sections and obtained the number density uncertainty due to the cross section error of about 4% for major heavy isotopes (^{235}U, ^{239}Pu, ^{241}Pu) after 400-day MC burnup calculations for a homogeneous model of an arbitrary fast reactor. Notably, the uncertainty due to the stochastic error in MCNP was much lower: about 0.03% for ^{241}Pu, 0.02% for ^{235}U, and $<$ 0.004% for ^{238}U. The Takeda model showed that the statistical error contribution to the total error in number densities of major heavy isotopes and FPs is less than 1% [102]. Finally, a substantial neutron population (N) increase can theoretically reduce the stochastic error to zero, but it is enormously expensive due to slow convergence ($O(\sqrt{N})$) of the MC method.

Garcia-Herranz *et al.* [44] used MCNP and in-house code ACAB to analyze the uncertainties on the nuclide inventory based on the random sampling technique for spherical fuel element (“pebble”) with coated PuO_2 particles. The random sampling or “brute force” method is the multi-step sequence of neutronics and depletion calculations that could be considered as a single process with an input (nuclear data) and output (final number densities). The authors performed a simultaneous random sampling of all the cross sections[1] 1000 times and obtained the distributions of the isotopic inventory. The relative error of the final number density for the 1200-day fuel cycle (800 MW_{th}d/kgHM burnup) due to the nuclear data uncertainty was reported in a range from 7% (for ^{244}Pu) to 46% (for ^{242}Pu) and found to be independent of a number of neutron histories. In contrast, relative error of the final number density due to stochastic error for reasonably large neutron history was less than 0.15% [44]. Thus, random sampling Monte Carlo results by Garcia-Herranz *et al.* agreed with Takeda's statement that nuclear data is the major source of uncertainty; the stochastic error contribution to the total nuclear density error is negligibly small ($< 1\%$) and reduces slowly if the number of neutron histories increases.

In a similar vein, Radaideh *et al.* used SCALE 6.2 with the Sampler module [82] to quantify the uncertainty in nuclide concentration in a BWR 10×10 assembly due to uncertainties in neutron cross sections, fission yields, and decay data [80]. Radaideh and colleagues used a 56-group covariance library in deterministic SCALE/TRITON transport calculations and, hence, introduced no stochastic error in the flux calculations. That work used 500 random samples in a 1174-day TRITON depletion calculation and reported number density uncertainty between 0.14% for ^{238}U and 6.56% for ^{238}Pu [79]. This approach benefits from the Sampler module available in the SCALE 6.2 package and can be used by all SCALE users around the globe.

All listed research efforts studied simplified, pin-cell, or single-assembly models of conventional LWRs and considered nuclear data uncertainty for the following elements: hydrogen, oxygen, zirconium, uranium, and plutonium. The nuclear data for these elements have relatively low uncertainty because they were measured many times for myriad weapon and

---

[1] Authors assumed that the influence of uncertainties in decay constants, fission yields, and other input parameters is negligible.

non-weapon applications. However, the TAP MSR and many other MSR designs rely on other elements such as lithium and fluorine, which have relatively large cross section covariances. The effect of ^{6}Li, ^{7}Li, and ^{19}F nuclear data uncertainty on the final isotopic composition uncertainty in molten fuel salt was never studied before. This chapter seeks to estimate the uncertainties on predicted isotopic compositions for the TAP MSR during lifetime-long depletion simulations.

In this chapter, the uncertainty in the fuel salt composition is investigated for two different sources of uncertainty separately. The uncertainty in the nuclide inventory due to the transport problem statistical error is evaluated by repeating multiple Serpent Monte Carlo code depletion simulations. By changing the code's initial random number seed, the output produced by 1000 runs is used to investigate the statistical error in the multiplication factor (k_{eff}) and fuel salt isotopic inventory. The uncertainty in depleted fuel salt composition due to nuclear data uncertainties - a major part of depletion calculation uncertainty - is determined using the SCALE/Sampler sequence in conjunction with NEWT (2D, Discrete Ordinates code) [82]. Uncertainties in nuclear data (e.g., neutron cross sections, fission yields, decay constants) are propagated into the response of interest (fuel salt isotopic composition) by generating a large number of samples with perturbed nuclear data. The two approaches are demonstrated using the TAP reactor model.

The following assumptions and simplifications are made for both approaches:

(a) Fuel salt is well mixed and can be treated as a single homogeneous material.
(b) Uncertainties in input parameters (size, density, enrichment, power) are ignored.
(c) Only one moderator rod configuration (startup, 1388 rods inserted) is considered.
(d) Online fission product removal and fresh fuel injection are ignored.

In a future, when SCALE 6.3b4 with online reprocessing capability [89, 19] will be available for the scientific community, the current work's approach might be implemented to quantify uncertainty in the depletion calculations with continuous online fuel salt treatment and processing.

7.1 Stochastic uncertainty in the isotopic inventory

This section presents a general approach to uncertainty propagation throughout the depletion calculations when using Monte Carlo burnup software. Only uncertainties due to the statistical nature of Monte Carlo neutron transport calculations were considered herein.

7.1.1 Methodology of estimating uncertainty due to the statistical error in Monte Carlo

The change in the isotopic composition with burnup causes the neutron flux change. Thus, a sequence of coupled transport problems and depletion calculations should be done to predict the isotopic inventory accurately. In such coupled calculations, the depletion time is divided into a few time intervals. A transport calculation is carried out for each time interval, and the evaluated reaction rates are then used to solve the system of Bateman equations to obtain the fuel isotopic composition at the end of the time interval. The goal is not only to calculate the isotopic vector at the end of each depletion step but also to estimate the stochastic error in the vector due to the statistical nature of Monte Carlo neutron transport calculations.

Monte Carlo methods use random sampling, which employs a pseudo-random number generator for sampling probabilities of neutrons from their "birth" until they are either absorbed or escaped [24]. Each neutron history is tallied, and when a sufficient number of histories are accumulated, statistical metrics (e.g., mean value, standard deviation) of the target parameters are calculated. The Monte Carlo method repeats this process for a user-defined number of cycles. The first few cycles have poor statistics due to insufficient neutron historical data. Accordingly, the first few cycles are usually marked "inactive" and used for source convergence only. Therefore, the user must define the number of inactive and active cycles to balance the need to assure source convergence and statistical accuracy with computational costs.

The Serpent Monte Carlo transport software calculates the relative statistical error of each output parameter of the transport problem. During each neutron source cycle, Serpent calculates the sum of the collisions, fissions, and other events in that cycle. After completion of all active cycles, Serpent computes the statistical mean and associated standard deviation based on cycle-specific data. Notably, Serpent estimates the uncertainty assuming that all events are independent, thus, neglecting to propagate the uncertainties from one depletion step to the next. Instead, the estimate uses only data from each separate depletion step by itself. Jaakko Lappänen stated, "Error propagation in Monte Carlo burnup calculation is a major research topic at the moment..." and mentioned unprecedented complexity of the problem [61].

In order to estimate the variance in the isotopic composition $[N]$ due to the statistical nature of Monte Carlo method, a bash scripting system was developed to run a depletion calculation with S burnup steps M times, *changing nothing except the seed value for the random number sequence in the Serpent input* (Figure 7.1). Once again, the nuclear data uncertainty is not propagated in this section. The multiple "replications" of each depletion sequence produce a set of M isotopic concentrations at the end of each depletion interval [103, 114].

After running depletion calculations for all samples, the mean and standard deviation of the isotopic concentration can be calculated as follows

$$\overline{N_i} = \frac{1}{M}\sum_{j=1}^{M} N_i^{(j)} \tag{7.1}$$

$$\sigma_{N_i} = \sqrt{\frac{1}{M-1}\sum_{j=1}^{M}(N_i^{(j)} - \overline{N_j})^2} \tag{7.2}$$

where

$\overline{N_i}$ = mean concentration of isotope i $[\frac{1}{cm^3}]$

$$M = \text{number of depletion runs with a unique seed } [-]$$

$$N_i^{(j)} = \text{concentration of isotope } i \text{ in the sample } j \ [\tfrac{1}{cm^3}].$$

The isotopic concentration $[N]_j$ can then be propagated throughout the criticality calculations to estimate the uncertainty of the multiplication factor k_{eff}. Serpent Monte Carlo code automatically calculates the mean and standard deviation of the k_{eff} in each run j, which is necessary to find the number of runs (samples) required for the convergence of k_{eff}.

The TAP full-core model in Serpent described earlier (see Section 4.2) is used for the uncertainty quantification study herein. The model benefits from 1/8 symmetry, which allowed me to significantly reduce the computational burden without losing accuracy (Figure 4.7). The number of neutron histories was selected to compromise between accuracy and computational costs. Running 15,000 neutrons with 500 active cycles and 200 inactive cycles (used for source convergence) gave a reasonable balance between statistical certainty

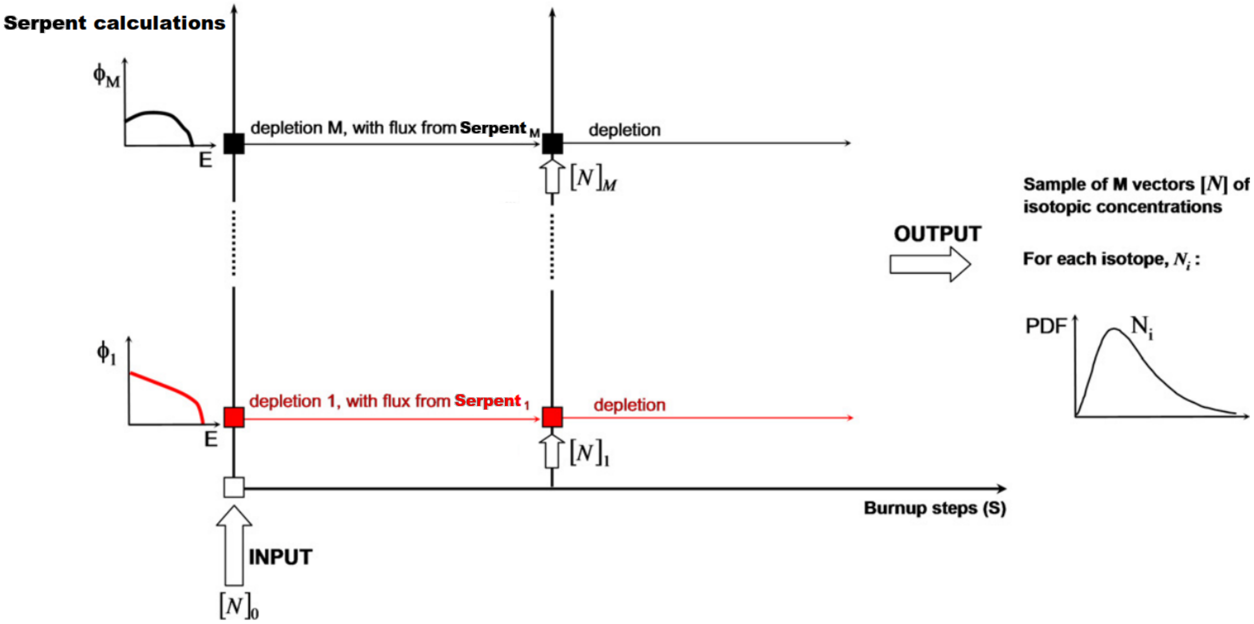

Figure 7.1: Methodology of using a normal distribution of random and independent events to estimate uncertainties in final isotopic concentrations (reproduced from Garcia-Herranz *et al.* [44]). Depletion calculation was performed with the Serpent Monte Carlo code 1000 times by changing only the initial random number.

and computation time. Thirty depletion time steps were selected for a 30-year depletion simulation (i.e., the isotopic composition is stored, and neutron flux is recalculated at the end of each year). Additionally, I selected the Chebyshev Rational Approximation Method (CRAM) with a predictor-corrector substep [78] to reduce isotopic composition uncertainty. The ENDF/B-VII.1 nuclear data library at 900 K is used for all simulations in the current chapter [27].

7.1.2 Results and analysis

A total of 1000 samples is propagated via the Serpent depletion calculation, and the histograms of eigenvalue samples at the BOL and EOL (30 Effective Full Power Year (EFPY)) are shown in Figure 7.2. The results show that the mean effective multiplication factor (k_{eff}) and its standard deviation both decrease gradually during 30 years of TAP reactor operation due to the stochastic nature of MC. An uncertainty in k_{eff} of approximately 35 *pcm* is observed at the BOL, while it slipped to about 29 *pcm* at the EOL. A 1000 independent Serpent runs were performed on Idaho National Laboratory's Falcon supercomputer to obtain a set of M=1000 vectors of isotopic concentrations in a depletion simulation with S=30 depletion time intervals each. The computational time for such an analysis was approximately 1,200 node-hours (4.9 core-years).

Figure 7.3 shows the observed and reported by Serpent uncertainties in k_{eff} for the TAP core during 30 years of operation. Notably, Serpent-calculated uncertainty in the multiplication factor is slightly lower than observed uncertainty. This discrepancy is due to statistical noise in the pseudo-randomly generated initial seed and agreed with results in the literature [114]. Across all 30 depletion steps, the mean observed and reported uncertainty in the k_{eff} is 30 and 25 *pcm*, respectively. A better match in these values could be obtained with more samples M (e.g., M = 10,000), which would require substantially more computational power.

The current depletion algorithm in Serpent uses the neutron flux solution obtained from

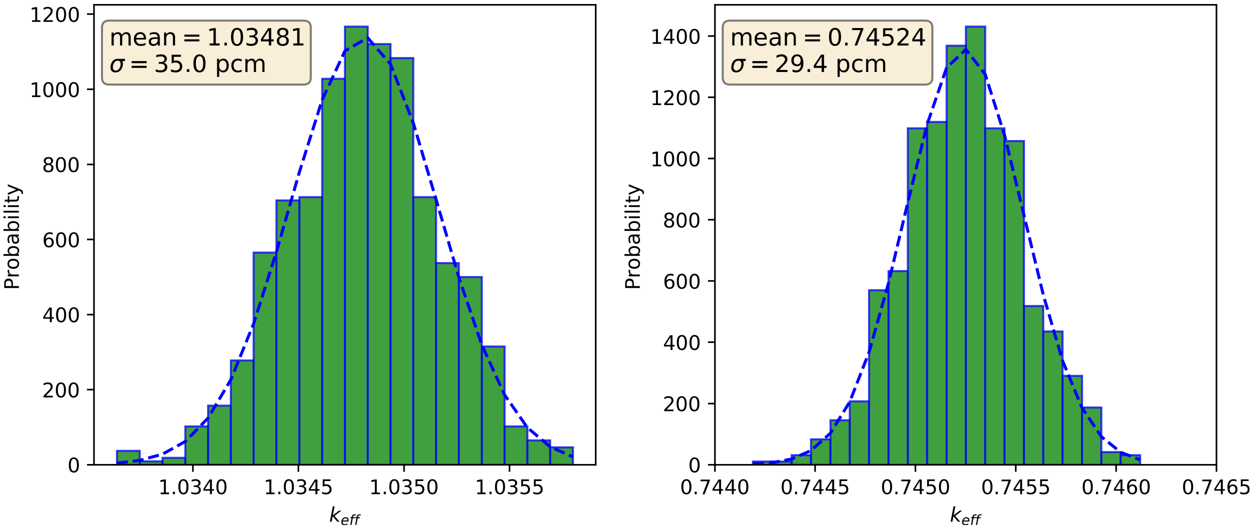

Figure 7.2: Histograms of k_{eff} samples obtained with 1000 independent Serpent depletion calculations at the BOL (left) and EOL (right).

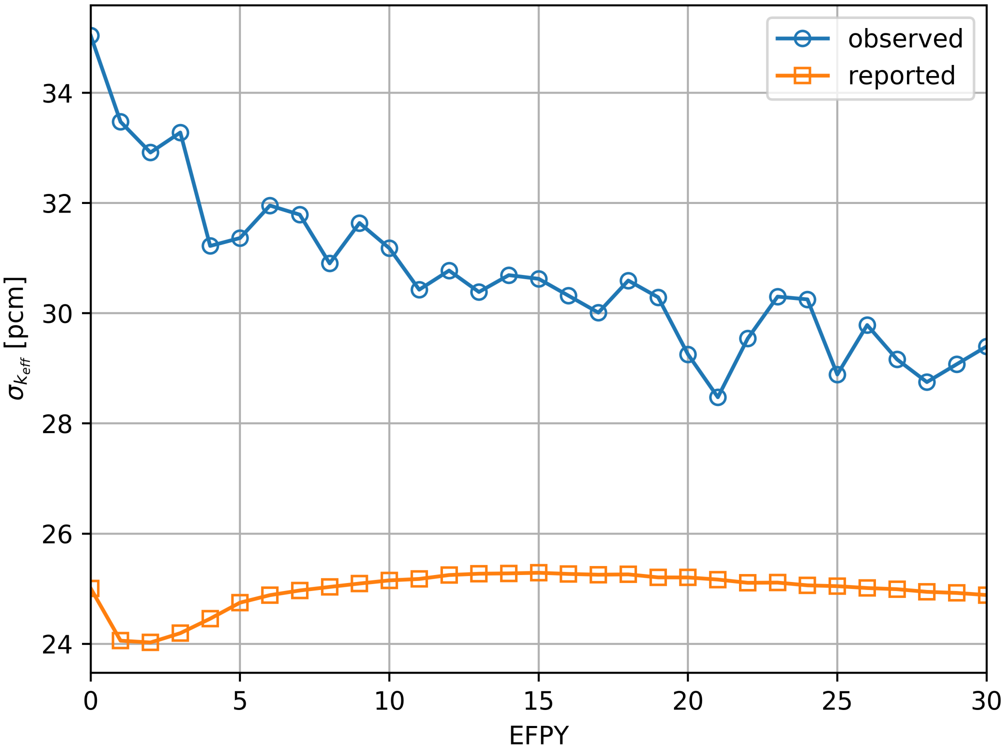

Figure 7.3: Observed and reported by Serpent uncertainty of the effective multiplication factor ($\sigma_{k_{eff}}$) for the full-core TAP core model during 30 years of operation.

the MC neutron histories to solve the Bateman equations to find the isotopic inventory evolution. As was discussed earlier, Serpent is unable to estimate the uncertainty of the isotopic number density like it does for the k_{eff} (reported $\sigma_{k_{eff}}$ in Figure 7.3). Thus, to gain insight into the uncertainties in the isotopic inventory, the standard deviation in observed isotopic inventories from the 1000 depletion runs was investigated. The observed uncertainties for the major actinides and poisonous FPs resulting from depletion calculations are shown on Figures 7.4, 7.5, and 7.6.

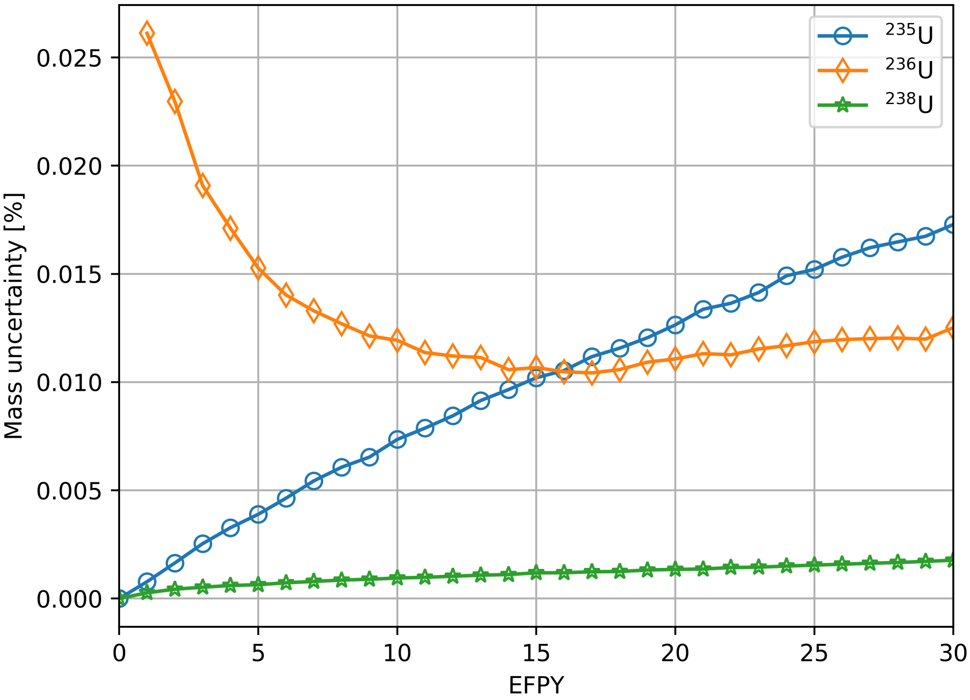

Figure 7.4: Stochastic uncertainty evolution in the uranium isotopic inventory during 30 years of depletion.

The relative uncertainty of ^{235}U mass increases with time due to its depletion, as the uranium enrichment steadily decreases from 5% to 0.7%. The uncertainty of ^{236}U mass is 0.026% after 30 days of operation when only a few grams of this isotope were produced in the core. The uncertainty of ^{236}U is between 0.011% and 0.013% once the ^{236}U approaches its equilibrium concentration. The relative uncertainties of fissile ^{239}Pu and ^{241}Pu are 0.01-0.07% and 0.04-0.18%, respectively. Mass uncertainties for the strongest neutron poison,

^{135}Xe, and its primary direct precursor, ^{135}I, are 0.0175-0.0275% and 0.01-0.0175%, respectively. Overall, stochastic error in depletion calculations is larger for isotopes with small concentrations in the core due to round-off error. Table 7.1 shows that the stochastic error in the isotopic inventories even for an unusually high burnup of 100 MW$_{th}$d/kgU (30 EFPY) is negligible ($< 0.1\%$).

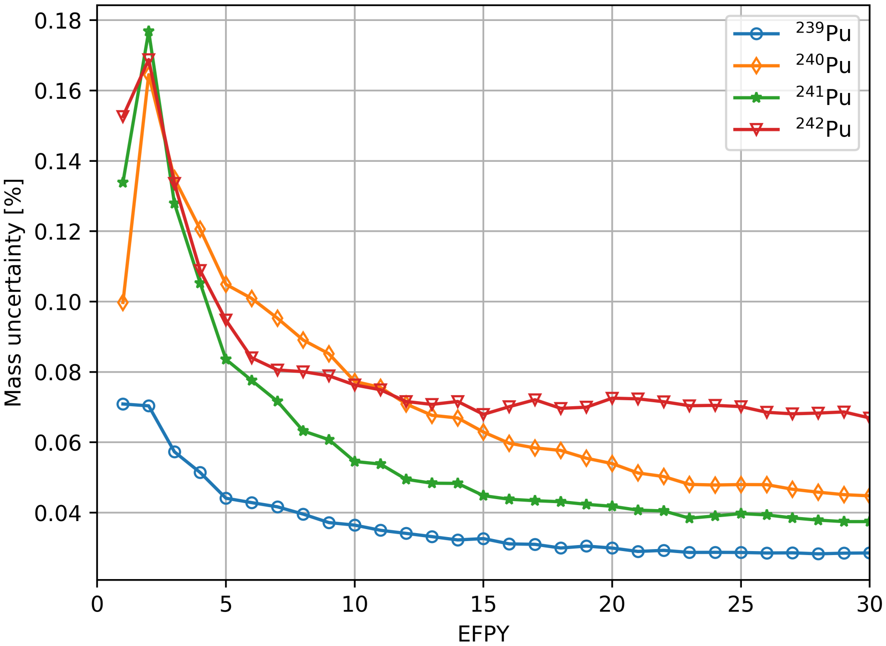

Figure 7.5: Stochastic uncertainty evolution in the plutonium isotopic inventory during 30 years of depletion.

All results presented in Figures 7.4, 7.5, 7.6, and Table 7.1 are based on 1000 samples (e.g., 1000 independent Serpent depletion simulations with unique random seeds). Figure 7.7 shows the convergence of k_{eff} and ^{235}U mass uncertainty with the number of samples. Notably, 300 samples were enough for $\sigma_{k_{eff}}$ convergence. The ^{235}U mass uncertainty at the EOL decreases steadily with the number of samples, but even 400 samples are sufficient to obtain reasonable uncertainty ($< 0.02\%$). Finally, it is possible to reduce the stochastic uncertainty in the isotopic inventory to almost zero by substantially increasing the neutron population (number of neutron histories and active cycles). However, this is extremely inefficient because Monte Carlo converges sublinearly ($O(\sqrt{N})$).

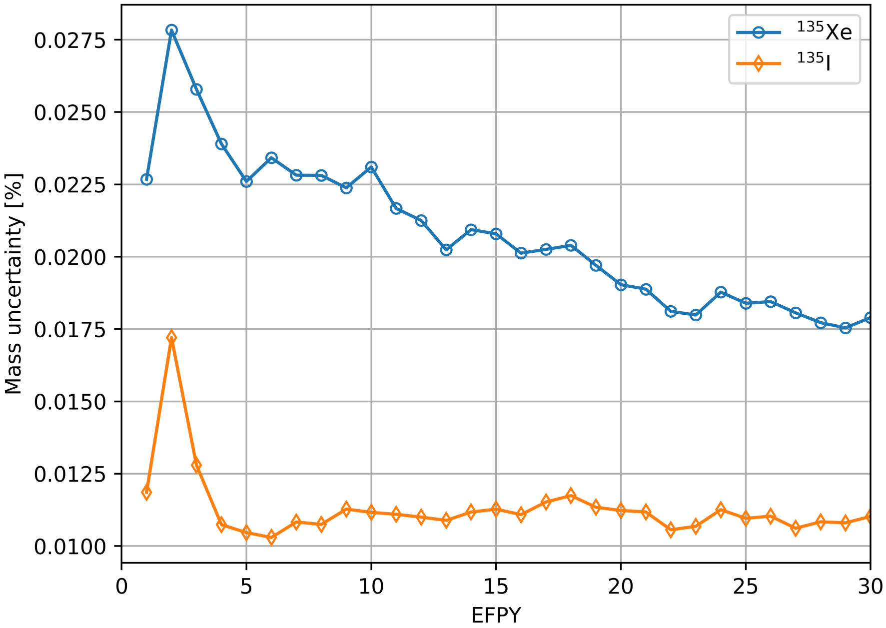

Figure 7.6: Stochastic uncertainty evolution in ^{135}Xe and ^{135}I isotopic inventory during 30 years of depletion.

Table 7.1: Mean value, Standard Deviation (STD), and Relative Standard Deviation (RSD) of mass for the major isotopes after 30-year depletion analysis for the TAP reactor. Only the stochastic error in the Monte Carlo calculations is considered.

Isotope	**Mean** (μ) **[kg]**	**STD** (σ) **[kg]**	**RSD** (σ/μ) **[%]**
^{234}U	25.8	0.0075	0.0290%
^{235}U	789.9	0.1365	0.0173%
^{236}U	1149.5	0.1439	0.0125%
^{238}U	112,084.8	1.9835	0.0018%
^{238}Pu	405.5	0.0884	0.0218%
^{239}Pu	5554.3	1.5860	0.0286%
^{240}Pu	1230.2	0.5510	0.0448%
^{241}Pu	763.1	0.2859	0.0375%
^{242}Pu	139.0	0.0930	0.0669%
^{241}Am	218.3	0.0566	0.0259%
^{135}Xe	0.03	< 0.0001	0.0179%
^{135}I	0.02	< 0.0001	0.0110%

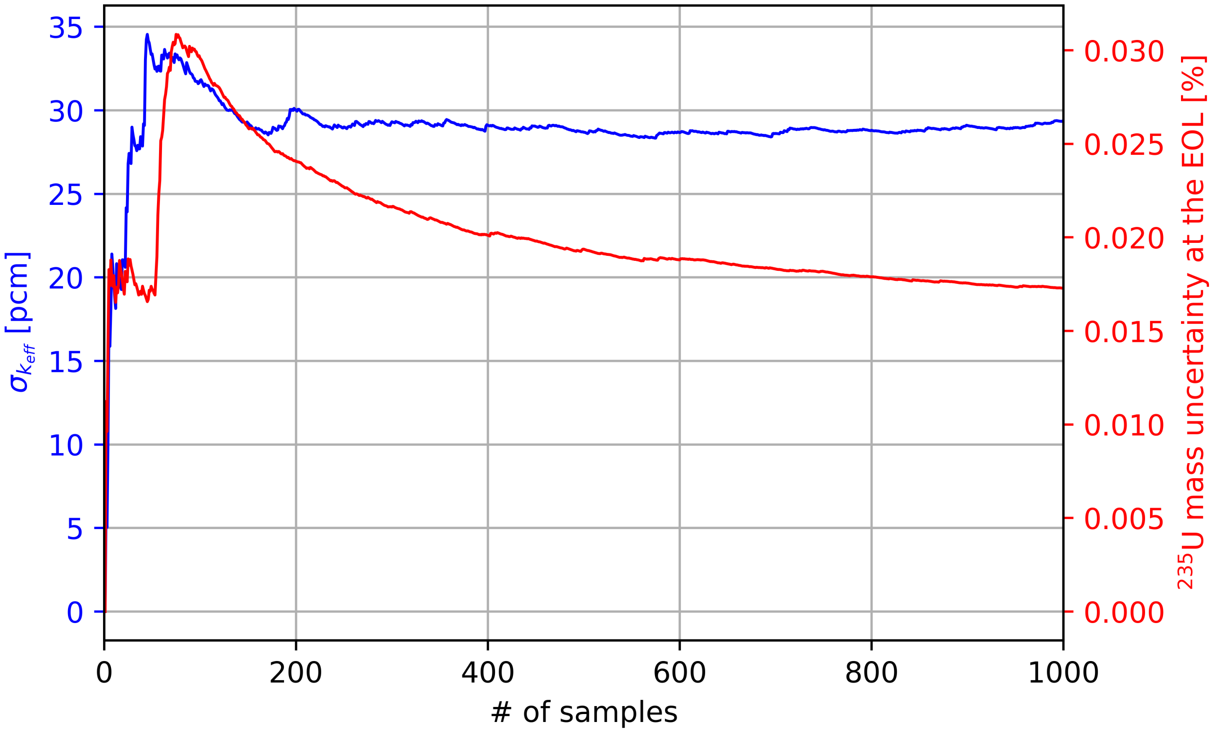

Figure 7.7: Convergence of k_{eff} and ^{235}U mass uncertainties due to the statistical error in Monte Carlo as a function of number of samples.

7.2 Nuclear data-related uncertainty in the isotopic inventory

This section focuses on evaluating uncertainty in a depletion calculation caused by uncertainties in nuclear data, namely, cross sections, fission yields, and decay constants. I used a deterministic S_N transport solver, SCALE/TRITON [82], to avoid statistical errors and isolate nuclear data-related uncertainty.

7.2.1 Methodology of uncertainty propagation by a random sampling

Nuclear data uncertainties are propagated through fuel depletion calculations using a random sampling method[2]. The multi-step sequence of deterministic neutronics and isotopic transmutation could be regarded as a single process with input parameters (cross sections, fission yields, decay constants) and an output (isotopic inventory). This sequence runs a large number of times, each time using a different nuclear data file (sample). This collection of random nuclear data files is produced by the SCALE Sampler module from a multivariate normal distribution using covariance matrices in the 56-group covariance library [82, 81]. This approach is summarized in the flowchart (Figure 7.8).

After generating the collection of random nuclear data files, SCALE performs depletion calculations for each sample. This work uses NEWT, a 2D-deterministic transport code, coupled with ORIGEN. ORIGEN solves a set of the Bateman equations using NEWT-calculated neutron fluxes. The unit cell model is used to achieve reasonable computing costs while providing an accurate neutron spectrum for depletion calculations (Figure 7.9) [15, 89, 19]. For this unit cell model, an 8×8 mesh with reflective boundary conditions is used. The 56-group ENDF/B-VII.1 nuclear data library along with the 56-group covariance

---

[2] Sometimes researchers also called it “Monte Carlo sampling,” [80] “brute force method,”[44] or “Fast Total Monte Carlo” [84]. However, in this chapter, this method is called “random sampling.”

library are used in these depletion calculations.

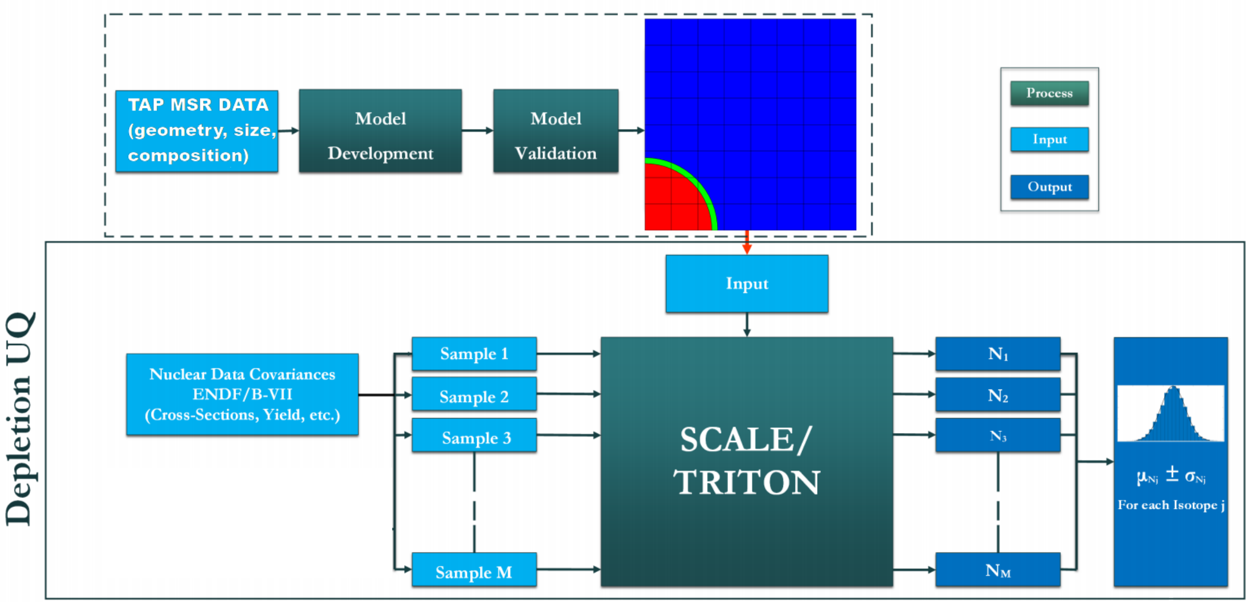

Figure 7.8: Flowchart of depletion uncertainty quantification using SCALE Sampler (figure courtesy of Majdi I. Radaideh [81]).

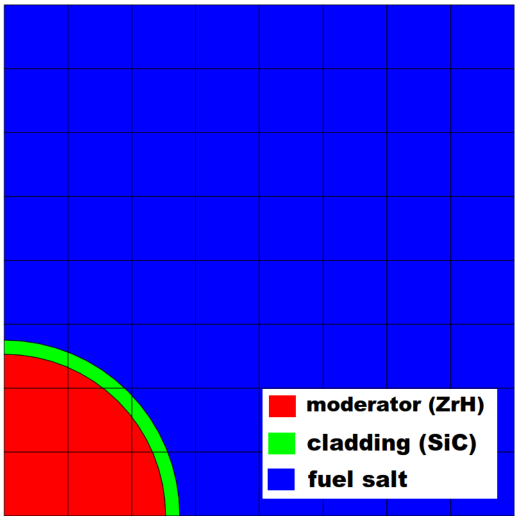

Figure 7.9: Unit cell model representation for the TAP MSR in SCALE.

The fuel salt composition, total depletion time, depletion time steps, and power density match the ones given in Section 7.1 for consistency of comparison. Overall, I repeated 800 SCALE depletion calculations using perturbed cross sections, fission yields, and decay constants, assuming that the probability density functions are multivariate normal distributions with covariances provided with the SCALE nuclear data library.

7.2.2 Results and analysis

Figure 7.10 shows histograms of the infinite multiplication factor (k_∞) at the BOL and EOL (30 EFPY) for 800 total random samples. Similar to stochastic uncertainty, the results show that the k_∞ standard deviation due to the nuclear data uncertainty decreases during 30 years of the TAP reactor operation. An uncertainty of about 804 *pcm* in k_∞ is observed at startup, while it is reduced to 469 *pcm* at the EOL. Notably, nuclear data-related uncertainty in the multiplication factor is about 20 times larger than uncertainty due to the stochastic error (see Section 7.1), which agrees well with results in the literature [102, 44]. Thanks to the unit cell model and a fast deterministic S_N NEWT transport code, the computational time for producing 800 random samples was only 576 core-days. Generation of the 800 samples with better accuracy (full-core, three-dimensional model solved with KENO-VI) would require substantially more computational power (about 10,000 times more).

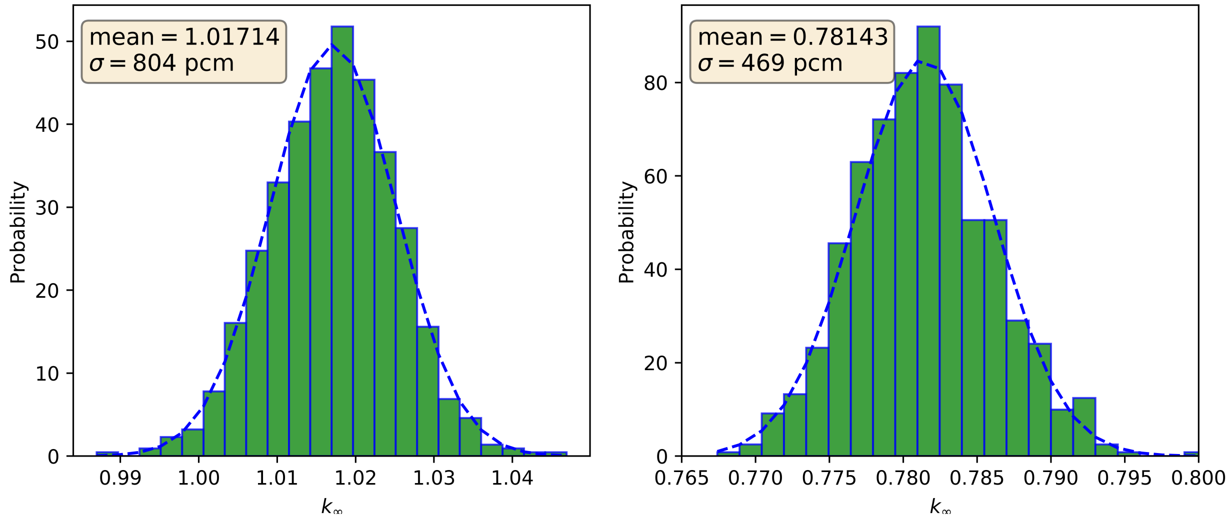

Figure 7.10: Histograms of k_∞ at the BOL (left) and EOL (right) obtained with SCALE Sampler by stochastically sampling the nuclear data (cross sections, fission yields, decay constants).

Figure 7.11 demonstrates nuclear data-related uncertainty in the k_∞ evolution during 30 years of operation. The k_∞ uncertainty decreased slowly because the k_∞ mean value reduces over time from 1.01714 to 0.78143 due to fuel burnup. Considering more specific nuclear

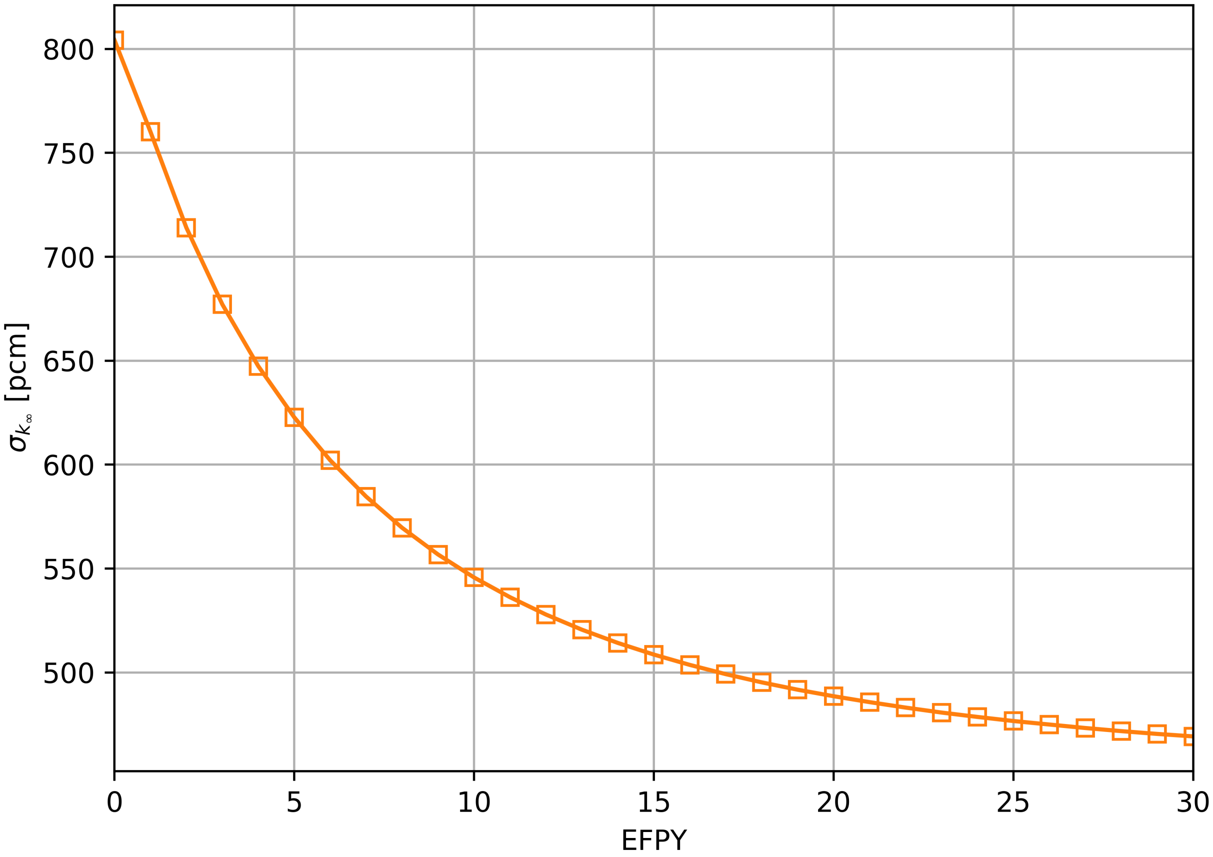

Figure 7.11: Calculated uncertainty in the infinite multiplication factor due to the nuclear data uncertainty as a function of depletion time.

data contributions, at the BOL the k_∞ uncertainty is most likely to come from the fissile ^{235}U fission (n, f) and neutron capture (n, γ) reaction cross sections; the ^{238}U (n, γ) reaction cross section; and the elastic scattering cross section of hydrogen in zirconium hydride. However, moving toward the EOL, the contributions to uncertainty from ^{235}U data are expected to diminish due to the burnup and be substituted by the cross section uncertainties of the fissile plutonium (e.g., ^{239}Pu, ^{241}Pu). Notably, the ^{235}U fission cross section uncertainty in intermediate and fast spectrum ranges (the TAP is an intermediate spectrum reactor, see Figure 4.16) reaches up to 4%, while it is less than 2.6% for ^{239}Pu and ^{241}Pu. ^{239}Pu and ^{241}Pu capture and fission cross sections formed the dominant source of uncertainty after ^{235}U was mostly depleted.

Moreover, the k_∞ relative uncertainty from nuclear data slipped from 0.78% at the BOL to 0.46% at the EOL. This error is slightly larger than results in the literature for conventional LWRs (e.g., 0.44% [113] or 0.55% [25] for a PWR). This discrepancy between k_∞ uncertainty for the TAP MSR and PWR likely originates with the ^{19}F and ^{7}Li nuclear data, which have significant covariances across reactions.

Figure 7.12 shows the standard deviations in uranium and plutonium isotopic inventory as a function of time. The uncertainty in ^{238}U is minimal ($< 0.1\%$) and almost constant with burnup because ^{238}U mass does not change significantly from its initial inventory. The ^{236}U uncertainty also is nearly constant during 30 years of operation and has a value of $\approx 3.8\%$. However, ^{235}U mass uncertainty increases steadily with burnup, due to its inventory decrease during 30 years of operation. The absolute mass uncertainty for ^{235}U demonstrated growth from 5 kg at 1 year after startup to approximately 30 kg at the EOL.

The uncertainty of major plutonium isotopes (e.g., ^{239}Pu, ^{240}Pu, ^{241}Pu) is below 2% over 30 years of burnup (Figure 7.12, lower plot). The fissile ^{239}Pu and poisonous ^{240}Pu relative standard deviations are increased slightly from 1.25% to 1.6% and from 1.65% to 1.95%, respectively. The relative standard deviation in fissile ^{241}Pu mass is significant at the beginning of the operation, when its inventory is small (4 kg), and then decreases and approaches an equilibrium value of ≈ 1.45% at the EOL. The most significant relative standard deviation is observed for ^{242}Pu mass (8.13%) because its concentration in fuel is minimal throughout 30 years of operation (Table 7.2).

Figure 7.13 shows the mass uncertainties for the selected FPs: ^{135}Xe and its primary direct precursor, ^{135}I. The masses of ^{135}Xe and ^{135}I are in the ranges of 24-27 g and 18-19 g, respectively. As expected, relative standard deviations for these isotopes are relatively low due to minimal uncertainty of fission yield for ^{235}U. The relative standard deviation of ^{135}Xe mass changes in a range from 0.47% to 0.6%, while the ^{135}I standard deviation ranges from 0.35% to 0.56%.

Table 7.2 summarizes the nuclear data-related uncertainty in the isotopic inventory for the TAP MSR after 30 years of operation. Overall, the mass uncertainties due to nuclear data uncertainties are two orders of magnitude larger than uncertainty due to the statistical error in MC.

All results presented in this section are based on 800 random samples obtained using the Sampler tool in SCALE. Figure 7.14 shows the convergence of k_∞ and ^{235}U mass uncertainty with number of random samples. Notably, after 500 samples the k_∞ and ^{235}U mass uncertainties stabilize. Overall, 500 random samples is enough to accurately estimate uncertainty in the isotopic inventory due to uncertainty in nuclear data.

7.3 Concluding remarks

Uncertainty propagation analysis was performed for the depletion calculation for the TAP MSR 30-year burnup. I separately considered two primary sources of uncertainty in the depletion calculations: stochastic uncertainty in the neutron flux distribution and uncertainty in the nuclear data. Stochastic error in the isotopic composition was obtained using the Serpent Continuous Energy Monte Carlo code by running the same depletion sequence 1000 times, each time with a new initial random seed. The Sampler module in SCALE

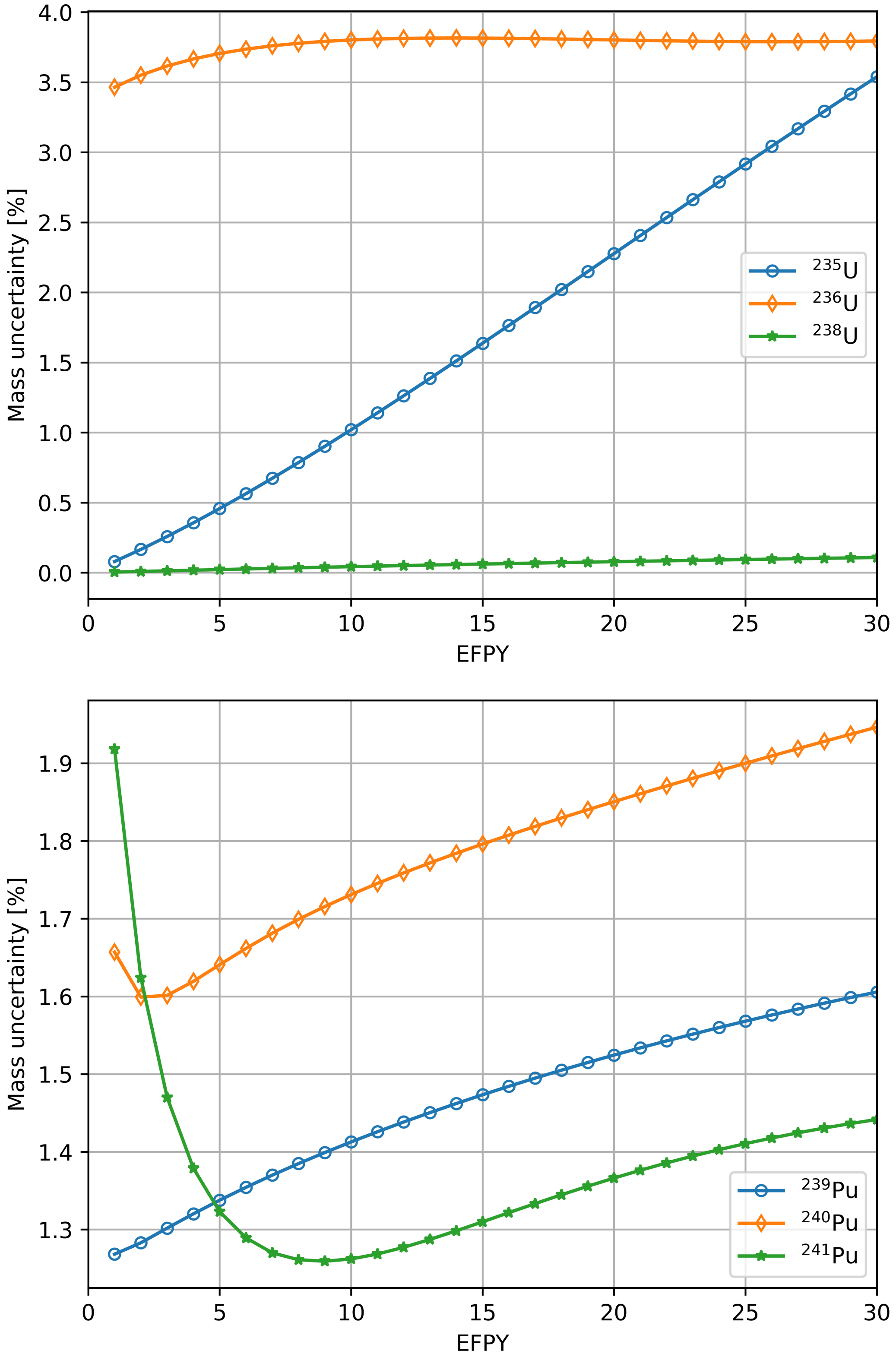

Figure 7.12: Nuclear data-related uncertainty evolution in the uranium (upper) and plutonium (lower) isotopic inventory during 30 years of depletion.

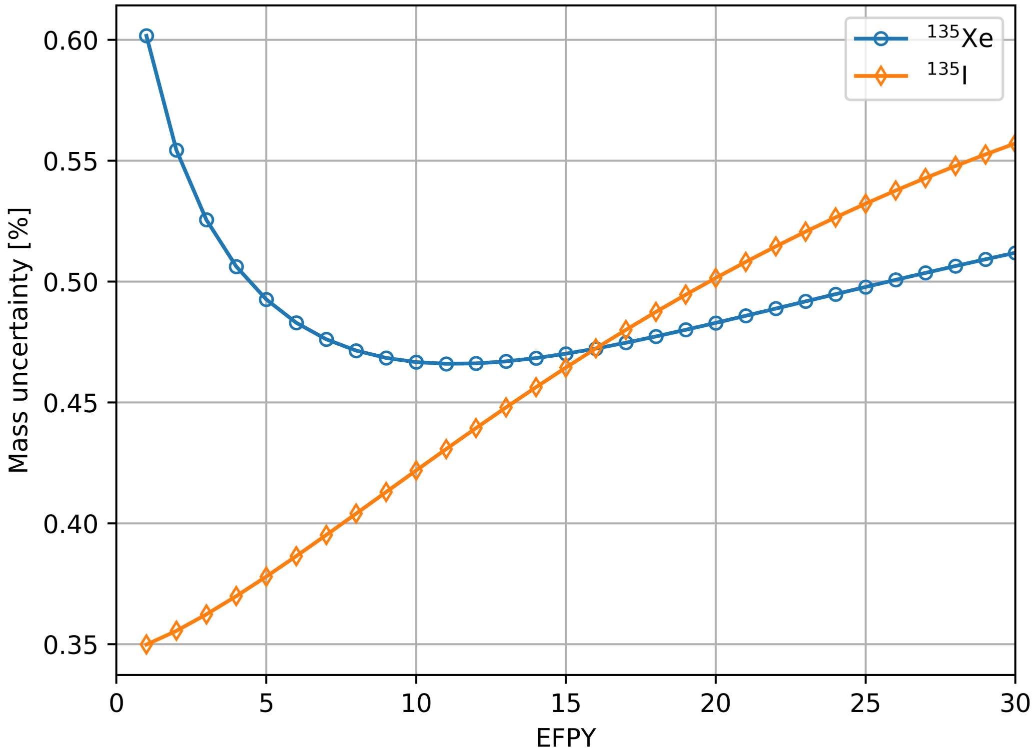

Figure 7.13: Nuclear data-related uncertainty evolution in ^{135}Xe and ^{135}I isotopic inventory during 30 years of depletion.

Table 7.2: Mean value, Standard Deviation (STD), and Relative Standard Deviation (RSD) of mass for the major isotopes after 30-year depletion analysis for the TAP reactor. Only nuclear data-related uncertainty is considered.

Isotope	**Mean [kg]**	**STD [kg]**	**RSD [%]**
^{234}U	21.6	0.75	3.48%
^{235}U	839.4	29.72	3.54%
^{236}U	1154.9	43.83	3.79%
^{238}U	112,206.1	122.32	0.11%
^{238}Pu	335.56	11.05	3.29%
^{239}Pu	5558.1	89.25	1.61%
^{240}Pu	1594.6	31.04	1.95%
^{241}Pu	639.1	9.21	1.44%
^{242}Pu	164.0	13.33	8.13%
^{241}Am	204.9	6.15	3.00%
^{135}Xe	0.03	< 0.01	0.51%
^{135}I	0.02	< 0.01	0.56%

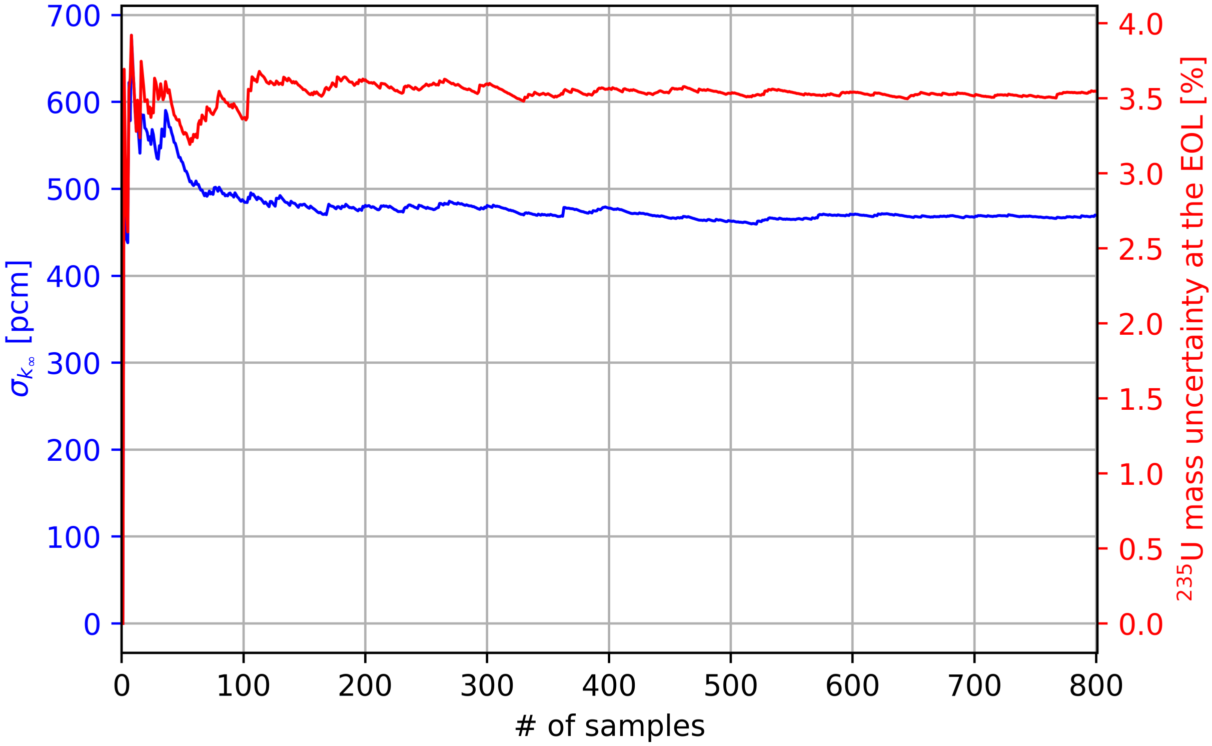

Figure 7.14: Convergence of k_∞ and ^{235}U mass uncertainties due to the nuclear data uncertainty as a function of the number of samples for simulation using SCALE with the Sampler module.

6.2 with a 56-group covariance library was used to obtain nuclear data-related uncertainty in the isotopic composition of the fuel salt. Uncertainties in the input nuclear data (cross sections, fission yields, decay constants) are propagated throughout all steps of the transport/depletion sequence, including self-shielding, space-energy flux calculation, and isotope transmutation.

The stochastic errors in isotopic masses are below 0.067% for 7.5 million neutron histories (total neutron flux relative stochastic error $< 0.01\%$). Therefore, it is unnecessary to consider the accumulation of the stochastic error for the fuel depletion in the TAP reactor considered in this dissertation. Finally, the stochastic error in the isotopic inventory could be reduced to almost zero by increasing the number of neutron histories, but it is impractical due to the sublinear convergence rate of the Monte Carlo method ($O(\sqrt{N})$).

On the other hand, the computed errors in the isotopic inventory due to the nuclear data uncertainties are a few orders of magnitude larger and cannot be ignored. The nuclear data-related errors are in the range from 1% to 2% for the masses of ^{239}Pu, ^{240}Pu, and ^{241}Pu, and about 3-8% for ^{234}U, ^{235}U, ^{236}U, ^{238}Pu, ^{242}Pu, and ^{241}Am. Finally, the mass uncertainty for the selected FPs (^{135}Xe and ^{135}I), which are the subject of interest of the current work, is below 0.6%. Overall, the principal source of uncertainty in depletion calculations arises from to the nuclear data covariances.

Finally, this chapter demonstrated that the standard deviation in the multiplication factor due to the nuclear data uncertainty ranges from 804 to 469 *pcm*, while the stochastic error is only about 30 *pcm*. Overall, to accurately capture the isotopic inventory evolution for the TAP concept using SaltProc v1.0 with Serpent Monte Carlo code, it is unnecessary to waste a vast computational power to simulate $10^7 - 10^9$ neutron histories per each depletion step because the impact of the stochastic errors in neutron fluxes is negligible compared with the nuclear data-related errors.

Chapter 8

Conclusions and future work

8.1 General Conclusions

Liquid-fueled nuclear reactors offer several advantages over their traditional solid-fueled counterparts, which makes them a promising option for nuclear fuel cycle closure while offering improved inherent safety. Simulating such systems presents a challenge because existing reactor physics software for fuel burnup historically has been developed for traditional, solid-fueled reactors.

This work demonstrated a flexible, open-source tool, SaltProc, for simulating fuel depletion in a wide range of circulating-fuel (e.g., liquid fuel circulating throughout the primary loop) nuclear reactors that takes into account unique features of such systems: online fuel reprocessing and refueling. SaltProc extends the continuous-energy Monte Carlo burnup calculation code, Serpent 2, for the simulation of material isotopic evolution in any nuclear reactors with circulating, liquid fuel with the main focus on the liquid-fueled MSRs. This work demonstrates a clear contribution to the nuclear engineering community by providing a tool for fuel depletion calculations in any generic nuclear system with circulating fuel.

The need for this work has been shown by a summary of the current state of the art of MSR depletion simulator capabilities. The literature review in Chapter 1 concluded that most MSR depletion simulators typically assume ideal (rather than realistically constrained) poison removal rates for the nuclear system performance modeling. Moreover, most of the simulators assumed constant extraction efficiency vectors, which must be determined by the user in the input file and cannot be a function of other parameters. SaltProc is capable of modeling the peculiarities of MSRs, namely: complex, multi-component reprocessing system structure and realistic extraction efficiency of fission product described as a function of many parameters. Furthermore, SaltProc can maintain reactor criticality by adjusting the reactor core geometry. In addition to fundamental simulation capabilities, SaltProc has a scalable design and allows the development of additional advanced capabilities in the future.

I demonstrated SaltProc for lifetime-long full-power operation for two perspective MSR designs: MSBR and TAP MSR. The MSBR analysis illuminated the simplified depletion of the fuel salt for 60 years of full-power operation with ideal fission product extraction efficiency (e.g., 100% of target poison is being removed). The online fission product removal with 100% efficiency and fresh fuel feed allowed the MSBR to operate at full-power for an extremely long time with effective fuel utilization due to exceptionally low parasitic neutron absorption. The obtained results are validated with published modeling efforts by ORNL [15].

Validation simulations for the TAP MSR have demonstrated the SaltProc capability to model reactors with adjustable moderator configuration. Results for a realistic multi-component model of the fuel salt reprocessing system with assumed ideal removal efficiency are validated with full-core TAP depletion analysis by Betzler *et al.* [17]. In the realistic reprocessing system with non-ideal removal, the fuel salt composition is strongly influenced by the neutron spectrum hardening due to presence of neutron poisons (e.g., ^{135}Xe) in the core. Thus, more effective noble gas extraction efficiency significantly reduced neutron loss due to parasitic absorption, which led to better fuel utilization and extended core lifetime.

I also used SaltProc to perform short-term depletion analysis with power maneuvering in the $P \in [0, 100\%]$ range to investigate load-following capability in the TAP MSR and MSBR designs. Online gaseous fission product removal significantly improved the load-following capability of the MSBR by reducing the reactivity worth of xenon poisoning from -1457 *pcm* to -189 *pcm*. I observed a negligible effect of xenon poisoning in the TAP MSR because its neutron energy spectrum is relatively hard even for the most thermal core configuration (all moderator rods are inserted). Thus, the TAP MSR can effectively load-follow even without continuous gas removal.

Once fuel salt composition evolution was obtained for various MSR designs and power levels, I analyzed a major safety and operational parameters at different moments during operation. Specifically, changes in temperature and void coefficients of reactivity and total control rod worth were evaluated for the TAP concept and MSBR for two timeframes: lifetime-long full-power operation and short-term load-following transient. On a long-timescale, the safety parameters worsened during full-time operation for both considered reactor designs due to a significant spectral shift. For the load-following transient, the combination of fuel and moderator temperature coefficient remained strongly negative throughout the transient for both reactors. Notably, the MSBR safety benefited from continuous fission gas removal, while the TAP MSR safety and operational parameters remained stable due to its harder spectrum. Unfortunately, the total control rod worth was insufficient to shut down the MSBR due to a considerable reactivity swing during the load-following transient. Thus, the reactivity control system of the MSBR must be redesigned to ensure safe power maneuvering. Finally, for scientific reproducibility, HDF5 databases generated with SaltProc in this work are published in Illinois Data Bank [91].

The current work also demonstrated a simple uncertainty propagation via Monte Carlo depletion calculations. I evaluated the uncertainty of predicted isotopic composition separately from two primary sources: stochastic error from the transport problem solution and measurement error in the nuclear data library. Nuclear data-related uncertainty in the isotopic masses is approximately 0.5-8% and varies widely from isotope to isotope due to widespread in the nuclear data covariances. The stochastic errors in isotopic masses are below 0.07% for a reasonable number of neutron histories (7.5×10^6). Fundamentally, we do not need to waste a substantial computational power to simulate a large number of neutron histories per each depletion step because the nuclear data-related uncertainty is dominating over the stochastic error.

Furthermore, the nuclear data-related uncertainty in the depletion calculations can be significantly improved by reducing cross section covariance of ^{6}Li, ^{7}Li, and ^{19}F, which are broadly used in the MSRs. The nuclear data for those isotopes were not measured accurately because lithium and fluorine rarely appear in conventional LWRs core. To further develop the MSR concepts, ^{6}Li, ^{7}Li, and ^{19}F cross sections must be thoroughly remeasured with improved uncertainty to reduce the nuclear-data related error in a neutronic calculations.

8.2 Suggested Future Work

Continued research into SaltProc-Serpent and related topics could progress in many different directions. First of all, other liquid-fueled MSR designs with on-site fuel salt reprocessing system should be modeled using SaltProc to improve the cross-code validation portfolio. For example, SaltProc can be validated with a recently published effort for the Chinese Single-fluid Double-zone Thorium Molten Salt Reactor (SD-TMSR) [5].

Next, optimization of reprocessing parameters (e.g., time step, feeding rate, removal rate for various fission product groups) could establish the best fuel utilization, breeding ratio, or safety characteristics for various designs. This might be performed with a parameter sweeping outer loop, which would change an input parameter by a small increment, run the simulation, and analyze output to determine optimal configuration. Alternatively, the existing RAVEN optimization framework [3] might be employed for such optimization studies.

Only the simple power drop-and-restart transient with a coarse time resolution has been considered in this work to investigate the load-following capabilities of liquid-fueled MSRs. Additional analyses should include realistic power load profiles with 15-minute or even 5-minute time resolution. The existing capabilities of SaltProc allow modeling of smart gas separation regulation during transient by adjusting, for example, the helium bubble sizes in the sparger. The scientific community would benefit enormously from standardized depletion analysis during the load-following operation for various liquid-fueled reactors, including exotic liquid metal fuel reactor designs.

Only the batch-wise online reprocessing approach has been treated in this work. However, Serpent 2 was recently extended for continuous online fuel reprocessing simulation [6]. This extension could be employed for immediate removal of fission product gases (e.g., Xe, Kr), which have a strong negative impact on core lifetime and breeding efficiency. Thus, using the built-in Serpent 2 Monte Carlo code online reprocessing & refueling material burnup routine would significantly speed up computer-intensive full-core depletion simulations.

Additional physical models for fission product extraction efficiency will enrich the capabilities of SaltProc.

References

[1] World Energy Outlook 2017. Technical report, IEA, November 2017. URL: `https://www.iea.org/weo2017/`.

[2] Ali Ahmad, Edward B. McClamrock, and Alexander Glaser. Neutronics calculations for denatured molten salt reactors: Assessing resource requirements and proliferation-risk attributes. *Annals of Nuclear Energy*, 75:261–267, January 2015. URL: `http://www.sciencedirect.com/science/article/pii/S0306454914003995`, `doi:10.1016/j.anucene.2014.08.014`.

[3] Andrea Alfonsi, Cristian Rabiti, Diego Mandelli, Joshua Joseph Cogliati, Congjian Wang, Daniel Patrick Maljovec, Paul William Talbot, and Curtis Lee Smith. RAVEN Theory Manual. Technical Report INL/EXT-16-38178, Idaho National Lab. (INL), Idaho Falls, ID (United States), June 2016. URL: `https://www.osti.gov/biblio/1260312`, `doi:10.2172/1260312`.

[4] O. Ashraf, Andrei Rykhlevskii, G.V. Tikhomirov, and Kathryn D. Huff. Preliminary design of control rods in the single-fluid double-zone thorium molten salt reactor (SD-TMSR). Part I: Design development, material selection, and worth analysis. *Submitted*, 2020.

[5] O. Ashraf, Andrei Rykhlevskii, G.V. Tikhomirov, and Kathryn D. Huff. Whole core analysis of the single-fluid double-zone thorium molten salt reactor (SD-TMSR). *Annals of Nuclear Energy*, 137:107115, March 2020. URL: `http://www.sciencedirect.com/science/article/pii/S0306454919306255`, `doi:https://doi.org/10.1016/j.anucene.2019.107115`.

[6] M. Aufiero, A. Cammi, C. Fiorina, J. Leppänen, L. Luzzi, and M. E. Ricotti. An extended version of the SERPENT-2 code to investigate fuel burn-up and core material evolution of the Molten Salt Fast Reactor. *Journal of Nuclear Materials*, 441(1–3):473–486, October 2013. URL: `http://www.sciencedirect.com/science/article/pii/S0022311513008507`, `doi:10.1016/j.jnucmat.2013.06.026`.

[7] C. J. Barton, H. A. Friedman, W. R. Grimes, H. Insley, R. E. Moore, and R. E. Thoma. Phase Equilibria in the Alkali Fluoride-Uranium Tetrafluoride Fused Salt Systems: I, The Systems LiF-UF4 and NaF-UF4. *Journal of the American Ceramic Society*, 41(2):63–69, 1958. tex.ids: barton_phase_1958-1 publisher: Wiley Online Library.

[8] H. F. Bauman, G. W. Cunningham III, J. L. Lucius, H. T. Kerr, and C. W. Jr Craven. Rod: A Nuclear and Fuel-Cycle Analysis Code for Circulating-Fuel Reactors. Technical Report ORNL-TM-3359, Oak Ridge National Lab., Tenn., January 1971. `doi:10.2172/4741221`.

[9] George I. Bell and Samuel Glasstone. *Nuclear Reactor Theory*. Van Nostrand Reinhold Company, New York, 1970.

[10] E. S. Bettis, L. G. Alexander, and H. L. Watts. DESIGN STUDIES OF A MOLTEN-SALT REACTOR DEMONSTRATION PLANT. Technical Report ORNL-TM–3832, 4668569, January 1972. URL: `http://www.osti.gov/servlets/purl/4668569/`, `doi:10.2172/4668569`.

[11] B. R. Betzler, J. J. Powers, N. R. Brown, and B. T. Rearden. Implementation of Molten Salt Reactor Tools in SCALE. In *Proc. of GLOBAL International Fuel Cycle Conference*, Jeju, Korea, April 2017.

[12] Benjamin Betzler. Personal communication, December 2017.

[13] Benjamin R. Betzler, Kursat B. Bekar, William Wieselquist, Shane W. Hart, and Shane G. Stimpson. Molten Salt Reactor Fuel Depletion Tools in SCALE. In *Proc. of GLOBAL International Fuel Cycle Conference*, Seattle, WA, United States, September 2019. American Nuclear Society. URL: `https://www.osti.gov/servlets/purl/1566988`.

[14] Benjamin R. Betzler, J. J. Powers, and A. Worrall. Modeling and simulation of the start-up of a thorium-based molten salt reactor. In *Proc. Int. Conf. PHYSOR*, May 2016.

[15] Benjamin R. Betzler, Jeffrey J. Powers, and Andrew Worrall. Molten salt reactor neutronics and fuel cycle modeling and simulation with SCALE. *Annals of Nuclear Energy*, 101(Supplement C):489–503, March 2017. URL: `http://linkinghub.elsevier.com/retrieve/pii/S0306454916309185`, `doi:10.1016/j.anucene.2016.11.040`.

[16] Benjamin R. Betzler, Jeffrey J. Powers, Andrew Worrall, L. Dewan, S. Robertson, and Mark Massie. Two-Dimensional Neutronic and Fuel Cycle Analysis of the Transatomic Power Molten Salt Reactor. Technical Report ORNL/TM-2016/742, Oak Ridge National Lab.(ORNL), 2017.

[17] Benjamin R. Betzler, Sean Robertson, Eva E. Davidson, Jeffrey J. Powers, Andrew Worrall, Leslie Dewan, and Mark Massie. Assessment of the Neutronic and Fuel Cycle Performance of the Transatomic Power Molten Salt Reactor Design. Technical Report ORNL/TM-2017/475 CRADA/NFE-16-06345, Oak Ridge National Lab.(ORNL), Oak Ridge, TN (United States), September 2017. URL: `http://www.osti.gov/servlets/purl/1410921/`, `doi:10.2172/1410921`.

[18] Benjamin R. Betzler, Sean Robertson, Eva E. Davidson, Jeffrey J. Powers, Andrew Worrall, Leslie Dewan, and Mark Massie. Fuel cycle and neutronic performance of a spectral shift molten salt reactor design. *Annals of Nuclear Energy*, 119:396–410, September 2018. `doi:10.1016/j.anucene.2018.04.043`.

[19] Benjamin R. Betzler, William Wieselquist, and Massimilliano Fratoni. Modeling Molten Salt Reactor Fission Product Removal with SCALE. Technical report, Oak Ridge National Lab.(ORNL), Oak Ridge, TN (United States), 2020.

[20] M. Blander, W. R. Grimes, N. V. Smith, and G. M. Watson. Solubility of Noble Gases in Molten Fluorides. II. In the Lif–NaF–LF Eutectic Mixtures. *The Journal of Physical Chemistry*, 63(7):1164–1167, 1959.

[21] Georg Brandl. Sphinx: Python Documentation Generator, 2009. URL: `https://www.sphinx-doc.org/`.

[22] R. B. Briggs. Molten-Salt Reactor Program semiannual progress report for period ending July 31, 1964. Technical Report Archive and Image Library ORNL-3708, Oak Ridge National Laboratory, Oak Ridge, TN, United States, 1964. URL: `https://digital.library.unt.edu/ark:/67531/metadc100304/`.

[23] R. B. Briggs. Molten-salt reactor program. Semiannual progress report. Technical Report ORNL-4396, Oak Ridge National Lab., Tenn., February 1969.

[24] F. Brown. Fundamentals of Monte Carlo Particle Transport. Technical Report LA-UR-05-4983, Los Alamos National Lab. (LANL), Los Alamos, NM (United States), 2005.

[25] Daniel Campolina and Jan Frybort. Uncertainty Propagation for Lwr Burnup Benchmark Using Sampling Based Code Scale/Sampler. *Acta Polytechnica CTU Proceedings*, 14:8–13, 2018.

[26] W. L. Carter and E. L. Nicholson. DESIGN AND COST STUDY OF A FLUORINATION–REDUCTIVE EXTRACTION–METAL TRANSFER PROCESSING PLANT FOR THE MSBR. Technical Report ORNL-TM-3579, Oak Ridge National Lab. (ORNL), Oak Ridge, TN (United States), January 1972. URL: `https://www.osti.gov/biblio/4667633`, `doi:10.2172/4667633`.

[27] M. B. Chadwick. ENDF/B-VII.1 Nuclear Data for Science and Technology: Cross Sections, Covariances, Fission Product Yields and Decay Data. *Nuclear Data Sheets*, 112(12):2887–2996, December 2011. `doi:10.1016/j.nds.2011.11.002`.

[28] Anshuman Chaube, Daniel O'Grady, Andrei Rykhlevskii, and Kathryn D Huff. TAP MSR model for Serpent 2. *Zenodo*, 2019. URL: `https://zenodo.org/record/1450733#.W7vA8BNKi3A`, `doi:10.5281/zenodo.1450733`.

[29] Jiaqi Chen and Caleb S. Brooks. CFD simulation of xenon removal by helium bubble sparging in molten salt. January 2019. URL: `https://experts.illinois.edu/en/publications/cfd-simulation-of-xenon-removal-by-helium-bubble-sparging-in-molt`.

[30] D. A. Close. IAEA Safeguards for the Fissile Materials Disposition Project. Technical report, Los Alamos National Lab., NM (United States), 1995.

[31] E. L. Compere, S. S. Kirslis, E. G. Bohlmann, F. F. Blankenship, and W. R. Grimes. Fission Product Behavior in the Molten Salt Reactor Experiment. Technical report, Oak Ridge National Lab., Tenn.(USA), 1975.

[32] L. Dagum and R. Menon. OpenMP: an industry standard API for shared-memory programming. *IEEE Computational Science and Engineering*, 5(1):46–55, January 1998. `doi:10.1109/99.660313`.

[33] Sylvie. Delpech, Céline Cabet, Cyrine Slim, and Gérard S. Picard. Molten fluorides for nuclear applications. *Materials Today*, 13(12):34–41, December 2010. URL: `http://www.sciencedirect.com/science/article/pii/S1369702110702224`, `doi:10.1016/S1369-7021(10)70222-4`.

[34] U. S. DoE. A technology roadmap for generation IV nuclear energy systems. In *Nuclear Energy Research Advisory Committee and the Generation IV International Forum*, pages 48–52, 2002. URL: `https://www.gen-4.org/gif/jcms/c_40481/technology-roadmap`.

[35] X. Doligez, D. Heuer, E. Merle-Lucotte, M. Allibert, and V. Ghetta. Coupled study of the Molten Salt Fast Reactor core physics and its associated reprocessing unit. *Annals of Nuclear Energy*, 64(Supplement C):430–440, February 2014. URL: `http://www.sciencedirect.com/science/article/pii/S0306454913004799`, `doi:10.1016/j.anucene.2013.09.009`.

[36] John Ellson, Emden R. Gansner, Eleftherios Koutsofios, Stephen C. North, and Gordon Woodhull. Graphviz and dynagraph – static and dynamic graph drawing tools. In *Graph Drawing Software*, pages 127–148. Springer-Verlag, 2003. URL: `https://link.springer.com/chapter/10.1007/978-3-642-18638-7_6`.

[37] Energy Information Administration. U.S. Electric System Operating Data, 2016. URL: `http://www.eia.gov/beta/realtime_grid/#/summary/demand?end=20160912&start=20160812&regions=g`.

[38] Carlo Fiorina. *The molten salt fast reactor as a fast spectrum candidate for thorium implementation.* PhD, Politecnico Di Milano, March 2013. URL: `https://www.politesi.polimi.it/handle/10589/74324`.

[39] Carlo Fiorina, Manuele Aufiero, Antonio Cammi, Fausto Franceschini, Jiri Krepel, Lelio Luzzi, Konstantin Mikityuk, and Marco Enrico Ricotti. Investigation of the

MSFR core physics and fuel cycle characteristics. *Progress in Nuclear Energy*, 68:153–168, September 2013. URL: `http://www.sciencedirect.com/science/article/pii/S0149197013001236`, `doi:10.1016/j.pnucene.2013.06.006`.

[40] Benoit Forget, Kord Smith, Shikhar Kumar, Miriam Rathbun, and Jingang Liang. Integral Full Core Multi-Physics PWR Benchmark with Measured Data. Technical report, Massachusetts Institute of Technology, 2018.

[41] Massimiliano Fratoni, David Barnes, Ehud Greenspan, and Augusto Gandini. Design and Analysis of Molten Salt Reactor Fueled by TRU from LWR. *PHYSOR 2004*, 2004. URL: `https://www.ipen.br/biblioteca/cd/physor/2004/PHYSOR04/papers/96144.pdf`.

[42] C. H. Gabbard. Development of an Axial-Flow Centrifugal Gas Bubble Separator for Use in Msr Xenon Removal System. Technical Report ORNL-TM–4533, Oak Ridge National Lab., Tenn. (USA), March 1974. URL: `https://www.osti.gov/scitech/biblio/4324438`, `doi:10.2172/4324438`.

[43] Emden R. Gansner, Stephen C. North, and Eleftherios Koutsofios. Drawing graphs with dot. *AT&T Bell Laboratories*, 1996. URL: `https://www.graphviz.org/pdf/dotguide.pdf`.

[44] Nuria García-Herranz, Oscar Cabellos, Javier Sanz, Jesús Juan, and Jim C. Kuijper. Propagation of statistical and nuclear data uncertainties in Monte Carlo burn-up calculations. *Annals of Nuclear Energy*, 35(4):714–730, April 2008. URL: `http://www.sciencedirect.com/science/article/pii/S0306454907001958`, `doi:10.1016/j.anucene.2007.07.022`.

[45] Ian C. Gauld, Georgeta Radulescu, Germina Ilas, Brian D. Murphy, Mark L. Williams, and Dorothea Wiarda. Isotopic Depletion and Decay Methods and Analysis Capabilities in SCALE. *Nuclear Technology*, 174(2):169–195, May 2011. URL: `http://epubs.ans.org/?a=11719`, `doi:dx.doi.org/10.13182/NT11-3`.

[46] The HDF Group. Hierarchical data format, version 5, 1997. URL: `https://www.hdfgroup.org/solutions/hdf5/`.

[47] Paul N. Haubenreich and J. R. Engel. Experience with the Molten-Salt Reactor Experiment. *Nuclear Technology*, 8(2):118–136, February 1970. `doi:10.13182/NT8-2-118`.

[48] D. Heuer, E. Merle-Lucotte, M. Allibert, M. Brovchenko, V. Ghetta, and P. Rubiolo. Towards the thorium fuel cycle with molten salt fast reactors. *Annals of Nuclear Energy*, 64:421–429, February 2014. URL: `http://www.sciencedirect.com/science/article/pii/S0306454913004106`, `doi:10.1016/j.anucene.2013.08.002`.

[49] David Eugene Holcomb, Roger A. Kisner, and Sacit M. Cetiner. Instrumentation Framework for Molten Salt Reactors. Technical report, Oak Ridge National Lab.(ORNL), Oak Ridge, TN (United States), 2018. URL: `https://info.ornl.gov/sites/publications/Files/Pub111607.pdf`.

[50] Kathryn Huff. Enabling Load-Following Capability in the TAP MSR, December 2018. URL: `https://arpa-e.energy.gov/sites/default/files/1300%20Huff_approved.pdf`.

[51] IEA. Nuclear Power in a Clean Energy System. Technical report, IEA, May 2019. URL: `https://webstore.iea.org/nuclear-power-in-a-clean-energy-system`.

[52] V. Ignatiev, O. Feynberg, I. Gnidoi, A. Merzlyakov, A. Surenkov, V. Uglov, A. Zagnitko, V. Subbotin, I. Sannikov, A. Toropov, V. Afonichkin, A. Bovet, V. Khokhlov, V. Shishkin, M. Kormilitsyn, A. Lizin, and A. Osipenko. Molten salt actinide recycler and transforming system without and with Th-U support: Fuel cycle flexibility and key material properties. *Annals of Nuclear Energy*, 64(Supplement C):408–420, February 2014. `doi:10.1016/j.anucene.2013.09.004`.

[53] G. J. Janz, G. L. Gardner, Ursula Krebs, and R. P. T. Tomkins. Molten Salts: Volume 4, Part 1, Fluorides and Mixtures Electrical Conductance, Density, Viscosity, and Surface Tension Data. *Journal of Physical and Chemical Reference Data*, 3(1):1–115, January 1974. URL: `https://aip.scitation.org/doi/10.1063/1.3253134`, `doi:10.1063/1.3253134`.

[54] R. J. Kedl and A. Houtzeel. DEVELOPMENT OF A MODEL FOR COMPUTING Xe-135 MIGRATION IN THE MSRE. Technical report, Oak Ridge National Lab., Tenn., 1967.

[55] C. W. Kee and L. E. McNeese. MRPP: multiregion processing plant code. Technical Report ORNL/TM–4210, Oak Ridge National Lab., 1976.

[56] Brendan Kirby and M. Milligan. Method and case study for estimating the ramping capability of a control area or balancing authority and implications for moderate or high wind penetration. Technical report, National Renewable Energy Lab., Golden, CO (US), 2005.

[57] Holger Krekel, Bruno Oliveira, Ronny Pfannschmidt, Floris Bruynooghe, Brianna Laugher, and Florian Bruhin. pytest: Python testing tool, 2004. URL: `https://github.com/pytest-dev/pytest`.

[58] John R. Lamarsh and Anthony John Baratta. *Introduction to nuclear engineering*, volume 3. Addison-Wesley Massachusetts, 1975. URL: `http://gwardok.hostingsiteforfree.com/q/introduction-to-nuclear-engineering-by-john-r-lamarsh.pdf`.

[59] David LeBlanc. Molten salt reactors: A new beginning for an old idea. *Nuclear Engineering and Design*, 240(6):1644–1656, June 2010. `doi:10.1016/j.nucengdes.2009.12.033`.

[60] David LeBlanc. Integral molten salt reactor, February 2015. URL: `http://www.google.com/patents/WO2015017928A1`.

[61] Jaakko Leppanen. Statistical uncertainties on number densities - Discussion forum for Serpent users, 2012. URL: `https://ttuki.vtt.fi/serpent/viewtopic.php?f=15&t=1556&p=3389&hilit=uncertainty+depletion#p3389`.

[62] Jaakko Leppanen, Ville Hovi, Timo Ikonen, Joona Kurki, Maria Pusa, Ville Valtavirta, and Tuomas Viitanen. The Numerical Multi-Physics project (NUMPS) at VTT Technical Research Centre of Finland. *Annals of Nuclear Energy*, 84:55–62, October 2015. URL: `http://www.sciencedirect.com/science/article/pii/S0306454914005532`, `doi:10.1016/j.anucene.2014.10.014`.

[63] Jaakko Leppanen, Maria Pusa, Tuomas Viitanen, Ville Valtavirta, and Toni Kaltiaisenaho. The Serpent Monte Carlo code: Status, development and applications in 2013. *Annals of Nuclear Energy*, 82:142–150, August 2014. `doi:10.1016/j.anucene.2014.08.024`.

[64] Jaakko Leppänen and Maria Pusa. Burnup calculation capability in the PSG2/Serpent Monte Carlo reactor physics code. *Proc. M&C*, pages 3–7, 2009. URL: `https://www.vttresearch.com/sites/default/files/julkaisut/muut/2009/MC2009.pdf`.

[65] R. B. Lindauer and C. K. McGlothlan. Design, Construction, and Testing of a Large Molten Salt Filter. *Oak Ridge National Laboratory, Tech. Rep. ORNL-TM-2478*, 1969.

[66] A. Lokhov. Load-following with nuclear power plants. *NEA News*, 29(2):18–20, 2011. URL: `http://inis.iaea.org/Search/search.aspx?orig_q=RN:43021104`.

[67] Alexey Lokhov. Technical and economic aspects of load following with nuclear power plants. *NEA, OECD, Paris, France*, 2011.

[68] Holger Ludwig, Tatiana Salnikova, Andrew Stockman, and Ulrich Waas. Load cycling capabilities of german nuclear power plants (NPP). *VGB powertech*, 91(5):38–44, 2011.

[69] Joanna Mcfarlane, Paul Allen Taylor, David Eugene Holcomb, and Willis Poore III. Review of Hazards Associated with Molten Salt Reactor Fuel Processing Operations. Technical report, Oak Ridge National Lab.(ORNL), Oak Ridge, TN (United States), 2019. URL: `https://info.ornl.gov/sites/publications/Files/Pub126864.pdf`.

[70] A. L. Nichols, M. Verpelli, and D. L. Aldama. *Handbook of nuclear data for safeguards: database extensions, August 2008*. IAEA, 2008.

[71] A. Nuttin, D. Heuer, A. Billebaud, R. Brissot, C. Le Brun, E. Liatard, J. M. Loiseaux, L. Mathieu, O. Meplan, E. Merle-Lucotte, H. Nifenecker, F. Perdu, and S. David. Potential of thorium molten salt reactorsdetailed calculations and concept evolution with a view to large scale energy production. *Progress in Nuclear Energy*, 46(1):77–99, January 2005. URL: `http://www.sciencedirect.com/science/article/pii/S0149197004000794`, `doi:10.1016/j.pnucene.2004.11.001`.

[72] OECD/NEA. The JEFF-3.1.2 Nuclear Data Library. Technical Report JEFF Report 24, OECD/NEA Data Bank, OECD/NEA, 2014.

[73] Jinsu Park, Yongjin Jeong, Hyun Chul Lee, and Deokjung Lee. Whole core analysis of molten salt breeder reactor with online fuel reprocessing. *International Journal of Energy Research*, 39(12):1673–1680, October 2015. URL: `http://doi.wiley.com/10.1002/er.3371`, `doi:10.1002/er.3371`.

[74] F. N. Peebles. Removal of Xenon-135 from Circulating Fuel Salt of the MSBR by Mass Transfer to Helium Bubbles. Technical Report ORNL-TM-2245, Oak Ridge National Laboratory, Oak Ridge, TN, United States, 1968.

[75] Nuclear Power. Production and Removal of Xenon 135, May 2020. https://www.nuclear-power.net/nuclear-power/reactor-physics/reactor-operation/xenon-135/. URL: `https://www.nuclear-power.net/nuclear-power/reactor-physics/reactor-operation/xenon-135/`.

[76] Transatomic Power. Transatomic Reactor Documentation, March 2019. original-date: 2018-11-08T00:08:31Z. URL: `https://github.com/transatomic/reactor`.

[77] J. J. Powers, T. J. Harrison, and J. C. Gehin. A new approach for modeling and analysis of molten salt reactors using SCALE. In *Transactions of the American Nuclear Society*, Sun Valley, ID, USA, July 2013. American Nuclear Society, 555 North Kensington Avenue, La Grange Park, IL 60526 (United States). URL: `https://www.osti.gov/scitech/biblio/22212758`.

[78] Maria Pusa and Jaakko Leppänen. Computing the matrix exponential in burnup calculations. *Nuclear science and engineering*, 164(2):140–150, 2010.

[79] Majdi I. Radaideh and Tomasz Kozlowski. Combining simulations and data with deep learning and uncertainty quantification for advanced energy modeling. *International Journal of Energy Research*, 43(14):7866–7890, 2019. _eprint: https://onlinelibrary.wiley.com/doi/pdf/10.1002/er.4698. URL: `https://onlinelibrary.wiley.com/doi/abs/10.1002/er.4698`, `doi:10.1002/er.4698`.

[80] Majdi I. Radaideh, Dean Price, and Tomasz Kozlowski. On using computational versus data-driven methods for uncertainty propagation of isotopic uncertainties. *Nuclear Engineering and Technology*, November 2019. URL: `http://www.sciencedirect.com/science/article/pii/S1738573319308551`, `doi:10.1016/j.net.2019.11.029`.

[81] Majdi Ibrahim Ahmad Radaideh. *A novel framework for data-driven modeling, uncertainty quantification, and deep learning of nuclear reactor simulations.* PhD Thesis, University of Illinois at Urbana-Champaign, 2019.

[82] B. T. Rearden and M.A. Jesse. SCALE Code System, Version 6.2. Technical Report ORNL/TM-2005/39, Oak Ridge National Laboratory, Oak Ridge, Tennessee, 2018.

[83] R. C. Robertson. Conceptual Design Study of a Single-Fluid Molten-Salt Breeder Reactor. Technical Report ORNL–4541, ORNL, January 1971.

[84] D. Rochman and C. M. Sciolla. NUCLEAR DATA UNCERTAINTY PROPAGATION FOR A TYPICAL PWR FUEL ASSEMBLY WITH BURNUP. *Nuclear Engineering and Technology*, 46(3):353–362, June 2014. URL: `http://www.sciencedirect.com/science/article/pii/S1738573315301303`, `doi:10.5516/NET.01.2014.712`.

[85] Andrei Rykhlevskii. Advanced online fuel reprocessing simulation for Thorium-fueled Molten Salt Breeder Reactor. Master's thesis, University of Illinois at Urbana-Champaign, Urbana, IL, April 2018. URL: `https://www.ideals.illinois.edu/handle/2142/101052`.

[86] Andrei Rykhlevskii. Computational Tools for Advanced Molten Salt Reactors Simulation, June 2018. URL: `http://arfc.github.io/pres/2018-04-07-comp-tools-msr.pdf`.

[87] Andrei Rykhlevskii, Jin Whan Bae, and Kathryn Huff. arfc/saltproc: Code for online reprocessing simulation of molten salt reactor with external depletion solver SERPENT. *Zenodo*, July 2018. `doi:10.5281/zenodo.1306628`.

[88] Andrei Rykhlevskii, Jin Whan Bae, and Kathryn D. Huff. Modeling and simulation of online reprocessing in the thorium-fueled molten salt breeder reactor. *Annals of Nuclear Energy*, 128:366–379, June 2019. URL: `http://www.sciencedirect.com/science/article/pii/S0306454919300350`, `doi:10.1016/j.anucene.2019.01.030`.

[89] Andrei Rykhlevskii, Benjamin R. Betzler, Andrew Worrall, and Kathryn D. Huff. Fuel Cycle Performance of Fast Spectrum Molten Salt Reactor Designs. In *Proceedings of Mathematics and Computation 2019*, Portland, OR, August 2019. American Nuclear Society.

[90] Andrei Rykhlevskii and Kathryn Huff. Milestone 2.1 Report: Demonstration of SaltProc. Milestone Report UIUC-ARFC-2019-04 DOI: 10.5281/zenodo.3355649, University of Illinois at Urbana-Champaign, Urbana, IL, June 2019. URL: `https://zenodo.org/record/3355649#.XZuyEEFKjdI`, `doi:10.5281/zenodo.3355649`.

[91] Andrei Rykhlevskii and Kathryn D. Huff. SaltProc output for TAP MSR and MSBR online reprocessing depletion simulations. 2020. Publisher: University of Illinois at Urbana-Champaign. URL: `https://databank.illinois.edu/datasets/IDB-7364919`, `doi:10.13012/B2IDB-7364919_V1`.

[92] Andrei Rykhlevskii, Alexander Lindsay, and Kathryn D. Huff. Full-core analysis of thorium-fueled Molten Salt Breeder Reactor using the SERPENT 2 Monte Carlo code. In *Transactions of the American Nuclear Society*, Washington, DC, United States, November 2017. American Nuclear Society.

[93] Andrei Rykhlevskii, Alexander Lindsay, and Kathryn D. Huff. Online reprocessing simulation for thorium-fueled molten salt breeder reactor. In *Transactions of the American Nuclear Society*, Washington, DC, United States, November 2017. American Nuclear Society.

[94] Andrei Rykhlevskii, Daniel O'Grady, Tomasz Kozlowski, and Kathryn D. Huff. The Impact of Xenon-135 on Load Following Transatomic Power Molten Salt Reactor. In *Transactions of the American Nuclear Society*, Washington, DC, United States, November 2019. American Nuclear Society.

[95] Eizo Sada, Hidehiro Kumazawa, Choul Ho Lee, and Hiroaki Narukawa. Gas-liquid interfacial area and liquid-side mass-transfer coefficient in a slurry bubble column. *Industrial & engineering chemistry research*, 26(1):112–116, 1987.

[96] Anthony Scopatz, Paul K. Romano, Paul P. H. Wilson, and Kathryn D. Huff. PyNE: Python for Nuclear Engineering. In *Transactions of the American Nuclear Society*, volume 107, San Diego, CA, USA, November 2012. American Nuclear Society.

[97] R. J. Sheu, C. H. Chang, C. C. Chao, and Y. W. H. Liu. Depletion analysis on long-term operation of the conceptual Molten Salt Actinide Recycler & Transmuter (MOSART) by using a special sequence based on SCALE6/TRITON. *Annals of Nuclear Energy*, 53:1–8, March 2013. URL: `http://www.sciencedirect.com/science/article/pii/S0306454912004173`, `doi:10.1016/j.anucene.2012.10.017`.

[98] Kirk Sorensen. One-Fluid MSBR Chemical Processing -, 2006. URL: `http://energyfromthorium.com/history/msbr-design-one-fluid-chem/`.

[99] Kirk Sorensen. Liquid-Fluoride Thorium Reactor Development Strategy. In *Thorium Energy for the World*, pages 117–121. Springer, 2016.

[100] Eliza Strickland. Transatomic power building a "walk-away safe" reactor. *IEEE Spectrum*, 51(7):25–26, July 2014. `doi:10.1109/MSPEC.2014.6840794`.

[101] Sebastian Svanström. *Load following with a passive reactor core using the SPARC design.* 2016.

[102] Toshikazu TAKEDA, Naoki HIROKAWA, and Tomohiro NODA. Estimation of Error Propagation in Monte-Carlo Burnup Calculations. *Journal of Nuclear Science and Technology*, 36(9):738–745, September 1999. Publisher: Taylor & Francis _eprint: https://doi.org/10.1080/18811248.1999.9726262. `doi:10.1080/18811248.1999.9726262`.

[103] Masayuki Tohjoh, Tomohiro Endo, Masato Watanabe, and Akio Yamamoto. Effect of error propagation of nuclide number densities on Monte Carlo burn-up calculations. *Annals of Nuclear Energy*, 33(17):1424–1436, November 2006. URL: `http://www.sciencedirect.com/science/article/pii/S0306454906001915`, `doi:10.1016/j.anucene.2006.09.010`.

[104] Reginald PT Tomkins and Narottam P. Bansal. *Gases in molten salts*, volume 45. Elsevier, 2016.

[105] Transatomic Power Corporation. Neutronics Overview. White Paper 1.1, Transatomic Power Corporation, Cambridge, MA, United States, November 2016. URL: `http://www.transatomicpower.com/new-neutronics-white-paper-2/`.

[106] Transatomic Power Corporation. Technical White Paper. White Paper 2.1, Transatomic Power Corporation, Cambridge, MA, United States, November 2016. URL: `http://www.transatomicpower.com/wp-content/uploads/2015/04/TAP-White-Paper-v2.1.pdf`.

[107] Transatomic Power Corporation. The Lost Moderator: The use of Zirconium Hydride in Reactor Application. White Paper 1.0, Transatomic Power Corporation, Cambridge, MA, United States, June 2018.

[108] Travis. travis-ci/travis-api, 2016. URL: `https://github.com/travis-ci/travis-api`.

[109] Nicholas Tsoulfanidis. *The Nuclear Fuel Cycle*. American Nuclear Society, La Grange Park, Illinois, USA, 2013. 00177.

[110] Wartsila. Combustion Engine vs Gas Turbine- Ramp rate, May 2020. https://www.wartsila.com/energy/learn-more/technical-comparisons/combustion-engine-vs-gas-turbine-startup-time. URL: `https://www.wartsila.com/energy/learn-more/technical-comparisons/combustion-engine-vs-gas-turbine-startup-time`.

[111] C. J. Werner. MCNP - A General Monte Carlo N-Particle Transport Code, 2017. URL: `http://mcnp.lanl.gov`.

[112] M. E. Whatley, L. E. McNeese, W. L. Carter, L. M. Ferris, and E. L. Nicholson. Engineering development of the MSBR fuel recycle. *Nuclear Applications and Technology*, 8(2):170–178, 1970. `doi:10.13182/NT70-A28623`.

[113] M. L. Williams, G. Ilas, M. A. Jessee, B. T. Rearden, D. Wiarda, W. Zwermann, L. Gallner, M. Klein, B. Krzykacz-Hausmann, and A. Pautz. A Statistical Sampling Method for Uncertainty Analysis with SCALE and XSUSA. *Nuclear Technology*, 183(3):515–526, September 2013. Publisher: Taylor & Francis _eprint: https://doi.org/10.13182/NT12-112. `doi:10.13182/NT12-112`.

[114] Timothy Joseph Wyant. *Numerical study of error propagation in Monte Carlo depletion simulations*. Thesis, Georgia Institute of Technology, June 2012. URL: `https://smartech.gatech.edu/handle/1853/44809`.

[115] S Yamanaka, K Yoshioka, M Uno, M Katsura, H Anada, T Matsuda, and S Kobayashi. Thermal and mechanical properties of zirconium hydride. *Journal of Alloys and Compounds*, 293-295:23–29, December 1999. URL: `http://www.sciencedirect.com/science/article/pii/S0925838899003898`, `doi:10.1016/S0925-8388(99)00389-8`.

[116] Dalin Zhang, Limin Liu, Minghao Liu, Rongshuan Xu, Cheng Gong, Jun Zhang, Chenglong Wang, Suizheng Qiu, and Guanghui Su. Review of conceptual design and fundamental research of molten salt reactors in China. *International Journal of Energy*

Research, 42(5):1834–1848, 2018. URL: `http://onlinelibrary.wiley.com/doi/10.1002/er.3979/abstract`, `doi:10.1002/er.3979`.

Appendix A: Reconfigurable moderator in TAP core

Table A.1: Geometric details for the full-core 3D model of the TAP with various moderator rod assemblies configurations.

Case	Number of $ZrH_{1.66}$ rods in the quarter core	SVF	Moderator-to-fuel ratio
1 (BOL)	347	0.917204	0.09027
2	406	0.903126	0.10727
3	427	0.898115	0.11344
4	505	0.879503	0.13700
5	576	0.862563	0.15933
6	633	0.848962	0.17791
7	681	0.837509	0.19402
8	840	0.799571	0.25067
9	880	0.790026	0.26578
10	900	0.785254	0.27347
11	988	0.764257	0.30846
12	1126	0.731329	0.36737
13	1338	0.680744	0.46898
14	1498	0.642567	0.55626
15 (EOL)	1668	0.602004	0.66112

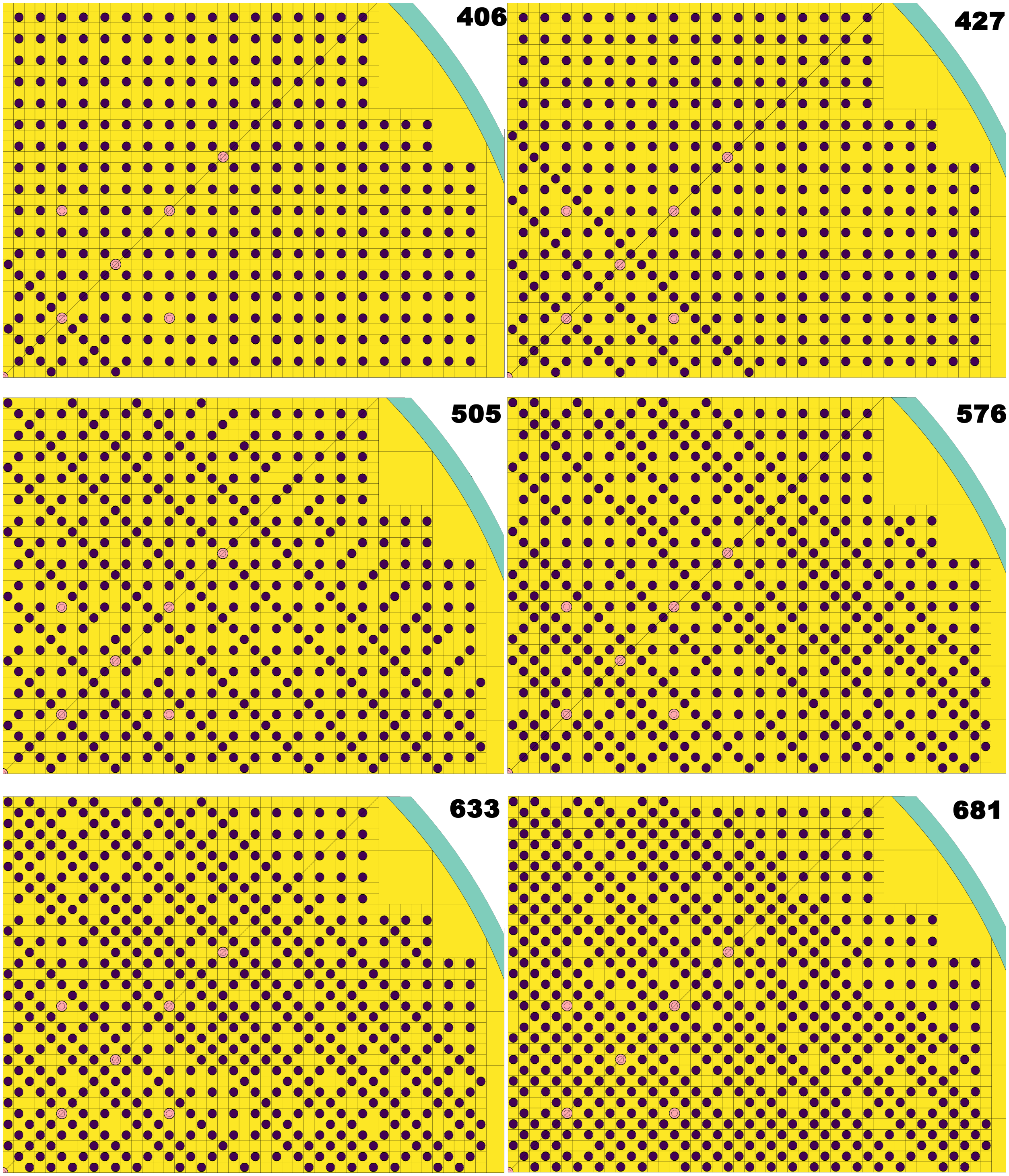

Figure A.1: An XY section of the TAP model at horizontal midplane for the first six years of operation (excluding startup moderator rods configuration) with the SVF between 0.91 and 0.84. The number in the top-right corner of each figure indicates the number of moderator rods in the case.

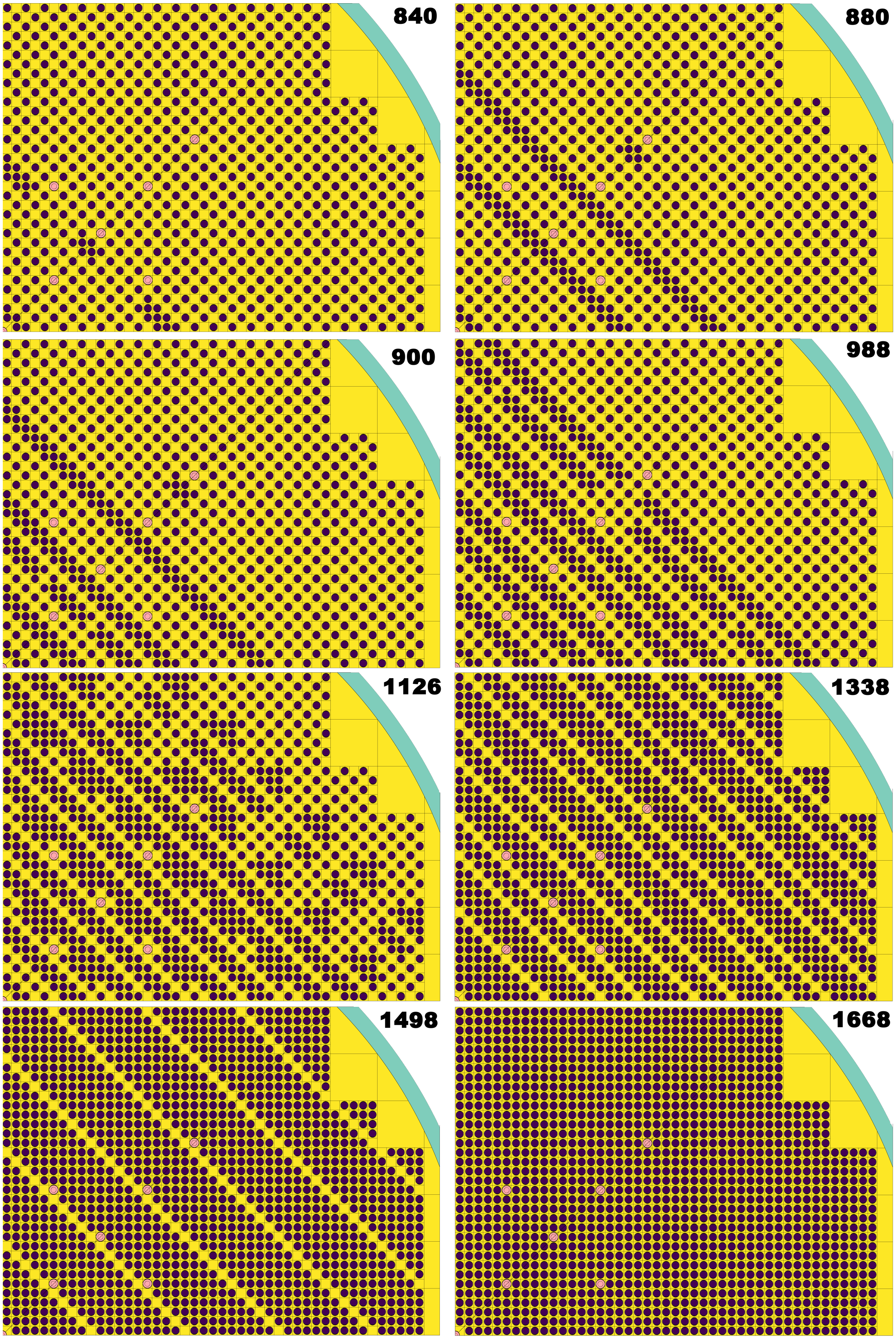

Figure A.2: An XY section of the TAP model at horizontal midplane the SVF between 0.8 and 0.6. The number in the top-right corner of each figure indicates the number of moderator rods in the case.